UNIVERSIDAD COMPLUTENSE DE MADRID

FACULTAD DE CIENCIAS QUÍMICAS

TESIS DOCTORAL

Cr(VI)-free surface treatments for aluminium alloys

Tratamientos superficiales libres de Cr(VI) para aleaciones de aluminio

MEMORIA PARA OPTAR AL GRADO DE DOCTOR

PRESENTADA POR

Rubén del Olmo Martínez

DIRECTORES

Raúl Arrabal Durán
Endzhe Matykina

© Rubén del Olmo Martínez, 2021

UNIVERSIDAD COMPLUTENSE DE MADRID

FACULTAD DE CIENCIAS QUÍMICAS

DEPARTAMENTO DE INGENIERÍA QUÍMICA Y DE MATERIALES

TESIS DOCTORAL

Cr(VI)-free surface treatments for aluminium alloys

Tratamientos superficiales libres de Cr(VI) para aleaciones de aluminio

MEMORIA PARA OPTAR AL GRADO DE DOCTOR PRESENTADA POR

Rubén del Olmo Martínez

DIRECTORES:

Dr. Raúl Arrabal Durán

Dra. Endzhe Matykina

Madrid, 2021

AGRADECIMIENTOS

En primer lugar, me gustaría agradecer a mis directores de tesis por todo lo que me han enseñado y ayudado en esta etapa. Raúl y Endzhe, muchas gracias por las eternas reuniones, vuestro apoyo a nivel personal, por todo lo que me habéis enseñado y el tiempo que me habéis dedicado from TFG to PhD.

A Marta y Bea por los buenos consejos y a enseñarme a adorar la science, sois dos grandes ejemplos a seguir. A toda la gente que ha formado y forma parte del grupo (Borja, Larita, Hugo, David, María Miguel, Yani, Ewa, Morty, etc.) por hacer esta etapa mucho más divertida y amena.

I would like to express my gratitude to all people from the Corrosion technology and electrochemistry group (TUDelft) for making this experience much more rewarding. Especially to Prof.dr.ir. Arjan Mol and Dr. Ursa Tiringer their priceless support, meetings during my research stay and make me feel at home.

A nivel más personal, la primera y más especial dedicatoria es para Mº Isabel Martínez y Miguel Ángel del Olmo, mis padres. Habéis sacrificado todo por mí, me habéis dado todo vuestro amor, valores y apoyo constante durante toda mi vida y, gracias a eso, soy quien soy y estoy donde estoy. Jamás podré devolveros todo lo que habéis hecho por mí. Carla, gracias por ser como eres, por estar siempre ahí, dejar que te robe el pan, enseñarme inglés y porque esta etapa y mi vida hubiese sido muy aburrida sin ti.

A los de siempre: Jony, Carlos, Adel, Romu, Juli, Rober, Luisa, Adri, Barco, Jorge, Javi, etc. Gracias por todas las tanadas, partidas de mus y reno renardo hasta en la sopa. Me siento muy afortunado de teneros como amigos. Pero tranquis, la primera pago yo porque… *"¿Y esto quien lo paga?"*.

Como no, para los que fueron compis de laboratorio y ahora son amigos: Ana, Vane, Mumu, Rober y un largo etcétera. Especialmente a Ángela Valentín, a la que quiero incondicionalmente y allá donde esté, estaría orgullosa de verme aquí…..*"Si la cançó mata la pena, som emisaris de la mort"*.

A el grupo de la Química aplicada a la cocteleria (José Luis, Javi y Óscar) por hacerme esta etapa mucho más amena, por vuestro apoyo constante y porque la vida se ve mejor con cócteles. En especial a Emilio, por contar conmigo, por llevarme en coche cada mañana pero sobre todo, por tu amistad.

Ana, estoy muy feliz de tenerte en mi vida, muchas gracias por tu consejos, por todo tu apoyo y en definitiva, por aguantarme y hacerme mucho más feliz esta etapa. Me gustaría agradecer a la familia Santos y a las Coquis por haberme incluido en la familia como uno más, especialmente a Gonzalo y MºJosé.

Table of contents

ABSTRACT

The most critical challenge in the aircraft industry is to reduce the operating costs, increase the aircraft's payload and, more importantly, to reduce the environmental impact during the whole life of the product. This can be achieved by decreasing the fuel consumption, hence by decreasing the material density. For that, the Al-Cu system has been the most widely used structural material for commercial aircrafts due to its unique high strength-to-weight ratio. Nevertheless, the main limitation of Al-Cu alloys is their low corrosion resistance in aggressive environments.

Currently, in order to overcome this limitation, Al-Cu alloys are usually surface treated to ensure the highest corrosion protection. Unfortunately, current surface treatments contain Cr(VI)-based compounds, which are categorized as highly toxic and carcinogenic. However, the lack of Cr(VI)-free alternatives has led to a setback of the new sunset date for Cr(VI) compounds elimination to 2024. On that basis, the development of novel Cr-free surface treatments has been targeted as the main challenge for aluminium in the aircraft industry.

The literature review carried out in the **Introduction** summarizes the specificities of Cr(VI) replacement and the alternatives that have been identified in the past. Both traditional and new surface treatments are reviewed. Besides, the suitability of novel processing methods such as additive manufacturing (AM) has been also identified as an important challenge for aluminium alloys, especially for Al-Si alloys.

The **Objective** of this Thesis is to address the most relevant challenges for aluminium in the aircraft industry in terms of protective surface treatments. In this context, the main challenge is to develop multifunctional Cr(VI)-free surface treatments on an Al-Cu alloy that are also compatible with Cr-free paints and novel sealing post-treatments. Another challenge is to study the formation of wear-resistant coatings on an AM Al-Si alloy.

Chapter 1 evaluates the corrosion resistance of anodizing surface treatments applied on a commercial Al-Cu alloy (AA2024-T3) for corrosion- and fatigue-sensitive applications. Different anodizing procedures that combine the highest corrosion resistance-to-thickness ratio were selected and evaluated after several screening processes for painted and non-painted components. For painted components, the *in situ* incorporation of cerium species into conventional sulphuric acid anodizing (SAA) and tartaric-sulphuric acid anodizing (TSA) was evaluated in terms of morphology, corrosion resistance, fatigue strength and

paint adhesion. The effect of Ce in short-term corrosion resistance was only noticeable in anodic films developed in SAA electrolyte. Ce-containing films were comparable to chromic acid anodizing (CAA) films in terms of long-term corrosion resistance, fatigue resistance and paint adhesion. For non-painted components, the *in situ* incorporation of different organic inhibitors into SAA and TSA electrolytes was also evaluated in terms of corrosion resistance. The *in situ* incorporation of citric acid in SAA electrolyte revealed a clear corrosion improvement and was further selected for hybrid sol-gel (HSG) sealing post-treatments with incorporated Li- and Ce-species. The Ce-loaded HSG coating showed the best self-healing properties.

In **Chapter 2**, "flash" plasma electrolytic oxidation (flash-PEO) is explored as an energy-efficient and eco-friendly strategy for painted and non-painted components. For that purpose, a preliminary study on commercially pure aluminium (AA1050-H18 alloy) was performed to study the main variables involved in the flash-PEO coating formation and energy consumption. To adapt the flash-PEO process for non-painted components, LDH sealing post-treatments were also studied in both pure aluminium and some selected flash-PEO coatings. Once the main factors involved in the flash-PEO coating formation were ascertained, the *in situ* incorporation of inhibitors in the polyphosphate-based electrolyte was evaluated as a strategy for corrosion protection of AA2024-T3 alloy for painted components. The *in situ* incorporation of Ce and EDTA yielded the best paint adhesion and the highest long-term corrosion resistance among all the evaluated coatings.
For non-painted components, LDH and lauric acid sealing strategies were evaluated in a selected flash-PEO coating on the AA2024-T3 alloy. However, the inhibitor-loading in LDH post-treatment was proved detrimental to the studied LDH formulations, whereas the lauric acid sealing for non-painted components was successful.

In **Chapter 3**, LDH coatings formed by *in situ* growth method on AA2024-T3 alloy are investigated as a new Cr-free conversion coating alternative for painted components in the aircraft industry. The first section of this chapter is focused on the development and screening of different LDH compositions at different operating conditions. As a result, Zn-Al-LDH and Ca-Al-LDH coatings were selected for further inhibitor-loading stage due to their optimal surface appearance and corrosion resistance-to-thickness ratio. The intercalation of Mn into the Ca-Al-LDH structure was successful, ensuring enhanced long-term corrosion resistance and excellent paint adhesion.

Chapter 4 was focused on the characterization and tribological evaluation of hard anodizing (HA) and PEO coatings on an Al10SiMg alloy obtained via AM for wear-sensitive applications. A361 cast alloy was also used for comparison. Findings revealed that the microstructure of the AM, which consisted of α-Al cells enclosed in a 3D Si network, produced more homogeneous coatings in comparison to the cast alloy. Regarding the hardness of the coatings, the formation of crystalline SiO_2 reduced the hardness and increased the wear rates of the AM-PEO specimens in comparison to the A361-PEO coating. For the AM alloy, both HA and PEO treatments demonstrated improved wear resistance compared to the bare substrates. More specifically, the wear rate was one order and two orders of magnitude lower for the HA coatings and PEO coatings, respectively.

As a result, the findings from **Chapters 1** to **3** disclosed the effects of the key steps of a Cr(VI)-free multi-layered systems for corrosion protection of aluminium in aircraft structures for painted and non-painted components. In **Chapter 4**, the findings confirmed the suitability of wear-resistant PEO coatings for Al-Si alloys obtained by AM processing method.

Resumen

RESUMEN

El reto más importante de la industria aeronáutica es reducir los costes de explotación, aumentar la carga útil del avión y, lo que es más importante, reducir el impacto medioambiental durante toda la vida útil del producto. Esto puede lograrse disminuyendo el consumo de combustible y, por tanto, la densidad de los materiales. En este sentido, el sistema Al-Cu ha sido el material estructural más utilizado para las aeronaves comerciales debido a su exclusiva y elevada relación resistencia-densidad. Sin embargo, la principal limitación de las aleaciones de Al-Cu es su baja resistencia a la corrosión en ambientes agresivos.

En la actualidad, con el objetivo de superar esta limitación, las aleaciones de Al-Cu suelen ser tratadas superficialmente para garantizar su máxima protección contra la corrosión. Desgraciadamente, los tratamientos superficiales actuales contienen compuestos a basados en Cr(VI), que están clasificados como altamente tóxicos y cancerígenos. Sin embargo, la falta de tratamientos alternativos libres Cr(VI) ha provocado un retraso en la nueva fecha de eliminación de los compuestos de Cr(VI) hasta 2024. En este contexto, el desarrollo de nuevos tratamientos superficiales de Cr(VI) se ha convertido en el principal reto para el aluminio en la industria aeronáutica. La revisión bibliográfica realizada en la **Introducción** resume las especificidades de la sustitución del Cr(VI) y las diferentes alternativas que se han investigado hasta la fecha. Se revisan tanto los tratamientos superficiales tradicionales como los más actuales. Además, la idoneidad de los nuevos métodos de procesamiento, como la fabricación aditiva (FA), también se ha identificado como un reto importante para las aleaciones de aluminio, especialmente para las aleaciones Al-Si.

El objetivo de esta Tesis es abordar los retos más relevantes para el aluminio en la industria aeronáutica en términos de tratamientos superficiales para protección frente a corrosion. En este sentido, el reto principal es desarrollar tratamientos superficiales multifuncionales libres de Cr(VI) en una aleación de Al-Cu y que también sean compatibles con pinturas libres de Cr y con novedosos post-tratamientos de sellado. El reto secundario es estudiar la formación de recubrimientos resistentes al desgaste sobre una aleación Al-Si producida por FA.

El **Capítulo 1** evalúa la resistencia a la corrosión de los tratamientos superficiales de anodizado sobre una aleación comercial de Al-Cu (AA2024-T3) para aplicaciones

sensibles a corrosión y fatiga. Se seleccionaron y se evaluaron diferentes procedimientos de anodizado que combinan la mayor relación resistencia a la corrosión/espesor tras varios procesos de selección para componentes pintados y no pintados. Para los componentes pintados, se evaluó la incorporación *in situ* de compuestos de cerio en el anodizado convencional con ácido sulfúrico (SAA) y en el anodizado con ácido tartárico-sulfúrico (TSA) en términos de morfología, resistencia a la corrosión, fatiga y adhesión de la pintura. El efecto del Ce en la resistencia a la corrosión a corto plazo sólo fue notable en las capas anódicas desarrolladas en el electrolito SAA. La incorporación de Ce se confirmó en la parte exterior de la película y produjo una notable alineación de los poros. Además, la resistencia a la corrosión a largo plazo, la resistencia a la fatiga y la adhesión de la pintura mejoraron considerablemente tras la incorporación de Ce en la capa anódica. Para los componentes no pintados, también se evaluó la incorporación *in situ* de diferentes inhibidores orgánicos en los electrolitos SAA y TSA en términos de resistencia a la corrosión. La incorporación *in situ* de ácido cítrico en el electrolito SAA reveló una clara mejora de la corrosión y se seleccionó además para el post-tratamiento de sellado híbrido sol-gel (HSG). Además, para evaluar la posible capacidad de auto-reparación del recubrimiento HSG, se evaluaron los recubrimientos HSG con Li y Ce. En este sentido, se consiguió una óptima protección activa contra la corrosión para el recubrimiento HSG cargado con Ce.

En el **Capítulo 2**, se estudia la oxidación electrolítica por plasma "flash" (flash-OEP) como una estrategia energéticamente eficiente y ecológica para componentes pintados y no pintados. Para ello, se realizó un estudio preliminar sobre aluminio comercialmente puro (aleación AA1050-H18) para analizar las principales variables que intervienen en la formación del recubrimiento flash-OEP y el consumo de energía. Para adaptar el proceso de flash-OEP a los componentes no pintados, se estudiaron también los post-tratamientos de sellado mediante hidróxidos doble laminares (HDL) tanto en aluminio puro como en algunos recubrimientos flash-OEP seleccionados. Una vez determinados los principales factores que intervienen en la formación de los recubrimientos flash-OEP, se evaluó la incorporación *in situ* de inhibidores en un electrolito base polifosfato como estrategia para la protección contra la corrosión de la aleación AA2024-T3 para componentes pintados. La incorporación *in situ* de Ce y EDTA produjo la mejor adhesión de la pintura y la mayor resistencia a la corrosión a largo plazo entre todos los recubrimientos evaluados.

Para los componentes no pintados, se evaluaron las estrategias de sellado con HDL y ácido láurico en un recubrimiento flash-OEP seleccionado sobre la aleación AA2024-T3. Sin embargo, la carga de inhibidores en el postratamiento HDL no resultó ser beneficiosa en los recubrimientos HDL estudiados, mientras que el sellado con ácido láurico para los componentes no pintados fue beneficioso.

En el **Capítulo 3**, se investigan los recubrimientos HDL formados por el método de crecimiento *in situ* sobre la aleación AA2024-T3 como un recubrimiento de conversión alternativo sin Cr para componentes pintados en la industria aeronáutica. La primera sección de este capítulo se centra en el desarrollo y la selección de diferentes composiciones de HDL a diferentes condiciones de síntesis. Como resultado, se seleccionaron los recubrimientos Zn-Al-LDH y Ca-Al-LDH para la carga de inhibidores debido a su óptimo aspecto superficial y a la relación resistencia a la corrosión/espesor. La intercalación de Mn en la estructura de Ca-Al-LDH fue exitosa, asegurando una mayor resistencia a la corrosión a largo plazo y una excelente adhesión de la pintura.

El **Capítulo 4** se centró en la caracterización y evaluación tribológica de los recubrimientos de anodizado duro (HA) y OEP sobre una aleación Al10SiMg obtenida mediante FA para aplicaciones sensibles a desgaste. También se utilizó la aleación de moldeo A361 a modo de comparativa. Los resultados revelaron que la microestructura de Al10SiMg (FA) consistía en células de α-Al encerradas en una red 3D de Si que dio lugar a la formación de recubrimientos más homogéneos en comparación con la aleación de moldeo. En cuanto a la dureza de los recubrimientos, la formación de SiO_2 cristalino redujo la dureza y aumentó la tasa de desgaste de las muestras de AM-PEO en comparación con el recubrimiento de A361-PEO. En el caso de la aleación FA, tanto los tratamientos FA como OEP demostraron una mayor resistencia al desgaste en comparación con los sustratos. Más concretamente, la tasa de desgaste fueron un orden y dos órdenes de magnitud menores para los recubrimientos de FA y OEP, respectivamente.

Como resultado, los resultados de los **Capítulos 1** a **3** revelaron los paso clave para desarrollar un sistema multicapa sin Cr(VI) para la protección contra la corrosión del aluminio en estructuras aeronáuticas para componentes pintados y no pintados. En el **Capítulo 4**, los resultados confirmaron la idoneidad de recubrimientos OEP resistentes al desgaste para las aleaciones de Al-Si obtenidas por FA.

List of Figures

List of Figures

List of Figures

List of Figures

List of Tables

List of Tables

List of Tables

Disclosure and Acknowledgements

Most of the experimental work including sample preparation, set-up and execution of surface treatments, corrosion tests (electrochemical impedance spectroscopy, laboratory-scale neutral salt spray test) and tribological tests have been carried out by the Author.

The Author has carried out characterization and analysis of the laboratory-size specimens by OM, SEM, TEM, XRD, RBS, as well as coating thickness measurements, surface metrology, wettability and paint adhesion tests.

XRD measurement were carried out at *Centro de Asistencia a la Investigación Difracción de Rayos X* of Complutense University of Madrid (Madrid, Spain). SEM and TEM studies were carried out at National Centre for Electron Microscopy (ICTS) of Complutense University of Madrid (Madrid, Spain). RBS measurements were performed at the Centre for Micro Analysis of Materials of Autonomous University of Madrid (Madrid, Spain). Nanoindentation tests were carried out at the Materials Science and Engineering Group of Rey Juan Carlos University (Madrid, Spain).

Up-scaling processes were carried out by the Author using Corrosion Technology and Electrochemistry Group facilities at *Technische Universiteit Delft* (Delft, The Netherlands). Hybrid sol-gel coatings were developed in collaboration with Dr. Ursa Tiringer which is gratefully acknowledged. Up-scaled coupons were painted industrially at Akzonobel (Sassenheim, The Netherlands) and collaboration of Dr. Peter Visser is gratefully acknowledged. Fatigue resistance of up-scaled coupons was evaluated at *Fundación Cidaut* (Valladolid, Spain) and collaboration of Alicia Rodriguez is gratefully acknowledged.

The data analysis was carried out in collaboration with Dr. Raúl Arrabal, Dr. Endzhe Matykina and Dr. Marta Mohedano.

This Thesis was enabled by funding from the following projects and scholarships, which is gratefully acknowledged:

- ALMAGIC project (EU, H2020 Clean Sky 2, Grant agreement N° 755515)
- ADITIMAT-CM (*Comunidad de Madrid* and the European Structural and Investment Fund S2018/NMT-4411)
- PROFABRICAD (MCIU/AEI/FEDER, UE, RTI2018-096391-B-C33)
- Erasmus+ programme Scholarship of Universidad Complutense de Madrid.

List of Publications

During the course of the Thesis several scientific manuscripts were prepared for publication in peer-reviewed journals:

Chapter 1

- **R. del Olmo**, U. Tiringer, I. Milošev, P. Visser, R. Arrabal, E. Matykina, J.M.C. Mol, *The effect of anodizing on hybrid sol-gel coatings applied on AA2024-T3 for active corrosion protection. Open Access. Submitted.*
- **R. del Olmo**, M. Mohedano, P. Visser, A. Rodriguez, E. Matykina , R. Arrabal, *Thin sulphuric acid anodizing of 2024 aluminium alloy with Cerium incorporation. Open access. Submitted.*

Chapter 2

- **R. del Olmo,** M. Mohedano, B. Mingo, R. Arrabal, and E. Matykina, LDH post-treatment of flash PEO coatings. Coatings, 2019. 9(6). *Open Access. DOI:10.3390/coatings0960354.*
- **R. del Olmo**, M. Mohedano, P. Visser, E. Matykina, and R. Arrabal, *Flash-PEO coatings loaded with corrosion inhibitors on AA2024*. Surface and coatings technology, 2020. 402. 126317. *Open Access. DOI:10.1016/j.surfcoat.2020.126317.*

Chapter 4

- H. Mora-Sanchez, **R. del Olmo**, J. Rams, B. Torres, M. Mohedano, E. Matykina, R. Arrabal, *Hard Anodizing and Plasma Electrolytic Oxidation of an Additively Manufactured Al-Si alloy. Submitted.*

The outcomes of Chapters 1 and 2 have been presented at various international conferences:

- **R. del Olmo**, M. Mohedano, R. Arrabal, A. Pardo, E. Matykina, *Corrosion protection for aluminium through PEO/LDH duplex systems (oral presentation)*, XV national meeting of material science, 2018, Salamanca (Spain).
- **R. del Olmo**, R. Arrabal, M. Mohedano, A. Rodriguez, A. Pardo, P. Visser, E. Matykina, *Ce-containing TSAA for corrosion protection of 2024-T3 aluminium alloy (oral presentation)*, EUROCORR, 2019, Seville (Spain).
- **R. del Olmo**, M. Mohedano, R. Arrabal, A. Pardo, P. Visser, E. Matykina, *Flash-PEO coatings on 2024-T3 (poster)*, EUROCORR, 2019, Seville (Spain).

List of Abbreviations

AC Alternating current

AM Additive manufacturing

BSA Boric-sulphuric acid anodizing

CAA Chromic acid anodizing

CC Conversion coating

CCC Chromium conversion coating

CPE Constant phase element

DC Direct current

E Elastic modulus

EDS Energy-dispersive X-ray spectroscopy

EIS Electrochemical impedance spectroscopy

GTS GPTMS-TEOS-Silica

H Hardness

HA Hard anodizing

HAZ Heat-affected zones

HSG Hybrid sol-gel

HWS Hot-water sealing

IMC Intermetallic compound

LDH Layered double hydroxide

MP Melt pool

MPB Melt pool borders

NSST Neutral salt spray test

OCP Open circuit potential

OM Optical microscopy

PBF Powder bed fusion

PEO Plasma electrolytic oxidation

PSA Phosphoric-sulphuric acid anodizing

RBS Rutherford backscattering spectrometry

SAA Sulphuric acid anodizing

SCA Sulphuric-citric acid anodizing

SCE Saturated calomel electrode

SEM Scanning electron microscope

SLM Selective laser melting

SPD Severe plastic deformation

SSM Semisolid metal processing

TEM Transmission Electron Microscope

TSA Tartaric-sulphuric anodizing

TSAA Thin sulphuric acid anodizing

XRD X-ray diffraction

|**Z**| impedance modulus

1. Introduction

1.1. Aluminium alloys in the aircraft industry

Over the last several decades, the aircraft industry has made considerable efforts towards reducing the weight of aircrafts and, consequently, the fuel consumption. Another significant challenge in this sector is cost reduction, which can be achieved by decreasing maintenance/operational costs, frequency of periodical controls and by increasing service life and number of passengers at a time [1]. According to the most common design trials, the best way of reducing the aircraft weight is by decreasing the material density; between 3 and 5 times more effective than increasing tensile strength, elastic modulus or damage tolerance. On that basis, the most promising light materials are based on aluminium, titanium, magnesium and composites [2-4].

As can be seen in **Table 1.1**, aluminium is one of the most interesting lightweight materials in the aircraft industry because of its relatively low price and singular combination of mechanical, physical and chemical properties (high specific strength, high electrical and thermal conductivity, good corrosion resistance in natural environments, ease of fabrication, ductility and good control of properties by thermo-mechanical treatments). In fact, aluminium alloys have been the primary structural materials for commercial and military aircrafts for almost 80 years.

Table 1.1. *Comparison of structural materials used in the aircraft industry [4-7].*

Material	Density ($kg\ m^{-3}$)	Yield strength (MPa)	Fatigue resistance (MPa at 10^7 cycles)	€ kg^{-1}
Al alloys	2720	109-439	68.2-169	2.22
Mg alloys	1810	109-216	75-140	2.58
Ti alloys	4610	470-1090	351-633	19.6
Steels	7800	257-1600	203-651	0.65-2.7
Composites	1550-1860	145-760	55-300	22.9-31.2

World aluminium production (~70 Mt/year) has continued to rise sharply year after year to reach an overall increase of 300% over 1995-2015. The main driving force behind this increasing demand is the aircraft industry [1, 2]. For instance, Boeing forecasts a need for 38.050 new aircrafts, valued at over 5.6 trillion dollars, over the next 20 years. Similarly, for the 2015-2034 period, Airbus Global Market foresees a demand for approximately 32.585 new passenger and freighter aircrafts at a value of around 4.9 trillion of dollars.

An additional advantage of aluminium over conventional materials is the widespread use of secondary or recycled material; 75% of all the aluminium ever produced is still in use today. However, the aircraft industry is reluctant to use secondary aluminium [8].

Aluminium alloys are categorized into cast and wrought alloys. The mechanical properties of cast and non-age-hardenable wrought alloys are often insufficient for aircraft structures, hence most of the aluminium used in highly loaded components is in the form of wrought heat-treatable alloys [9]. The latter include the 2XXX, 6XXX, 7XXX and 8XXX series (**Table 1.2**).

Table 1.2. *Examples of aluminium alloys used in aircraft structures [10-14].*

Required property	Aluminium alloy	Applications
Damage tolerant/ medium strength/ corrosion resistance	2024-T3, 2524-T3, 2524-T351 7050-T7451	Fuselage (clips, rivets, stringer/frames and skin panels) / Pressure cabin skins
Damage tolerant/ corrosion resistance	2024-T351, 2324-T39, 2624-T351, 2624-T39	Lower wing covers
Damage tolerant/ corrosion resistance	2024-T3, 2024-T3511, 2026-T3511, 2024-T4312, 6110-T6511 - Al-Li: 2196-T8511	Lower wing stringers, Fuselage/ Pressure cabin stringers
High strength	2219-T87	Launch vehicle, cryogenic tanks
High strength/ Corrosion resistance	7150-T7751, 7055-T7751, 7055-T7951, 7255-T7951	Upper wing covers
High strength	7175-T7351, 7050-T7452 - Al-Li: 2050-T84	Wing/Fuselage
Medium strength	7050-T7451	Spars, ribs, other internal structures
Medium/high strength/ Corrosion resistance	7075-T73511, 7075-T79511, 7150-T6511, T7175-T79511, 7055-T77511, 7055-T79511 - Al-Li: 2099-T83, 2196-T851	Fuselage stringers and frames, upper wing stringers, floor beams, seat rails

The 2XXX (Al-Cu) series has been the warhorse for damage tolerant-fatigue sensitive structures that require high specific strength. For instance, the well-known 2024 alloy is used in the fuselage (stringers, bulkhead and longerons), upper and lower wings (spars, carry-through, stressed skins) and internal structures (trusses), and in non-structural parts such as fairings cowlings, wheel pants and wing tips [9] (**Figure 1.1**).

Another important group of alloys is the 7XXX (Al-Zn) series which are used when high strength is the key factor. One example is the 7075 alloy or the more recent 7150, which is used in building upper wing skin, stringers and stabilizers [1, 9].

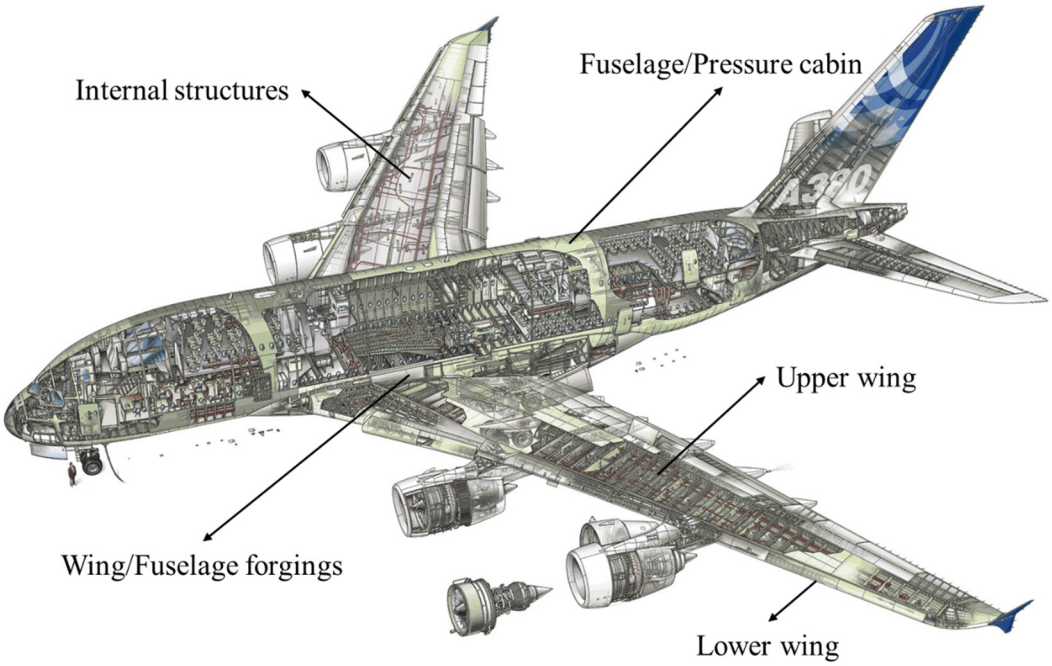

Figure 1.1. *Schematic view of the different parts in Airbus A380. Adapted from [11, 15].*

Figure 1.2 shows a simplified timeline of the introduction of some relevant 2XXX and 7XXX aluminium alloys in passenger aircrafts.

Figure 1.2. *Timeline of the introduction of some relevant 2XXX and 7XXX aluminium alloys in passenger aircrafts. Adapted from [11].*

1. Introduction

On average, aluminium alloys constitute 60–80% of the structural weight of the last decade passenger airliners [1, 4], e.g. 61 % in Airbus A380 [16]. However, the dominant use of aluminium alloys has been challenged recently. **Figure 1.3** shows the rapid increase of composites and titanium alloys in the latest Airbus and Boeing models. The attractiveness of titanium alloys and composite materials in the aerospace industry is mainly due to their high specific strength and superior corrosion and fatigue performances [4]. For example, instead of aluminium-graphite fibre composites, Boeing 7E7 series make use of more expensive composite-titanium systems in order to avoid galvanic corrosion issues [17]. However, continuous developments in chemically inert organic fibres of high elastic modulus may provide future opportunities for aluminium-composite multi-material approaches [18].

Figure 1.3. *Percentages of composites and titanium alloys used in Airbus and Boeing series aircraft. Adapted from [1, 4].*

1.2. Challenges for aluminium in the aircraft industry

Despite the evident importance of aluminium alloys in the aircraft industry, there are several limitations that need to be overcome in order for these alloys to remain attractive and to compete with other materials such as composites, titanium and magnesium. The most relevant limitations of aluminium alloys are their relatively low elastic modulus and fatigue strength and mechanical properties at elevated temperatures as well as susceptibility to stress-corrosion cracking and galvanic corrosion in contact with carbon-fibre-reinforced polymer composites [12, 17].

According to ALFED, the trade association representing the British aluminium industry, the demand for aluminium is forecasted to continue well into the future as building rates for single aisle and long-range aircraft continue to be ramped up [19]. As a direct consequence, some of the world´s largest and best-known aircraft manufacturers such as Airbus and Boeing [12, 17] have defined new aluminium alloy challenges that can be categorized into three groups (**Figure 1.4**). The successes and remaining challenges in these groups are briefly discussed in the following sections.

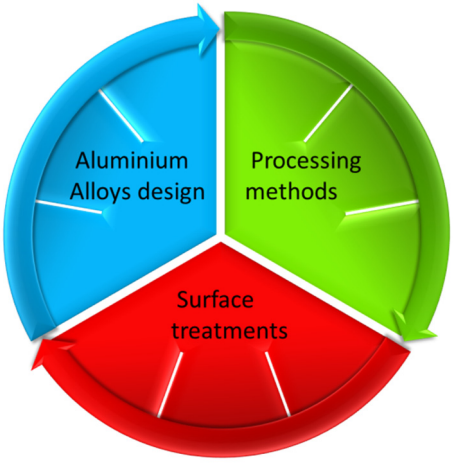

Figure 1.4. *Areas of research for aluminium alloys in the aircraft industry.*

1.2.1. Aluminium alloy design

Recent developments in 2XXX, 7XXX series and Al-Li alloys, mostly 8XXX, have been successful in tailoring the mechanical properties for aircraft applications (**Figure 1.5**). For instance, Sn, In, Cd and Ag have been used to refine the microstructure of 2XXX alloys. In 7XXX series, impurity control has shown to play an important role, e.g. 7475 alloy has a total Fe and Si concentration of 0.22 wt.% compared with 0.9 wt.% of the more conventional 7075 alloy [4].

1. Introduction

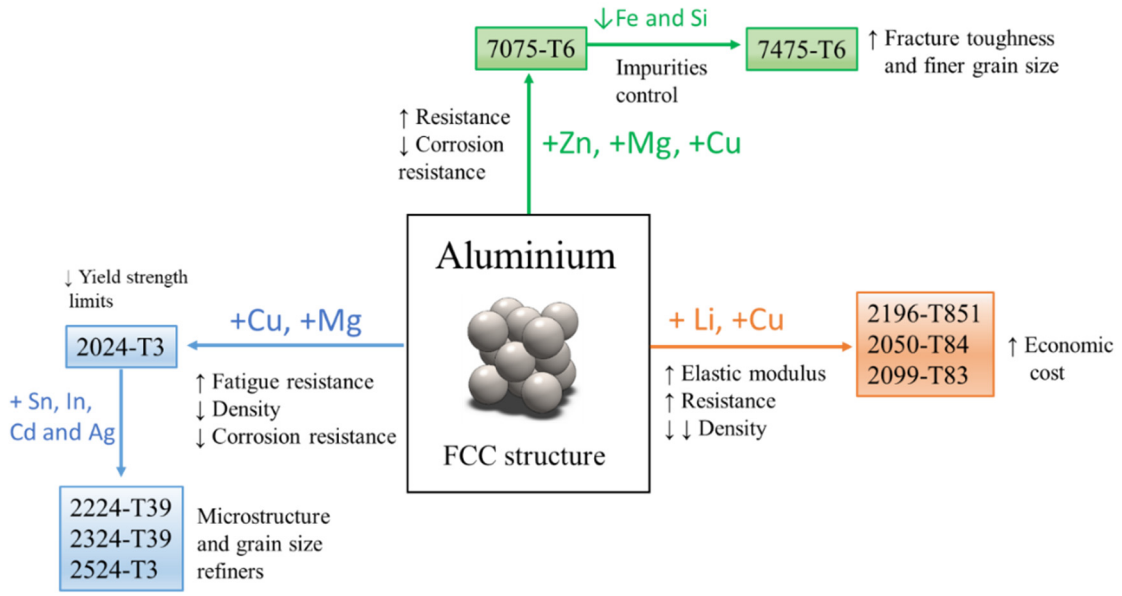

Figure 1.5. *Summary of aluminium alloys development in the aircraft industry. Adapted from [1, 4, 20].*

1.2.2. Processing methods

The need of metallic structures with complex geometries and improved mechanical properties at a lower cost has triggered the development of new processing methods. In case of aluminium alloys the latest efforts have been focusing on severe plastic deformation (SPD) [18, 21], semisolid metal processing (SSM) [22] and additive manufacturing (AM) [23, 24].

In recent years, AM has attracted a great deal of attention from many companies since it has the potential to replace or complement conventional processes [23, 25]. The number of publications and patents on AM of aluminium alloys has doubled from 2016 to 2019 [26]. Recent reports, such as the one written by the ADDISPACE Project, demonstrate that AM is becoming increasingly popular and will continue to grow at a very high rate in the next 5-15 years. Foreseen developments include reduced equipment costs (between 25-45% by 2020), higher production rates (e.g. combination of multiple lasers) and optimized control systems. In fact, this report forecasts a growth from 15.8 to 26.5 M$ in AM products and services between 2019 and 2021 [27].

AM encompasses a wide range of technologies where objects with complex geometries are manufactured from a three-dimensional (3D) computer model by adding layer upon-layer of material (**Figure 1.6**).

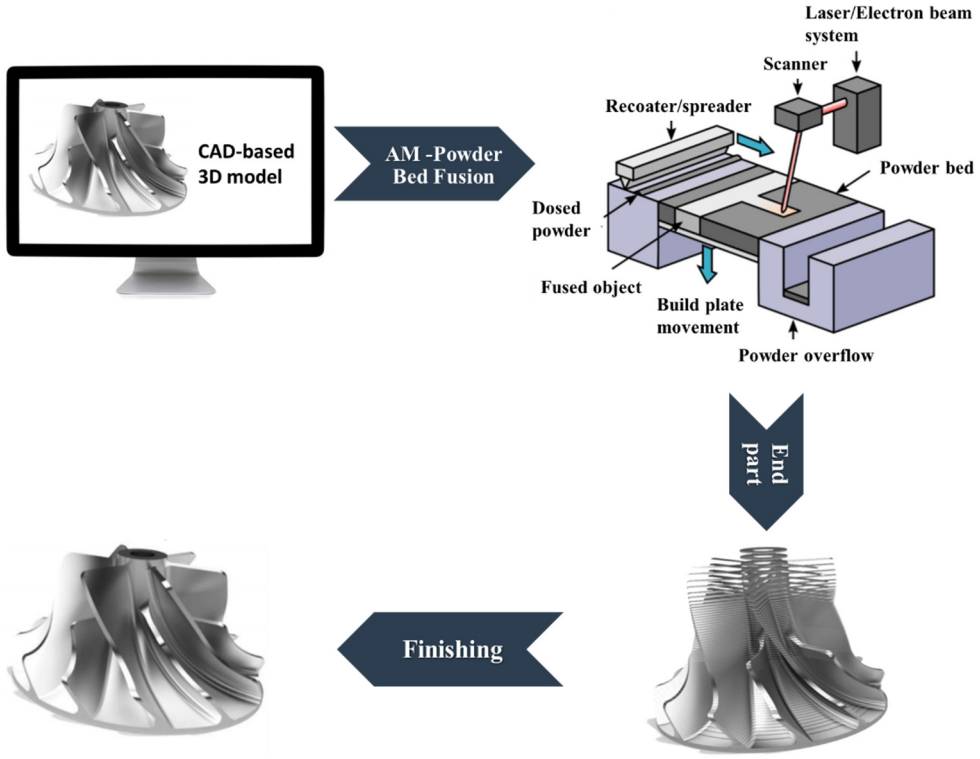

Figure 1.6. *Additive manufacturing process flow. Adapted from [28, 29].*

There are more than 30 AM technologies. Powder bed fusion (PBF), *i.e.* a set of AM technologies in which the solids are formed from the melting or sintering of the material in powder layers, and directed energy deposition (DED), *i.e.* when powders or wires are melted while they are sprayed or fed, are the two most relevant for AM of metals. Subcategories exist depending on the raw material (wire or powder) and energy source (laser, electron beam, etc.). Most suppliers of AM machines offer PBF with a laser source, as this method provides better surface finishing and greater freedom of design and a greater variety of raw materials compared with electron beam sources, although the production rate is lower [23, 28]. DED technologies have seen less frequent implementation due to their lower precision and need of postprocessing [30].

1.2.3. Surface treatments

Although the aluminium industry has made great advances from the alloy design and processing points of view, there are still major challenges in terms of surface treatments for corrosion protection. The most critical factors to consider are the corrosive environment (temperature, humidity, salinity and pollutants) and galvanic corrosion issues derived from the aircraft design itself, which inevitably involves multimaterial systems [14, 31, 32]. As a consequence, the aircraft industry is forced to follow costly inspection and maintenance procedures such as re-spray every 6 years [33].

1. Introduction

Aluminium alloys are highly susceptible to a wide range of corrosion mechanisms, including uniform corrosion, pitting, galvanic corrosion and stress-corrosion cracking. **Figure 1.7** shows examples of failed Al components due to several corrosion mechanisms.

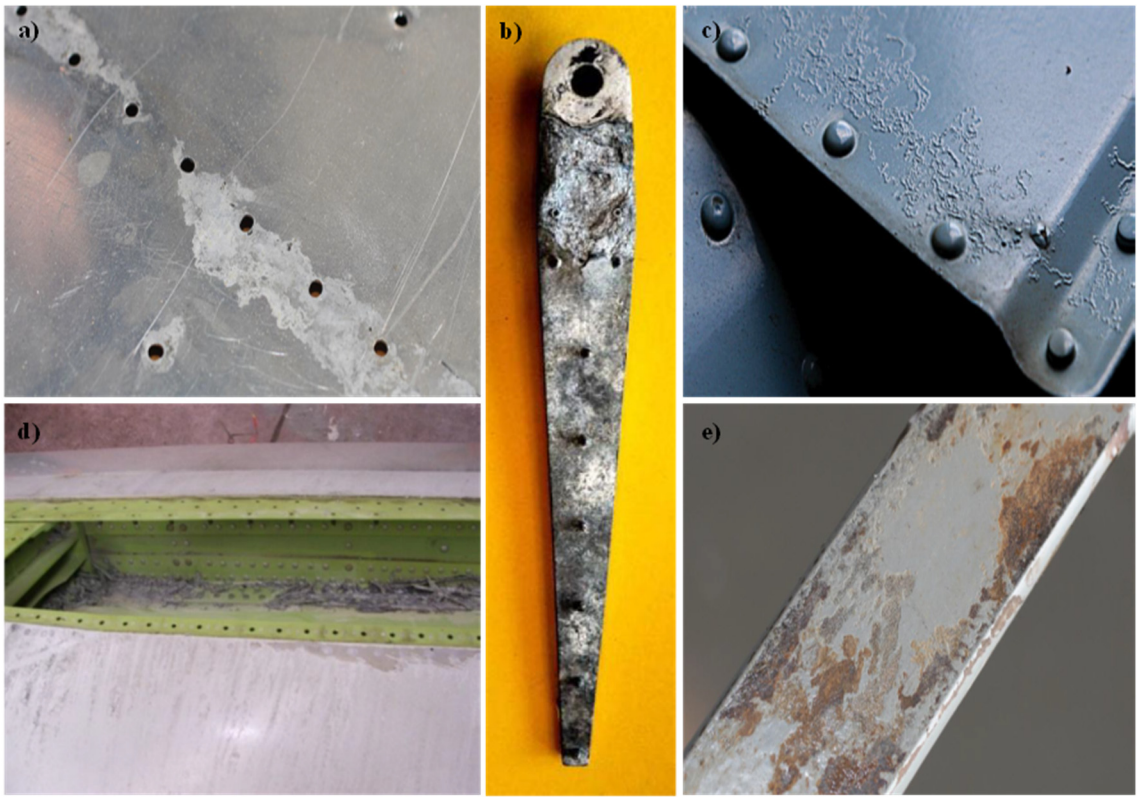

Figure 1.7. *Examples of (a) uniform corrosion, (b) galvanic corrosion (aluminium alloy on carbon contact, (c) filiform corrosion, (d) exfoliation corrosion and (e) stress corrosion in aircraft industry. Adapted from [32, 34].*

In general, two protection schemes are used in modern aircrafts (**Figure 1.8**). Interior coatings are designed to protect the structural parts of the aircraft (**Figure 1.8a**), whereas exterior systems are applied on the fuselage and other areas exposed to a huge range of environmental conditions, including corrosive species and stresses (**Figure 1.8b**). Both corrosion protection schemes consist of multiple layers. A pre-treatment which can be a chemical conversion coating or an anodic film is combined with multiple organic-based layers such as primers, base-, clear- and top-coats [35, 36].

As can be seen in **Figure 1.8c**, Cr(VI)-containing substances are used in many of these layers. There are four main reasons for this ubiquity of Cr such as excellent corrosion resistance, minimal impact on fatigue endurance, good paint adhesion and, in case of anodic films, no risk of corrosion due to acid residues in confined spaces [14].

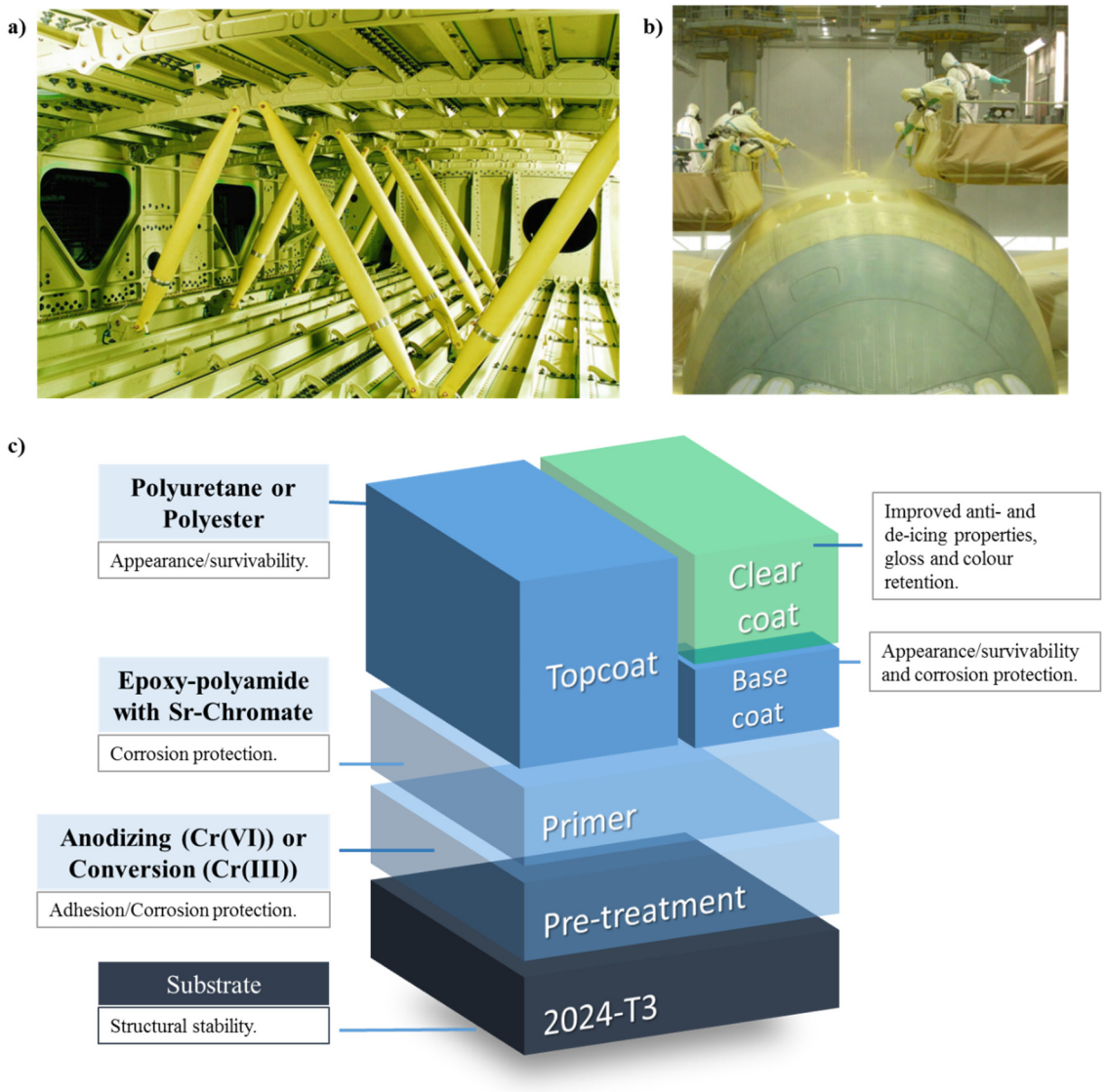

Figure 1.8. *Appearance of aircraft with (a) interior and (b) exterior corrosion protection schemes, and (c) general build-up of a coating system for interior and exterior components. Interior parts are finished with a topcoat, whereas exterior components can be finished with dual topcoat (base- and clear-coat). a and b) adapted from [36].*

Cr(VI)-based compounds are categorized as substances of very high concern (SVHC) and are listed on Annex XIV of REACH ("Authorisation List" [37]) due to their high toxicity and carcinogenic properties. In this context, serious efforts to find replacements for Cr(VI) substances have been ongoing within the aerospace industry during the last 30 years. The level of industry investment to date has been estimated to be at least €100 million [14].

One of the most critical challenges is to find alternatives to chromic acid anodizing (CAA). Tartaric-sulphuric anodizing (TSA) and boric-sulphuric anodizing (BSA),

developed by Airbus and Boeing, respectively, are two Cr-free alternatives that have achieved some degree of success. However, it should be noted that currently neither of these alternatives offer the all four combined benefits of CAA, which is still being used for critical components. The lack of Cr(VI)-free alternatives has led to new sunset dates for many Cr(VI) compounds. For instance, the sunset date of chromium trioxide (CrO_3) has moved from 21 September 2017 to 2024 [14].

1.3. Corrosion and surface treatments of Al-Cu alloys

1.3.1. Fundamentals of Al-Cu alloys corrosion and protection

Pure aluminium exhibits excellent corrosion resistance in many environments due to the formation of an adherent, compact and thin passive layer (2-10 nm) with self-healing properties. As illustrated by the Pourbaix diagram in **Figure 1.9**, passivity occurs between pH 4 and 8.5. However, there are many circumstances where breakdown of passivity occurs, resulting in aluminium dissolution ($Al \rightarrow Al^{3+} + 3e^-$) together with a cathodic reaction; oxygen reduction ($O_2 + 2H_2O + 4e^- \rightarrow 4OH^-$) or water reduction ($2H_2O + 2e^- \rightarrow 2OH^- + H_2$) in neutral and alkaline environments [38].

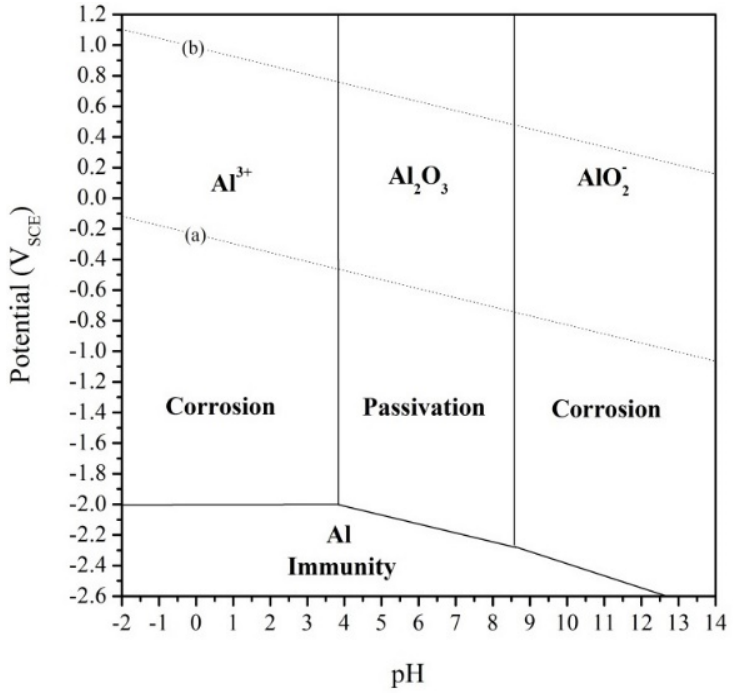

Figure 1.9. *Pourbaix diagram for pure Aluminium at 25 ºC (SCE). The lines (a) and (b) correspond to water stability [39].*

Al-Cu alloys are less resistant to corrosion than alloys of other series which contain much lower amounts of Cu [40]. There are three main reasons for this: (i) non-uniform distribution of Cu in solid solution; (ii) the presence of Cu-rich intermetallic compounds

and (iii) Cu particles or films deposited as a result of corrosion/redeposition. In all these situations, galvanic cells are created with Cu-rich areas acting as cathodes. **Table 1.3** and **Figure 1.10** show common corrosion features of 2XXX alloys.

Table 1.3. *Microstructural features and associated corrosion in high strength Al alloys. Adapted from [41].*

Microstructural feature	Size	Associated corrosion
Atomic defects	-Points: < 1 Å -Lineal: tens of nm (dislocations)	Grain etch out associated with higher grain stored energy
Grain boundaries	Tens of nm (wide)	Intergranular attack
Hardening precipitates	(20 x 200) nm	Facilitate intergranular attack
Dispersoids	(50 x 400) nm	Under some conditions undergo preferential attack
Constituent particles and impurity particles:	(0.5-50) µm	Localized attack of anodic particles or trenching in surrounding matrix of cathodic particles
Clusters of precipitates	(50-500) µm	Pitting attack

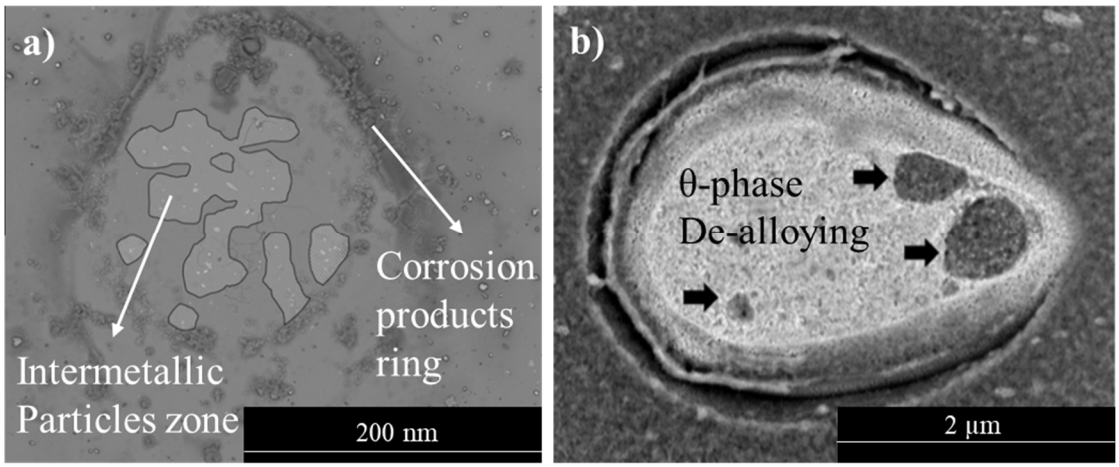

Figure 1.10. *Scanning electron micrographs of (a) corrosion products ring formed around intermetallic particles zone in 2024-T3 alloy and (b) Trenching and de-alloying of θ phase (Al_2Cu) after immersion in 3.5 wt.% NaCl solution for 10 h (black arrows point at pits produced by preferential attack of S-phase (Al_2CuMg) islands). Adapted from [42, 43].*

Al cladding, conversion coatings and anodizing are the most common corrosion countermeasures for 2XXX Al alloys [35]. Equally important to these are the surface pre-treatment steps to guarantee a surface free of contaminants, corrosion products and other foreign matter, since inhomogeneous surfaces will result in unpredictable corrosion performance of subsequent coatings. **Table 1.4** provides examples of the most common pre-treatments for 2XXX alloys prior to conversion coatings and anodizing.

Table 1.4. *Typical pre-treatment procedures for 2XXX aluminium alloys. Adapted from [44, 45].*

Stage	Chemical Composition (aqueous solution)	Conditions (Temperature, time)
Etch cleaning	Na_2CO_3: 1.5 wt.% Sodium Silicate: 1.0 wt.% Na_3PO_6: 0.3 wt.% Wetting agent: 0.2 wt.%	(50-80) ºC 5 min
Alkaline etching	NaOH (5 wt.%)	(40-60) ºC 10-20 min
De-smutting	HNO_3: 20-50 vol. % HF: 2-5 vol. %	25ºC 30 s

In the aircraft industry, Cr-based surface treatments have been widely used since 1923 to provide better corrosion resistance, improved paint adhesion, low electrical contact resistance or enhanced wear resistance [46]. The typical conditions and characteristics used for chromium conversion coatings (CCC) and chromium acid anodizing (CAA) of 2XXX alloys are summarized in **Table 1.5**.

Table 1.5. *Typical composition and procedures for Chromium conversion coating (CCC) and Chromic acid anodizing (CAA). Adapted from [14, 40, 47].*

Procedure	Chemical Composition (aqueous solution)	Conditions	Thickness (µm)
Chromium conversion coating (CCC)	CrO_3 and/or chromates. -Activators: NaF -Additives: $K_3Fe(CN)_6$	- pH: 1.8-2	0.05-2
Chromic acid anodizing (CAA)	CrO_3: (3-10) wt.% in aqueous solution	- Voltage: 40-50 V - Current density: 0.15-0.3 A m^{-2} - Temperature: 30-45 ºC - Time: 40-60 min	2-5

Chromium Conversion Coatings (CCCs) provide a very thin protective layer on the substrate generated by a chemical reaction between the chemical conversion solution and the aluminium alloy [36]. In this process, aluminium is oxidized (**Equation 1.1**) and Cr(VI) is reduced to Cr(III) (**Equation 1.2**) and the coating formation evolves by hydrolysis, polymerization, and condensation of Cr(III), triggered by the pH increase near the surface of the aluminium alloy [48].

$$2Al \rightarrow 2Al^{3+} + 6e^{-};\ 2Al^{3+} + 3H_2O \rightarrow Al_2O_3 + 6H^{+} \qquad \textit{Equation (1.1)}$$

$$2(CrO_4)^{2-} + 10H^{+} + 6e^{-} \rightarrow 2Cr(OH)_3 + 2H_2O \qquad \textit{Equation (1.2)}$$

Additionally, fluoride species are added to the conversion solutions to activate the aluminium and to prevent repassivation of the surface resulting in a thicker coating (**Figure 1.11**).

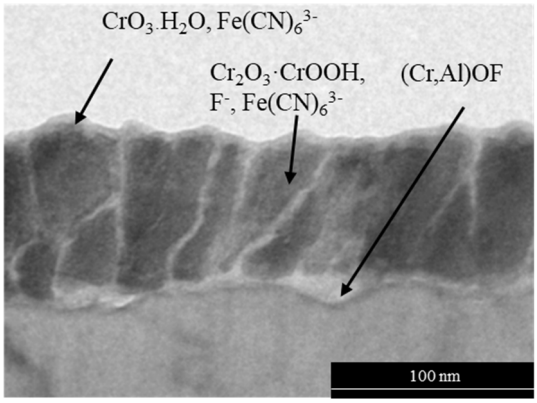

Figure 1.11. *Bright field transmission electron micrographs of ultramicrotomed cross-sections of Cr-based CCC coating formed on electropolished aluminium. Adapted from [48, 49].*

The formed layer shows important advantages:

- Good base for paint adhesion.
- Good stand-alone corrosion protection. The presence of traces of Cr(VI) species in the layer provide "self-healing" ability due to the repassivation of damaged areas by formation of Al^{3+} and Cr^{3+} mixed oxides.

Chromic acid anodizing (CAA) involves the electrochemical growth of an aluminium oxide film in an aqueous solution. An example of the porous oxide layer with enhanced adhesion and corrosion resistance is depicted in **Figure 1.12** [40].

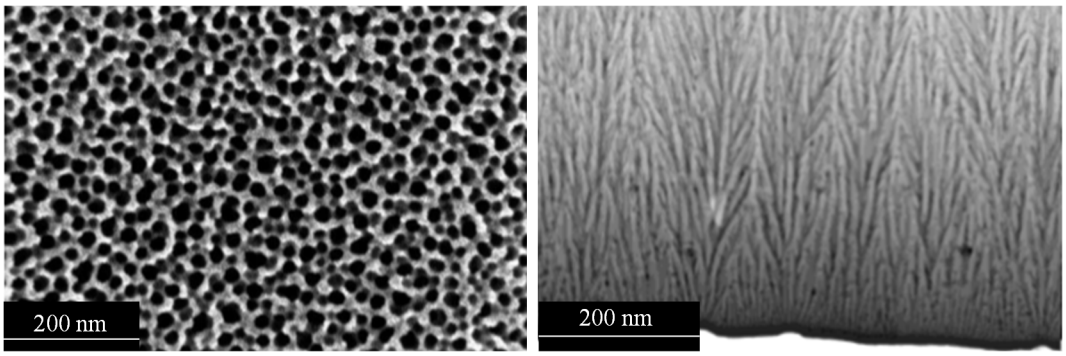

Figure 1.12. *Secondary electron micrographs of CAA anodic films formed on 2024-T3 aluminium alloy: (a) longitudinal and (b) cross section views. Adapted from [50].*

The main advantages of this process are:

- Residual electrolyte trapped in complex geometries, weldments and lapped or recessed parts is not a concern since chromic acid inhibits aluminium corrosion.

- Uniform coatings can be obtained when anodizing multiple alloy assemblies.
- It can be applied to fatigue critical components and it shows excellent corrosion resistance and fair paint adhesion.

CAA is more expensive than a chemical conversion process and not suitable for all types of parts. However, critical structures are usually anodized for maximum corrosion protection and paint adhesion [51]. The requirements of the key functionalities for Cr-based processes in the aircraft industry are shown in **Table 1.6**.

Table 1.6. *Requirements of the key functionalities for Cr-based processes in aircraft industry. Adapted from [14].*

Process	Key functionality	Requirement
CCC	Corrosion resistance	- Unpainted parts: 168-336 h (ISO 9227, ASTM B117). - Painted parts: length from scratch < 2-3 mm after 960 h (EN3665), some companies require < 0.5 mm.
	Layer thickness	≤ 1 µm.
	Adhesion to subsequent layer	GT0 dry, GT1 wet after 168 h (Cross-Cut Test ISO 2409), partial immersion for 14 days.
	Chemical resistance	168-750 h (ISO 2812, ISO 2409, BS3900 Part G5).
CAA	Corrosion resistance	- Unpainted parts: 336-2000 h (ISO 9227, ASTM B117) for equipment and structural parts. - Painted/sealed parts: 3000 h (ISO 9227, ASTM B117) length from scratch < 2-3 mm, no blisters in the surface, max 1.25 mm blisters from artificial scratch after 960 h (Filiform corrosion test, EN3665), some companies require < 0.5 mm.
	Layer thickness	2-7 µm.
	Adhesion to subsequent layer	After immersion in various fluids, oils or grease: corrosion resistance in Salt Spray equivalent to chromium trioxide system.
	Chemical resistance	GT0 dry, GT1 wet after 168 h in demineralized water (Cross-Cut Test ISO 2409).

1.3.2. Anodizing

1.3.2.1. Fundamentals of anodizing

Anodizing is an electrochemical surface treatment used to artificially thicken the oxide layer of the workpiece, which serves as the anode in an electrolytic cell (**Figure 1.13**). In case of Al alloys, the oxide layer or 'anodic film' is typically formed in an acidic solution with voltage and current density values between 20-100 V and 1-10 A dm^{-2}, respectively.

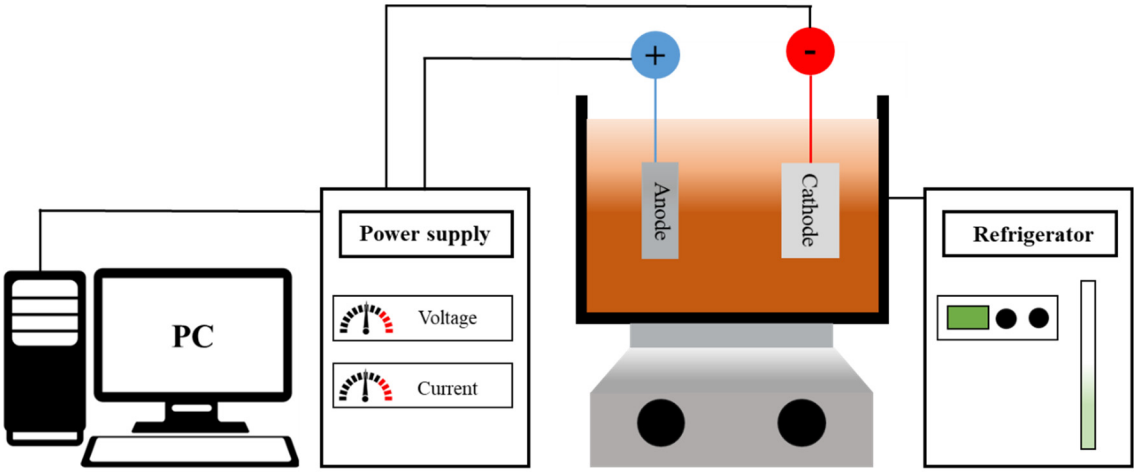

Figure 1.13. *Schematic illustration of experimental anodizing system. Adapted from [52, 53].*

The morphology of the anodic film depends on the electrolyte composition and electric conditions. In neutral or slightly alkaline electrolytes, barrier-type anodic films are formed; approximately 60% of the coating thickness is formed by migration of the ions O^{2-}/OH^{-} to the metal-oxide interface, and the remaining 40 % is formed by the migration of the cations Al^{3+} to the metal-electrolyte interface [3]. In acidic electrolytes, a thin barrier layer and a thicker outer layer with vertical pores constitute the anodic film (**Figure 1.14**). The applied voltage and the electrolyte determine the thicknesses of the barrier and the porous layers as well as the cell dimensions. The growing mechanism of porous anodic films is still under debate, although the *field assisted dissolution* and *flow models* are commonly cited [54-57]. From an industrial point of view, the anodizing process is capable of producing dense anodic oxide films which consist of a thick porous part (2-30 µm) and a very thin compact part (barrier layer, ~1 nm V^{-1}) with a remarkable effect on corrosion, fatigue and paint adhesion performances [46].

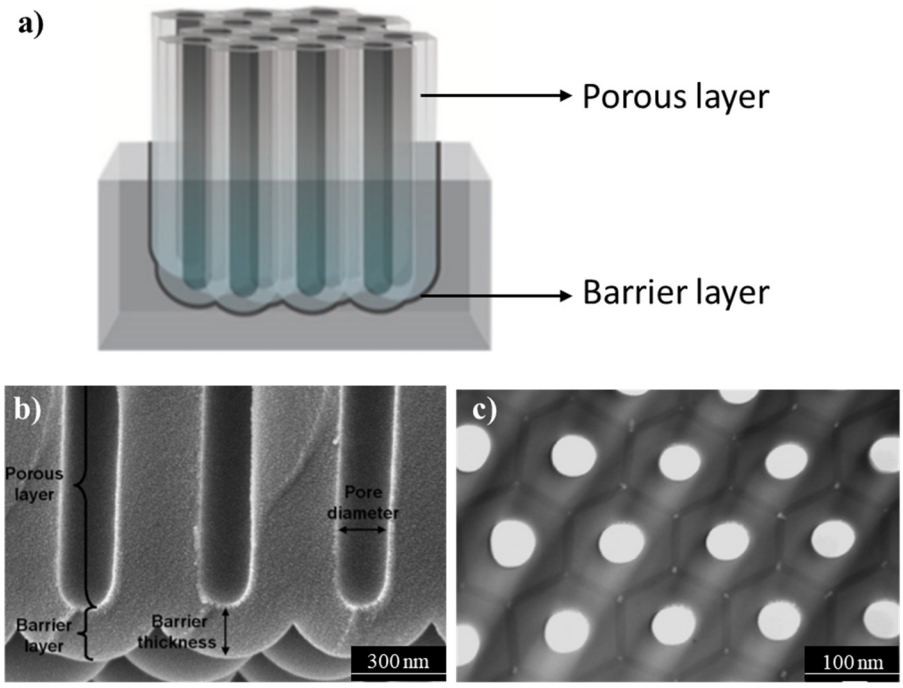

Figure 1.14. *(a) Schematic of the structure of the anodic aluminium oxide, (b,c) cross-section and plan views of an anodic film on pure aluminium. Adapted from [46, 58].*

Nevertheless, anodizing of Al alloys differs from that of pure aluminium. In the specific case of Al-Cu alloys, Cu can be strongly enriched in the alloy (~2 nm thick layer) immediately beneath the anodic film (up to 40 at.% Cu), by the initial formation of a Cu-free alumina film [59]. Then copper gets incorporated into the anodic film and promotes the generation of high pressure bubbles containing oxygen gas [60]. The bubbles can grow, coalesce and later burst to release the contained oxygen resulting in lateral porosity (**Figure 1.15**) [59].

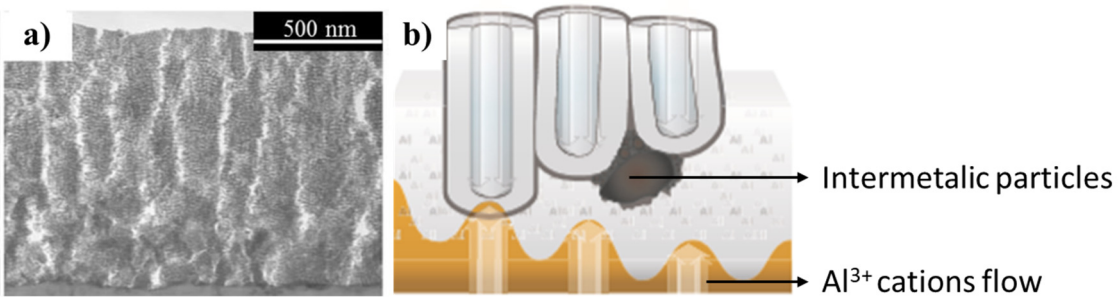

Figure 1.15. *(a) Lateral porosity detailed in TEM cross section view and (b) schematic of the structure of the anodic film in Al-Cu alloy. Adapted from [46, 61].*

The origin of this characteristic less-regular pore orientation has been also related to the field-assisted dissolution of the anodic alumina at the base of pores, while the film thickens by growth of new material at the metal/film interface [62].

Further, the film growth efficiency is relatively low (23-41% of the total cell charge corresponding to Al^{3+} ions present in the oxide film for anodizing in sulphuric acid in 2-8 V voltage range) compared with the efficiency of alloy oxidation (35-54% of the total cell charge corresponding to Al^{3+} ions in the consumed substrate), which means that 12-13% of oxidized aluminium does not end up in the oxide film (as a result of chemical dissolution and field-assisted losses). Note that the rest of the cell charge is used in oxygen generation [63].

1.3.2.2. Cr-free anodizing processes

The implications for substance substitution in the aerospace industry sets out a strong case for long review periods for the aerospace sector based on the airworthiness requirements. It requires that all components, equipment, materials and processes incorporated in an aircraft must be developed (3-5 years), qualified (8-15 years), certified (6 months), and industrialised (1.5-5 years) before production can commence. For this reason, alternatives are not foreseen to be commercially available for key applications in this sector for at least 13 or 22 years [14].

The following sections describe the existing alternatives to CAA. Some of them have successfully replaced Cr-based treatments for certain components, but they fail in several ways in the overall comparison to CAA and may not be used as general alternatives to Cr-containing surface treatment process chains.

a) Sulphuric acid anodizing (SAA)

SAA is typically used for decorative and corrosion protection applications. It produces a thick and dense oxide film that results in poor bonding with primers/adhesives, but with sufficient porosity for colour finishing. Layer thickness is greater (10-20 μm) than CAA (2-7 μm) (**Figure 1.16**). Thus, a significant reduction in fatigue strength might be observed. Nevertheless, in unpainted and painted conditions, SAA has been able to replace CAA for many corrosion-sensitive applications [64]. Recently, thin sulphuric acid anodizing (TSAA) (**Figure 1.16**) has been used to obtain ~3 μm thick-films in order to match fatigue requirements (**Table 1.7**), although these films do not achieve the corrosion protection of thicker films [65].

b) Tartaric sulphuric acid anodizing (TSA)

A promising alternative to overcome the limitations of SAA is to mix sulphuric acid with tartaric acid. This process was reported in the 1960s and is widely applied for non-

bonding applications as it is an environmentally-compliant process. This process provides anodic films with less corrosion resistance than CAA, but the combination of TSA with Cr-based sealing reaches the corrosion and paint adhesion requirements of the aviation sector for some applications. Tartaric acid decreases the current density and thereby the oxide growth rate; the film thickness and its impact on fatigue being lower than that of SAA (**Figure 1.16**) and comparable to TSAA and CAA [14]. Additionally, improved corrosion resistance is also observed and explained by the "buffering effect" of tartrate ions trapped in the oxide [66]. Similarly to SAA, TSA has shorter processing times and similar process temperatures than CAA, which leads to a more efficient process by reducing time and energy consumption and simultaneously offering an increase in production capacity (**Table 1.7**).

c) Boric sulphuric acid anodizing (BSA)

This process was patented by Boeing as an alternative to CAA in 1991 [67] and is widely applied for non-fatigue sensitive applications. The anodic film thickness and structure resembles TSAA with bigger ordered pores, improving primer penetration, adhesion and extending oxide durability (**Figure 1.16**) [68]. Nevertheless, fatigue and corrosion resistance of the resultant coatings are lower than that of CAA, since neither sulphate nor borate anions are effective inhibitors of aluminium corrosion. It should be noted that a dilute CrO_3-based sealing is still required to achieve the aviation sector corrosion requirements [65]. However, since boric acid is also hazardous, using it as a replacement is less favourable. **Table 1.7** provides a summary of the process parameters of BSA.

d) Phosphoric sulphuric acid anodizing (PSA)

PSA morphology is similar to that of CAA in terms of thickness and pore size (**Figure 1.16**). However, the corrosion resistance of PSA is lower than CAA and, as a consequence, the use of PSA anodic films is only qualified as a replacement of CAA for structural bonding applications [69]. Presently, requirements are met only for certain applications and only in combination with Cr-containing paint systems. PSA does not meet the requirements for military specifications (MIL-A8625) and research is ongoing. Similarly to SAA and TSA, PSA is also an efficient process; experimental parameters are comparable to TSA and SAA (**Table 1.7**).

Table 1.7. *Typical composition and procedures for anodizing Cr-free processes.*

Procedure	Chemical Composition (aqueous solution)	Conditions	Thickness (µm)	Refs
SAA	H_2SO_4: (0.4-2) M	14-40 V 0.15-1.5 A m^{-2} 22-25 ºC 5-30 min	5-20	[70-74]
TSAA	H_2SO_4: 1-1.8 M	15-20 V 0.1-2 A m^{-2} 20-25 ºC 5-20 min	3-5	[75-77]
TSA	H_2SO_4: 0.46 M $C_4H_6O_6$: 1 M	15-20 V 0.1-2 A m^{-2} 20-25 ºC 5-20 min	3-5	[66, 78-80]
BSA	H_2SO_4: 0.4-1.5 M H_3BO_3: 0.13-0.5 M	15 V 0.15 A m^{-2} 22-40 ºC 20-30 min	~3	[81, 82]
PSA	H_2SO_4: 0.75-0.85 M H_3PO_4: 1.1-1.3 M	18 V 0.15 A m^{-2} 26-28 ºC 23 min	1-5	[50]

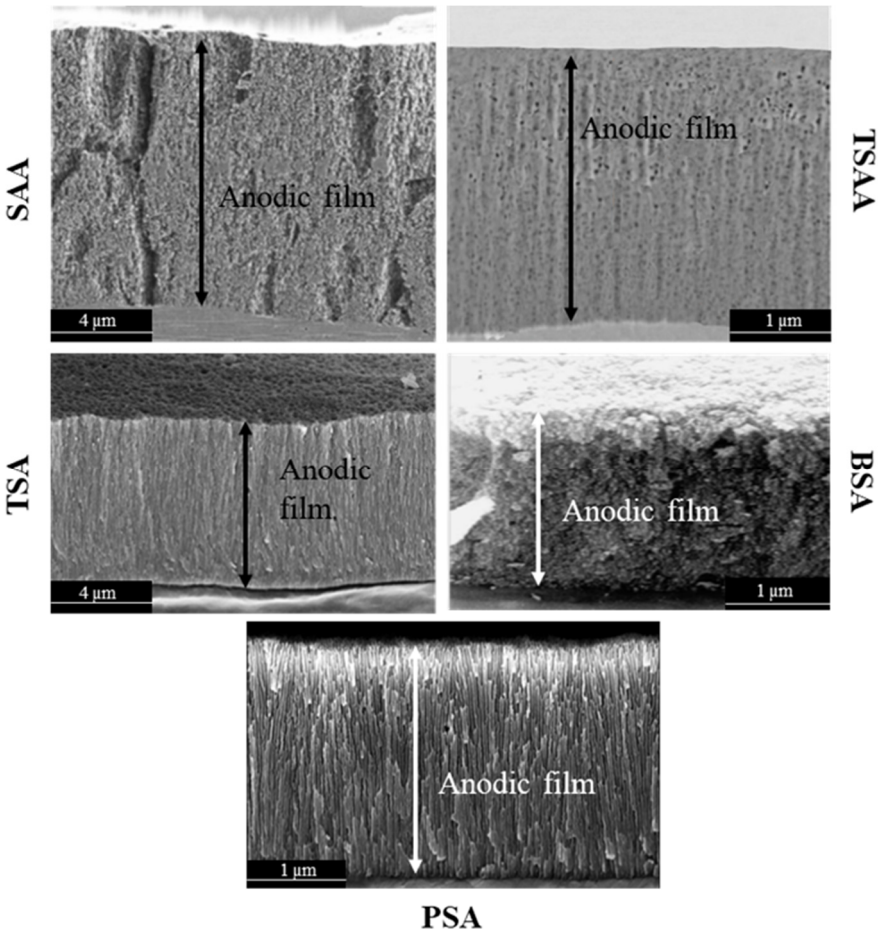

Figure 1.16. *Cross-section view SEM micrographs of 2024-T3 alloy anodized in (a) SAA, (b) TSAA, (c) TSA, (d) BSA and (e) PSA. Adapted from [50, 68, 74, 75].*

e) Conventional anodizing processes with in-situ inhibitor loading

SAA, TSAA, TSA, BSA and PSA are all being used in the aircraft industry only for non-critical components in terms of corrosion and fatigue performances. Therefore, the search for alternatives to CAA is still ongoing. *In situ* doping is one of the most interesting alternatives currently being researched as it is simple and allows for tailoring the properties and corrosion performance of the anodic film [83]. There are two main categories of additives:

- **Cations/anions**: rare-earth modified conventional anodizing of aluminium has been explored since late 1990s using numerous salt additions into SAA/TSA electrolytes [84]. The addition of permanganate, vanadate, molybdate and other oxyanion salts has also received some attention in recent years [61, 85-87].
- **Organic compounds**: organic inhibitors are much more abundant than inorganic ones due to the high variety of functional groups and organic molecules. Several studies reported that the incorporation of organic carboxylic acids with low dissociation constants (e.g. oxalic, citric, malonic, formic, glycolic, EDTA, etc.) promote the formation of porous-type protective anodic films with improved corrosion resistance [83, 84, 88, 89].

Table 1.8 summarizes some of these strategies and their effects on anodic film properties.

Table 1.8. *Most relevant additives and their effects in conventional anodizing processes. Adapted from [61, 83-89].*

Electrolytes	Observations
SAA/TSA + Cations/anions	**$Ce(SO_4)_2$ (SAA): (0.1-0.23) M** - Increases oxide growth rate and modify its morphology. - The incorporation mechanism remains unclear. **$KMnO_4$ (SAA): (0.05-0.1) M** - In high concentrations, decreases pore size, therefore increasing film compactness. - The thickness of barrier and porous layers increases with increasing concentrations. of permanganate ions. **Na_2MoO_4 (SAA/TSA): (0.04-0.25) M** - Does not change the film morphology. - Generates a thinner anodic film and reduces barrier layer thickness.
SAA + Organic compounds	**Glycerol, glycolic and oxalic acids: 0.65 M** - These species are absorbed on the oxide surface. - Less pore diameter and a porous oxide structure is obtained. - No corrosion data. **Malic, malonic, salicylic and succinic acids:** - Inhibit the anodic layer dissolution at specific concentrations. - Malic acid increases pore size, whereas salicylic and succinic acids decrease it. - Succinic and salicylic acids increase the corrosion resistance. **Citric, trimesic, mellitic and EDTA: (0.01-0.05) M** - Lower concentrations inhibit oxide layer dissolution. - Corrosion resistance depends on organic additive concentration.

1.3.2.3 Post-treatment of anodic films

a) Cr-based sealings

Up to date, Cr-based sealing and paints are still required for suitable corrosion protection for many Al components. Cr-based sealings are usually performed in a hot aqueous chromate solution (**Table 1.9**). An example of the CAA porous oxide layer with industrial Cr-based sealing is depicted in **Figure 1.17**.

Table 1.9. *Typical composition and procedures for commercial Cr-based sealing post-treatments.*

Procedure	Chemical Composition (aqueous solution)	Conditions	Refs
SOCOSURF TCS™	31 - 41% (v/v) SOCOSURF TCS + demineralized water	10-40 min 40ºC pH 3.8-4 (5 wt.% Ammonia)	[90]
SurTec 650™	20 % (v/v) SurTec 650 + demineralized water	5-10 min 25-35ºC	[50]
Alodine® 1200	110 g L^{-1} Alodine 1200 + demineralized water	1-5 min 21-38ºC	[91]

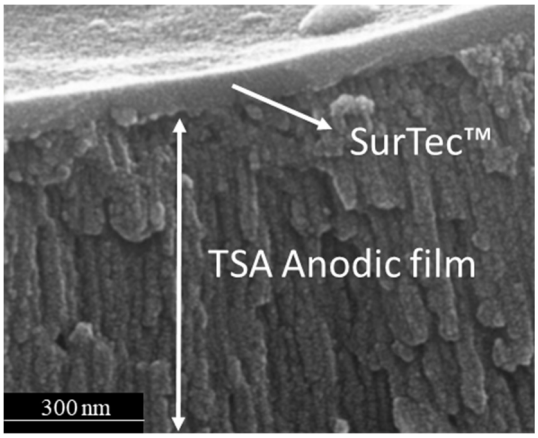

Figure 1.17. *Cross-section view SEM micrograph of 2024-T3 alloy anodized in TSA with SurTec 650™. Adapted from [50].*

Cr-sealing provides a very thin protective layer on the anodic film generated by the precipitation of Cr-hydroxides in the anodic film pores. By this process, the pores are closed and hydrated. Depending on the pH, Cr-based sealing forms either aluminium oxychromate (**Equation 1.3**) (at pH <6) or aluminium dioxychromate (**Equation 1.4**) in the coating micropores [92].

$$AlOOH + HCrO_4^- \rightarrow AlOHCrO_4 + OH^- \qquad \textit{Equation (1.3)}$$

$$(AlO(OH))_2 + HCrO_4^- \rightarrow (AlO)_2CrO_4 + OH^- + 2H_2O \qquad \textit{Equation (1.4)}$$

Finally, the formation of boehmite (Al_2O_3-hydrated) (**Equation 1.5**) which has a larger volume than Al_2O_3 interlocks the pores along with Cr-based compounds.

$$Al_2O_3 + H_2O \rightarrow 2AlO(OH) \qquad \textit{Equation (1.5)}$$

The sealed layer shows important advantages over those obtained without chromium:

- An adequate wear resistance and corrosion resistance is provided to the surface.
- Good stand-alone corrosion protection due to traces of chromate species providing "self-healing" ability (i.e. repassivation of cracked areas).

b) High temperature-based sealings

- **Hot water sealing (HWS)/Ni-acetate:**

Immersion in hot water is often used to seal off the pores by formation of boehmite (AlOOH) (**Figure 1.18a**). For anodizing processes without stringent surface protection requirements, hot water sealing is an economic and suitable method. However, during the sealing process of Al-Cu alloys, Cu-rich compounds may precipitate at the grain boundaries, decreasing the abrasion resistance and hardness. Also, the results of paint adhesion and corrosion performance are often unacceptable [92]. In order to overcome these limitations, nickel acetate (**Table 1.10**) is used as an additive. Ni incorporates into the film pores forming compounds that improve the adhesion and corrosion resistance in comparison to HWS (**Figure 1.18b**). Unfortunately, this improvement is still not valid for military aircraft standards [46, 92].

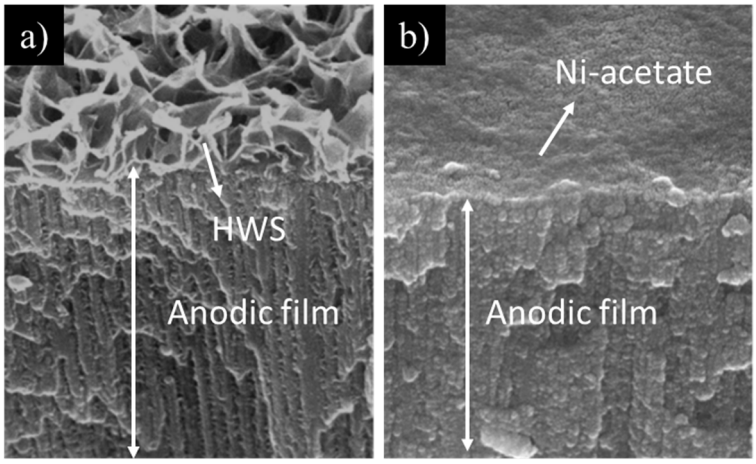

Figure 1.18. *Cross-section view SEM micrographs HWS of 2024-T3 anodized sample in (a) sulphuric acid at 20 V and 25ºC and (b) Ni-acetate. Adapted from [93].*

c) Low temperature sealings

- **Nickel fluoride sealing**

Cold seals, based upon nickel fluoride chemistries, can be developed at rather low temperatures (30 °C) being an economic feasible alternative (**Table 1.10**).

Because the temperature of the reaction is low, these seals tend to be shallower than hydrothermal seals. A possible scheme has been proposed based on the following simultaneous reactions (**Equations 1.6-1.8**) [94]:

$$Ni^{2+} + 2OH^- \rightarrow Ni(OH)_2 \qquad \textit{Equation (1.6)}$$

$$Al_2O_3 + 6F^- + 3H_2O \rightarrow 2AlF_3 + 6OH^- \qquad \textit{Equation (1.7)}$$

$$Al_2O_3 + 3H_2O \rightarrow 2Al(OH)_3 \qquad \textit{Equation (1.8)}$$

Table 1.10. *Typical composition and operational conditions for medium temperature (HWS and Ni-acetate) and low temperature (NiF) sealings. Adapted from [94].*

Procedure	Chemical Composition (aqueous solution)	Conditions
HWS	Distilled water	20-40 min 85-95 ºC pH 5.5-6.5
Ni-acetate	$NiSO_4$: 0.009-0.011 M CH_3COOH: 0.5 wt.%	15-25 min 85-95 ºC pH 5.5-6
NiF	- NiF_2: 0.015-0.02 M - Organic additive: 2-5 %	5-15 min 30-35 ºC pH 5.5-6

These synergistic reactions lead to precipitates within the micropores of anodic coatings, eventually plugging them. Fluoride ions act as accelerators while also forming aluminium fluoride complexes. This method has not been tested by the aircraft industry because it would not constitute a shift to less hazardous substances and additionally, this process does not fulfil the requirements of the aircraft industry [92].

d) Other sealing alternatives

During the last years, alternatives to conventional high-low temperature sealings have been developed. From a general point of view, they can be summarised in three categories as shown in **Table 1.11**.

Table 1.11. *Examples of current trends of Cr-free sealing post-treatments.*

Coating/Refs	Properties	Advantages	Disadvantages
Sol-Gel [95-98]	Based on the use of organosilane-based compounds which form a network of oxides on the anodic oxide surface which provide additional protective hydrophobic properties.	- Low-cost - Simple - Eco-friendly - Active corrosion protection	- High processing and curing temperatures - Synthesis control - Low corrosion performance - Not suitable for complex geometries
Layered Double Hydroxides (LDH) [99, 100]	Based on the presence of intelligent nanocontainers, which are charged with corrosion inhibitors.	- Ease of operation - Strong adhesion. - Properties can be adjusted (time, pH, Temperature) - Active corrosion protection	- Highly time consuming - High temperatures - Not evaluated as a full-system
Super-hydrophobic [101-103]	Based on the interaction of organic functional-based groups such as fatty acids and their salts. It forms a water-repellent coating which can avoid the corrosive species penetration through the coating.	- Ease of operation. - Eco-friendly. - High corrosion performance.	- Intermediate operational temperature - Not evaluated as a full-system - Passive protection

However, the majority of these novel developments for key applications have not yet been established; notwithstanding, numerous researches are being carried out to find adequate corrosion inhibitors and full-system benchmarking.

1.3.3. Plasma electrolytic oxidation (PEO)

1.3.3.1. Fundamentals of PEO

Plasma electrolytic oxidation (PEO) is a plasma-assisted electrochemical surface treatment characterized by the use of high voltages (100–600 V) in alkaline electrolytes. From an experimental point of view it is quite similar to conventional anodizing, since both are electrolytic bath processes that involve oxidation of the substrate. The PEO process can be conducted under different electrical regimes (DC, AC, bipolar, etc.) involving polarization of the alloy to voltages above the dielectric breakdown of the oxide [104]. This results in the formation of multiple short-lived microdischarges (50 μs- 4 ms) with high local temperatures and pressures (T ~10^4 °C and P ~10^2 GPa) as shown in **Figure 1.19a**.

PEO involves multiple electrochemical, thermodynamic and plasma-chemical reactions on the metallic surface that trigger the formation of highly stable ceramic phases such as α-Al_2O_3 and γ-Al_2O_3 [105]. The *dielectric breakdown*, *discharge-in-pore* and *contact*

glow electrolyte models are some of the PEO mechanisms that have been proposed in the past [106-108].

PEO of aluminium alloys has been explored more than PEO of any other type of substrate. On aluminium alloys, the final oxide is 5-150 μm-thick and usually contains a relatively high fraction of α-Al_2O_3, yielding an excellent wear resistance, hardness, thermal stability and corrosion resistance. PEO coatings often surpass other surface treatments for wear-sensitive applications such as conventional hard anodizing (HA) and hard-chrome coatings [104, 105, 109]. PEO coatings typically show a distinct morphology consisting of a three layered structure (**Figure 1.19b**).

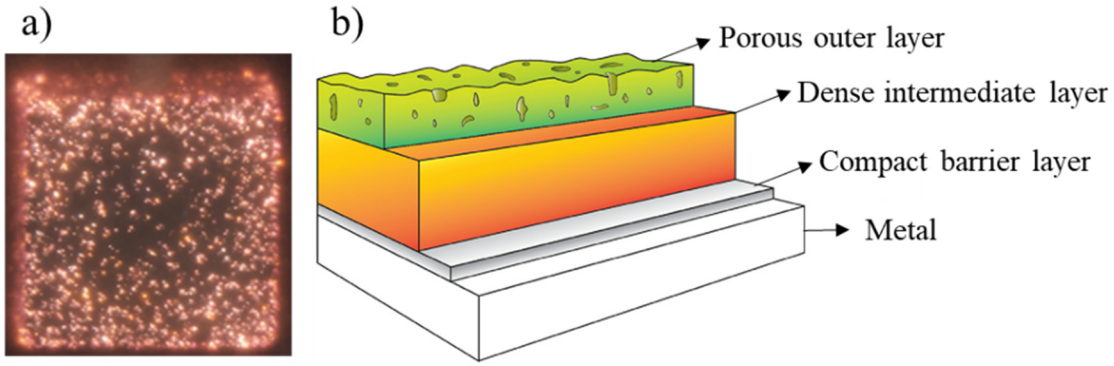

Figure 1.19. *Example of (a) microdischarges produced during PEO process and (b) three-layered structure of a typical PEO coating. Adapted from [109, 110].*

- Outer thick layer (5-30% of the coating thickness): composed of γ-Al_2O_3 and electrolyte derived compounds.
- Intermediate layer (70-80% of the coating thickness): provides thermal barrier and tribological properties due to its high hardness and low porosity (formed by α-Al_2O_3 and aluminium oxides).
- Barrier layer (200-500 nm): dense layer composed of amorphous aluminium oxide and mostly responsible for the anticorrosion properties of the coating and its bonding to the substrate.

Table 1.12 summarizes the characteristics of PEO versus conventional anodizing. One of the key advantages is the use of environmentally-friendly electrolytes with high throwing power. Additional advantages are little or no requirement for substrate pre-treatment and enhanced wear and anti-corrosion properties. Disadvantages are mainly related to the relatively high cost of the process which restricts the wide use of PEO in mass-production industries.

Table 1.12. *Comparative characteristics of conventional anodizing and PEO of Al. Adapted from [104, 111, 112].*

Characteristic	Conventional anodizing	Plasma electrolytic oxidation
Voltage (V)	15−160	300−600
Current density (A m^{-2})	≤ 50	100−500
Electrolyte	Acid	Dilute neutral or alkaline
Substrate pretreatment	Critical	Not too important
Temperature control	Precise	20−50 °C
Thickness (μm)	5−50	50−150
Growth rate (μm min^{-1})	≤ 1−1.5	2−5
Microhardness (HV)	≤ 500	1400−1700
Wear (mm^3 N m^{-1})	(3−6) 10^{-4}	(0.33−3.3)·10^{-7}
Dry friction coefficient	0.35	0.17−0.32
Fatigue limit (10^7 cycles) (MPa)	100−210	160−270
Salt spray (ASTM B117) (h)	300−1000	2000−7000
Energy consumption (kW h m^{-2} m^{-1})	0.1−0.5	3−26.7

As in conventional anodizing, the relative thicknesses of the various layers, their structure, porosity, composition and hardness are mainly influenced by electrolyte composition and electrical process parameters. Examples of typical electrolyte compositions and the resultant phases in the PEO coatings are given in **Table 1.13**.

Table 1.13. *Examples of electrolyte compositions and phases of PEO coatings on aluminium alloys.*

Electrolyte	Phase	Properties	Refs
Aluminate-based AlO_2^-	α-Al_2O_3 γ-Al_2O_3 δ-Al_2O_3	- Promote the formation of α-Al_2O_3 - Increase the coating hardness	[113, 114]
Phosphate-based PO_4^{3-}	α-Al_2O_3 γ-Al_2O_3 $AlPO_4$	- Promote the formation of α-Al_2O_3	[114, 115]
Silicate-based SiO_3^{2-}	α-Al_2O_3 γ-Al_2O_3 δ-Al_2O_3 mullite	- Coating growth rate increases	[114-117]

Nevertheless, PEO coatings formed in the same electrolyte can show a wide variation of properties depending on the employed current/voltage regime (**Table 1.14**).

Table 1.14. *Different modes of PEO processing. Adapted from [104, 108, 118].*

Regime	Characteristics	Advantages	Disadvantages
DC	- Bi-layered structure (no intermediate layer) - Thin and porous coating - Lower oxide growth rate	- Easy upscaling	- Limited control over microdischarge life-time and intensity
DC-pulsed	- Morphology and composition can be tailored	- Enables the discharge duration control by duty cycle adjustment	- Industrial application is limited
AC	- Three-layered structure - Thick coatings	- Wider options of process parameters to control the microdischarges	- High power supply costs - Restricted commercial upscaling
Bipolar mode	- Improved hardness and corrosion resistance - Low porosity - Allow post-treatments - High thickness	- Avoids intense long-lasting plasma microdischarges with excessive temperature - Compact coatings - Wide options of process parameters to control the microdischarges	- Slightly reduced mechanical properties - Higher power supply costs

As can be seen in **Table 1.15**, PEO treated aluminium alloys are often used as a replacement of heavier components, reducing their weight and wear, thus increasing the lifetime. Nowadays, the most known commercial processes for PEO on aluminium are Keronite (UK), Kepla-Coat, CeraFuse (CCT1, USA), Mofratech/Ceratronic (France) and Machaon (Torset, Russia) [118].

Table 1.15. *Examples of applications of PEO coatings on aluminium and their advantage over substituted materials. Adapted from [105].*

Industry/ Material	Material/ treatment to be substituted	New material/ treatment	Phases, thickness and hardness	Comments
Textile machine building /Rotors	High strength Al-alloy/ deep anodising	High strength Al-alloy/PEO	α-Al_2O_3 100–150 μm 15–18 GPa	200–300% increased lifetime
Gas industry/ Operating wheels	Stainless steel	Al–Mg alloy/ PEO	γ-Al_2O_3 60–120 μm 10–14 GPa	150–200% increased lifetime, weight and inertial force reduction
Engine industry/Cases	Al-alloy/coloured anodising	Al–Mg alloy/ PEO	γ-Al_2O_3 60–120 μm 10–14 GPa	Improved heat exchange
Electrical engineering & electronics/ Electrode foils	Al/anodising	Al/PEO	γ-Al_2O_3 30–50 μm 10–14 GPa	Up to 80% reduced oxidation time
Vacuum engineering/ Rotors, stators,	Stainless steel	High strength Al-alloy/PEO	γ-Al_2O_3 50 μm 14 GPa	200% increased lifetime and reduced vibration
Air & space industry/ Gears, wheels	Stainless steel	High strength Al-alloy/PEO	γ-Al_2O_3 60–120 μm 10–14 GPa	Up to 100% increased lifetime

Nevertheless, PEO technology does not usually compete with conventional anodizing due to several factors:

- High energy consumption: high voltages, current densities and long treatment times are used to form ≥15 μm-thick thick PEO coatings. Only 20-25% of the applied energy is used for coating formation [119], the rest of it is spent on secondary processes such as heating of the electrolyte, gas evolution and water vaporization [120].
- Thick PEO coatings (≥15 μm-thick) strongly affect the fatigue properties, thus limiting its use as CAA feasible alternative [112, 121, 122].

1.3.3.2. Flash-PEO

If PEO technology is to be proposed as an alternative to CAA, thin PEO coatings need to be developed with minimal energy consumption. Not only that, their fatigue and corrosion performance and paintability need to be comparable to those of CAA, SAA or TSA. This

is only possible by wise selection of treatment time, electrolyte composition and implementation of innovative strategies. A possible approach to overcome these limitations could be the development of short-time or *Flash-PEO* with *in situ* incorporation of inhibitors (**Figure 1.20**).

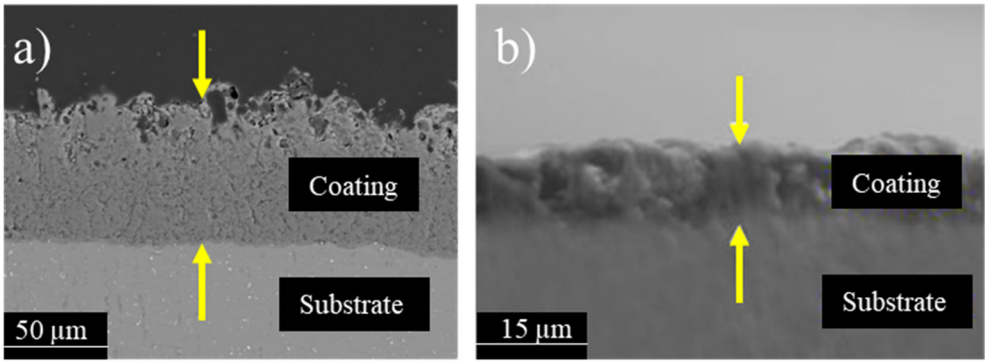

Figure 1.20. *(a) Cross-sectional BSE micrographs of conventional PEO coating on pure aluminium and (b) Flash-PEO on 2024-T3 alloy. Adapted from [123, 124].*

As shown in **Table 1.16**, there have been already some efforts to produce relatively thin PEO coatings with incorporation of corrosion inhibitors. However, most of these coatings are too thick for the aircraft industry. Future developments should aim at producing thinner coatings (<10 µm). Also, there are corrosion strategies that remain relatively unexplored in the field of PEO and deserve more attention (e.g. active corrosion protection, superhydrofobicity, etc.).

Table 1.16*. Typical corrosion inhibitor effect for silicate/phosphate PEO electrolytes. Adapted from [125-129].*

Inhibitors-Observations
• $KMnO_4$ (silicate) – (1.5-10) µm: (6-25) mM - Increases oxide growth rate and decrease the pore size - Promote the formation of MnO_2 on the surface and increase the corrosion resistance
• $La(NO_3)_3$ (silicate) – (5-10) µm: (0.15-0.6) mM - Promote thicker and denser coating increasing the corrosion resistance
• $Na_2WO_4{\cdot}2H_2O$ (silicate) – 30 µm: (1-6) mM - Facilitate the formation of a dense layer, probably by forming mixed oxides of silicon and tungsten - Increase the corrosion resistance
• $Ce(SO_4)_2$ (silicate) – (13-29) µm: (1-5) mM - Increase the oxidation voltage - Increases oxide growth rate, homogeneity and corrosion resistance
• NH_4VO_3 (phosphate) – 10 µm: - Promote de formation of V_2O_3 - Increases corrosion resistance

1.3.3.3. Post-treatment of PEO coatings

PEO-treated aluminium alloys are usually not painted or sealed since they are mainly used for wear-and thermal-resistant applications and because the corrosion resistance of stand-alone PEO coatings is usually sufficient for such applications [130]. As a result, in order to suit Flash-PEO coatings as a feasible alternative to CAA, studies to find effective corrosion inhibitors and sealing post-treatments are needed.

As can be seen in **Table 1.17**, the major part of novel Cr-free sealing post-treatments originally developed for anodizing can be adapted for PEO; notwithstanding their remarkable corrosion performance, these sealed systems cannot find direct application in industry due to relatively high PEO coating thickness.

Table 1.17. *Examples of current trends of sealing treatments on PEO coatings on aluminium alloys.*

Sealing method	PEO coating thickness (µm)	Properties	Refs
LDH	1-20: LDH is formed ≥ 20: LDH is not formed	PEO coating thickness is a direct determining factor for the possibility of LDH growth; its formation is favoured at lower thickness. Provides active protection if additionally loaded with inhibitors.	[131-133]
Hydrophobic fat acids	9-100	Higher corrosion protection can be attributed to the sealed pore morphology and prevent the infiltration of corrosive Cl- ions into the coatings.	[134-138]
Sol-gel	10-30	Sol-gel coating increases the hydrophobicity, corrosion resistance and the durability/stability of the PEO coating due to the pore sealing.	[139-141]

1.3.4. Conversion coatings (CCs)

1.3.4.1 Fundamentals of CCs

A conversion treatment is a chemical process used to form a thin protective layer. This is achieved by a redox process between the chemical conversion solution and the substrate. Conversion coatings (CCs) serve as a good base for paint adhesion and provide good stand-alone corrosion protection [40, 47]. CCs can be applied by conventional techniques (rinse, immersion or spray) or by wipe techniques and non-rinse processes. From an industrial point of view, immersion in an acidic bath containing inorganic salts is the most common approach [92, 142].

The inhibition mechanism of CCs on Al alloys may include barrier layer protection, active corrosion protection and anodic or cathodic inhibition [142, 143]. CCs on alloys differ from those obtained on pure aluminium. For Al-Cu alloys, the coating performance is influenced by the presence of copper. Cu enrichment in the alloy is observed in the initial stages of coating development until a critical concentration is achieved. Then Cu can enter the coating limiting the achievable thickness [144].

1.3.4.2. Cr-free CCs

CCCs fulfill the most demanding requirements and have a proven track record for over ~100 years. Replacements for CCCs has been an ongoing topic for more than 20 years due to the lack of proper alternatives [142, 145]. A wide range of technologies has been investigated, demonstrating the array of alternative chemistries available for aluminium (**Table 1.18**).

Table 1.18. *Current trends in Cr-free conversion coatings. Adapted from [47, 143, 146, 147].*

Procedure	Chemical Composition and pH interval	Status in aircraft industry
MnCC	$KMnO_4$ (7-14)	- Adhesion properties and layer thickness equivalent to Cr-CC - Moderate corrosion protection - Poor wet adhesion - Multistep process and expensive
Sol-gel	(TEOS), (GPTMS).	- Low corrosion protection and paint adhesion - High thickness - Complex formulations
Phosphates	Zn^{2+}, H_3PO_4 (3-4)	- Good adhesion - Low corrosion performance
CeCC	$CeCl_3$, $Ce(NO_3)_3$ (2)	- Good corrosion protection and paint adhesion - Unstable chemical bath and expensive
Oxyanions (MoCC, VCC)	Na_2MoO_4 (4-6) $NaVO_3$ (1.7)	- Moderate corrosion resistance - Expensive
LiCC	$LiCO_3$ and/or LiOH (11-13.5)	- Poor wet adhesion - Single process bath - Eco-friendly
Zr/TiCC	K_2ZrF_6 and /or K_2TiF_6 or their acids (2-4)	- Good paint adhesion and moderate corrosion protection. - One step but expensive
CrCC (TCP)	Cr(III) salt and K_2ZrF_6 (4-5)	- Meets no environmental requirements - Contains Cr(VI)

After several screening processes, Naval Air Systems Command (NAVAIR) developed and patented a process using trivalent chromium and zirconium fluoride technology (TCP) [148]. However, recent studies found Cr(VI) compounds in a conversion layer after Cr(III)/K_2ZrF_6 treatment. Furthermore, some active protection on an artificial scratch

seems to arise from mobile Cr^{6+} species that are formed locally by the oxidation of Cr^{3+} [149]. Therefore, the search for Cr(VI)-free alternatives is still a reality.

In the last decade, there has been an increasing interest in layered double hydroxides (LDH) for corrosion protection strategies [100, 150, 151]. LDH systems, also known as hydrotalcite-like systems or anionic clays, can be described as positively-charged mixed metal (M(II)-M(III)) hydroxide layers and interlayers occupied by anions (A^{m-}) and water molecules. The general formula of the most common LDHs can be represented as $[M^{II}_{1-x}M^{III}_{x}(OH)_2]^{x+}[(A^{m-})_{x/n}\cdot nH_2O]^{x-}$, where M(II) and M(III) represent divalent (e.g. Mg^{2+}, Ca^{2+}, Cu^{2+}, Mn^{2+}, Zn^{2+}) and trivalent metallic cations (e.g. Al^{3+}, Cr^{3+}, Fe^{3+}, Co^{3+}), respectively, and A^{m-} represents the interlayer anion (e.g. NO_3^-, Cl^-, CO_3^{2-}, PO_4^{3-}) [152]. The M(II)/M(III) ratio may vary according to the co-precipitation conditions and initial salts concentrations (in the majority of cases lies between 0.10 and 0.33). The stability of LDH increases in the order $Mg^{2+} < Mn^{2+} < Co^{2+} \approx Ni^{2+} < Zn^{2+}$ for divalent cations, and $Al^{3+} < Fe^{3+}$ for trivalent cations [99]. Size, charge and ratio of metal cations, charge and orientation of anions and the amount of water determine crystal structure parameters of LDHs, bond strength and anion exchange capacity [99, 152].

LDH structures show an attractive combination of features such as low cost, relative ease of preparation, large number of composition/preparation alternatives, high chemical and thermal stability and, more important, high ion exchange capacity [153]. **Figure 1.21** shows the typical structure of a natural LDH structure.

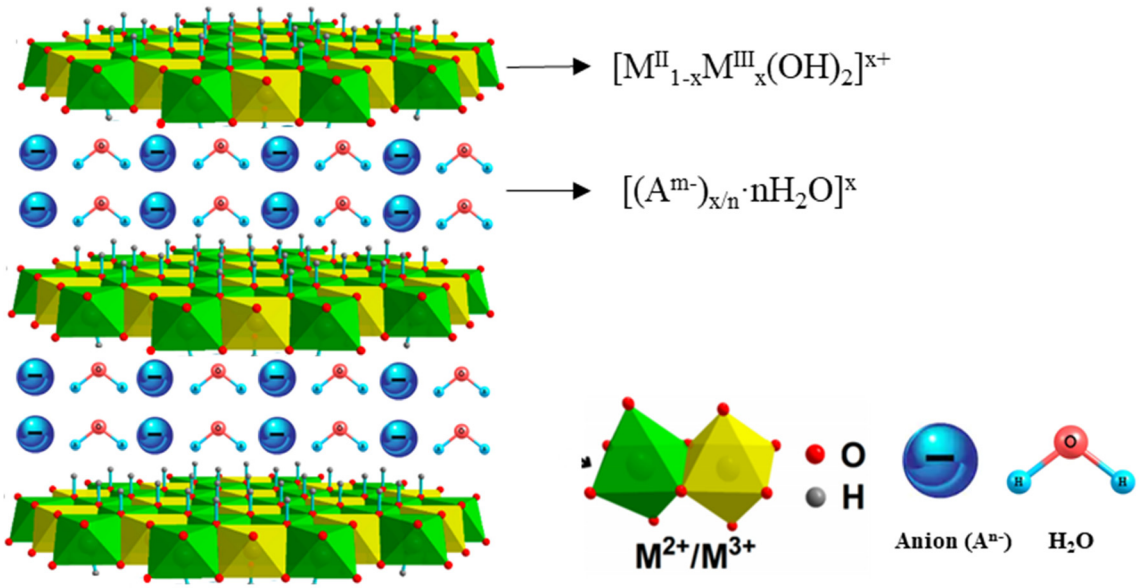

Figure 1.21. *Schematic illustration of LDH structure and chemical components. Adapted from [153, 154].*

There are many synthesis methods for LDHs, namely, Co-precipitation, Urea method, Induced Hydrolysis, Reconstruction, Sol-Gel, Hydrothermal, Microwave, Ultrasound Treatments, etc. **Table 1.19** shows the main features of most common LDH syntheses.

Table 1.19. *Features of the LDH synthesis methods. Adapted from [100, 152, 155].*

Method	Features/Advantages	Challenges/Disadvantages
In situ growth	- Ease of operation - Strong adhesion by chemical bonds - Size of LDH particles and coating density can be adjusted (T, pH, t)	- Substrate as only source of Al^{3+} cations - Time consuming - High temperatures
Co-precipitation	- Ease of operation - Controllable chemical compositions - High reacting activity, wide scope of application, it could be combined with hydrothermal process.	- Time consuming - Weak adhesion, aggregates of sheet-like LDH results in heterogeneous LDH coatings
Electrochemical deposition	- Effective technique due to purity of phases - High deposition rates - Simple equipment and applicability to complex geometries	- Complex operation - High cost - Requires several treatment steps

In the particular case of Al-Cu alloys, the *in situ* approach produces a direct growth of a layer of 2-3 µm LDH "flakes" over the metallic surface (**Figure 1.22**). Zn-Al-LDHs have shown to provide superior adhesion and corrosion performance compared with other contenders [156, 157]. This coating can be achieved by immersing the Al substrate in Zn^{2+} containing electrolyte at specific pH conditions (**Table 1.20**).

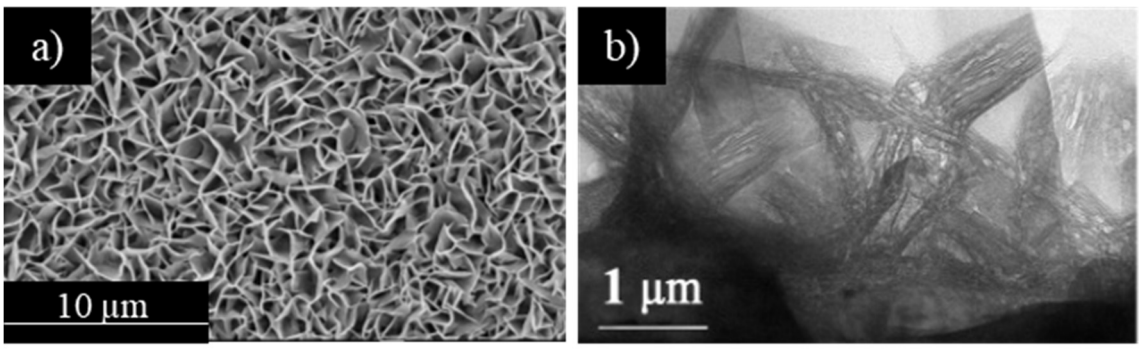

Figure 1.22. *(a) SEM planar and (b) TEM cross section view of Zn-Al-LDH on 2024-T3 alloy. Adapted from [158, 159].*

Table 1.20. *Zn-Al-LDH on 2024-T3. Adapted from [158, 159].*

LDH recipe	Chemical Composition (aqueous solution)	Conditions (Temperature, time)
Zn-Al-LDH	0.005 M $Zn(NO_3)_2$ 0.3 M NH_4NO_3	pH: neutral range (45-100) ºC 30 min-24 h

Corrosion protection of LDH coatings is typically attributed to several factors:

- Hydroxides act as a barrier against the corrosive environment.
- The layered structure entraps or absorbs corrosive anions such as Cl^-.
- The corrosion properties can be further enhanced by loading corrosion inhibitors. These are liberated on demand under the action of particular triggers, e.g. pH and presence of corrosive anions (ion-exchange).

So far, LDH coatings need to be loaded with corrosion inhibitors to achieve active corrosion protection (**Figure 1.23**).

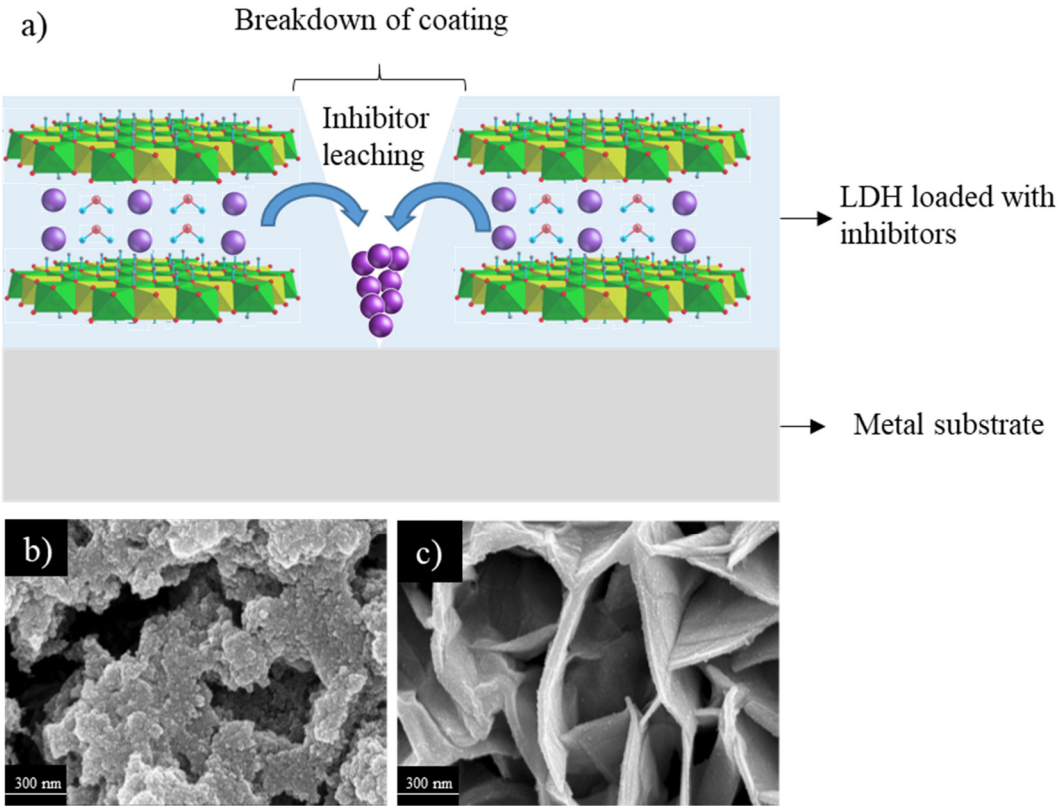

Figure 1.23. *(a) Active corrosion mechanism of Zn-Al-LDH loaded with vanadate as a corrosion inhibitor, (b) SEM planar view of inhibitor-free Zn-Al-LDH and (c) Zn-Al-LDH loaded with vanadate after 28 days of immersion in 0.05 M NaCl solution. Adapted from [158, 160].*

A priori, there is no theoretical limit. Intercalation of all types of anions should be possible, namely, halides, non-metal oxoanions, anionic complexes of transition metals, volatile organic anions and anionic polymers. Among the different species, the ones based on oxometallate anions, such as vanadate, are the best reported up to the date [99], although these species have also been catalogued equally toxic as chromate [161]. The mechanism of active-protection is practically the same for all studied inhibitors; an external trigger, for example, coating breakdown due to the presence of chlorides, leads

to release of corrosion inhibitors and entrapment of Cl^- anions between the LDH layers. Consequently, the corrosion process is halted or delayed [156, 162].

1.4. Corrosion and surface treatment of additive manufactured (AM) Al alloys.

1.4.1. Microstructure of AM alloys

The number of Al alloys currently used in AM is quite limited for several reasons. The high laser reflectivity and relatively low cost and easy machining of Al alloys often tilt the balance towards more conventional technologies [163]. In fact, some high-performance wrought Al alloys are hardly weldable due to the high volatility of some of their elements (e.g. Zn) and, therefore, poorly adaptable to AM [164].

Nevertheless, one of the key advantages is that the high thermal conductivity of Al reduces internal thermal stresses and allows for faster AM, although it requires larger laser power and the heat can affect the already built parts. Another advantage is the microstructural enhancement due to the high cooling rates associated with SLM (Selective Laser Melting) without altering the chemical composition [165, 166]. It is important because cast alloys are traditionally strengthened by adding alloying elements, which strongly affect other mechanical and anticorrosion properties [167]. The two most common Al alloys for AM available today are AlSi10Mg and Al12Si due to their low melting point and weldability, although they show relatively low yield strength and ductility [168, 169].

Casting of Al-Si alloys produces a fibrous microstructure with α-Al dendrites and eutectic α-Al/Si, where Si segregates in large needle-shaped crystals dispersed throughout the α-Al matrix. The presence of Mg in cast alloys is known to induce hardening of the alloy by forming Mg_2Si precipitates [167, 170]. As-cast Al-Si alloys have not been widely used in aircraft components due to their relatively low mechanical properties, although they find application in wing ribs, ducting, tanks and frameworks [9].

The microstructures of AM Al-Si alloys present a very fine distribution of silicon, forming a lamellar microstructure that encapsulates the aluminium phase in very small cells (**Figure 1.24**) [171]. These features should in theory improve the corrosion and wear resistances of AM alloys, thus widening their applications in the transport sector.

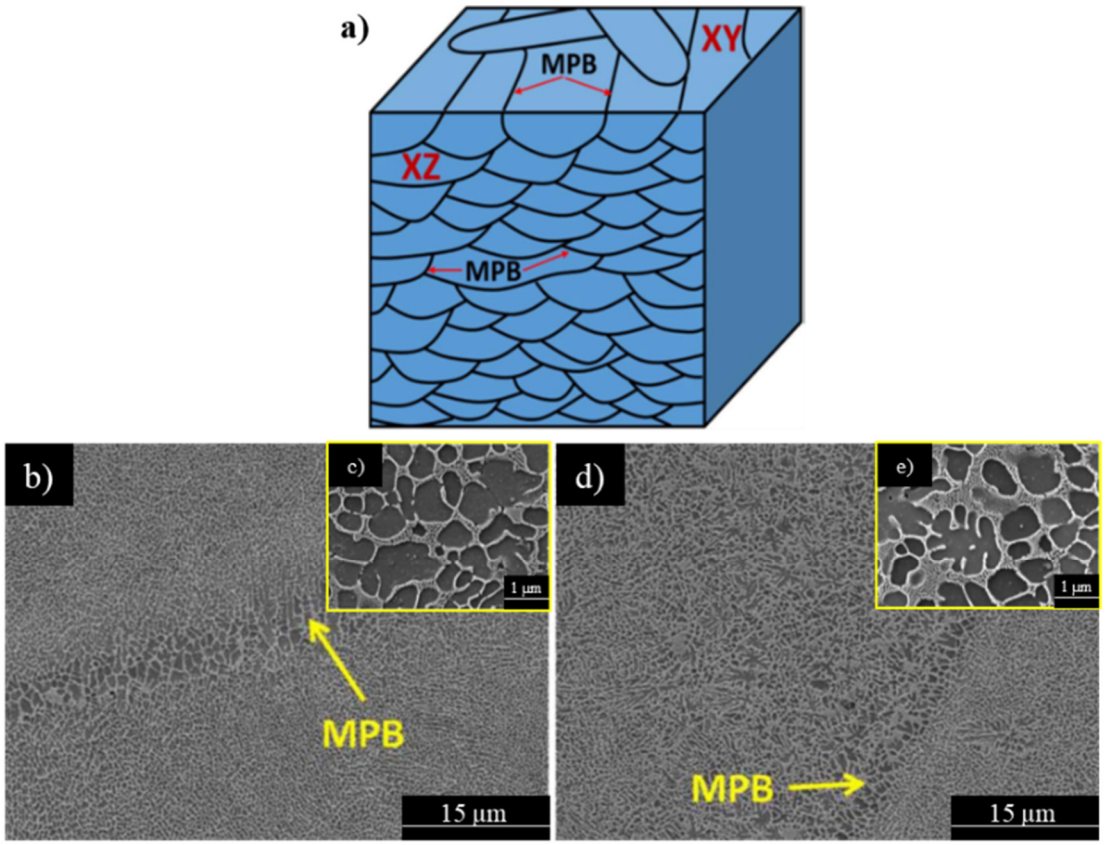

Figure 1.24. *Secondary electron microscopy images of the surface of Al10SiMg (a) with MPB detail (b) and Al12Si (c) with MPB detail (d). Adapted from [171, 172]. MPB: melt pool border.*

1.4.2. Corrosion and wear of AM alloys

It has been reported that the finer microstructure of AM alloys compared to cast alloys results in improved electrochemical properties [173-175]. There are mainly two reasons for this improvement:

- The absence of certain intermetallics (α-AlFeSi, Mg_2Si, etc.) and the lack of separated regions with eutectic aggregate (α-Al/Si) and primary α-Al phase in AM alloys results in a reduced number of galvanic pairs.
- The lower porosity of AM alloys and their homogeneous microstructure prevent or delay the onset of localised corrosion phenomena which is a common feature of cast alloys.

Table 1.21 presents some of the key factors associated with the corrosion behaviour of AM Al alloys produced by SLM.

Table 1.21. *Factors related to the corrosion resistance of AM Al alloys. Adapted from [173-180].*

Factor	Description
Porosity	It is related to the high Al laser reflectivity and the presence of oxides/humidity during the SLM process. SLM produces a selective porosity at the MPB boundaries, which may promote intergranular stress corrosion cracking. The porosity can be reduced by optimising the printing conditions (laser energy, scanning rate and scanning direction).
Roughness	AM alloys showed higher roughness values than cast alloys due to the balling phenomena. Polished AM samples prevent localised corrosion phenomena, especially in MPB.
Plane orientation	Anisotropic corrosion behaviour was observed in AM alloys. A lower density of MPBs in the XY plane increases the corrosion resistance. It is caused by the faster solidification rate of the Z-axis compared to x- and y- axes.
Heat treatment	Heat treatments do not reduce the susceptibility to the penetrating selective attack. However, high temperatures can promote the coalescence of Si-based IMCs (galvanic pairs formation) promoting selective pitting corrosion.

In terms of alloy composition and its effect on corrosion, it has been reported by Revilla *et al.* that higher Si content alloys, such as Al-12Si, show higher corrosion resistance in comparison to Al10SiMg alloy [172], possibly due to a greater level of connectivity of the Si network, which temporarily protects the underlying Al matrix from corrosion. Regardless of the Si content, corrosion attack is more visible at the regions of heat-affected-zones (HAZ) next to the MPB, where the Si network is disrupted (**Figure 1.25**).

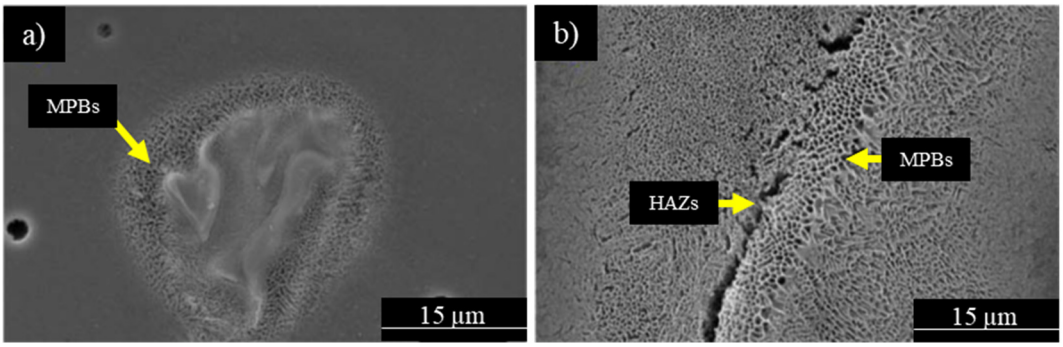

Figure 1.25. *Secondary electron microscopy images of corroded areas in the surface of the samples, (a) Al12Si, and (b) Al10SiMg, taken after immersion for 48 h in 0.1 M NaCl. Adapted from [172].*

It has also been reported that the finer Si distribution, lower grain size and high Si content in AM alloys results in enhanced wear properties compared to cast alloys [181-183]. Apparently, the lower porosity of AM alloys and the homogeneous Si distribution delay the propagation of cracks and defects during wear test. Wear resistance can also be increased by heat treating at low temperatures (inhibits the coalescence of Si particles) and adjusting the processing parameters (e.g. building direction and environmental conditions) [175, 181, 184]. For example, Prashanth *et al.* studied the wear resistance of

Al-12Si AM alloy produced by SLM and reported that as-prepared AM Al alloys show the least wear rate compared to the cast and high temperature-annealed samples (**Figure 1.26**) [184].

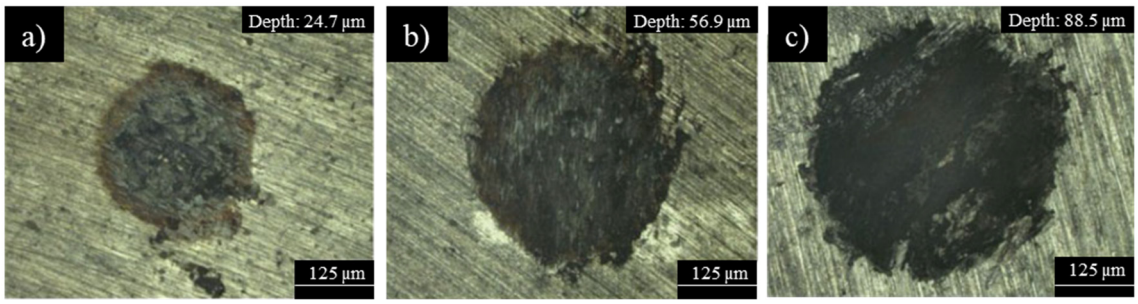

Figure 1.26. *OM images of the fretting wear scars and their corresponding depth values for the Al–12Si as-prepared AM (a), cast (b) and AM annealed at 723 K. Adapted from [184].*

1.4.3 Surface treatments of AM Al alloys

Recent studies by Revilla *et al.* confirm that AM samples can be anodized, although there are several differences in comparison to cast counterparts regarding the Si distribution and other surface features as summarized in **Table 1.22**.

Table 1.22. *Differences between anodizing of cast and AM Al-Si alloys. Adapted from [171, 172, 185].*

Factor	Description
Oxide growth rate	The presence of the larger dendritic eutectic silicon structures in AM alloy in comparison to cast alloy, decrease the oxide growth rate of the anodic film due to the preferential Si oxidation.
Silicon concentration	The higher oxidation rate of Si in the AM alloy results in a reduced anodizing efficiency compared to the cast alloy, increasing the voltage measured during anodizing. This effect is more accused at higher Si content in the alloy.
Plane orientation	Independent of the amount of Si in the alloy, an asymmetric anodizing behaviour is always observed in AM alloys. A lower voltage response is obtained during the anodizing of the XZ plane compared to the XY plane (lower density of MPBs) and as a consequence, a thinner anodic oxide layer is grown.
Porosity	The average diameter of the pores formed in the XY surface of the AM specimens was larger than that of the pores grown in the XZ surface; both were larger than the pores formed in the cast alloy.

Conventional anodizing is not the ideal surface treatment for Al–Si alloys in sliding wear applications. Hard anodizing (HA), which has been commercially available since 1940, is a more effective process. HA can be applied to some aircraft parts such as landing

gears, cylinders, pistons heads, etc. [186]. The mechanism involved in oxide growth during HA is almost the same as the one in conventional anodizing, although the higher

H_2SO_4 concentration and current densities used in HA result in thicker and denser oxide layers (**Table 1.23**). To the author´s best knowledge, there is no available data focused on HA of AM Al alloys.

Table 1.23. *Typical procedure for hard anodizing. Adapted from [40, 46, 187].*

Procedure	Chemical Composition (aqueous solution)	Conditions	Thickness (µm)
Hard anodizing	H_2SO_4: 2-3.5 M	45-50 V 220-350 A m^{-2} (-10-10) ºC	25-60

In case of PEO coatings, it is known that they show superior corrosion and tribological properties compared with HA coatings [188]. Pezzato, *et al.* studied the PEO process on Al10SiMg processed by casting and AM methods. The obtained results demonstrated that the PEO process on AM alloy is possible and resulted in a more uniform thickness and comparable corrosion resistance to that of the PEO-treated cast alloy [189].

2. Hypothesis and Objectives

2.1. Hypothesis

This research work is based on the following two hypotheses:

I. It is possible to develop thin and multifunctional Cr-free coatings on wrought aluminium alloys that are compatible with Cr-free paints and innovative sealing post-treatments. These coatings can be formed by conventional anodizing, flash-PEO or LDH conversion treatment by using environmentally friendly electrolytes. Coatings can be loaded with corrosion inhibitors by an *in situ* approach or post-treated by several strategies (hydrophobic sealing, LDH, sol-gel, etc.) in order to tailor their surface properties and close their gap with regards to conventional Cr-based processes used in the aircraft industry. The fatigue performance of the best candidates should be comparable to that of CAA.

II. It is possible to obtain wear resistant coatings on an AM Al-Si alloy through HA and PEO. The obtained coatings should be more uniform than those obtained on a conventional Al-Si cast alloy due to the more uniform distribution of Si within the material.

2.2. Objectives

The specific objectives of this thesis are summarised as follows:

O1. Enhancement of corrosion resistance of anodic films on 2024 alloy

The goal is to evaluate the corrosion behaviour of TSAA and TSA films (<3 μm) on 2024-T3. The films are modified *in situ* with corrosion inhibitors under different anodizing regimes (current and voltage controlled). Electrochemical impedance screening is performed in order to identify the best candidates for further additional sealing post-treatments and detailed morphological, microstructural and compositional characterization. The best candidates for stand-alone and painted applications are identified, including evaluation of fatigue performance. Evaluation of the full systems including inhibitor-bearing or inhibitor-free epoxy primers is carried out according to accelerated corrosion and paint adhesion testing standards commonly used in the aircraft industry.

O2. Development of flash-PEO coatings

The main objective is to evaluate the corrosion behaviour of flash-PEO coatings (~5 μm, <3 min) modified *in situ* with corrosion inhibitors. Identification of the best inhibitor-containing coatings is performed by electrochemical impedance screening. Investigated post-treatments include LDH conversion coatings and hydrophobic sealing. Identification and detailed characterization of the best candidates is performed for stand-alone and painted applications. Evaluation of the best candidates as a full system including inhibitor-bearing or inhibitor-free epoxy primers is carried out according to accelerated corrosion and paint adhesion testing standards commonly used in the aircraft industry.

O3. LDH conversion coatings on 2024 alloy

The aim is to develop LDH conversion coatings (≤ 1 μm) on 2024-T3 based on Zn-Al and Ca-Al systems and to study the effect of the inhibitor loading on corrosion resistance. Identification of the best inhibitor-containing coatings is performed by electrochemical impedance screening. Detailed morphological and compositional characterization is also performed. Additional testing include paint adhesion and long term immersion testing.

O4. PEO and HA of AM Al10SiMg alloy

The main goals are (i) the metallographic study of both A361 cast and Al10SiMg AM alloys; (ii) development and characterization of conventional HA and PEO coatings on both A361 and Al10SiMg AM alloys and; (iii) study of the tribological properties of non-coated, HA- and PEO-coated on both A361 and Al10SiMg AM alloys.

3. Experimental Part

3.1. Materials

3.1.1. Wrought alloys

The base wrought aluminium alloys used for this study were 2024-T3 and 1050-H18. Their chemical compositions are summarised in **Table 2.1**.

Table 2.1. *Nominal composition of wrought studied alloys.*

	Elements (wt.%)									
Alloy	**Cu**	**Mg**	**Mn**	**Fe**	**Si**	**Zn**	**Ti**	**Cr**	**V**	**Al**
2024-T3	3.8-4.9	1.2-1.8	0.3-0.9	<0.5	<0.5	<0.25	<0.15	<0.10		balance
1050-H18	<0.05	<0.05	-	<0.4	<0.25	<0.07	<0.05	-	<0.03	balance

The samples were cut from sheets into specimens of 20×20×1.5 and 40×40×1.5 mm^3 for 2024-T3 and 30×20×1.5 mm^3 for 1050-H18, respectively. Both alloys were supplied by *SMW Engineering Group*, Inc. (Madrid, Spain) and Amari Metals Ibérica, S.L.U (Madrid, Spain), respectively. The 2024-T3 alloy was selected as it represents the most widely used bulk material for commercial Cr-based surface treatments in the aircraft industry. The 1050-H18 alloy was used in some of the studies to avoid a significant effect from alloying elements.

3.1.2. AM and cast alloys

Additive manufactured Al10SiMg samples were prepared by DMLS. The AM process was performed using a 370 W laser in an Argon atmosphere and a laser energy density of 10.6 J mm^{-3}. This parameter indicates the laser energy input into the material and is equal to the laser power divided by the scanning speed (1300 mm s^{-1}), the layer thickness (0.03 mm), and the hatch distance (0.09 mm). A361 cast aluminium alloy with similar chemical composition (wt.%: 0.10 Cu, 0.36 Mg, 0.12 Mn, 0.53 Fe, 10.5 Si, 0.11 Zn and Al balance) to the AM alloy was used as the reference material.

Both Al10SiMg and A361 specimens were cut from 30×30×30 mm^3 cubes and a large ingot into specimens of 30×10×2 mm^3 and 30×20×5 mm^3 dimensions, respectively. Al10SiMg AM alloy was supplied by *Fundación Idonnial* (Madrid, Spain). Duralcan USA provided the A361 cast alloy.

3.2. Specimen preparation

3.2.1. Metallographic preparation

Specimens were wet ground through successive grades of silicon carbide abrasive papers from P120 to P1200, followed by diamond finishing to 0.1 μm. Keller reagent (5 mL nitric acid + 3 mL hydrochloric acid + 2 mL hydrofluoric acid + 190 mL of deionised water) was used to reveal the constituents of the studied cast and AM alloys. Poulton reagent (2.5 mL nitric acid + 1.5 mL hydrochloric acid + 0.5 mL hydrofluoric acid + 95 mL of deionised water) was used to reveal the constituents of the studied wrought alloys. The same procedures were used for the preparation of the cross-sections of the coated materials (embedded in MA2+ commercial epoxy resin), followed by diamond polishing to 1 μm.

3.2.2. Pre-treatment procedures

1050-H18 specimens were pre-treated in an alkaline bath at room temperature. In the case of 2024-T3, specimens were cleaned following the steps recommended by *Henkel*. Both treatments are shown in **Table 2.2**.

Table 2.2. *Pre-treatment procedures of studied wrought alloys.*

Alloy	**Cleaning procedure**[1,2]		
	Degreasing	**Etching**	**Desmutting**
2024-T3	70 g L^{-1} BONDERITE C-AK 4215NC solution for 10 min at 60ºC	85 g L^{-1} BONDERITE C-AK ALUM ETCH 2 AERO at 40ºC	Immersion in BONDERITE C-IC SMUTGO NC AERO for 5 min
1050-H18		15 wt.% NaOH solution for 20 s	

1. Each procedure was followed by rinsing in deionised water.
2. Total surface to clean in Henkel procedure was 500 cm^2 per one litre of each solution.

A361 and Al10SiMg samples were wet ground through successive grades of silicon carbide abrasive papers from P120 to P1200, followed by water rinsing and drying with alcohol and warm air. All studied specimens were stored in a desiccator for at least 24 h before their manipulation.

3.3. Surface treatments

3.3.1. Anodizing

Anodic films were obtained on 2024-T3 alloy using different acidic electrolytes with different amounts of inorganic and organic additives in aqueous solution under constant current density or voltage-controlled modes (**Table 2.3**). HA coatings were developed on AM and A361 alloys in H_2SO_4 (200 g L^{-1}) at 20 mA cm^{-2} for 3000-4000 s at 0ºC.

Note that a CAA reference specimen provided by MTU AeroEngines was also analysed to compare its properties with the most promising anodic films.

Table 2.3. *Range of studied variables for anodizing the Al alloy 2024-T3. Further specified in Section C1.1.2, C1.1.3 and C1.2.2.*

Anodizing variables	Range of values
Base electrolyte (SAA) (g L^{-1})	45-150 g L^{-1} (H_2SO_4)
Voltage (V)	6-18
Current density (mA cm^{-2})	1.5-15
Treatment time (min)	5-140
Temperature (ºC)	22.5-37
Organic inhibitor concentrations (etidronic, tartaric, glycolic, citric and succinic acids) (M)	0.05-1
Inorganic inhibitor concentrations $Ce(SO_4)_2$ (M)	0.023-0.1

The anodizing station was equipped with a 2 L double-walled glass cell in order to keep a constant electrolyte temperature (**Figure 2.1**). Water running through a chiller (Huber mini-chiller Plus) was used as a coolant for conventional anodizing processes, whereas a commercial fluid (HUBER SynOil, M10.120.08) was used for the hard anodizing experiments. In both cases, a magnetic stirrer was used to maintain continuous electrolyte agitation. Two different DC power supplies were used depending on the anodizing conditions and size of the specimens (SM400-AR-8 Systems Elektronika at UCM and SM120-AR-8 Systems Elektronika at TUDelft). Delta Elektronika Power supply Control data acquisition software was used to record voltage−time and current−time dependencies per 0.2 s time interval.

Aluminium alloy 1085 sheet (85 mm in diameter, 170 mm long and 1 mm thick) was used as a counter electrode. After anodizing, specimens were rinsed in deionised water followed by drying with isopropanol and warm air.

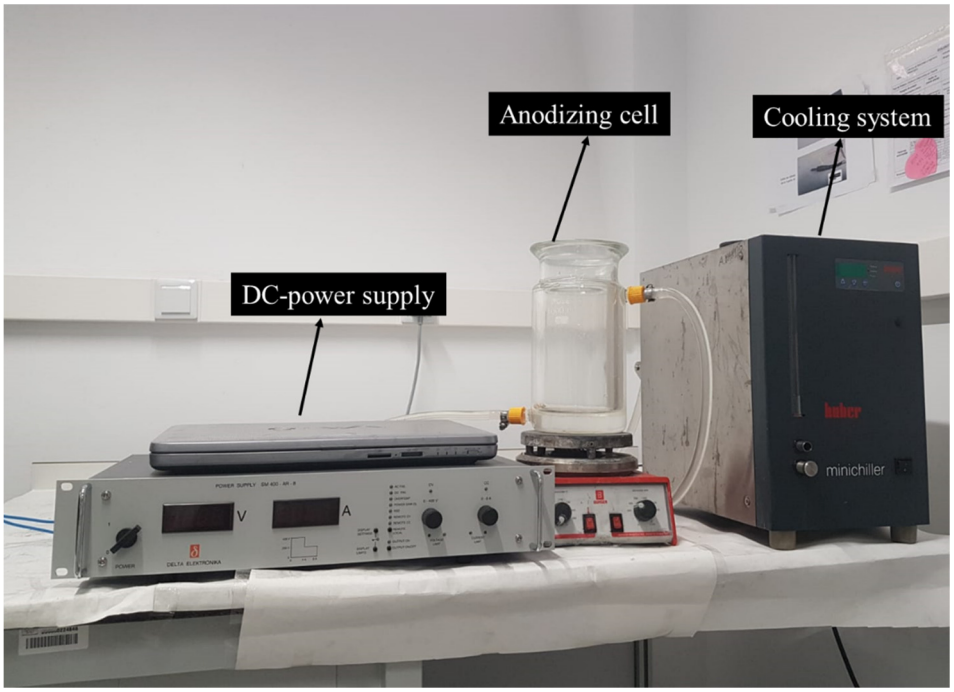

Figure 2.1. *Experimental system used for the studied anodizing treatments.*

3.3.2. Plasma electrolytic oxidation (PEO)

PEO coatings were formed using different electrolytes and conditions as shown in **Tables 2.4** and **2.5**. DC PEO coatings were obtained by using a DC voltage/current-controlled power supply (SM400-AR-8 Delta Elektronika). For AC PEO coatings, a 2 kW power supply with a square electrical signal was used (EAC-S2000, ET Systems Electronic). For the latter, instantaneous voltage and current signals were recorded using a 2-channel Tektronix TDS 2012B oscilloscope (**Figure 2.2**). Root mean square values of voltage and current during AC PEO were continuously acquired with a time resolution of (0.1-0.2)s. For this, a KUSB-3116 Keithley data acquisition card (500 kS/s) was used to record voltage−time and current−time dependencies.

The glass cell used for DC and AC PEO coatings was similar to that described in **Section 2.3.1** for conventional anodizing processes, although a stainless steel sheet (AISI 316L, 7.5 × 15 cm^2) was used as the counter-electrode. Due to the higher energy involved during AC PEO, and in order to maintain the temperature at (25 ± 1) ºC, a more powerful closed-loop cooling system was used (WK 120 LAUDA).

Following PEO, the specimens were rinsed in deionised water and dried in isopropanol and warm air. Treated specimens were stored in a desiccator for at least 24 h before manipulation.

Table 2.4. *Range of studied variables for PEO of 1050-H18 and 2024-T3 alloys under DC conditions. Further specified in Sections C2.1.2, C2.2.1.2 and C2.2.1.3.*

Variable	Range of values
Base electrolytes (silicate, phosphate, aluminate, borate and mixture of thereof) (g L^{-1})	4-50
Voltage (V)	≤ 400
Current density (mA cm^{-2})	50-100
Treatment time (s)	100-200
Temperature (ºC)	25
Inhibitor concentrations ($NaVO_3$, Na_2MoO_4, $La_2(SO_4)_3$, Na_2SnO_3, Na_2WO_4, $Ce_2(SO_4)_3$) (mM)	0.5-12
Note: All base electrolytes contain KOH (1-10) g L^{-1}	

Table 2.5. *Range of studied variables for PEO of 2024-T3 alloy under AC conditions. Further specified in Section C2.2.1.2.*

Variable	Range of values
Base electrolytes (silicate, phosphate, borate and mixture of thereof) (g L^{-1})	10.5-20
Voltage waveform positive/negative amplitudes (V)	490/-110, 50 % duty cycle
Current density (mA cm^{-2})	100-500
Treatment time (s)	40-3300
Frequency (Hz)	50-100
Temperature (ºC)	25
Note: All base electrolytes contains KOH (1-5) g L^{-1}	

PEO coatings were developed on AM and A361 alloys in sodium silicate electrolyte ($Na_2O(SiO_2)x \cdot xH_2O$, ≥27% SiO_2, ρ= 1.39 kg dm^{-3}, 10.5 g L^{-1}; KOH, 2.8 g L^{-1}). The electrical signal applied consisted of a square signal (+490V/-110V, 50 % duty cycle and 50 Hz) with an initial voltage ramp of 60 s. The maximum current density was limited to 500 mA cm^{-2}.

The specific energy consumption was calculated by integration of the voltage-time and current-time transients acquired by the specified power supplies during the PEO treatment. With the obtained results, the energy consumption was calculated in terms of kW h m^{-2} according to **Equation (2.1)**, and the specific energy consumption in kW h m^{-2} μm^{-1} was obtained dividing energy consumption by the coating thickness.

$$\int_{t_0}^{t} [V \cdot j] \left[\frac{W \cdot s}{m^2}\right] \qquad \textit{Equation (2.1)}$$

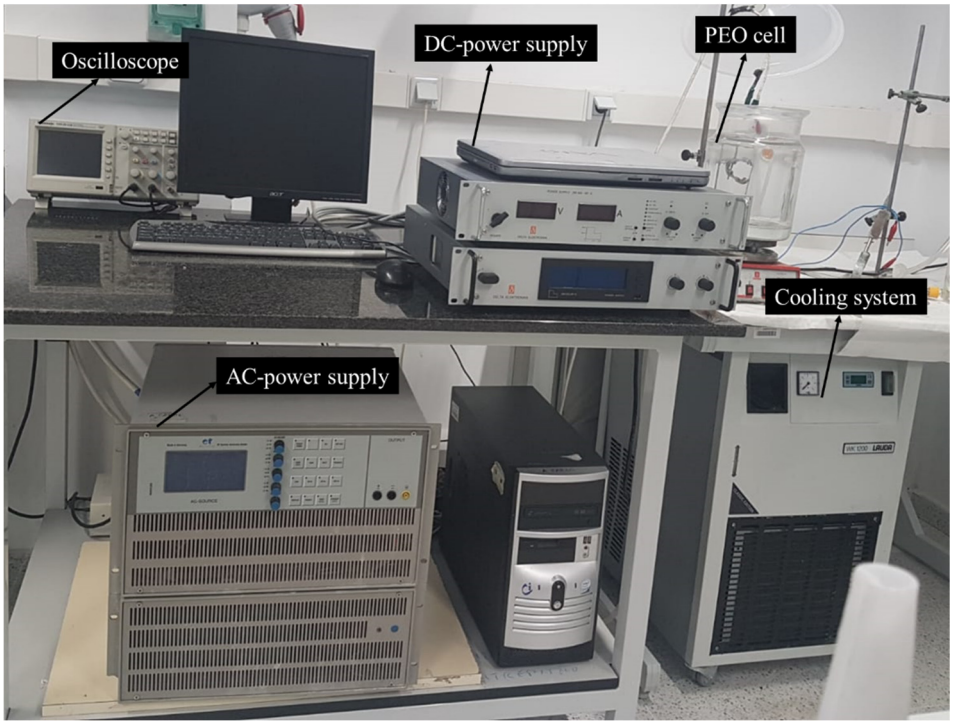

Figure 2.2. *Experimental system used for the studied PEO treatments.*

3.3.3. Post-treatment procedures

3.3.3.1. LDH post-treatment

Selected anodized and PEO-treated specimens of 1050-H18 and 2024-T3 alloys were immersed in the LDH solution (**Table 2.6**) following the synthesis route detailed in **Figure 2.3**.

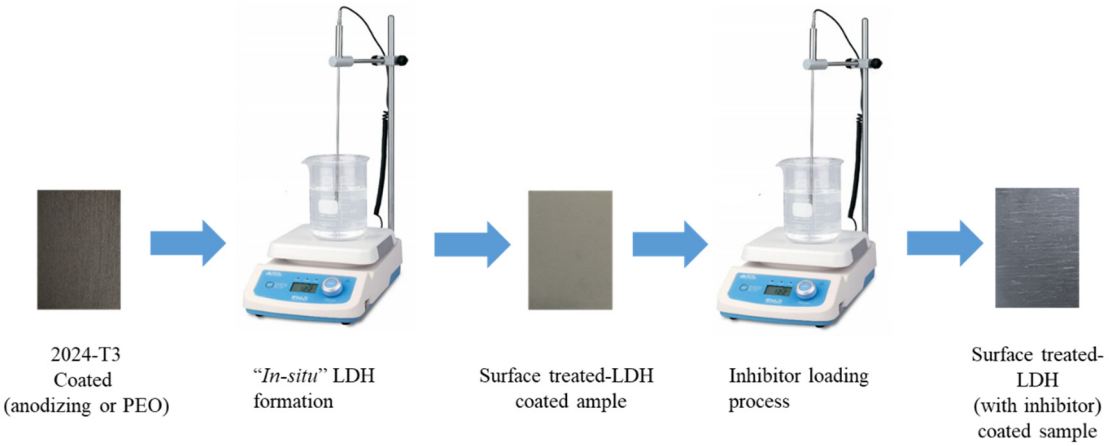

Figure 2.3. *In-situ growth method scheme for LDH conversion coatings.*

Table 2.6. *Range of LDH post-treatment conditions for PEO-treated 1050-H18 and 2024-T3 alloys. Further specified in Section C2.1.4 and C2.2.3.*

Variable	Range of values
Base electrolytes ($Zn/Ca(NO_3)_2$ and NH_4NO_3, $NaNO_3$) (M)	0.01-0.3
Treatment time (min)	30-60
Temperature (ºC)	~ 95
pH	6-10
Inhibitor concentrations ($NaVO_3$, $LiNO_3$, $KMnO_4$, Na_2MoO_4,) (M)	0.05-0.2

3.3.3.2. Sol-gel

The selected anodized specimen on the 2024-T3 alloy was immersed in the hybrid sol-gel solutions, which consist of a mixture of inorganic (SiO_2) and organic (TEOS and GPTMS) components (**Table 2.7**). The synthesis route is further detailed in **Figure 2.4**.

Table 2.7. *Hybrid sol-gel post-treatment conditions for anodized 2024-T3 alloy.*

Coating	Composition	Molar ratio
GTS	- TEOS (tetraethoxysilane) - GPTMS (3-(glycidyloxypropyl)trimethoxy silane) - SiO_2 (aqueous suspension 40 wt.%)	TEOS/GPTMS/SiO_2/EtOH: 0.5/0.5/0.54/3.83
GTS-Li	-TEOS (tetraethoxysilane) - GPTMS (3-(glycidyloxypropyl)trimethoxy silane) - SiO_2 (aqueous suspension 40 wt.%) - $LiNO_3$	TEOS/GPTMS/SiO_2/EtOH/Li: 0.5/0.5/0.54/0.3/0.03
GTS-Ce	-TEOS (tetraethoxysilane) - GPTMS (3-(glycidyloxypropyl)trimethoxy silane) - SiO_2 (aqueous suspension 40 wt.%) - $Ce(NO_3)_3 \cdot 6\ H_2O$	TEOS/GPTMS/SiO_2/EtOH/Ce: 0.5/0.5/0.54/0.3/0.03

Note that concentrated HNO_3 (65 vol.%) as a catalyst for polycondensation was added before SiO_2 addition.

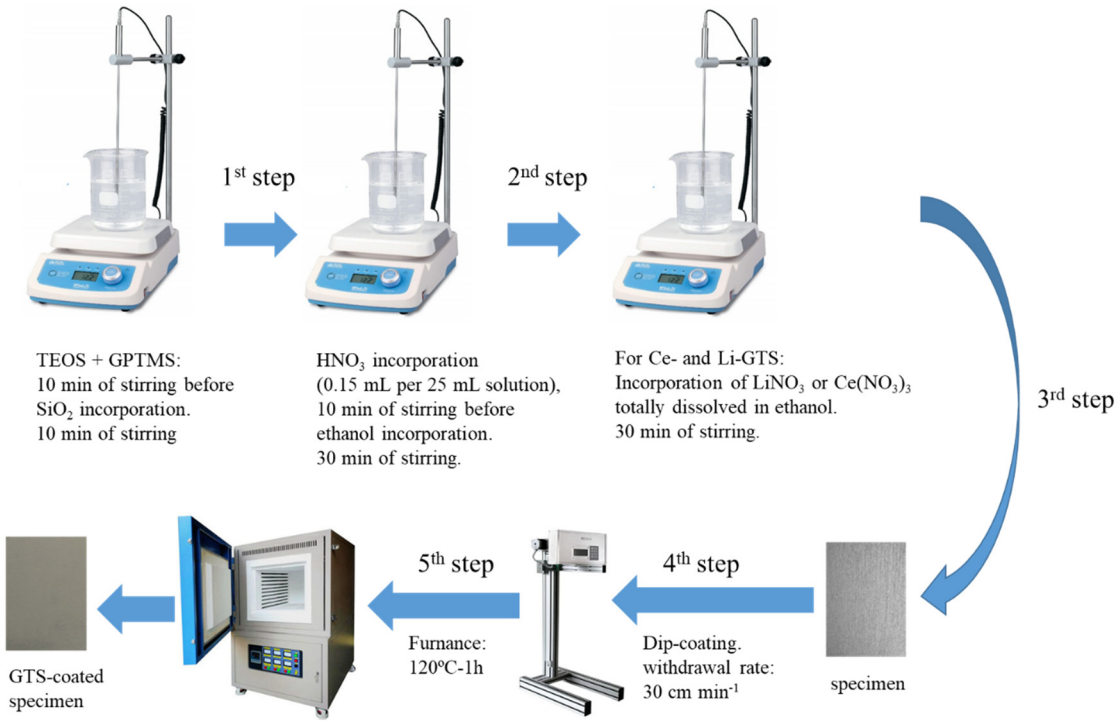

Figure 2.4. *Hybrid sol-gel route scheme for selected anodized specimen on 2024-T3.*

It should be noted that the experimental part involved in the sol-gel synthesis route (**Figure 2.4**) was carried out in the *Corrosion technology and Electrochemistry group in Technische Universiteit Delft (TUD)* in Delft (The Netherlands).

3.3.3.3. Hydrophobic sealing

For the hydrophobic surface modification, anodic and PEO surface coated specimens were immersed vertically in an organic acid-based ethanol solution at different conditions under continuous stirring (**Table 2.8**). Then, the samples were immediately rinsed with ethanol and placed in an oven for 1h at 60 °C.

Table 2.8. *Hydrophobic sealing conditions for surface-coated 2024-T3 alloy. Further specified in Section C2.2.2.2.*

Variable	Range of values
Base solutions (wt.%)	5 and 10
Treatment time (min)	30, 90 and 120
Temperature (ºC)	~ 25

3.3.4. LDH conversion coatings

LDH coatings were synthesized on 2024-T3 and 1050-H18 alloys by *in situ* growth method as shown previously in **Figure 2.3**. After the LDH synthesis, the inhibitor intercalation was carried out by immersion in an inhibitor-loading solution under specific conditions. After both processes, the samples were rinsed in deionized water and dried in isopropanol and air at room temperature (**Tables 2.9** and **2.10**).

Table 2.9. *Range of studied variables for LDH synthesis on 1050-H18 alloy. Further specified in Section C2.1.4.*

Variable	**Range of values**
Base solutions ($ZnNO_3$, NH_4OH, $NaNO_3$) (M)	0.01-0.06
Treatment time (min)	30-60
Temperature (ºC)	~ 95
pH	6.5

Notes:
1. All treatments were performed under continuous stirring in 250 mL solution.
2. pH values were adjusted by Ammonia solution (1 vol.%)

Table 2.10. *Studied variables for LDH synthesis on 2024-T3 alloy. Further specified in Section C3.1.2 and C3.2.2.*

Variable	**Range of values**
Base solutions (Zn-, Ce-, Li-, Mg-, Al, Ca-NO_3 ; Mg/LiOH; $CaCO_3$/OH^- and NH_4OH, $NaNO_3$) (M)	0.01-0.3
Treatment time (min)	30-360
Temperature (ºC)	~ 95
pH	6-10
Inhibitor concentrations ($CaNO_3$, $CeNO_3$, $NaVO_3$, $LiNO_3$, $KMnO_4$, Na_2MoO_4, $Ni(CH_3COO)_2$ and Na_2WoO_4) (M)	0.05-0.2

Note:
1. All treatments were performed under continuous stirring in 250mL solution.
2. pH values were adjusted by NaOH (1M)/Ammonia solution (1 vol.%)

3.4. Characterization techniques

3.4.1. Optical and electronic microscopy

The studied aluminium alloys and coated specimens were examined by optical microscopy (OM) using a Leica-Reichert MEF4 A/M and a Keyence VHX-100 equipped with a 12-megapixel digital camera (Olympus EPM1) and an 18-megapixel CCD camera, respectively.

Planar and cross-sectional views of coated specimens were examined using JEOL JSM 6400 and JEOL IT100 scanning electron microscopes (SEM). For higher magnification micrographs, a JEOL JSM 6335F field emission scanning electron microscope (FESEM) was also used. All these instruments were equipped with an energy dispersive (EDS) spectrometer for semi-quantitative analysis. Operating voltages ranged between 3 and 20 kV and working distances varied between 8 and 15 mm.

Cross-sectional views of selected anodic films were examined by transmission electron microscopy (TEM) using a JEM 2100 instrument with an accelerating voltage of 200 kV. 20 nm-thin TEM specimens were prepared by sectioning in an ultramicrotome (Leica Ultracut S) equipped with a diamond knife (Microstar Technologies Inc., USA).

Prior to sectioning, specimens were embedded in Agar resin which was prepared from two mixtures:
Mixture A: 24 g resin + 26 g Dodecenyl Succinic Anhydride (DDSA).
Mixture B: 24 g resin +26 g Methyl Nadic Anhydride (MNA).

Mixtures A and B were mixed with Benzyldimethylamine (BDMA) (1:1:0.04 ratio) and polymerised at 60ºC for 24 h).

3.4.2. Surface metrology

Real and topographic 2D and 3D images of studied alloys were obtained by using an InfiniteFocusSL optical profilometer (ALICONA, Gmbh). High-resolution 3D measurements (10 nm vertical resolution with ×50 objective) over large image fields were carried out by using a motorized stage. Topographic information was analysed with the IF-Measure Suite software to extract roughness parameters such as Ra (arithmetic mean value in a roughness profile), Rz (maximum roughness value), Sa (the difference in height of each point compared to the arithmetical mean of the surface) and Sz (the sum of the largest peak height value and the largest pit depth value within the defined area).

3.4.3. X-ray diffraction (XRD)

Phase identification of specimens was carried out by XRD analysis using a Philips X'Pert-MPD instrument (Cu Kα = 1.54056 Å). The XRD spectra were taken in the range of 2θ from 10° to 90° with a step size of 0.04° and a dwell time of 1 s per step and evaluated using X'Pert High Score software (ICDD PDF4+). The XRD patterns using grazing incidence were taken with a step size of (0.01º–1º) and a dwell time of 6 s per step at room temperature.

3.4.4. Rutherford backscattering spectrometry (RBS)

In the RBS technique, a very high-energy beam of particles (in the MeV range) of low mass ions ($^{1}He^{+}$ or $^{4}He^{+}$) is accelerated, collimated, and focused upon the sample under test. This beam penetrates deep into the sample (several microns) causing little sputtering of the surface atoms and elastic scattering from the coulomb repulsion between ion and nucleus, better known as Rutherford scattering. By measuring the energy of these particles and other complex physical processes at a well-defined angle, it is possible to obtain information on the nature and concentration of the target atoms as well as on their depth distribution with a resolution of 20-30 nm.

The stoichiometric compositions of oxide films were determined using He^{+} ions with the energy of 2 MeV produced by the van de Graff accelerator of the Centre for Micro Analysis of Materials (Autonomous University of Madrid). The incident ion beam with the diameter of 1 mm was normal to the specimen surface; 5-10 μC doze of scattered ions was detected by a mobile detector at 170◦. Data were interpreted using the SIMNRA software.

3.4.5. Coating thickness measurements

The thickness of all studied coatings was determined by using a Fischer ISOSCOPE instrument based on the eddy current method according to DIN EN ISO 2360 [190]. Cited values are the average of ten measurements per specimen. Measurements were validated with cross-sectional SEM and TEM images depending on the surface treatment.

3.4.6. Wettability

The wettability of selected specimens was evaluated using an FTA 1000/FTA instrument. Three drops of deionized water were analysed separately in two different samples using FTA32 software, within 25 s from the moment the drop touched the surface. Fifty photographs taken at a frame rate of 0.5 s were analyzed per each drop and the presented results provide the mean average value of all measurements.

3.4.7. pH and ionic conductivity

The pH of selected electrolytes was evaluated using a GLP 21 instrument equipped with a Pt reference electrode C.A.T 1000. The ionic conductivity was measured using an EC-Metro GLP 31 equipped with conductivity cell 5072 (C: 10 cm^{-1}). All the presented results provided the mean average value of all measurements.

3.5. Corrosion resistance evaluation

3.5.1. Electrochemical impedance spectroscopy (EIS)

EIS is an electrochemical technique widely used in the study of electrochemical systems. It gives reliable information about the structure of the anodic films and their electrical properties. EIS of all coated specimens was performed to evaluate the corrosion resistance in an aqueous saline solution (3.5 wt.% NaCl) at 25 ºC. Specimens with an exposed area of 1 cm^2 were used in a three-electrode cell with a GillAC (ACM Instruments) potentiostat (some measurements were also carried out with a Biologic VMP-300 multichannel computer-controlled potentiostat located at TUDelft). A graphite rod and silver–silver chloride (Ag/AgCl, 3 M KCl) were used as counter and reference electrodes, respectively. A sinusoidal perturbation of 10 mV amplitude in the frequency range of 30 kHz–0.01 Hz was applied after different immersion times (up to 672 h). All measurements were repeated at least twice. Equivalent circuits were simulated by using ZView and EC-Lab softwares. Fits of the experimental data were obtained with chi-squared values in the range of 0.001–0.0001.

3.5.2. Neutral salt spray test (NSST)

NSST was carried out for coated and coated-and-painted specimens using a salt spray cabinet (CCI/CCM-MX,CCI) according to the ASTM B117 standard [191]. The specimens were inclined 6 degrees from the vertical and exposed for varying times up to 1000 h. The salt fog atmosphere was created using an aqueous solution of 5 wt.% NaCl at 6.5-7.2 pH range and 35°C. After the tests, the specimens were rinsed with water at ~ 38°C in order to remove solid salt deposits and dried in air.

The sample sizes were 40×40×1.5 mm^3 and in some cases 250×75×2 mm^3 coupons. In some samples, NSST was performed in painted and scratched specimens. The defect (scratch or cross) in the center of the samples was made with a scratching tool (ISO 17872 [192]) with a 0.5 mm tungsten carbide tip. On 40×40×1.5 mm^3 specimens the length of the scratch was 1.5 cm; on 250×75×2 mm^3 coupons a 50×50 mm^2 cros was made. Rating numbers of scratched specimens were defined according to ASTM D 1654-92 [193].

3.6. Mechanical properties

3.6.1. Fatigue strength

Fatigue resistance of a material is the range of cyclic stress that can be applied to a material without causing a progressive and localised structural damage. In order to determine the S–N curves of selected specimens, fatigue tests were performed according to ASTM E466 [194] at five strains levels, four repetitions for level, 15 Hz of frequency, 0.1 of load ratio and at room temperature. All measurements were performed in *Fundación Cidaut* (Valladolid, Spain), using a servohydraulic test system (MTS 318HCF) with a load cell (MTS, 661.19F-12) and Termohigrometer (TESTO, 175-H2).

3.6.2. Wear resistance

The tribological properties of the HA and PEO coatings were evaluated in dry conditions on a MT/60/NI ball-on-disc tester (MicroTest) at room temperature (~21 °C) and ~35% humidity.

Tests were performed in ball-on-flat linear reciprocating mode (according to ASTMG133). The coatings served as the plates and the counterpart was a WC ball of 6 mm in diameter and 1800 HV hardness. The tests were carried out at a sliding speed of 40 mm/s for a maximum sliding distance of 70 m (~30 min) with a stroke length of 10 mm. Normal loads applied were 5-10 N.

The wear rates after the tests were calculated by dividing the wear volume loss at the track by the total sliding distance and load. The volume loss was obtained by high resolution 3D measurements (InfiniteFocusSL, Bruker Alicona) of the worn surfaces. For each condition, the reported wear rate values corresponded to the average of the volume loss measured for three independent tests. Worn surfaces were examined by SEM in order to identify the dominant wear mechanisms.

It is important to mention that specific wear rate values of PEO coatings so calculated should be considered with caution due to the inherent porosity of the coatings.

Wear tests of PEO coatings were performed after removing the outer porous layers with P320 silicon carbide abrasive paper. The HA coatings were ground down to eliminate the undulating irregular top region. The final target thickness in both cases was 50 μm.

3.6.3. Nanoindentation

Nanoindentations were performed on polished cross-sections to obtain their bulk mechanical properties using a nano-indenter XP (Nano Instruments, MTS Systems Corporation, USA) with a standard Berkovich indenter in load control mode up to a

maximum load of 100 mN. Hardness (H) and reduced Elastic modulus (E) were calculated from the load-displacement curves following the Oliver and Pharr methodology. The Poisson's coefficients to calculate the E were 0.34 for Al and 0.22 for Al_2O_3. Indentations were performed at approximately half of the coatings thickness and at sufficient distance between each other to avoid interference from previous plastic deformation. Typically 15 indents were obtained for individual specimens, from which average values were calculated. This test was performed in the Rey Juan Carlos University facilities in Madrid (Spain).

3.7. Paint adhesion

All paints were provided by Azkonobel (Epoxy Primer 37076 and XP-420). Paint adhesion was evaluated on selected coated samples in triplicate per coating type following ISO 2409 standard [195]. The different components were mixed according to the technical data sheet. The paint application was performed by a metallic paint roller under the specific instructions of use and safety precautions. Painted substrates were cured at 80ºC for 1 h. The results obtained are classified in a six-rating classification considering the detached surface (%) from the cross-cut grid after the test. The result is considered to be 0 when none of the paint is detached and 5 for complete detachment.

4. Results and Discussion

Chapter 1: Enhancement of corrosion resistance of anodic films on 2024 alloy

Prior studies have demonstrated that *in situ* incorporation of inhibitors is an effective way to increase the corrosion resistance of anodic films on aluminium. Sealings are also a common approach to further enhance the corrosion performance of anodic films. In this context, Chapter 1 is focused on the development of TSAA and TSA anodic films with improved corrosion resistance for painted and non-painted aircraft applications. The structure of the chapter is divided in two sections: (i) *in situ* incorporation of cerium-based inhibitors into TSAA and TSA anodic films for painted components; and (ii) *in situ* incorporation of organic inhibitors into TSAA and TSA anodic films followed by sol-gel sealings for added active protection for non-painted parts. The critical goal is to produce Cr-free anodic films on a commercial Al-Cu alloy (2024) that combine low thickness with improved corrosion resistance for both stand-alone and painted components. Results are compared to a state-of-the-art CAA film produced on the same alloy. **Figure 3.1** shows the graphical abstract of Chapter 1.

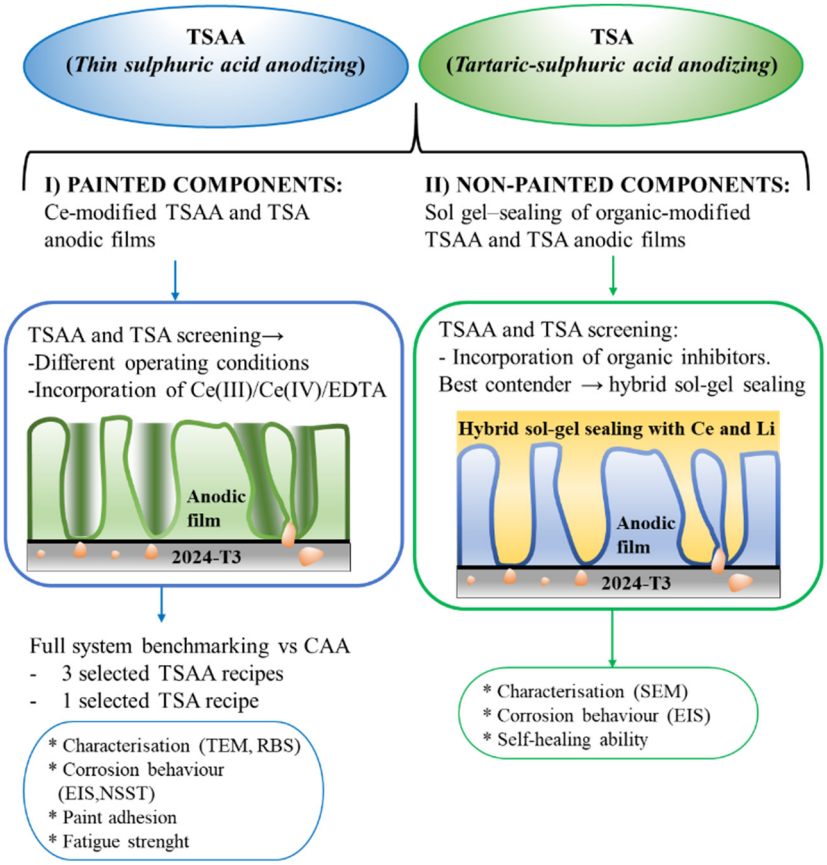

Figure 3.1. *General scheme of Chapter 1.*

Chapter 1

C1.1. Ce-modified TSAA and TSA anodic films

C1.1.1. Introduction

As described in **Section 1.3.2.2**, Ce species have been targeted several times in the past for improving the corrosion resistance of anodic films [86, 196, 197]. Although the improved performance of anodic films produced in the presence of Ce has been demonstrated in several studies, there is still a knowledge gap regarding the influence of Ce species on parameters such as anodizing efficiency, film morphology, corrosion resistance, fatigue life and paint adhesion.

In this section, the abovementioned features are investigated for the 2024 alloy under typical anodizing conditions in TSAA and TSA based electrolytes containing Ce(III)/(IV) species with and without the addition of a complexing agent (ethylenediaminetetraacetic acid disodium salt, $EDTANa_2$). In theory, EDTA may form Ce-containing complexes, thereby facilitating Ce incorporation into the anodic films. Screening of the best modified TSAA and TSA films is carried out by EIS. Then, the best candidates are characterized and evaluated in terms of corrosion resistance, fatigue life and paint adhesion in comparison to a CAA reference specimen.

C1.1.2. Screening of TSAA anodic films

TSAA anodic films were obtained on 2024 alloy in 15 different sulphuric acid electrolytes with and without Ce(III)/Ce(IV) and $EDTANa_2$ in equimolar concentration (**Table 3.1**). Anodizing treatments were performed at constant current density (15 mA cm^{-2}) or constant voltage (18 V). The anodizing regime conditions and the concentrations used for sulphuric acid and Ce species were selected considering typical examples from the literature [46, 65, 196, 198-200]. The addition of $Ce(SO_4)_2$ resulted in transparent yellow solutions since solvated Ce^{4+} ions are known for their yellow colour in aqueous solutions [201]. In the case of $Ce_2(SO_4)_3$ additions, no colour change was observed. It is worth noting that $Ce_2(SO_4)_3$ was more difficult to dissolve than $Ce(SO_4)_2$ [202].

The screening process to select the best TSAA anodic films was according to (i) the lowest possible thickness (≤ 3 μm) and (ii) the highest corrosion resistance, which is based on the value of the impedance modulus at low-frequency (10^{-2} Hz) obtained by EIS, i.e. high values of |Z| indicate a low corrosion rate. All measurements were performed after 1 hour of immersion in naturally aerated 3.5 wt.% NaCl solution at room temperature.

Table 3.1. *Anodizing conditions for screening of TSAA films on 2024 alloy.*

Anodic film	Electrolyte (g L^{-1})				Conditions		
	H_2SO_4	$Ce_2(SO_4)_3$	$Ce(SO_4)_2$	$EDTANa_2$	V_{max} (V)	j (mA cm^{-2})	Time (min)
TSAA-300s	150	-		-	-	15	5
TSAA-900s	150	-		-	-	15	15
TSAA-18V	150	-		-	18		25
Ce (III)-300s	150	7.5		-	-	15	5
Ce (III)-900s	150	7.5		-	-	15	15
Ce (III)-18V	150	7.5		-	18	-	25
Ce (III)-EDTA-300s	150	7.5		4.9		15	5
Ce (III)-EDTA-900s	150	7.5		4.9		15	15
Ce (III)-EDTA-18V	150	7.5		4.9	18	-	25
Ce (IV)-300s	150		7.5	-		15	5
Ce (IV)-900s	150		7.5	-		15	15
Ce (IV)-18V	150		7.5	-	18	-	25
Ce (IV)-EDTA-300s	150		7.5	8.4		15	5
Ce (IV)-EDTA-900s	150		7.5	8.4		15	15
Ce (IV)-EDTA-18V	150		7.5	8.4	18	-	25

As shown in **Figure 3.2a**, short treatment times (300 s) yielded thinner anodic films (≤ 2 µm) in comparison to long treatment times (900 s) and constant voltage (18 V) treatments (≥ 3 µm). The treatments carried out at 18 V produced the thickest layers. This is consistent with the greater charge associated with longer treatment times. Note that film thicknesses with values close to or below 1 µm should be taken with care as they are accompanied by a larger uncertainty associated with the limitations of the eddy current meter used for measuring film thickness.

Findings revealed that the thicknesses of anodic films produced in the Ce-containing electrolytes were slightly lower, indicating lower anodizing efficiencies than that of TSAA reference film (e.g. for the constant current regime: ~0.015 µm C^{-1} for Ce-TSAA vs ~0.022 µm C^{-1} for TSAA reference). This is opposite to the results by Moutarlier *et al*. [203], who, based on SEM examinations, found an accelerated anodic film growth in the presence of 0.1 M or ~33 g L^{-1} $Ce(SO_4)_2$ for the 2024 alloy. According to them, a 30 min treatment under 1.5 mA cm^{-2} should produce a 5-7 µm thick film with or without cerium. This is roughly three times more than should be expected from Faraday's Law assuming a 100% efficiency and 10% porosity. Unfortunately, the study by Moutarlier *et al*. does

not provide direct evidence of the film thicknesses in the form of SEM or TEM cross sections.

Concerning EDTA addition, our findings revealed its negligible effect on film thickness. This suggests that EDTA-Ce complexes are not formed/incorporated under these conditions, possibly due to the low pH and corresponding protonation of EDTA [204].

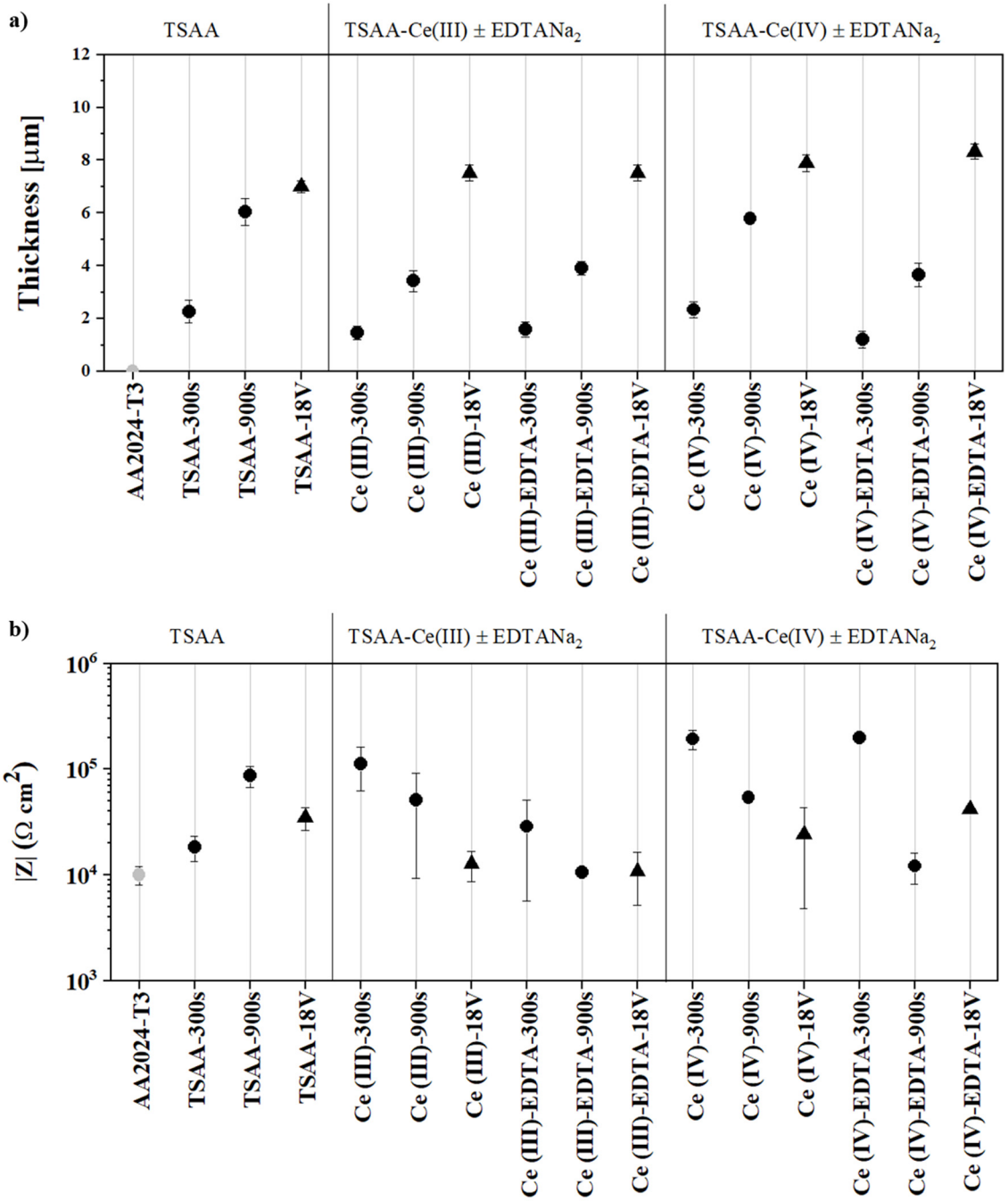

Figure 3.2. *Scatter diagram of the (a) thicknesses and (b) impedance modulus values at low frequency (10^{-2} Hz) for modified TSAA anodic films. Filled circles indicate oxide films developed at 15 mA cm^{-2}. Filled triangles indicate anodic films carried out at 18 V.*

Based on |Z| values, the corrosion protection of the anodic film greatly depended on the anodizing conditions. The best results were obtained for thin films and with Ce incorporation. The effect of Ce was more noticeable for Ce(IV)-containing electrolytes. This beneficial effect of Ce(IV) is further discussed in **Section 1.1.5**. The effect of EDTA was negligible (**Figure 3.2b**). Therefore, the Ce(IV)-300s treatment which achieved the best corrosion protection was selected for further optimization.

C1.1.2.1. Fine-tuning of Ce(IV)-TSAA anodic films

Based on the results from the previous section, further studies were carried out to optimize the Ce(IV)-TSAA films (**Table 3.2**). Different amounts of $Ce(SO_4)_2$, 7.5 or 33 g L^{-1}, at constant current density (1.5 or 15 mA cm^{-2}) or voltage (6 or 18 V) were evaluated and compared to the results obtained in the Ce(IV)-free electrolyte. Note that constant voltage treatments included an initial ramp with a rate of 60 mV s^{-1}.

Table 3.2. *Anodizing conditions for fine-tuning of Ce(IV)-TSAA films on 2024 alloy.*

Anodic film	Electrolyte (g L^{-1})		Conditions		
	H_2SO_4	$Ce(SO_4)_2$	V_{max} (V)	j (mA cm^{-2})	Time (min)
S1	150	-	-	15	5
S2	150	-	-	15	15
S3	150	-	-	15	25
S4	150	-	-	1.5	5
S5	150	-	-	1.5	15
S6	150	-	-	1.5	25
S7	150	-	18[a]	-	25
S8	150	-	6[a]	-	119[b]
SC1.1	150	7.5	-	15	5
SC1.2	150	7.5	-	15	15
SC1.3	150	7.5	-	15	25
SC1.4	150	7.5	-	1.5	5
SC1.5	150	7.5	-	1.5	15
SC1.6	150	7.5	-	1.5	25
SC1.7	150	7.5	18[a]	-	25
SC1.8	150	7.5	6[a]	-	130[b]
SC2.1	150	33	-	15	5
SC2.2	150	33	-	15	15
SC2.3	150	33	-	15	25
SC2.4	150	33	-	1.5	5
SC2.5	150	33	-	1.5	15
SC2.6	150	33	-	1.5	25
SC2.7	150	33	18[a]	-	25
SC2.8	150	33	6[a]	-	137[b]

[a] An area of 150 cm^2 was used in order to get current values large enough for the acquisition system.
[b] Time adjusted to have a charge equal to that of 18 V treatment.

As shown in **Figure 3.3**, Ce(IV)-containing electrolytes produced films of similar thickness. This suggests that there is little or no incorporation of Ce species into the films.

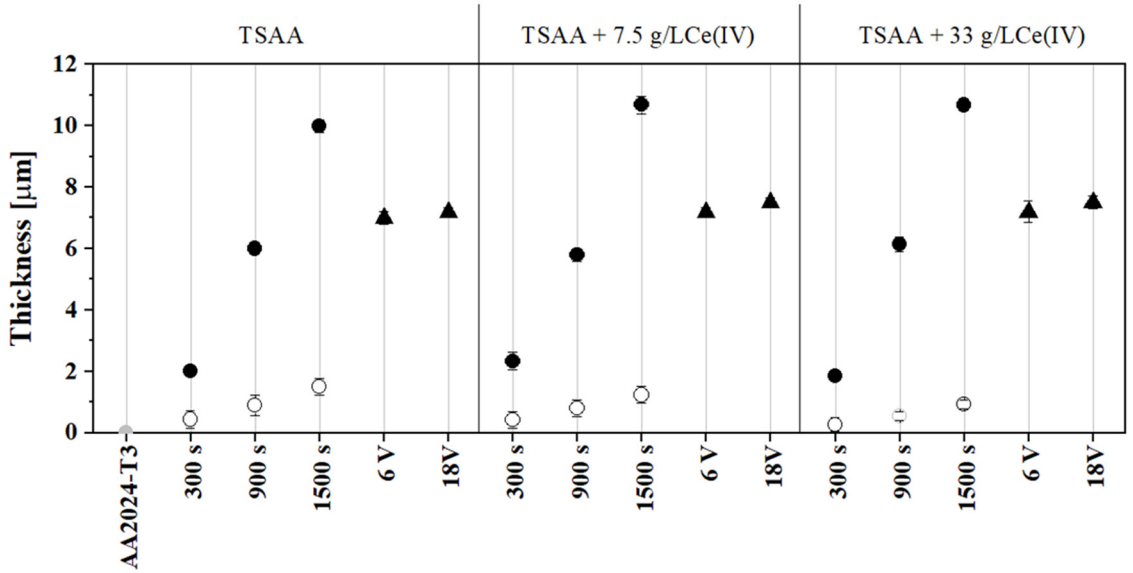

Figure 3.3. *Scatter diagram of the thicknesses of Ce(IV)-TSAA anodic films as a function of treatment time, Ce(IV) concentration and anodizing regime. Filled and empty circles indicate oxide films developed at 15 mA cm^{-2} and 1.5 mA cm^{-2}, respectively. Filled triangles indicate anodic films carried out under voltage-controlled mode.*

Figure 3.4 depicts the voltage-time responses under current-controlled mode for the 2024 alloy anodized at 1.5 (**Figures 3.4a,b**) and 15 mA cm^{-2} (**Figures 3.4c,d**). The voltage signal shows several changes that are related to phenomena such as thickening of the barrier layer, copper oxidation, oxygen evolution and dissolution of intermetallic particles [71]. As shown in **Figure 3.4**, the voltage increases at a lower rate in the region between 3 to 6 V. This is more evident in the case of the low current regime (**Figures 3.4a,b**) and is typically associated with the dissolution of intermetallic particles [205, 206]. For longer anodizing times, the voltage signal reaches a steady state where the barrier layer maintains a constant thickness and the porous layer keeps developing. Final measured voltages are ~4-4.5 V and ~ 19.5-21 V for 1.5 mA cm^{-2} and 15 mA cm^{-2} curves, respectively. The larger voltage values for the higher current regimes are associated with the formation of a thicker barrier layer [203].

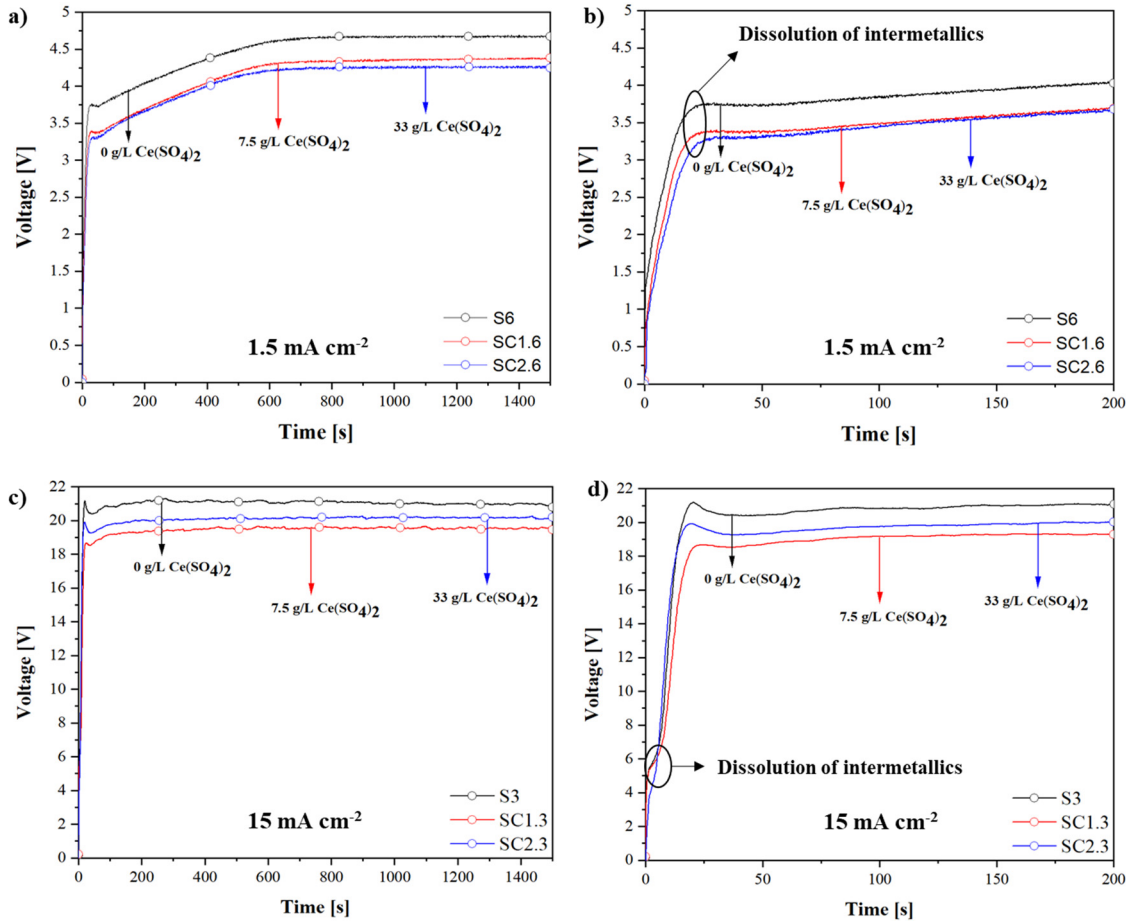

Figure 3.4. *Voltage-time curves for anodizing with different amounts of $Ce(SO_4)_2$ at (a,b) 1.5 mA cm^{-2} and (c,d) 15 mA cm^{-2}.*

Regardless of the applied current density, the addition of $Ce(SO_4)_2$ decreases the final voltage by 0.5-1.5 V in comparison to the reference electrolyte (**Figures 3.4a,c**). A similar effect was observed by Moutarlier *et al*. [207]. This could be to some extent due to the increased conductivity of the acidic solution. The measured electrolyte conductivities were: (339±5) mS cm^{-1}, (639±4) mS cm^{-1} and (660±5) mS cm^{-1} for 0, 7.5 and 33 g L^{-1} $Ce(SO_4)_2$, respectively. These values, as opposed to those of Moutarlier (~240 µS cm^{-1} and 310 µS cm^{-1} without and with $Ce(SO_4)_2$, respectively), are consistent with the sulphuric acid concentration used in this work.

However, if one considers these values and other parameters such as the cathode-to-anode distance (~4 cm), the size of the specimen (~20 cm^2) and the applied current, then the effect of electrolyte conductivity on measured voltage values should only be of the order of several millivolts. In fact, ~10 mV for 1.5 mA cm^{-2} and ~100 mV for 15 mA cm^{-2}. Therefore, the lower final voltages in the presence of $Ce(SO_4)_2$ are likely to be related to other factors such as a thinner barrier layer due to the increased dissolving power of the

modified electrolyte. For example, assuming an anodizing ratio of 1.0 nm V^{-1} in 15% sulphuric acid [203], a slightly thinner barrier layer, by just 1 or 2 nm, would explain the observed differences in the final voltages. It is worth noting that the high current regime in the 33 g L^{-1} $Ce(SO_4)_2$ electrolyte produced a final voltage that was slightly higher than that of 7.5 g L^{-1}. The exact reason for this finding is unclear. It could be related to experimental uncertainties or small differences in the barrier layer thickness.

The voltage-controlled treatments at 18 V (**Figure 3.5a**) and 6 V (**Figure 3.5c**) reveal several distinct features during the initial voltage ramp at 60 mV s^{-1}.

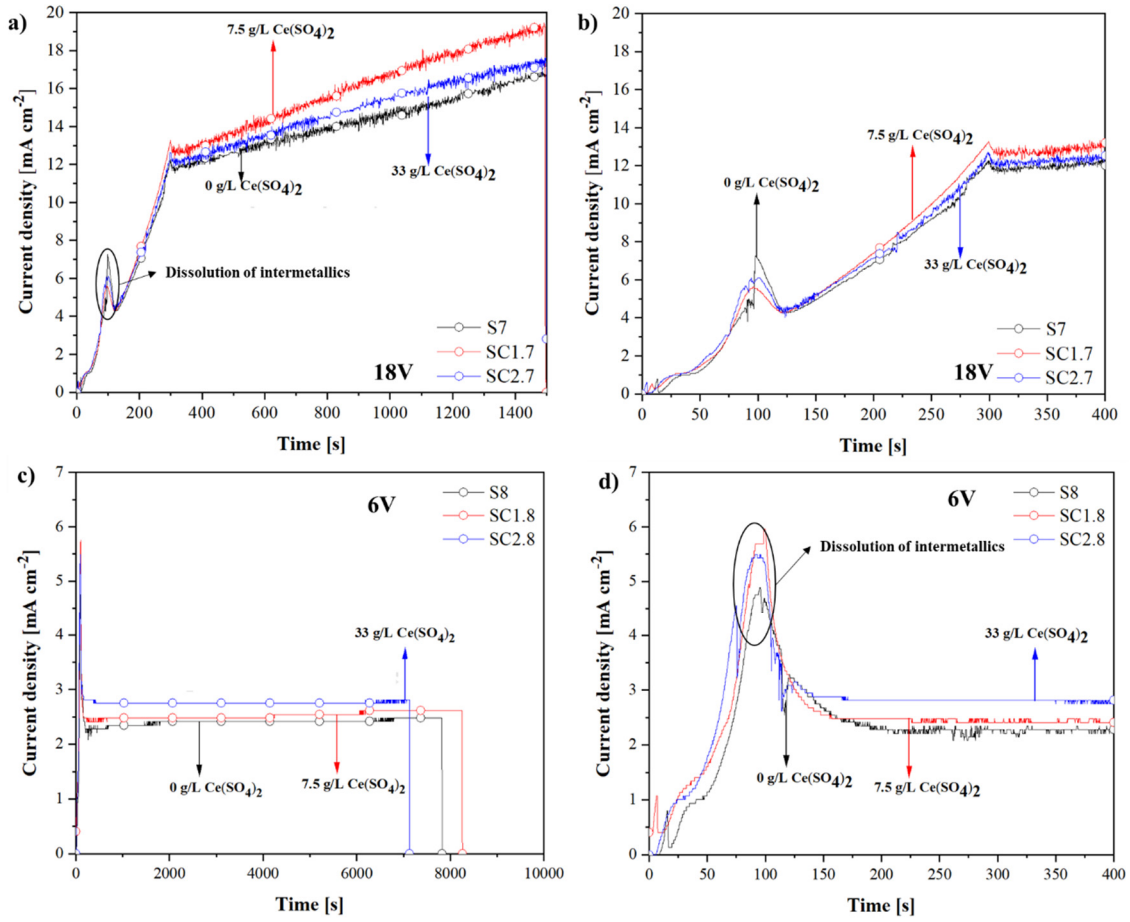

Figure 3.5. *Current density-time curves for anodizing with different amounts of $Ce(SO_4)_2$ at (a,b) 18 V and (c,d) 6 V.*

The current increases from the commencement of anodizing until it reaches a plateau at ~1 mA cm^{-2} that lasts for ~15 s (this period corresponds to the interval between ~1.5 to 3 V). The initial current surge is related to non-uniform thickening of the film, whereas the plateau is due to the constant field strength being maintained by uniform film growth [206]. Later, at ~95 s (i.e. ~5.7 V), there is a current peak which is again associated with the dissolution of secondary phases. After that, the current remains relatively constant at

2.3-2.8 mA cm^{-2} for the 6 V treatment, while a non-steady-state is observed in the case of the 18 V regime; the current density increases up to 17-19 mA cm^{-2} by the end of the treatment. This is due to heating of the electrolyte volume (in the presence of a large size specimen) decreasing the overall resistance.

The presence of Ce(IV) species increases the final current density by approximately 0.5 and 2 mA cm^{-2} for 6 and 18 V curves respectively. This is again in part due to the higher conductivity of the modified electrolyte and probably to the development of a thinner barrier layer in the presence of Ce(IV) species. Note that the concentrated electrolyte (33 g L^{-1}) yields lower current values than the dilute one (7.5 g L^{-1}) for the 18 V treatment. This could be again associated with experimental uncertainties or small differences in the barrier layer thickness.

The anodic films developed under low current density show the best corrosion performance (**Figure 3.6**). These results indicate an unusual non-linear dependence between film thickness and corrosion resistance [46]. This effect is more remarkable for the 1500 s treatments. The addition of Ce(IV) is in general positive, with SC1.6 (7.5 g L^{-1}, 1500 s, 1.5 mA cm^{-2}) and SC2.6 (33 g L^{-1}, 1500 s, 1.5 mA cm^{-2}) anodic films providing the best results. These specimens were further characterized and evaluated in terms of corrosion, paintability and fatigue life testing. The inhibitor-free anodic film S6 (0 g L^{-1}, 1500 s, 1.5 mA cm^{-2}) was also analysed for comparison.

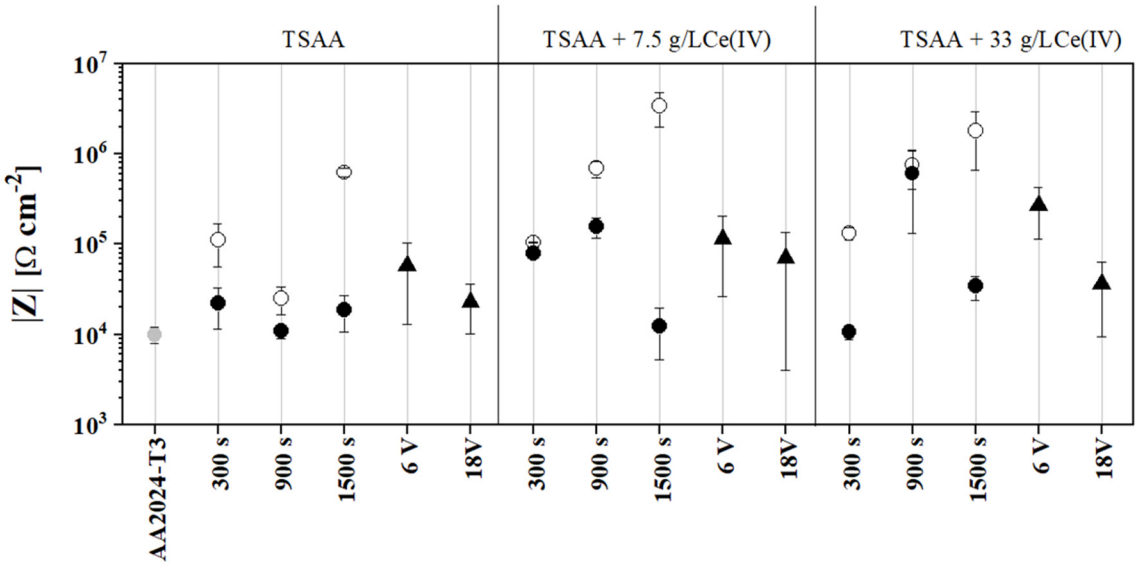

Figure 3.6. *Scatter diagram of the impedance modulus at low frequencies values (10^{-2} Hz) for Ce(IV)-TSAA films. Filled and empty circles indicate oxide films developed at 15 mA cm^{-2} and 1.5 mA cm^{-2}, respectively. Filled triangles indicate anodic films carried out under voltage-controlled mode.*

C1.1.3. Screening of TSA anodic films

TSA anodic films were obtained on 2024 alloy in 6 different sulphuric-tartaric acidic electrolytes with and without Ce(IV) and EDTA (**Table 3.3**). Anodizing treatments were performed at constant current density (1.5 mA cm^{-2}) or voltage (14 V) at two different temperatures (25 and 37ºC). Note that the 14 V treatment included an initial ramp at ~47 mV/s. The operating conditions and electrolyte composition concentrations were established considering the previous studies [66, 78, 196, 197, 208, 209] and the findings from the previous section (**Section 1.1.3**).

It should be noted that the TSA electrolyte with added $Ce(SO_4)_2$ was initially intense yellow to later become colourless in a matter of hours. When Ce(IV) is added to the electrolyte, it is likely to be reduced to Ce(III) by its interaction with tartaric acid. This explains the colour change since solvated Ce^{3+} ions are known to be colourless [201]. Simultaneously, tartaric acid is converted into formic acid and carbon dioxide [210] (**Equation 3.1**).

$$HOOC-CHOHCHOH-COOH+2H_2O+8Ce^{4+}\rightarrow HCOOH+3CO_2+8Ce^{3+}+8H^{+} \quad \textit{Eq. (3.1)}$$

Table 3.3. *Anodizing conditions for screening of TSA films on 2024 alloy.*

Anodic film	Electrolyte (g L^{-1})			Conditions			
	H_2SO_4/ $C_4H_6O_6$	$Ce(SO_4)_2$	$EDTANa_2$	V_{max} (V)	j (mA cm^{-2})	T (ºC)	Time (min)
T1	45/79.5			14	-	25	25
T1.1	45/79.5			14	-	37	25
T2	45/79.5			-	1.5	25	25
T2.2	45/79.5			-	1.5	37	25
TC2	45/79.5	7.5		-	1.5	25	25
TC2-E	45/79.5	7.5	8.4	-	1.5	25	25

Following the same procedure as in **Section 1.1.3**, the screening process was based on the same parameters; (i) the lowest possible thickness (≤ 3 μm) and (ii) the highest corrosion resistance after 1 hour of immersion in naturally aerated 3.5 wt.% NaCl solution.

Similar to the previous results, anodic films developed under low current density showed relatively low thicknesses (**Figure 3.7**). The addition of $Ce(SO_4)_2$ slightly decreased the film thickness, whereas changing the temperature from 25ºC to 37ºC resulted in a thicker film. This is in accordance with previous studies where an increase in the anodic film growth rate is observed at higher temperatures [66, 211]. Note that 37ºC is commercially used for TSA films.

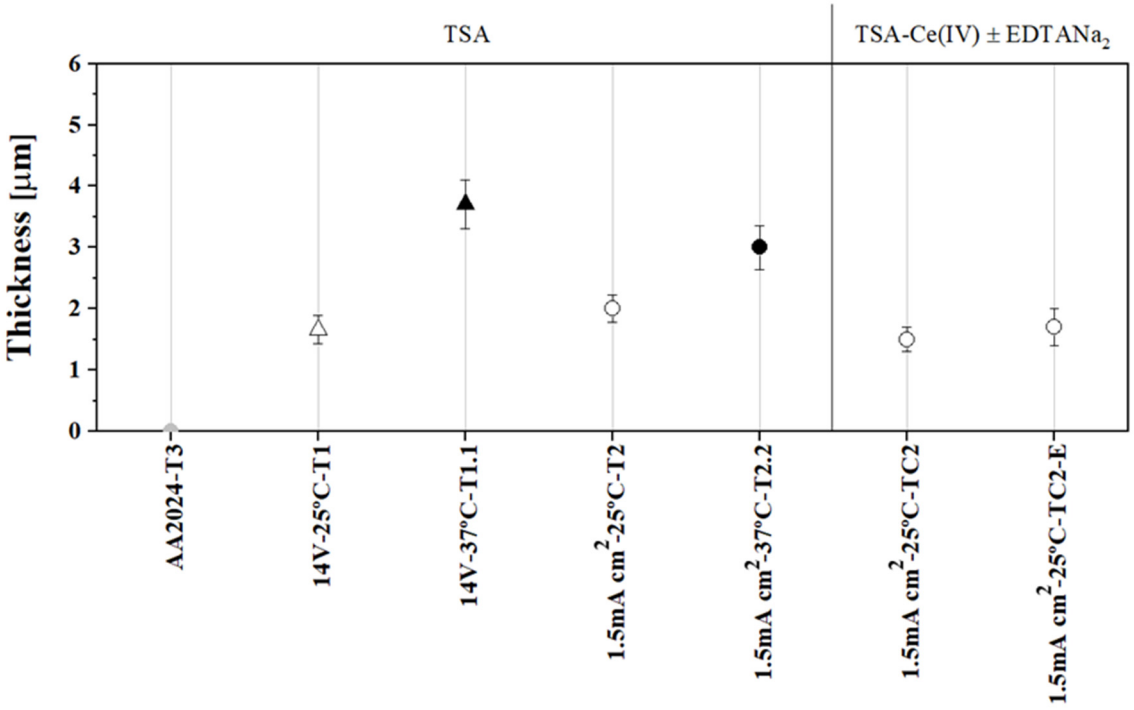

Figure 3.7. *Scatter diagram of the thicknesses for TSA anodic films. Circles and triangles indicate oxide films developed at 1.5 mA cm^{-2} and 14 V, respectively. Filled and empty symbols indicate oxide films developed at 37ºC and 25ºC, respectively.*

Figure 3.8 depicts voltage- and current-time responses for the 2024 alloy anodized in TSA at 1.5 mA cm^{-2} and 14 V, respectively.

Under a constant-current regime and during the first 50 s, the voltage increases similarly for all the studied conditions due to the thickening of the barrier layer. At longer times the slope decreases due to phenomena such as the dissolution of secondary phases and oxygen evolution [66]. Finally, when the barrier layer reaches its maximum thickness, the voltage values remain relatively constant.

The final voltage value depends on the presence of additives and the electrolyte temperature. For anodic films developed at 25ºC, the voltage signal reached a steady state at ~10.5 V for the T2 specimen, which is higher than TC2 and TC2.2 anodic films (~ 8.5 V). The lower voltages in the presence of cerium again may be attributed to the increased

conductivity of the acidic solution and, more likely to the reduced barrier layer thickness. The measured electrolyte conductivities were: (191 ± 2) mS cm^{-1}, (213 ± 3) mS cm^{-1} and (216 ± 5) mS cm^{-1} for T2, TC2 and TC2.2, respectively. The effect of Na_2EDTA on voltage response was negligible.

With respect to the effect of temperature, the T2.2 specimen treated at 37ºC showed a final steady voltage of ~3.2 V. This value is lower than those obtained at 25ºC. This is typically associated with an increase in the mass transfer rates of O^{2-} and Al^{3+} ions at higher temperatures [211] and the higher dissolving power of the electrolyte resulting in a barrier layer of smaller thickness.

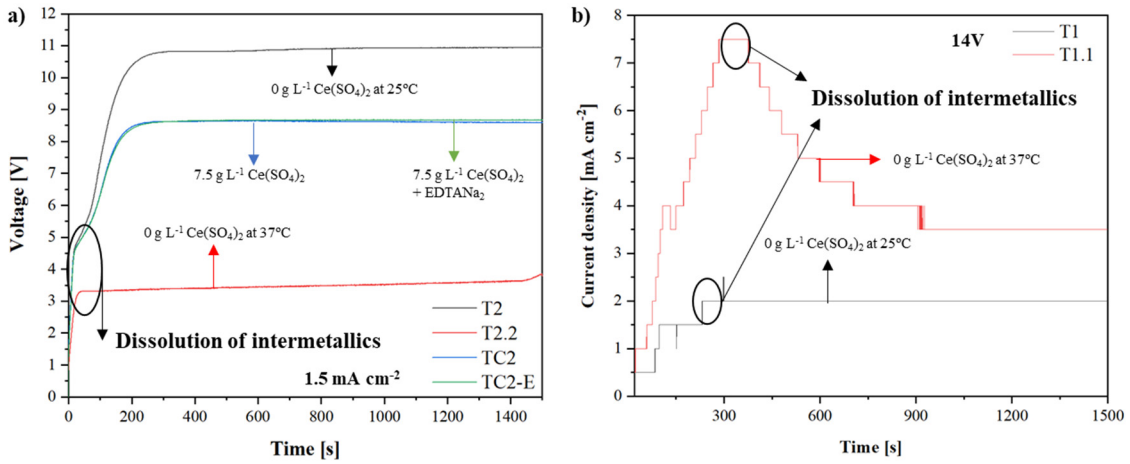

Figure 3.8. *(a) Voltage- and (b) current density-time curves for studied TSA electrolytes.*

The voltage-controlled treatments at 14 V (**Figure 3.8b**) show current densities that increase during the initial voltage ramp and then remain relatively constant at ~2 mA cm^{-2} and 3.5 mA cm^{-2} for the T1 (25ºC) and T1.1 (37ºC) specimens, respectively. The current peak or overshoot observed for the T1.1 specimen could be related to the decrease of the initial pore density with the steady-state growth of major pores [212] or the enhanced dissolution of secondary phases [213]. The T1 specimen is likely to produce a similar current peak, but the limited resolution of the acquired data makes it difficult to resolve. These fluctuations in current are therefore indicative of the simultaneous formation of the barrier layer and development of the porous layer on the surface of the specimen [211]. The final plateau observed in both specimens is mainly due to uniform film growth. The higher current values in T1.1 are associated with the higher electrolyte conductivity due to the higher temperature (255 ± 3 at 37ºC *vs.* 191 ± 2 mS cm^{-1} at 25ºC) and possibly to the higher dissolving power of the electrolyte yielding a thinner barrier layer.

In terms of corrosion resistance, it is evident that increasing the bath temperature is detrimental for all the treatments (**Figure 3.9**). The low current regimes (T2 and T2.2) produced better results than the constant voltage ones (T1 and T1.1), which is similar to the result found for TSAA films in the previous section. This better behaviour of anodic films developed under low current conditions is further discussed in **Section 1.1.5**.

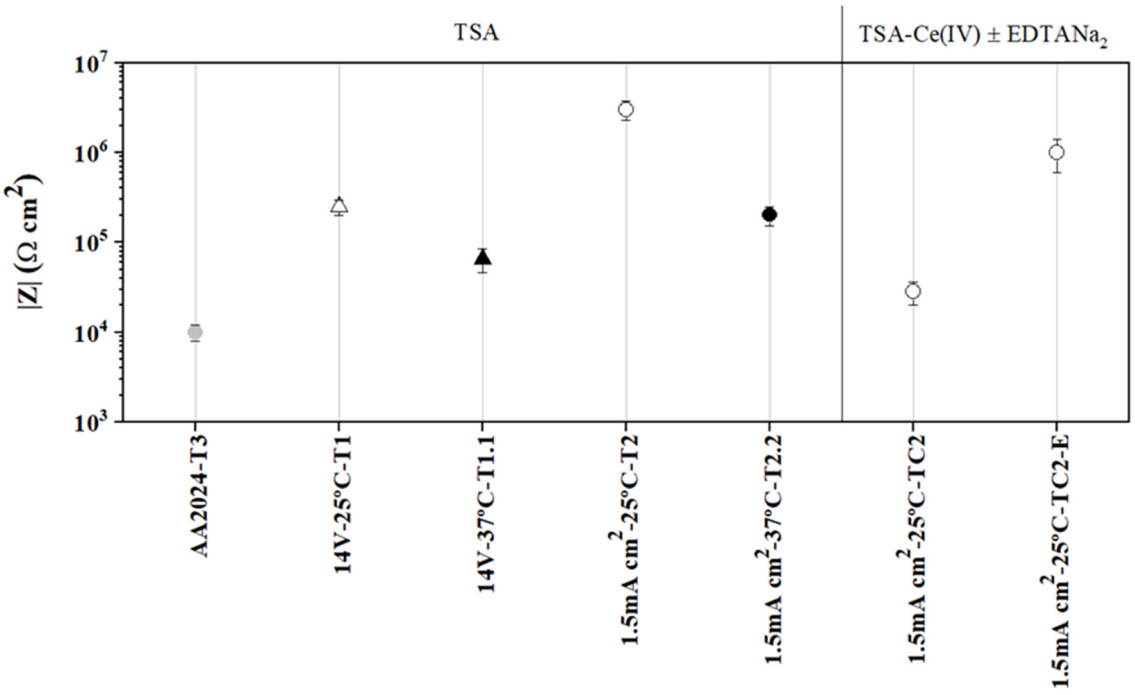

Figure 3.9. *Scatter diagram of the impedance modulus values at low frequency (10^{-2} Hz) for TSA anodic films. Circles and triangles indicate oxide films developed at 1.5 mA cm^{-2} and 14 V, respectively. Filled and empty symbols indicate oxide films developed at 37ºC and 25ºC, respectively.*

It is interesting to note that Ce addition is detrimental from a corrosion point of view in the case of TSA, which is opposite to the results found for TSAA electrolyte. The addition of EDTA increased the impedance modulus of the Ce-containing treatment, but the value was still lower than that of the unmodified recipe. The detrimental effect of Ce addition could be associated with its interaction with tartaric acid, reducing its known protective effect on anodic films [213]. Indeed, in the present study, it was observed that tartaric-sulphuric acid mixtures with added Ce were unstable and resulted in the precipitation of a white powder after several days. This powder may correspond to cerium tartrate [210]. The addition of EDTA counteracts the negative effect of Ce, possibly due to the formation of Ce-EDTA complexes instead of cerium tartrate. Curioni *et al.* [197] reported a very small beneficial effect on the corrosion resistance of 2024 T3 alloy when $Ce(NO_3)_3$ was

added to a tartaric-sulphuric mixture. The different anodizing conditions (constant voltage anodizing at 6 V) and the small amount of Ce salt (1.2 g L^{-1}) may explain the observed differences with respect to the present study. The use of cerium nitrate instead of cerium sulphate should not be the reason for this discrepancy since nitrate ions (NO_3^-) are relatively aggressive to aluminium.

Based on the previous screening, T2 anodic film was selected for detailed characterization and evaluation in terms of corrosion, paintability and fatigue life.

C1.1.4. Full system benchmarking of selected anodic films vs. CAA

C1.1.4.1. Characterization of anodic films

Figure 3.10 depicts the cross-sectional transmission electron micrographs of ultramicrotomed sections of the selected anodic films; S6, SC1.6, SC2.6 and T2. CAA is also included for comparison. All the anodic films reveal a thin barrier layer and a porous layer with lateral porosity. This observation agrees with previous studies where the porous layer is strongly disorganized due to the presence of Cu-containing intermetallic particles promoting oxygen evolution during the anodizing process [60].

Regarding the role of Ce on anodic film morphology, S6 showed a maze or chaotic pore alignment, whereas SC1.6 and SC2.6 films reveal more vertical and aligned pores. A similar change in pore morphology was observed by Li *et al*. [196] for the 1420 Al-Li alloy anodized in sulphuric acid, although the composition and the exact amount of Ce(IV) salt were not provided. Li *et al*. suggested that the change in pore morphology was associated with the surface adsorption of Ce-sulphate complexes which, in turn, affected the growth of the anodic film. It is also possible that the addition of Ce(IV) reduces oxygen evolution during anodizing, therefore decreasing the likelihood of lateral porosity. This statement is based on the lower voltage values recorded for the SC1.6 and SC2.6 specimens in comparison to S6.

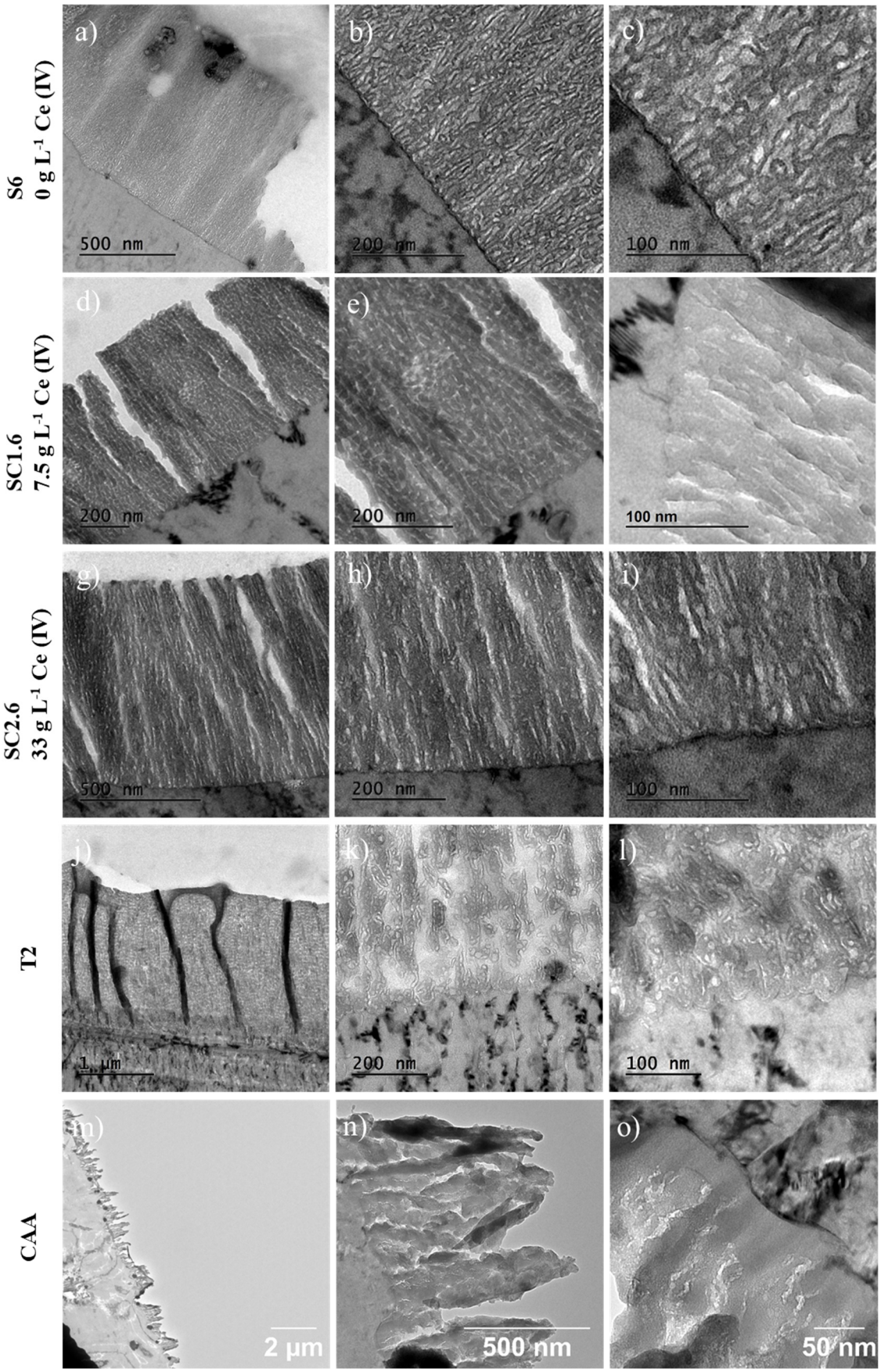

Figure 3.10. *Transmission electron micrographs of anodic films: (a-c) S6, (d-f) SC1.6, (g-i) SC2.6, (j-l) T2 and (m-o) CAA.*

Table 3.4 shows the measured values for oxide and barrier layer thickness. S6, SC1.6, SC2.6 and T2 were all anodized at a constant current density of 1.5 mA cm^{-2} during 1500 s. Applying the Faraday's Law and assuming a 100% anodizing efficiency, the maximum achievable thickness is 1.7 µm. T2 specimen almost reaches this limit with a 94% efficiency. TSAA specimens show efficiencies in the range between ~40-50%, which are typical for sulphuric-based electrolytes [63, 214]. The higher efficiency in TSA is attributed to tartaric acid reducing the film dissolution under the applied electric field [203].

Table 3.4. *Film and barrier layer thickness values of the studied anodic films.*

Anodic film	S6	SC1.6	SC2.6	T2	CAA
Film thickness (nm)	847 ± 16	689 ± 14	894 ± 8	1580 ± 20	730 ± 20
Barrier layer thickness (nm)	4 ± 1	6 ± 1	5 ± 1	9 ± 2	29 ± 3
*Anodizing efficiency (%)	50	40	52	94	-

*Assuming the following values: ρAl_2O_3: 3.1 g cm^{-3}; porosity: 25%

According to Moutarlier, a ~20 % increase in the growth rate was observed for 33 g L^{-1} Ce(IV) concentration in sulphuric acid electrolyte [86]. However, as already mentioned, this study does not provide direct evidence for this conclusion. Smith *et al*. reported a ~50% oxide film thickness decrease when incorporating 7.5 g L^{-1} of $Ce(SO_4)_2$ in a conventional sulphuric acid bath [84], but they did not specify the exact anodizing conditions and failed to provide visual evidence for this. In this study, eddy current measurements and TEM examination revealed a non-linear dependence between film thickness and Ce(IV) concentration in the electrolyte, with smaller thicknesses found for the SC1.6 specimen.

Measurements of the barrier layer thickness yielded values that correlated well with the final voltage values and the anodizing ratio of ~1 nm V^{-1} that is typically reported for sulphuric-based electrolytes [63]. For instance, the T2 anodic film shows a thicker barrier layer (~9 ± 2 nm, 10.5 V) in comparison with the S6 specimen (~4 ± 1 nm, 4.5 V) (**Table 3.4**). This is in accordance with previous studies where it has been demonstrated that anodizing in TSA electrolyte leads to the formation of a thicker barrier layer in comparison to a stand-alone sulphuric acid bath [66, 211].

The presence of Ce slightly increases the thickness of the barrier layer for SC1.6 (~ 6 ± 1 nm, 4.3 V) and SC2.6 (~ 5 ± 1 nm, 4.3 V) films in comparison to reference film (**Table 3.4**). Considering the lower final voltage values measured for these specimens it is suggested in this work that Ce species facilitate charge transfer across the barrier layer, i.e. the anodizing ratio is above 1 nm V^{-1} in the Ce-containing solutions. Other studies where TEM characterization of Ce-SAA films has been performed do not provide high magnification micrographs of the barrier layer [215].

So far, this work has shown that the addition of $Ce(SO_4)_2$ modifies the voltage response, morphology and thickness of the anodic films developed in sulphuric acid under constant current conditions. The lower voltages are associated with the higher conductivity of the electrolyte and possibly due to the increased conductivity of the barrier layer in the presence of Ce species. The reduced lateral porosity of the anodic films developed in the presence of Ce(IV) is possibly linked to a lower amount of oxygen evolution during anodizing. With respect to anodic film thickness, the effect is less clear, although it seems that Ce addition tends to decrease the growth rate.

Many studies concerning the role of Ce species during anodizing fail to ascertain their role in film composition. One exception is the PhD thesis by Banks [203] who using Rutherford backscattering spectroscopy reported very low or no detectable concentrations of cerium species (<0.003 at.%) in the 2024-T6 alloy anodized in sulphuric acid with $Ce(SO_4)_2$.

By applying the same characterization technique, the results shown in **Figure 3.11** were obtained for the S6, SC1.6, SC2.6, T2 and CAA specimens.

It is important to note that fitting was affected by the roughness of the films, consequently, the simulation of the spectra was performed as multi-layered systems.

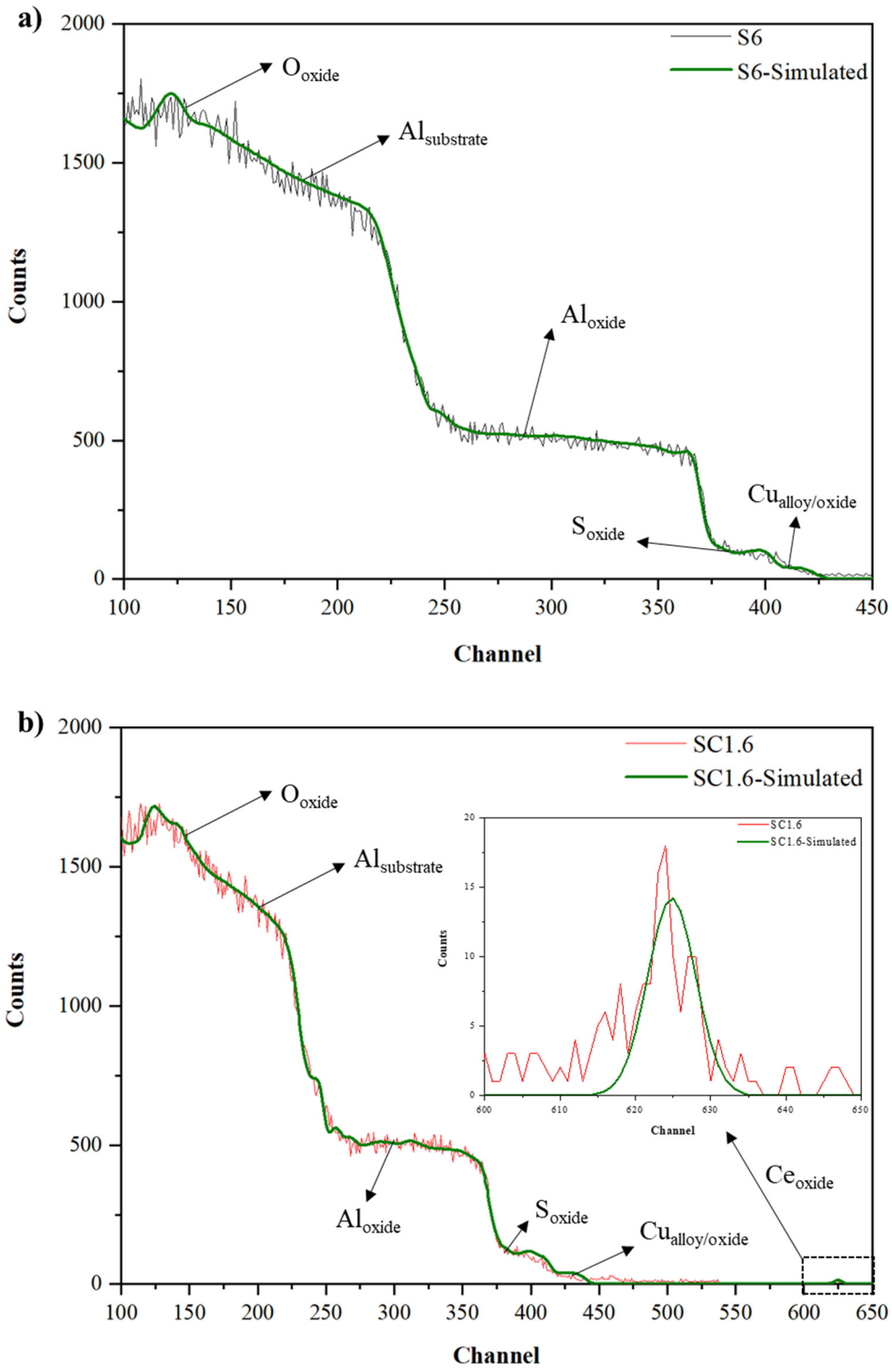

Figure 3.11. *Continuation.*

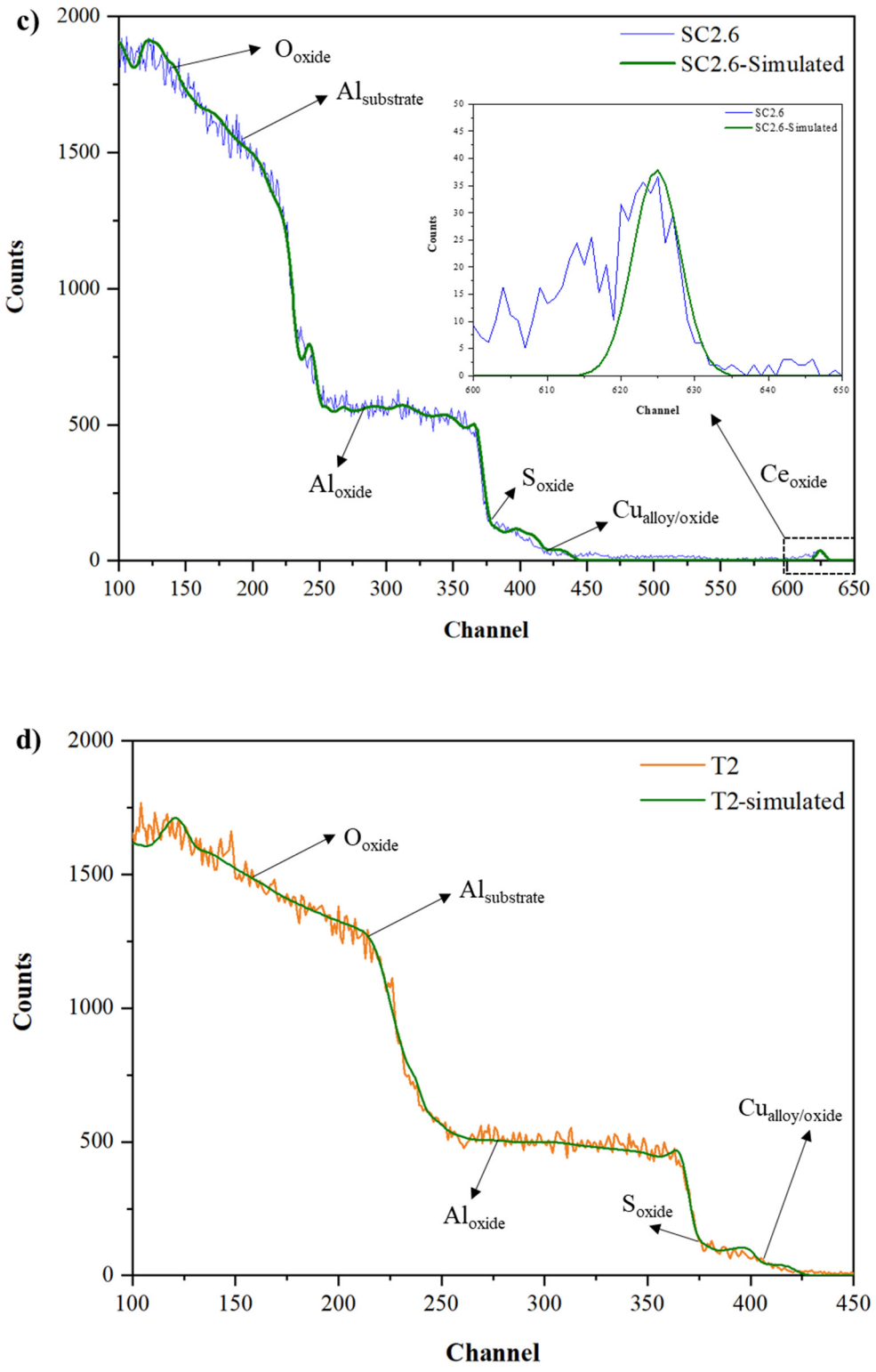

Figure 3.11. *Continuation.*

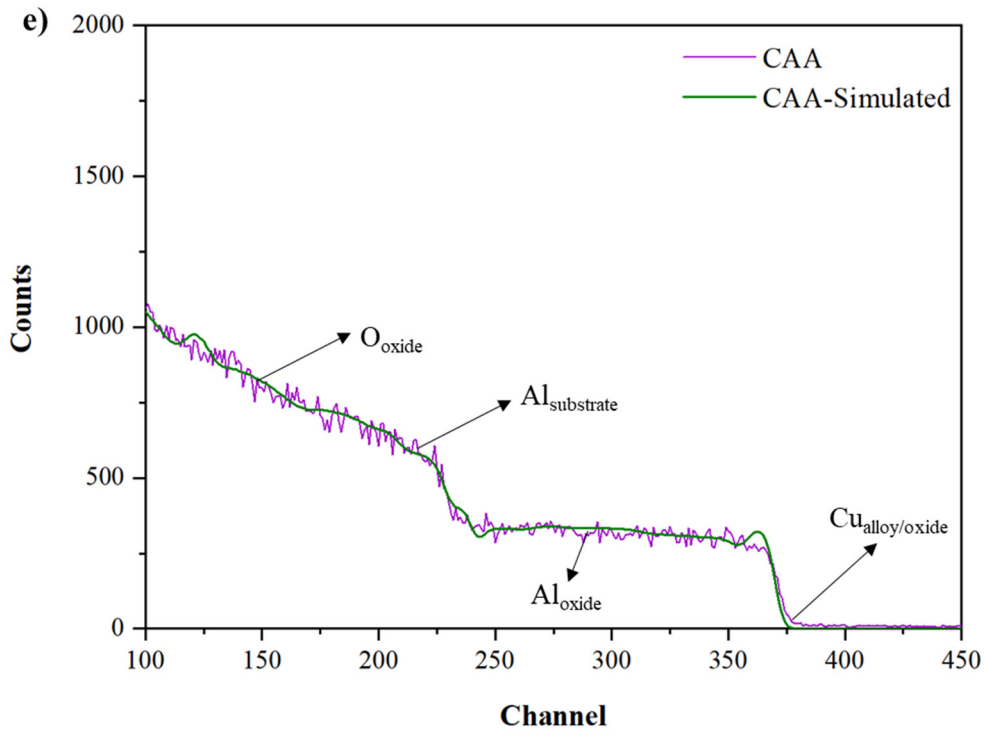

Figure 3.11. *Experimental and simulated RBS spectra of (a) S6, (b) SC1.6, (c) SC2.6, (d) T2 and (e) CAA anodic films.*

The effects of the rough metal/film and film/air interfaces are reflected by the presence of sloping edges at ~400 and ~450 channels, which correspond to the presence of Cu and S through the oxide layers. S and Cu incorporation is a common feature of anodic films in 2024 alloy [203]. In all studied films, a step associated with the interface between the bulk alloy and the anodic film is revealed (~360 channel). Al manifested itself in the overall spectrum yield with two marked slopes at ~200 and ~360, which correspond to Al in the substrate and oxide, respectively.

Table 3.5. *RBS results of S6, SC1.6, SC2.6, T2 and CAA anodic films.*

Anodic film	Al_{oxide} (10^{20} at cm^{-2})	Cu_{oxide} (10^{20} at cm^{-2})	O_{oxide} (10^{20} at cm^{-2})	S_{oxide} (10^{20} at cm^{-2})	Ce_{oxide} (10^{20} at cm^{-2})
S6	0.803	0.015	1.670	0.073	-
SC1.6	0.675	0.017	1.533	0.131	0.001
SC2.6	0.765	0.018	1.602	0.145	0.002
T2	1.231	0.019	1.527	0.072	-
CAA	0.751	0.003	3.237	-	-

Ce manifested as a small peak at the high energy end of the spectra (620-630 channel), which confirms its incorporation (~0.05 at.%) in the outer part of SC1.6 and SC2.6 anodic films (**Figure 3.11**). The larger Ce incorporation in the SC2.6 film can be related to the higher Ce(IV) concentration in the electrolyte. It is also worth noting that a higher amount of S is detected in SC1.6 and SC2.6 specimens (~5.6 and 5.7 at.% *vs.* 2.8 at.% in S6) due to the higher sulphate (SO_4^{2-}) concentration in the electrolyte.

It should be noted that, in principle, Ce^{4+} ions in sulphuric acid medium are positively charged and, therefore, are not supposed to be attracted by the electric field at the pore base and incorporated into the anodic oxide [216]. However, the RBS results indicate Ce incorporation in the outer region of the anodic film. This is possibly due to the formation of negatively charged sulphate complexes with Ce^{4+} which certainly can be attracted to the growing film. According to Paulenova *et al*. [217], the activity of free ceric Ce^{4+} is considerably lower than its formal concentration, because practically all the Ce^{4+} in sulphuric acid medium is complexed and present as negatively charged complex, i.e. $Ce(SO_4)_3^{2-}$ [202]. On the other hand, as stated in the work by Paulenova, Ce^{3+} tends to form a positively charged complex $[Ce(SO_4)]^+$. Therefore, this demonstrates that Ce(IV) is better suited than Ce(III) for modifying the anodic film composition.

C1.1.4.2. EIS long-term testing

Figure 3.12 shows the Bode and Nyquist diagrams with the fitted results for S6, SC1.6, SC2.6 and T2 selected anodic films in comparison to CAA reference specimen after immersion in 3.5 wt.% NaCl solution up to 28 days.

For 1 h of immersion, there are two relaxation processes related to the responses of the outer porous and inner barrier layers of the coatings at high and low frequencies, respectively. The protective behaviour of SC1.6, SC2.6, T2 and CAA films is evident in the Bode plots since a marked slope is observed in the entire frequency range, denoting the low mobility of the corrosive ions through the layer in comparison to S6 anodic film [76].

This protective effect of the anodic films is highly remarkable for CAA. In this case, the two time constants are clearly separated and the impedance modulus is the highest at all frequencies (**Figures 3.12a,c**). However, the relaxation processes observed at low frequencies in all specimens are related to the overall corrosion processes of the barrier layer [76, 85, 218].

After 28 days of immersion, all the specimens show a decrease of the low-frequency impedance modulus (10^{-2} Hz) associated with partial loss of the barrier effect of the anodic film [75, 218-220].

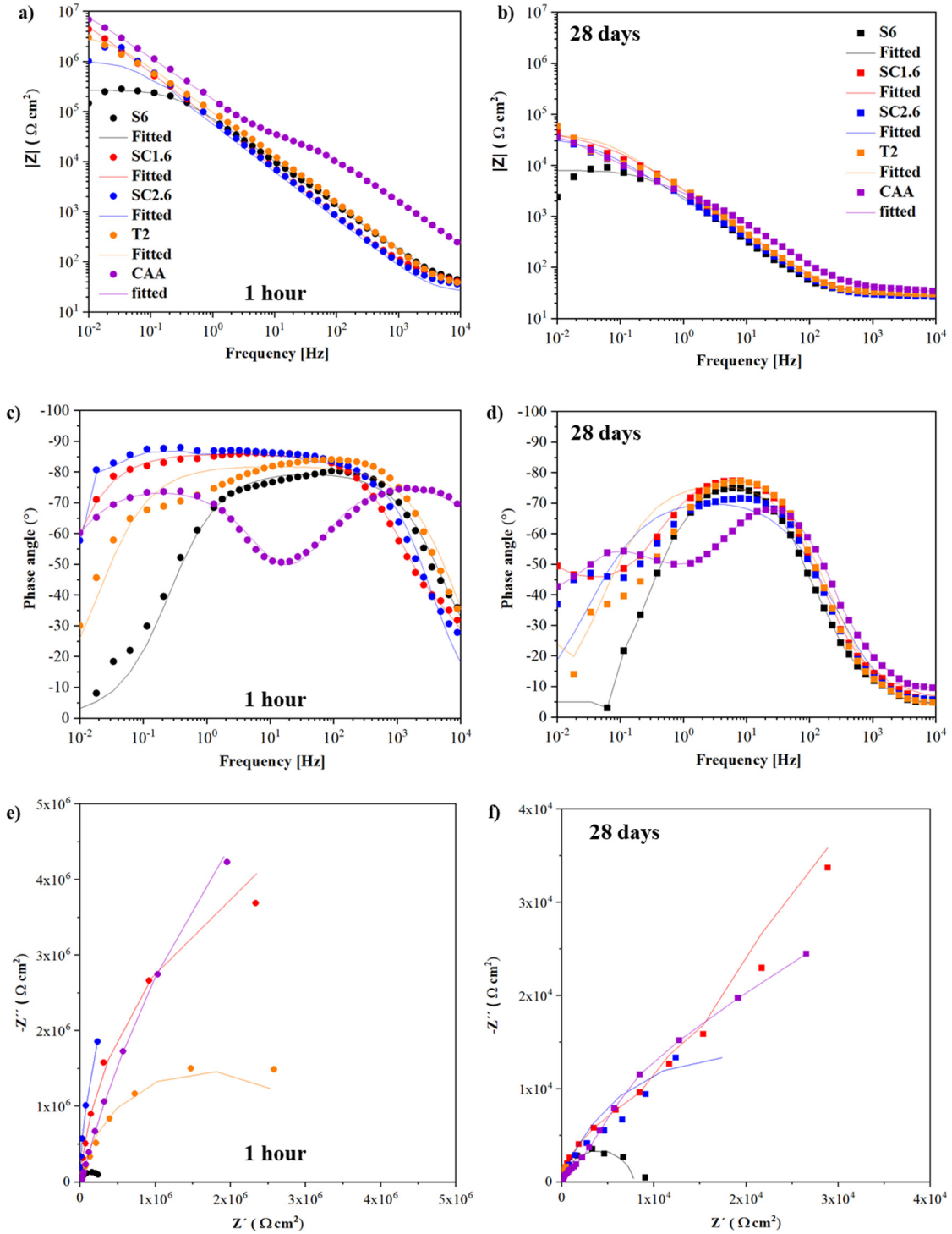

Figure 3.12. *(a-d) Bode and (e,f) Nyquist plots of all selected specimens after 1 h and 28 days of immersion in 3.5 wt.% NaCl solution.*

The penetration of Cl^- anions towards the substrate is also revealed by the degradation of the outer porous layer since the time constant at high frequencies almost disappears, except for the CAA film. In any case, SC1.6, SC2.6 and T2 still show better corrosion resistance than the S6 film and are comparable to the CAA film after 28 days.

Figure 3.13 provides the schematic illustration of the corresponding equivalent circuit to interpret the EIS results for studied specimens after 1 hour (**Table 3.6**) and 28 days (**Table 3.7**) of immersion. The use of constant phase elements (CPE) instead of capacitors is mainly due to the non-ideal nature of the developed anodic films (e.g. roughness and defects). The impedance of a CPE is described as (**Equation 3.2**):

$$Z_{CPE} = \frac{1}{Q(iw)^n} \qquad \textit{Equation (3.2)}$$

Where Q is the CPE constant, which nominally equals to the admittance of the system at 1 rad/s; $i = \sqrt{-1}$, ω is the angular frequency (rad/s) and the value of n ranges between 0 and 1.

In both equivalent circuits, R_{sol} represents the solution resistance, CPE_{por}/R_{por} are associated with the porous layer, and CPE_b/R_b correspond to the barrier layer [76]. After 28 days of immersion, the equivalent circuit in **Figure 3.13b** was used. This includes the CPE_{pw} or the capacitive response of the pore walls due to their gradual degradation with time [80].

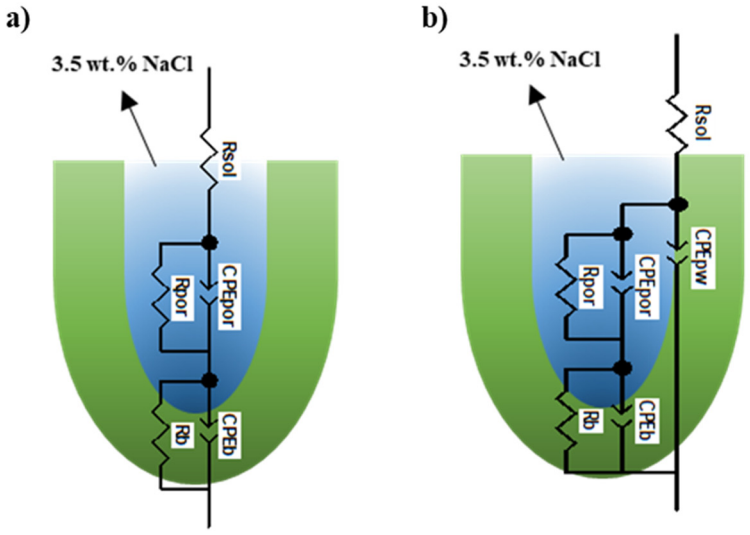

Figure 3.13. *Equivalent circuits used to fit the experimental EIS data. (a) 1h and (b) 28 days.*

For 1 hour of immersion time (**Table 3.6**), the beneficial effect of Ce(IV) addition into sulphuric acid electrolyte is evident since the R_b value of the reference anodic film (S6) was one order of magnitude lower than those of SC1.6 and SC2.6. This protective barrier

effect was likewise confirmed by the near-capacitive behaviour of the SC1.6 and SC2.6 films (*n* value closer to 1) in comparison with S6. It may be also related to the beneficial effect of Ce incorporation in the outer film part. Regarding T2 anodic film, the R_b and CPE_b values were comparable to those for SC1.6 and CAA anodic films.

Table 3.6. *Fitted electrical parameters of EIS spectra after 1 h of immersion in 3.5 wt.% NaCl.*

Anodic film	CPE_{por} ($F\ s^{(n-1)}\cdot cm^{-2}$)	n	R_{por} ($\Omega\ cm^2$)	CPE_b ($F\ s^{(n-1)}\cdot cm^{-2}$)	n	R_b ($\Omega\ cm^2$)
S6	$4.7\cdot10^{-8}$	0.82	300	$2.5\cdot10^{-6}$	0.81	$2.7\cdot10^{5}$
SC1.6	$8.3\cdot10^{-6}$	0.92	440	$2.6\cdot10^{-6}$	0.96	$8.1\cdot10^{6}$
SC2.6	$1.9\cdot10^{-7}$	0.92	410	$2.7\cdot10^{-6}$	0.92	$1.4\cdot10^{6}$
T2	$1.4\cdot10^{-9}$	0.94	730	$2.0\cdot10^{-6}$	0.91	$3.4\cdot10^{6}$
CAA	$4.4\cdot10^{-7}$	0.88	1700	$1.2\cdot10^{-6}$	0.85	$2.6\cdot10^{7}$

Table 3.7. *Fitted electrical parameters of EIS spectra after 28 days of immersion in 3.5 wt.% NaCl.* R_{sol} *= 150-300* $\Omega\ cm^2$ *for the studied specimens.*

Anodic film	CPE_{pw} ($F\ s^{(n-1)}\cdot cm^{-2}$)	n	CPE_{por} ($F\ s^{(n-1)}\cdot cm^{-2}$)	n	R_{por} ($\Omega\ cm^2$)	CPE_b ($F\ s^{(n-1)}\cdot cm^{-2}$)	n	R_b ($\Omega\ cm^2$)
S6	$8.7\cdot10^{-4}$	0.81	$4.8\cdot10^{-4}$	0.84	37	$6.0\cdot10^{-5}$	0.92	$7.7\cdot10^{3}$
SC1.6	$5.5\cdot10^{-5}$	0.88	$3.5\cdot10^{-7}$	0.96	59	$8.7\cdot10^{-5}$	0.84	$5.6\cdot10^{4}$
SC2.6	$6.3\cdot10^{-6}$	0.90	$6.3\cdot10^{-8}$	0.93	65	$1.1\cdot10^{-4}$	0.86	$3.2\cdot10^{4}$
T2	$4.6\cdot10^{-5}$	0.88	$1.7\cdot10^{-7}$	0.93	57	$7.2\cdot10^{-5}$	0.86	$4.4\cdot10^{4}$
CAA	$4.6\cdot10^{-6}$	0.78	$4.6\cdot10^{-9}$	0.96	68	$9.4\cdot10^{-5}$	0.77	$5.4\cdot10^{4}$

After 28 days of immersion, there is a decrease in the resistance values and the corresponding increase of CPE values (**Table 3.7**). This indicates that the electrolyte can penetrate through the anodic films leading to their gradual degradation [80, 85]. Interestingly, the resistances of the barrier layers (R_b) of SC1.6 and T2 were comparable to that of CAA. This indicates a non-linear dependence between barrier film thickness and long-term corrosion resistance. The enhanced corrosion performance of SC1.6, SC2.6 and T2, compared to the S6 anodic film may be explained by several factors:

- The addition of Ce(IV) modifies the morphology of the anodic film, reducing its lateral porosity. This suggests a porous layer of higher structural stability. The presence of small amounts of Ce in SC1.6 and SC2.6 may induce precipitation of Ce(IV) oxides/hydroxides when the pH is higher than 3 [221, 222], thus plugging or

sealing the pores in the anodic film. This Ce(IV) may come from electrolyte remnants within the pores or from Ce incorporated in the alumina film. The thicker barrier layer in the Ce-containing films may also enhance the corrosion resistance.

- It has been suggested that remnants of tartrate ions provide a buffering effect that avoids large pH swings during service, thus enhancing the short- and long-term corrosion resistance of the alumina layer [61, 223]. The formation of a thicker barrier layer in TSA electrolytes may also contribute to this improvement. Compared to other studies with the 2024 alloy anodized in TSA, the T2 treatment provides a slightly higher impedance, possibly due to the low current reducing the lateral porosity of the outer layer [203].

C1.1.4.3. Paintability evaluation

Contact angle and paint adhesion measurements are presented in **Figure 3.14**. The contact angle is a useful predictive tool that informs about the surface wettability, which is directly related to paintability, e.g. a lower contact angle should correspond to a higher paintability. Present findings reveal that all studied anodic films are hydrophilic (contact angles < 90º) [224]. The literature studies on paint adhesion to anodic films are limited but, in general, good results are achieved largely due to the typical porous morphology of anodic films [14, 50, 209].

The paintability testing was performed according to ISO 2409 standard on selected anodic films using a commercial paint (Epoxy Primer 37076) provided by *AkzoNobel*.

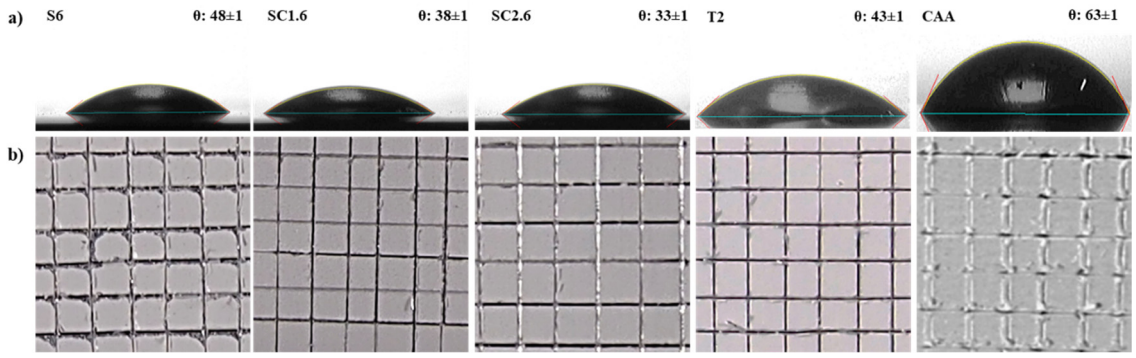

Figure 3.14. *(a) Water contact angle with as-received anodic films and (b) surface appearance of painted anodic films after the adhesion test. S6-rating 1, SC1.6-rating 0, SC2.6-rating 0, T2-rating 0 and CAA-rating 0.*

The observed differences in paint adhesion of SC1.6 and SC2.6 (rating 0) in comparison to S6 anodic film (rating 1) are in accordance with contact angle values. This may be related to changes in surface chemistry and pore alignment as seen in TEM micrographs.

In the case of T2 (rating 0), the better paintability in comparison to the S6 layer may be ascribed to bigger pores of the former as a result of the higher anodizing voltages (~10 V_{T2} *vs.* ~5V_{S6}).

C1.1.4.4. NSST evaluation

An additional corrosion test based on the ASTM D1654-92 standard was performed for SC1.6 and T2 films since they showed the best overall corrosion resistance-to-thickness ratio among all the studied specimens (**Figure 3.15**).

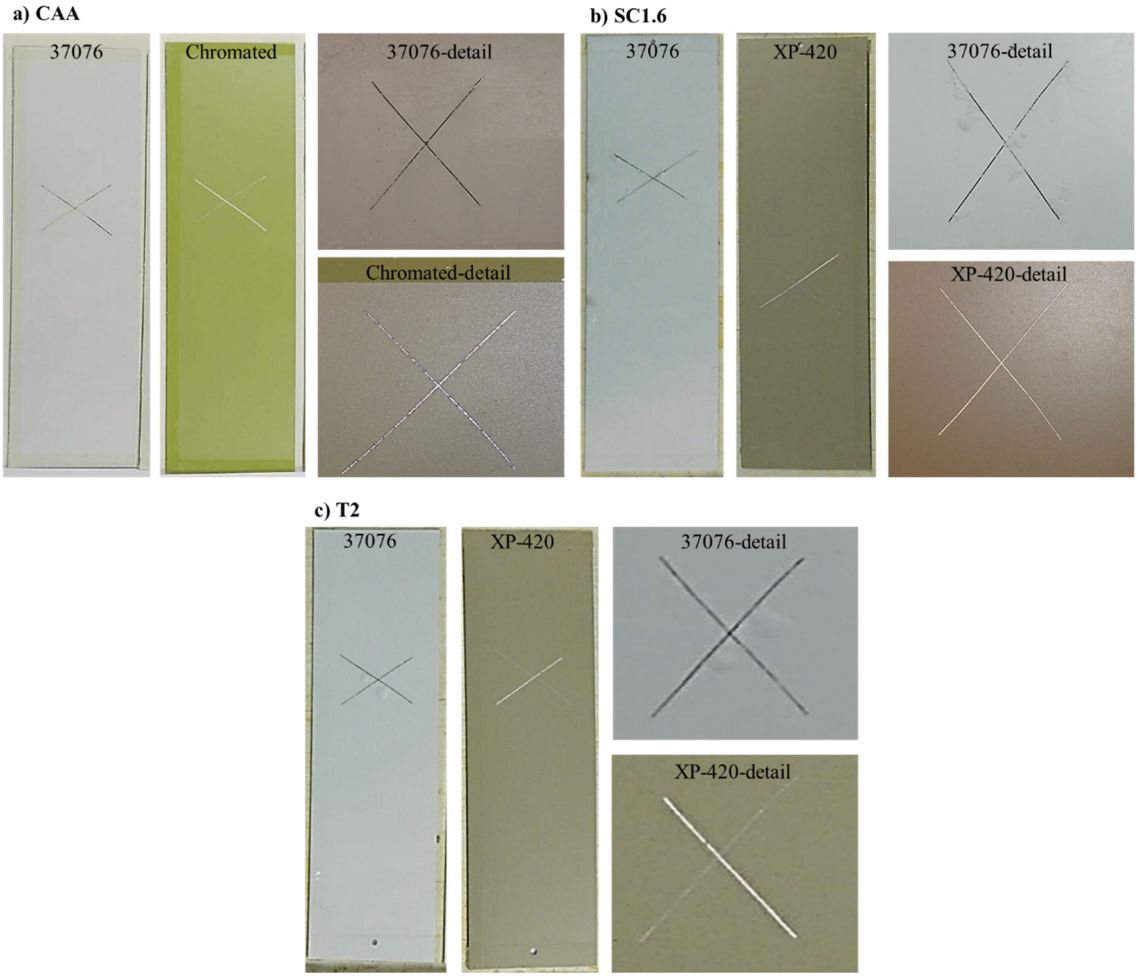

Figure 3.15. *Macrographs of (a) CAA, (b) SC1.6 and (c) T2 painted specimens after 1000 h of NSST as per ASTM D1654-92.*

The test consists in exposure of 250×75×2 mm^3 painted and scratched coupons in a salt fog environment (5 wt.% NaCl at 6.5-7.2 pH range and 35°C) for 1000 h. The CAA reference sample was also included for comparison. In this test, two additional paints supplied by *AkzoNobel* were evaluated for selected specimens. A lithium-leaching active inhibition paint (XP-420) for the Cr-free specimens and a Cr-bearing commercial paint typical of the aircraft industry "chromated" in case of the CAA film.

As shown in **Figure 3.15**, SC1.6 and T2 anodic films with the inhibitor-free paint (37076) revealed ~3±0.5 mm and ~5±0.4 mm blisters after 1000 h, respectively. These results are worse than the CAA ones with the same paint, which did not show signs of corrosion. Better results were obtained for these specimens when the active protection-bearing paint (XP-420) was used since no blisters were observed and the performance was comparable to that of CAA. Compared to other studies [50, 209], which obtained a similar corrosion performance with thicker anodic films, present findings are highly relevant since a comparable corrosion resistance to CAA can be reached with thinner anodic films and produced in shorter times.

C1.1.5.5. Fatigue evaluation

Fatigue life curves were obtained for the best specimens (SC1.6 and T2) and are presented in **Figure 3.16**. CAA reference sample and the 2024 alloy are also evaluated. The highest endurance limit, measured after 10^7 cycles, was 300 MPa for the bare 2024 alloy. Values of 270, 265 and 256 MPa were measured for T2, SC1.6 and CAA, respectively. It is known that the anodizing process reduces the fatigue strength by the formation of pit-like cavities at the film-substrate interface during anodizing in the active Cu-intermetallic particles. This produces local stress concentration points, leading to crack propagation under loading [225, 226].

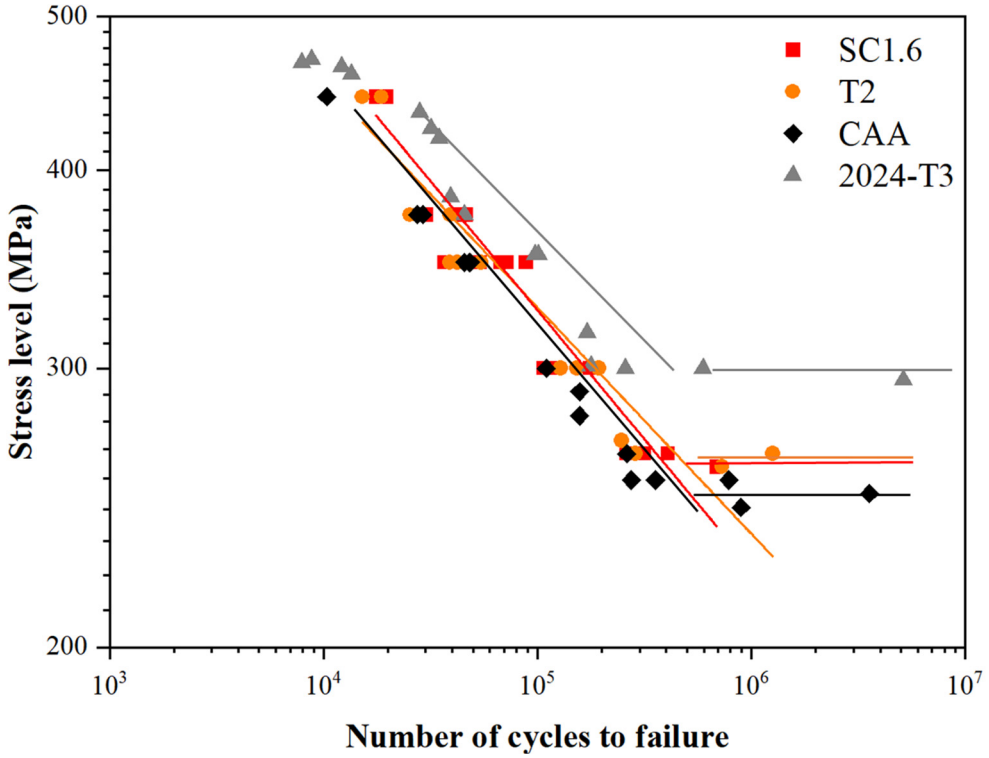

Figure 3.16. *Fatigue life of CAA reference sample, SC1.6 anodic film and 2024 alloy.*

A well-known factor on the fatigue life of anodic layers is the coating thickness since the passage of the fatigue cracks from the coating to the substrate is favoured at higher thickness values [226, 227]. For instance, Rateick *et al.* [226] report maximum stress values at 10^6 cycles of 210 and 225 MPa for SAA (5 μm) and CAA (1.6 μm) anodic films. The obtained results suggested that anodic film thickness was not the main factor for the fatigue life increase since SC1.6 (0.7 μm) thickness is similar to the CAA-reference sample (0.7 μm) and thinner than T2 (1.9 μm). This is also in accordance with other studies where other factors such as the pits formed during the anodizing and the ductility/brittleness of the anodized layer can act as stress raisers during fatigue loading. This can significantly affect the fatigue life, thus spreading cracks into the underlying substrate material [228-230]. From the fatigue endurance point of view, the developed anodic films performed favourably compared with CAA film.

C1.1.5.Concluding remarks on TSAA and TSA films on 2024 alloy

Several conclusions can be drawn regarding the effects of Ce incorporation into TSAA and TSA anodic films:

- TSAA and TSA films with ~0.5-1.5 μm thickness developed at 1.5 mA cm^{-2} for 25 minutes on 2024 alloy showed the best short-term corrosion performance among the all studied operation conditions. Enhanced short-term corrosion performance was achieved for Ce-containing TSAA films whereas, the *in situ* incorporation of Ce into TSA electrolytes resulted in negligible difference in corrosion performance.
- The present findings for TSAA films indicate a clear dependence between pore morphology and Ce presence in the electrolyte, regardless of the used concentrations. Anodizing in both Ce-containing TSAA electrolytes leads to the incorporation of Ce species in the outer film part. In both Ce-containing TSAA and TSA electrolytes, a thicker barrier layer and reduced lateral porosity were achieved in comparison to a stand-alone sulphuric acid bath.
- The long-term corrosion resistance of Ce-containing TSAA films is films is attributed to the higher structural stability of the Ce-containing films and to the precipitation of Ce(IV) oxides/hydroxides. For TSA films, the enhanced corrosion resistance may be attributed to the reduced lateral porosity and the buffering effect provided by tartrate ions. In both Ce-TSAA and TSA films the formation of a thicker barrier layer is observed which may also contribute to their higher corrosion resistance.

More specifically, the best corrosion performance was achieved for SC1.6 (7.5 g L^{-1}, 1500 s, 1.5 mA cm^{-2}) and T2 (1500 s, 1.5 mA cm^{-2}). Key performance characteristics of the SC1.6 and T2 anodic films in comparison with CAA reference film are summarized in **Table 3.8**.

Table 3.8. *Comparison of SC1.6 and T2 key properties with CAA reference film.*

Coating	Thickness (nm)	|Z| at 10^{-2} Hz (Ω cm^2) 1 hour/28 days	NSST-1000h blisters (mm) 37076/XP-420	Fatigue strength (MPa)
CAA	730 ± 20	$8.0 \cdot 10^6/3.0 \cdot 10^4$	No corrosion	270
SC1.6	689 ± 14	$4.0 \cdot 10^6/5.0 \cdot 10^4$	~3±0.5/No corrosion	265
T2	1580 ± 20	$3.0 \cdot 10^6/4.0 \cdot 10^4$	~5±0.4/No corrosion	256

By way of comparison between the SC1.6 and T2, both anodic films show similar corrosion resistance (EIS and NSST) and optimal paint adhesion. In more detail, SC1.6 shows the best corrosion resistance surrounding the scratched zone. Both anodic films fulfil the layer thickness requirement (2-7 µm) and offer an increase (comparable in both SC1.6 and T2) in fatigue strength in comparison to the CAA reference film.

For this reason, SC1.6 is the most promising alternative to CAA among the anodizing treatments developed in this work, which, in painted conditions, may be able to replace CAA in corrosion-sensitive applications. Further research of these anodic films on industrial testing purposes is needed in order to reveal their full potential for key fatigue-sensitive applications.

C1.2. Hybrid sol-gel sealing of modified TSAA and TSA anodic films

C1.2.1. Introduction

The *in situ* incorporation of organic inhibitors into TSAA anodic film has been identified in the past as a promising way for improving the corrosion resistance of these anodic films [83, 88]. A special case is the addition of tartaric acid (TSA) which shows an improved corrosion performance [213]. However, there is still a knowledge gap regarding the influence of many organic inhibitors on parameters such as anodic film formation, corrosion resistance and, especially, their compatibility with sealing post-treatments.

On that basis, the incorporation of organic acids (e.g. glycolic, oxalic, malic, succinic and citric acid) is actively being researched with the aim of clarifying the abovementioned effects [231].

Regarding the different sealing routes stated in the introduction (**Section 1.3.2.3**), hybrid sol-gel (HSG) coatings stand out due to their overall improved corrosion and mechanical performance compared to conventional organic-based sol-gel coatings.

Herein, two strategies are combined for corrosion protection of 2024 alloy: (i) *in situ* incorporation of organic inhibitors into TSAA and TSA anodic films; and (ii) HSG sealings of one selected anodic film. The ultimate goal is to develop thin anodic films on 2024 alloy with enhanced corrosion resistance for non-painted components.

C1.2.2. Screening of TSAA and TSA anodic films with organic inhibitors

Screening of anodic films modified with organic inhibitors was conducted on 2024 alloy in 26 different tartaric-sulphuric (TSA) and sulphuric (TSA) acid electrolytes (**Table 3.9**). Preliminary tests and available literature showed that anodic film thickness should be above 3 μm in order to develop a homogenous HSG top-layer [80, 232-235]. For this reason, the operating conditions for TSA and TSAA were selected based on MIL-A-8625F specification for type IIB coatings in the aircraft industry [236]. The inhibitor concentrations were established considering previous studies [46, 88].

Table 3.9. *Anodizing conditions for 2024 alloy in TSAA and TSA electrolytes with organic corrosion inhibitors.*

Base electrolyte (g L^{-1})			Inhibitor	
Anodic film	**H_2SO_4**	**$C_4H_6O_6$**	**Concentration (M)**	**Corrosion inhibitor**
TSA-reference	45	79.5		-
TSUA-0.1M	45	79.5	0.1	Succinic acid
TSUA-0.25M	45	79.5	0.25	HOOC-$(CH_2)_2$-COOH
TSUA-0.5M	45	79.5	0.5	
TSGA-0.1M	45	79.5	0.1	Glycolic acid
TSGA-0.25M	45	79.5	0.25	HOOC-CH_2-OH
TSGA-0.5M	45	79.5	0.5	
TSEA-0.1M	45	79.5	0.1	Etidronic acid
TSEA-0.25M	45	79.5	0.25	$(HO)_2(O)P$-$C(CH_3)(OH)$-$P(O)(OH)_2$
TSEA-0.5M	45	79.5	0.5	
TSCA-0.1M	45	79.5	0.1	Citric acid
TSCA-0.25M	45	79.5	0.25	HOOC-CH_2-(OH)COOH-CH_2-COOH
TSCA-0.5M	45	79.5	0.5	
TSAA-reference	150	-		
SSUA-0.1M	150	-	0.1	Succinic acid
SSUA-0.25M	150	-	0.25	HOOC-$(CH_2)_2$-COOH
SSUA-0.5M	150	-	0.5	
SGA-0.1M	150	-	0.1	Glycolic acid
SGA-0.25M	150	-	0.25	HOOC-CH_2-OH
SGA-0.5M	150	-	0.5	
SEA-0.1M	150	-	0.1	Etidronic acid
SEA-0.25M	150	-	0.25	$(HO)_2(O)P$-$C(CH_3)(OH)$-$P(O)(OH)_2$
SEA-0.5M	150	-	0.5	
SCA-0.1M	150	-	0.1	Citric acid
SCA-0.25M	150	-	0.25	HOOC-CH_2-(OH)COOH-CH_2-COOH
SCA-0.5M	150	-	0.5	

Notes:
- Anodizing conditions for TSAA: 15 V; ramp 50 mV s^{-1}; 25ºC; 25 min.
- Anodizing conditions for TSA: 14 V; ramp 47 mV s^{-1}; 37ºC; 25 min.

Screening of the anodic films with inhibitors was conducted according to: (i) their thickness and (ii) modulus of impedance at low frequency (10^{-2} Hz) in 3.5 wt.% NaCl after 1 h of immersion.

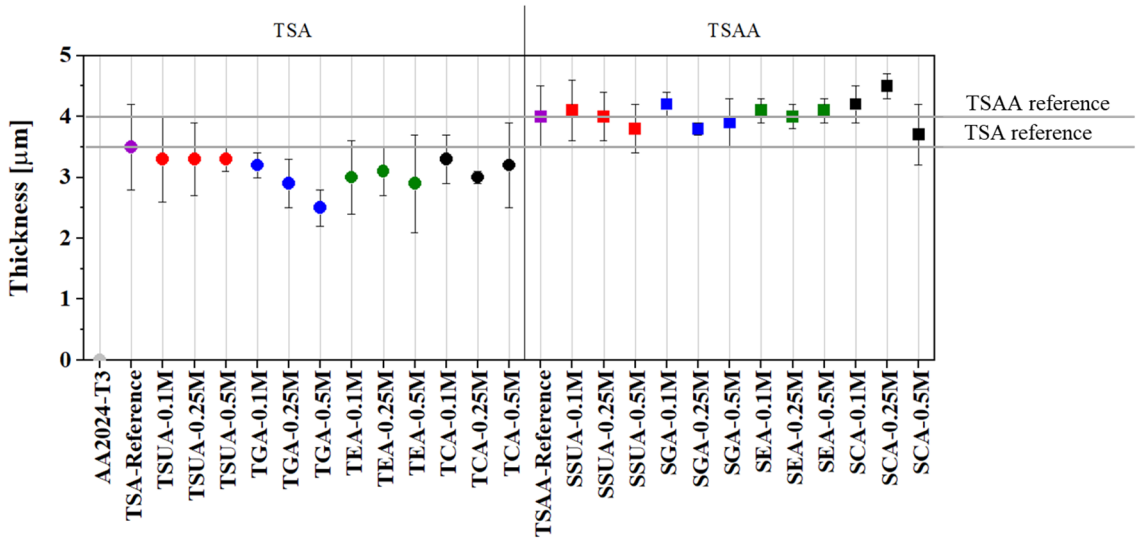

Figure 3.17. *Scatter diagram of the thickness values for studied anodic films. Filled circles and squares indicate oxide films developed in TSAA and TSA electrolyte, respectively. Colours: violet-TSAA and TSA references, red-succinic, blue-glycolic, green-etidronic and black-citric acid.*

As can be seen in **Figure 3.17**, different thickness values were obtained depending on the nature of the inhibitors and their concentrations. In the case of TSA films, a coating thickness decrease in comparison to TSA-reference was observed after the incorporation of organic additives. Note that the base concentration of tartaric acid is 0.5M, so the incorporation of studied additives in relatively high concentrations (0.1, 0.25 and 0.5M) probably promoted the dissolution of the TSA film due to an increased dissolving power of the electrolyte.

For TSAA films, additions of succinic, glycolic and etidronic acid revealed a negligible effect on TSAA film thickness. Note that the reference electrolyte is already quite acidic and concentrated (1.5 M H_2SO_4, pH~0). This suggests that these organic additives with lower acidity in comparison to sulphuric acid do not affect the dissolving power of this electrolyte significantly.

Based on the pK_a values of the studied additives, they are expected to protonate at pH~0 [89]. Therefore, for both TSA and TSAA electrolytes, there should be a very small concentration of negatively charged ions (deprotonated species) and they should not participate in the film growth significantly. Their effect, if any, should be expected to occur at later stages such as the buffering effect observed in previous studies for tartrate ions within the pores.

Citric acid is also expected to protonate in TSAA electrolyte and should have a negligible effect on coating thickness. However, the thickness values for 0.1M and 0.25M citric acid are slightly higher than that of the reference TSAA film. It should be noted that anodizing treatments in citric acid gave relatively high values of current density (**Figure 3.18**). Therefore, it is possible that the higher charge passed during these treatments resulted in thicker films. This effect however, apparently disappears for the 0.5 M citric acid concentration, which also showed a high current density, since a lower thickness was measured. This is again possibly due to the increased dissolving power of the electrolyte and a lower anodizing efficiency [83, 237].

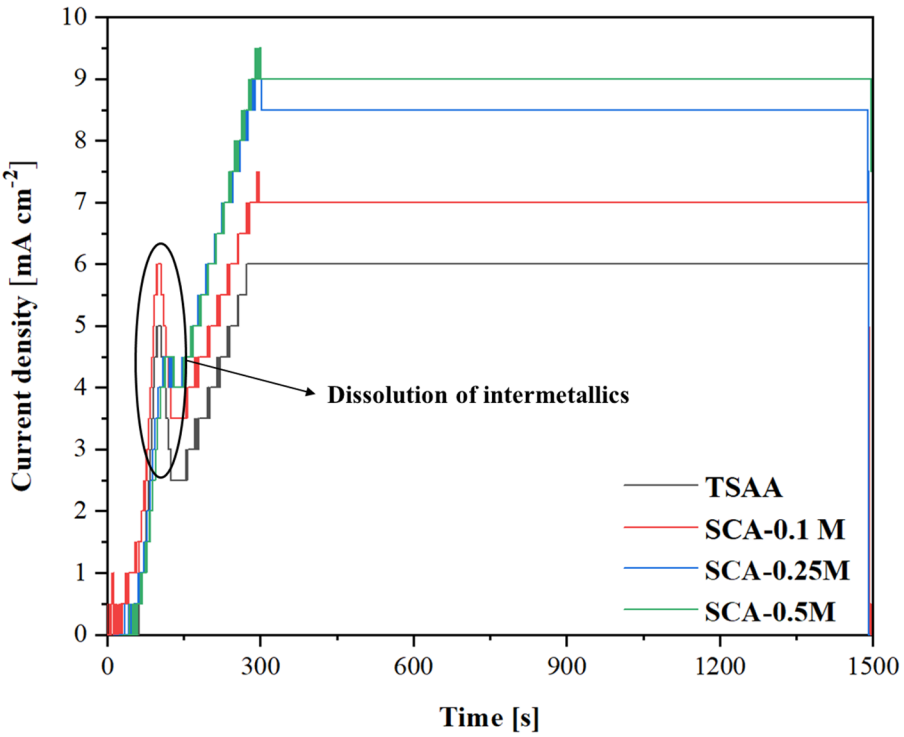

Figure 3.18. *Current density-time curves for citric- and TSAA-based anodic films developed at 15 V.*

As shown in **Figure 3.18**, there is a first current peak associated with the dissolution of secondary phases, which is similar in all electrolytes (i.e. 4.5-6 mA cm^{-2}; ~5V). Then, the current density keeps increasing until the voltage ramp is finished. At this point, the current reaches a constant value of ~6 mA cm^{-2} for the reference TSAA electrolyte and 7, 8.5 and 9 mA cm^{-2} for increasing concentrations of citric acid.

This current density increase for SCA electrolytes is in part due to the higher conductivity of the electrolytes in the presence of citric acid (0.1M: 489 ± 3 mS cm^{-1}; 0.25M: 579 ± 3 mS cm^{-1}, 0.5M: 620 ± 3 mS cm^{-1}) in comparison to TSAA-reference (339 ± 5 mS cm^{-1}).

Figure 3.19 shows the corrosion response of TSA and TSAA films. In general, all the formulations yielded lower impedance values than the reference films. The reasons for this could be varied and are outside of the scope of this work. For instance, oxidation of the additives may induce gas evolution and increased lateral porosity of the films, thus reducing their structural stability. In the particular case of TSA films, it is also possible that the additives reduce the amount of tartrate anions within the pores, thus reducing their beneficial effect. The only exception was the specimen anodized in TSAA in the presence of 0.25M citric acid, which revealed a greater impedance value. Contrarily to the other studied additives, citrate anions are known to form an insoluble salt with aluminium, which may be responsible for the enhanced corrosion resistance. Something similar has been proposed for tartrate ions. According to other studies, insoluble aluminium tartrate may already form during the rinsing step after anodizing due to the increased pH within the pores. However, there is not direct evidence of such product [238, 239]. Note that chemical databases indicate that aluminium citrate is slightly less soluble in water than aluminium tartrate [240], suggesting that it should be more protective.

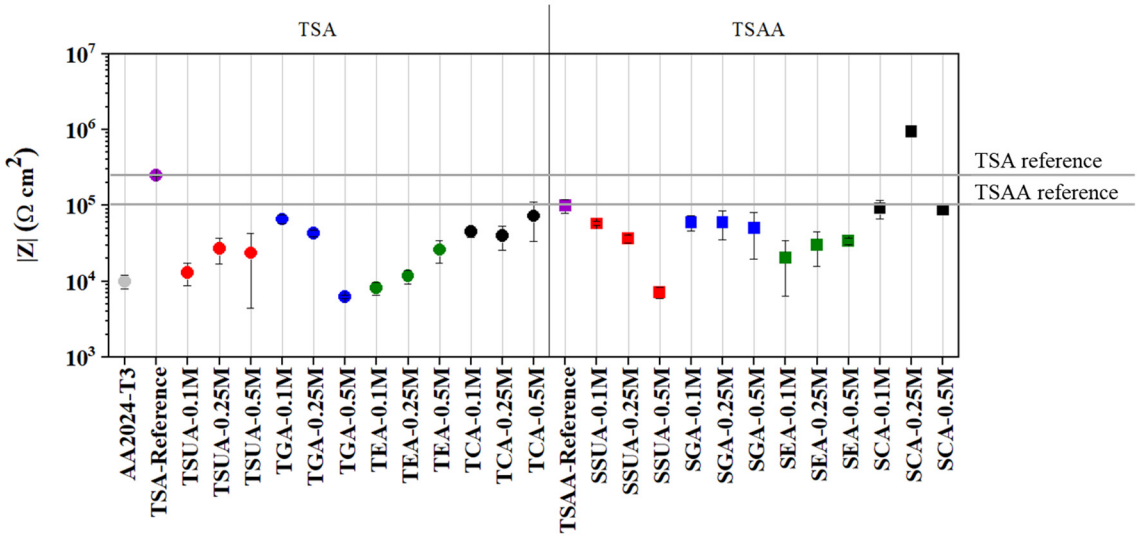

Figure 3.19. *Scatter diagram of the impedance values for studied anodic films. Filled circles and squares indicate oxide films developed in TSAA and TSA electrolyte, respectively. Colours: violet-TSA and TSAA reference films, red-succinic, blue-glycolic, green-etidronic and black-citric acid.*

The fact that citric acid was only beneficial for TSAA and in a 0.25M concentration reveals the complex nature of this additive. On the one hand, citric acid may be beneficial due to precipitation of an insoluble aluminium salt but, on the other hand, citric acid may compete with tartrate anions, reducing their buffering activity within the pores. Also, an excessively high concentration of citric acid during anodizing results in a smaller coating

thickness due to increased field assisted dissolution, thus producing a less resistive film. Based on these results, the coating combining the highest and closely reproducible |Z| with the lowest thickness (~4.5 μm) was selected for further studies HSG sealing, i.e. SCA-0.25M film (from now on SCA).

C1.2.3. Sealing of SCA anodic film

As introduced in **Section 1.3.2.3**, Hybrid sol-gel coatings (HSG) have been proposed as one of the most promising sealing post-treatments for anodic films. In comparison to conventional sol-gel technology, the formation of HSG coatings combines inorganic and organic polymerization [20, 241]. The inorganic part provides enhanced mechanical support, whereas the organic compound adds flexibility and decreases treatment temperature. Although HSG coatings provide efficient barrier protection to aluminium alloys, HSG does not provide active corrosion protection when damage occurs. An approach to overcome this limitation is to incorporate $Ce(NO_3)_2$ [242] and $LiNO_3$ [20] species during the HSG synthesis.

Although the self-healing ability of Ce- and Li-containing HSG coatings have been previously proven in several studies, there is still a lack of information on the growth of these HSG coatings on thin anodic films and their self-healing ability in this case. In the present section, three silane-based HSG coatings (stand-alone, doped with Li or Ce) were formed by mixing GPTMS, TEOS and SiO_2 (GTS), and deposited by the dip-coating technique on SCA film. A detailed characterization and corrosion testing were performed on intact and scribed specimens in order to evaluate the self-healing ability.

C1.2.3.1. Characterization of SCA and SCA-HSG specimens

Figure 3.20 shows the scanning electron micrographs of the plan views of SCA, SCA-GTS, SCA-GTS-Li and SCA-GTS-Ce coatings. After GTS sealing, the SCA film reveal similar thickness values for SCA-GTS (6.5±0.2 μm) and SCA-GTS-Ce (6.4±0.3 μm) coatings and slightly lower for SCA-GTS-Li (5.5±0.4 μm).

The surface of SCA (**Figure 3.20a**) exhibits a typical TSAA homogeneous layer morphology with visible rolling lines and randomly distributed scallops due to the dissolution of intermetallic compounds from the 2024 surface (mainly S-phase particles, Al_2CuMg) (**Figure 3.20b**) at the early stages of the anodizing process or during pre-treatment [46, 62, 71].

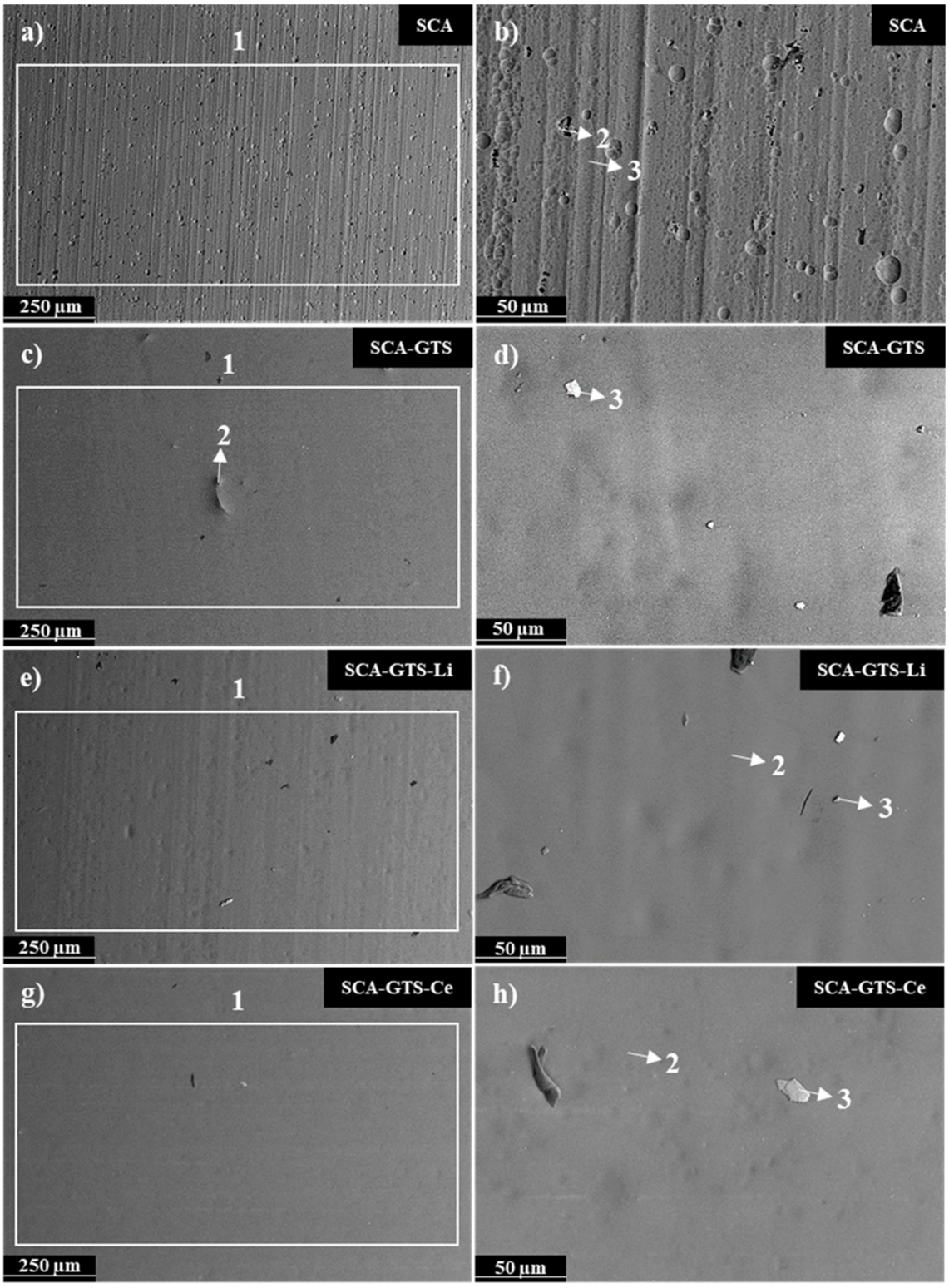

Figure 3.20. *Scanning electron micrographs corresponding to the plan views of (a, b) stand-alone SCA anodic film and SCA/HSG duplex coatings: (c, d) SCA-GTS; (e, f) SCA-GTS-Li; and (g, h) SCA-GTS-Ce.*

Several authors reported that copper gets incorporated into the anodic film promoting the generation of oxygen gas during the anodizing process and a highly tortuous pore

network, better known as *lateral poro*sity [60, 63]. EDS analysis at different locations (marked as 3 in **Figure 3.20**) shows the usual elements found on TSAA films on Al-Cu-Mg alloys, such as Cu, Mg and S [88, 243].

Studied SCA-GTS and SCA-GTS-Ce coatings showed a similarly smooth homogeneous morphology (**Figures 3.20c-h**). This indicates a sound interaction between inorganic (SiO_2) and organic (TEOS and GPTMS) components [244, 245]. In the case of the SCA-GTS-Ce specimen, Ce^{3+} cations tend to promote the condensation and polymerization of organic GTS networks. This could explain its slightly smoother surface. Conversely, the SCA-GTS-Li specimen was almost transparent and exhibited rolling patterns and scallops of the underlying anodic film **(Figures 3.20e,f)**. This could be due to its relatively low thickness in comparison to SCA-GTS and SCA-GTS-Ce coatings. This is opposite to the results by Trentin *et al*. [246], who found that lithium addition induced homogeneous distribution of highly condensed silica nodes in a PMMA-based matrix, thus increasing the thickness and connectivity of the hybrid network on a 7075 alloy surface. According to the present findings, lithium addition may have a detrimental effect on the condensation of the studied GTS formulation and the resulting GTS-Li film thickness.

The EDS analysis of the studied HSG coatings reveals that the surface is composed mainly of C, O, and Si (**Table 3.10**). This is in accordance with previous studies [235, 245].

Some Al and Mg from the SCA anodic film were incorporated in both SCA-GTS (**Figures 3.20c,d**; **Table 3.11**) and SCA-GTS-Ce coatings (**Figures 3.20g,h**; **Table 3.11**). This is usually associated with interfacial diffusion processes during the curing step of HSG coatings, thereby denoting an optimal interaction between the HSG coating and the substrate [80, 232, 247, 248], i.e. SCA film. Regarding SCA-GTS-Li coating, Al and Mg were not detected (**Figures 3.20e,f**; **Table 3.11**). This may be related to the low diffusion of Al throughout the HSG coating, corresponding to a lesser interaction of the Li-containing GTS coating with the SCA anodic film [246].

Table 3.10. *EDS analysis of the 2024 coated with SCA, SCA-GTS, SCA-GTS-Li and SCA-GTS-Ce coatings (at. %). Locations are denoted on SEM image in* ***Figure 3.20****.*

Coating	Location	C	O	Mg	Al	S	Cu	Si
SCA	1	5.6	58.9	0.4	31.5	3.2	0.4	
	2	4.5	60.1		32.1	3.3		
	3	3.5	60.5	0.4	32.3	3.3		
SCA-GTS	1	37.1	47.3		0.5			15.1
	2	34.3	48.7		0.4			16.6
	3	22.0	54.4	6.2	0.6			16.8
SCA-GTS-Li	1	36.3	47.5					16.2
	2	34.7	48.5					16.8
	3	34.5	48.4					17.1
SCA-GTS-Ce	1	37.1	46.8					16.1
	2	32.5	49.6		0.2			17.7
	3	24.1	53.1	7.3				15.5

It is interesting to note that Li or Ce were not detected by the EDS analysis (**Table 3.10**). For Li, this is due to its low atomic number, which makes it undetectable by SEM/EDS analysis [249-251]. Regarding Ce, it is likely that it is incorporated in the inner coating part and, thereby, is non-detectable by EDS analysis carried out on the surface. The exact reason for this preferential incorporation has been previously associated with the precipitation of cerium-containing nanoparticles within the coating structure [242].

C1.2.3.2. EIS testing of SCA and SCA-HSG coatings

Figure 3.21 shows the Bode plots obtained for SCA and HSG coatings after 28 days of immersion in 0.1 mol L^{-1} NaCl solution.

The presence of different relaxation processes can be observed in the Bode plots of all studied specimens. Three distinct regions are evident: (i) high frequency range (10^3-10^5 Hz) related to the outer part of the coating at the coating/electrolyte interface, (ii) intermediate frequency range (10^0-10^2 Hz) related to the intermediate anodic-HSG layer and (iii) low frequency range (10^{-2} Hz) related to corrosion process at the inner metal/barrier layer interface. The latter provides an estimation of the overall corrosion resistance, where higher values of $|Z|$ indicate a lower corrosion rate [232].

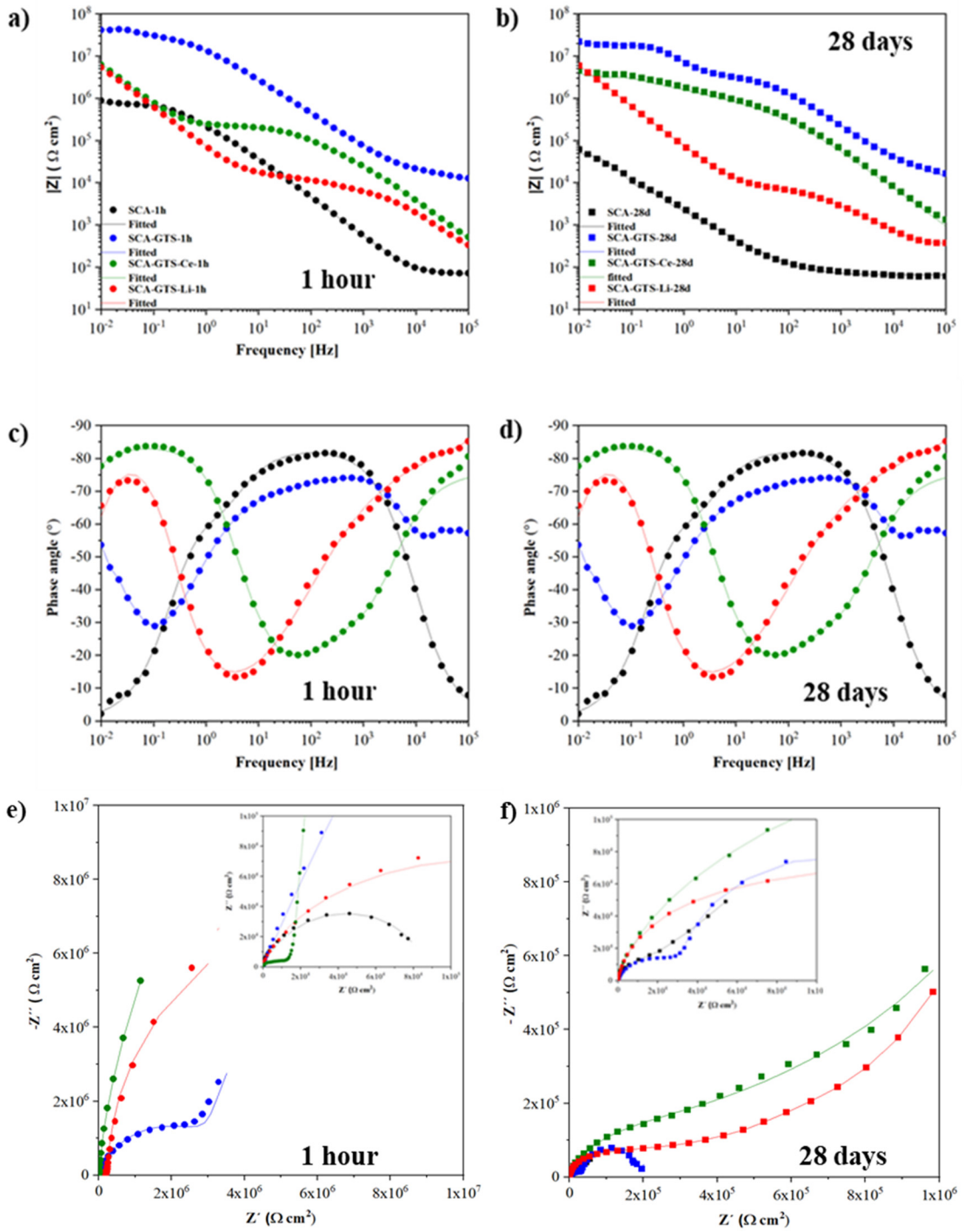

Figure 3.21. *Bode and Nyquist plots of all studied samples after (a, c, e) 1 h and (b, d, f) 28 days for GTS coatings in 3.5 wt.% (SCA) and 0.1 mol L^{-1} (SCA-GTS coatings) NaCl solutions.*

For short immersion time (1 h), the impedance modulus response of SCA (**Figure 3.21a**) revealed two relaxation processes related to the response of the outer porous layer (medium/high frequencies) and the inner barrier layer of the anodic film (low frequency) [232]. The impedance modulus at 10^{-2} Hz of SCA film was about one order of magnitude

lower compared to SCA-GTS, SCA-GTS-Ce and SCA-GTS-Li, showing the corrosion resistance improvement after the HSG application on the SCA layer [232, 233].
The impedance modulus for the entire frequency range for SCA-GTS was higher than SCA-GTS-Ce and SCA-GTS-Li, respectively (**Figure 3.21a**). This could be related to the higher coating thickness of SCA-GTS coating in comparison to SCA-GTS-Ce and SCA-GTS-Li coatings [252]. However, in the phase angle-frequency plots (**Figure 3.21c**), higher angle values at high/low frequency were achieved for SCA-GTS-Li and SCA-GTS-Ce coatings, thereby indicating their higher stability compared to the SCA-GTS coating [232, 233]. This was likewise confirmed in Nyquist plots (**Figure 3.21e**) since the slopes of SCA-GTS-Li and SCA-GTS-Ce coatings were higher at low/high frequencies in comparison to that of the SCA-GTS coating [253].

After 28 days of immersion, GTS-coated specimens show a negligible decrease of the impedance modulus in comparison to stand-alone SCA film (**Figure 3.21b**). Thus, indicating the beneficial effect of GTS coating in long-term corrosion resistance [254].
Regarding phase angle plots of the SCA-GTS specimen (**Figure 3.21d**), a lower value at high/low frequencies was identified, indicating the increased mobility of the corrosive ions within the layer [232, 255]. For SCA-GTS-Li and SCA-GTS-Ce specimens, the phase angle values at high and low frequencies were superiors to stand-alone SCA-GTS coating (**Figure 3.21d**). This is attributed to their higher stability, indicating that the electrolyte hardly penetrates throughout the coating structure [246, 252]. Again, this is more aggravated in the case of SCA-GTS coating since the presence of a semicircle in the Nyquist plot (**Figure 3.21f**) is associated with a higher coating degradation in comparison to both inhibitor-containing GTS coatings.

To further investigate the corrosion performance of studied specimens, equivalent circuits were used to fit the experimental data after 1h (**Figure 3.22**; **Table 3.11**) and 28 d of immersion time (**Figure 3.23**; **Table 3.12**). In all circuits, R_{sol} accounts for the resistance of the electrolyte and constant phase elements (CPE) were used instead of capacitances to account for the non-ideal behaviour of the system [203].

After 1 h of immersion of stand-alone SCA anodic film, CPE_{por}/R_{por} are ascribed to the outer porous layer and CPE_b/R_b to the barrier layer (**Figure 3.22a**) [80, 85]. For SCA-GTS duplex coatings, CPE_{GTS}/R_{GTS} represent the outer sol-gel coating and CPE_{hl}/R_{hl} the mixed anodic/sol-gel layer (**Figure 3.22b**) [233, 254].

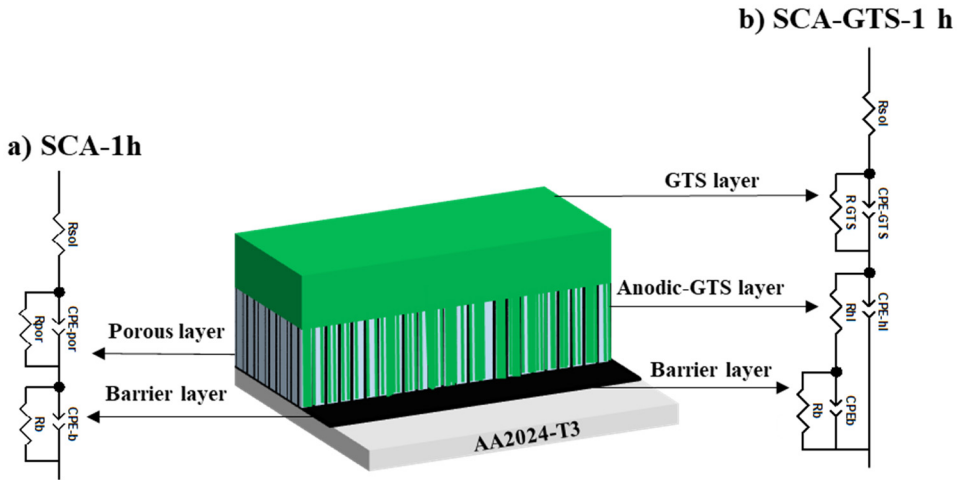

Figure 3.22. *Equivalent circuits used to fit the experimental EIS data for a) stand-alone SCA film and b) SCA-GTS coatings after1h of immersion time.*

For 1 h immersion (**Table 3.11**), the incorporation of Ce and Li into the GTS formulation resulted in lower R_{GTS}, R_{hl} and R_b values in comparison to SCA-GTS coating. It could be related to the higher coating thickness of the SCA-GTS coating compared to SCA-GTS-Ce and SCA-GTS-Li coating [246, 254].

Table 3.11. *Fitted electrical parameters of EIS spectra after 1 hour of immersion in 3.5 wt.% (SCA) and 0.1 mol L^{-1} (SCA-GTS coatings) NaCl solutions.*

Coating	R_{GTS} (Ω cm^2)	CPE_{GTS} (μF cm^{-2} $s^{(n-1)}$)	n_{GTS}	R_{hl} (Ω cm^2)	CPE_{hl} (μF cm^{-2} $s^{(n-1)}$)	n_{hl}	R_b/R_{por} (Ω cm^2)	CPE_b/CPE_{por} (μF cm^{-2} $s^{(n-1)}$)	n_b/n_{por}
SCA	-	-	-	-	-	-	$7 \cdot 10^5$/ 100	0.6/ 0.1	0.9/ 0.8
SCA-GTS	$3 \cdot 10^4$	0.041	0.86	$2 \cdot 10^6$	0.21	0.92	$2.5 \cdot 10^7$	0.28	0.88
SCA-GTS-Li	$1 \cdot 10^3$	0.04	0.96	$3.5 \cdot 10^4$	0.17	0.93	$9.0 \cdot 10^6$	0.23	0.89
SCA-GTS-Ce	$7 \cdot 10^3$	0.05	0.98	$1.6 \cdot 10^5$	0.13	0.92	$9.4 \cdot 10^6$	0.21	0.92

After 28 d of immersion, the equivalent circuit of stand-alone SCA anodic film (**Figure 3.23a**) is the same that used in **Section 1.1.4.2**. This circuit includes the additional CPE_{pw} element, which is associated with the capacitive response of the pore walls due to their gradual degradation with time [80].

For SCA-GTS coatings, CPE_{GTS}/R_{GTS} represent the outer sol-gel coating and CPE_b/R_b the mixed anodic barrier layer (**Figure 3.23b**) [256-258].

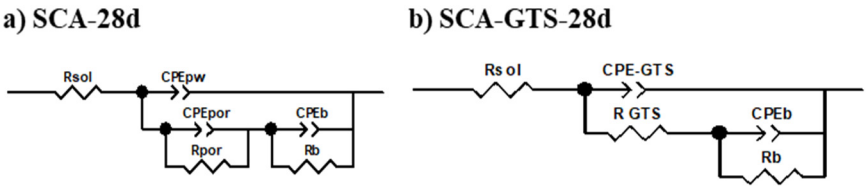

Figure 3.23. *Equivalent circuits used to fit the experimental EIS data for a) stand-alone SCA anodic film and b) SCA-GTS coatings after 28d of immersion time.*

Table 3.12. *Fitted electrical parameters of EIS spectra after 28 days of immersion in 3.5 wt.% (SCA) and 0.1 mol L^{-1} (SCA-GTS coatings) NaCl solutions.*

Coating	R_{GTS} (Ω cm^2)	CPE_{GTS} (μF cm^{-2} $s^{(n-1)}$)	n_{GTS}	R_b/R_{por} (Ω cm^2)	CPE_b/ CPE_{por} (μF cm^{-2} $s^{(n-1)}$)	n_b/n_{por}
SCA	-	-	-	$7 \cdot 10^4/10$	0.7/0.1	0.6/0.4
SCA-GTS	$4 \cdot 10^4$	0.06	0.88	$1.0 \cdot 10^7$	0.17	0.97
SCA-GTS-Li	$1.5 \cdot 10^3$	0.04	0.91	$8.7 \cdot 10^6$	0.62	0.88
SCA-GTS-Ce	$1 \cdot 10^4$	0.04	0.86	$9.0 \cdot 10^6$	0.18	0.88

After 28 d of immersion time, all specimens reveal a slight decrease of the barrier properties (R_{GTS}, R_{hl} and R_b) due to the gradual electrolyte penetration throughout the GTS structure [233, 254]. Interestingly, CPE_{GTS}, CPE_{hl} and CPE_b values of SCA-GTS-Li and SCA-GTS-Ce coatings were higher than stand-alone SCA-GTS coating. This suggest a lower coating permeability or long-term stability after the incorporation of Ce and Li into the GTS formulation [246, 252].

After EIS tests, GTS-coated specimens were analyzed by SEM (**Figure 3.24**) and EDS analysis (**Table 3.13**). SCA film was not included in this test due to its low corrosion resistance.

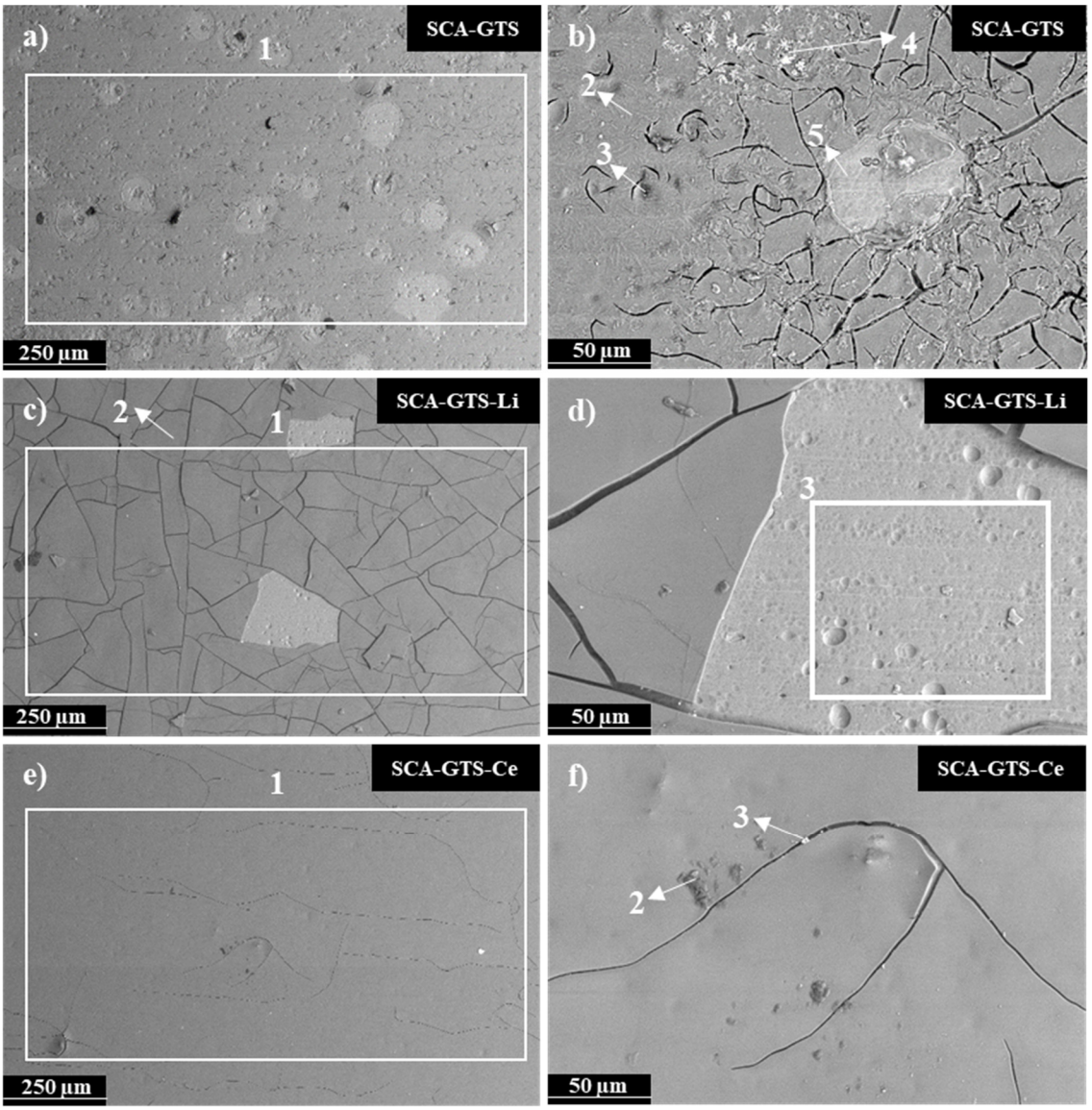

***Figure 3.24**. Scanning electron micrographs corresponding to the plan views of (a,b) SCA-GTS, (c,d) SCA-GTS-Li, and (e,f) SCA-GTS-Ce, after 28 days immersion in 0.1 mol L^{-1} NaCl solution.*

SCA-GTS coating surface reveals numerous bright deposits and cracks (**Figures 3.24a,b**), thus confirming the abovementioned lower GTS coating stability observed in the EIS tests. These bright deposits revealed a high content of aluminium and oxygen (marked as 5 in **Figure 3.24a**), suggesting the formation of aluminium oxides/hydroxides as corrosion products from the deterioration of the inner coating layers, i.e. SCA oxide film. The relatively high corrosion resistance of SCA-GTS coating after 28 days suggests that these Al-based compounds still offer some corrosion protection [246, 253].

SCA-GTS-Li coating (**Figures 3.24c,d**) showed a cracked surface and partial coating detachment. EDS analysis (marked as 3 in **Figure 3.24d**) showed S in the detached areas, indicating that the SCA film remains on the surface (**Table 3.13**).

Table 3.13. *EDS analysis of the 2024 coated with SCA-GTS, SCA-GTS-Li and SCA-GTS-Ce coatings (at. %). Locations are denoted on SEM image in* ***Figure 3.24****.*

Coating	Location	C	O	Al	S	Si
SCA-GTS	1	29.7	51.5	2.0		16.8
	2	23.0	56.0	1.4		19.6
	3	31.1	44.6	1.2		23.1
	4	17.3	55.8	16.5	1.7	8.7
	5	27.5	49.1	1.6		21.8
SCA-GTS-Li	1	36.3	47.5			16.2
	2	36.8	47.2	0.3		15.7
	3	21.4	55.3	15.9	1.3	6.1
SCA-GTS-Ce	1	37.1	47.5	0.2		15.2
	2	68.3	27.6			4.1
	3	37.7	45.2	0.4		16.7

These results are opposite to those of Trentin *et al*. [246] who observed that regardless of the used concentration, the addition of Li in PMMA-based HSG coatings increases the HSG coating adhesion with the substrate. The lower adhesion of Li-containing GTS coating in this study could be to some extent due to the HSG formulation. Also, the relatively low curing temperature and the high concentration of Li in this study could result in low diffusion of Al species from the SCA, thereby compromising the adhesion of the top-layer. Nonetheless, according to the EIS data and SEM examination there is no damage of the Al substrate.

Conversely, a much lesser cracked surface and no coating detachment was observed for SCA-GTS-Ce coating, thus confirming its high stability as stated in the EIS test. This is in accordance with previous studies where $Ce(NO_3)_3$ addition favours the condensation and polymerization of both inorganic and organic networks of the hybrid sol-gel coating, which results in improved coating stability [198, 259].

C1.2.4. Characterization and corrosion behaviour of scribed samples

Although Li and Ce addition in HSG tends to decrease the impedance values of stand-alone SCA-GTS coating, the influence of these species on the self-healing ability of anodic/HSG duplex system when damage occurs remains undisclosed. That is why SCA-GTS-Ce and SCA-GTS-Li scribed specimens were exposed to 0.5 mol L^{-1} NaCl solution

and examined by SEM/EDS. The inhibitor-free SCA-GTS coating was also analyzed for comparison.

C1.2.4.1. Immersion test of SCA-HSG coatings

Figure 3.25 shows the micrographs of the scribed GTS-coated specimens as a function of immersion time. SCA-GTS coating reveals several corrosion points after 3 days of immersion and with the scribe width increasing due to corrosion products formation (**Figure 3.25a**). Corrosion of the SCA-GTS-Li coating was observed after just 1 day of immersion, spreading over the whole scribed surface after 3 days (**Figure 3.25b**). Conversely, SCA-GTS-Ce coating reveals several corrosion points after 3 days, whereas the corrosion products were not observed till after 7 days of immersion (**Figure 3.25c**).

Compared to other studies on the 2024 alloy coated with Li- [246] and Ce-containing [242] HSG coatings, the present GTS-coated specimens provide better corrosion resistance on the scribed surface. This corrosion improvement was possibly due to the presence of anodic layer and a possible self-healing ability, especially in case of the SCA-GTS-Ce coating.

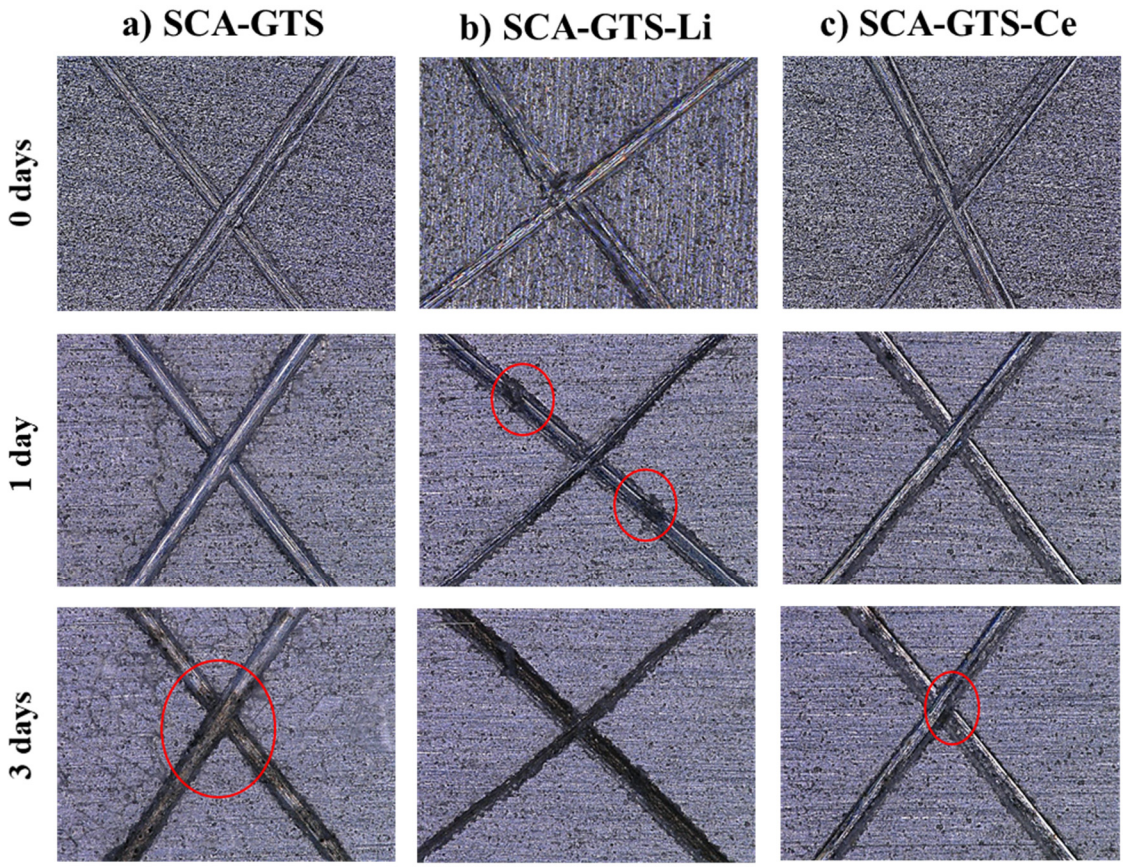

Figure 3.25. *Continuation.*

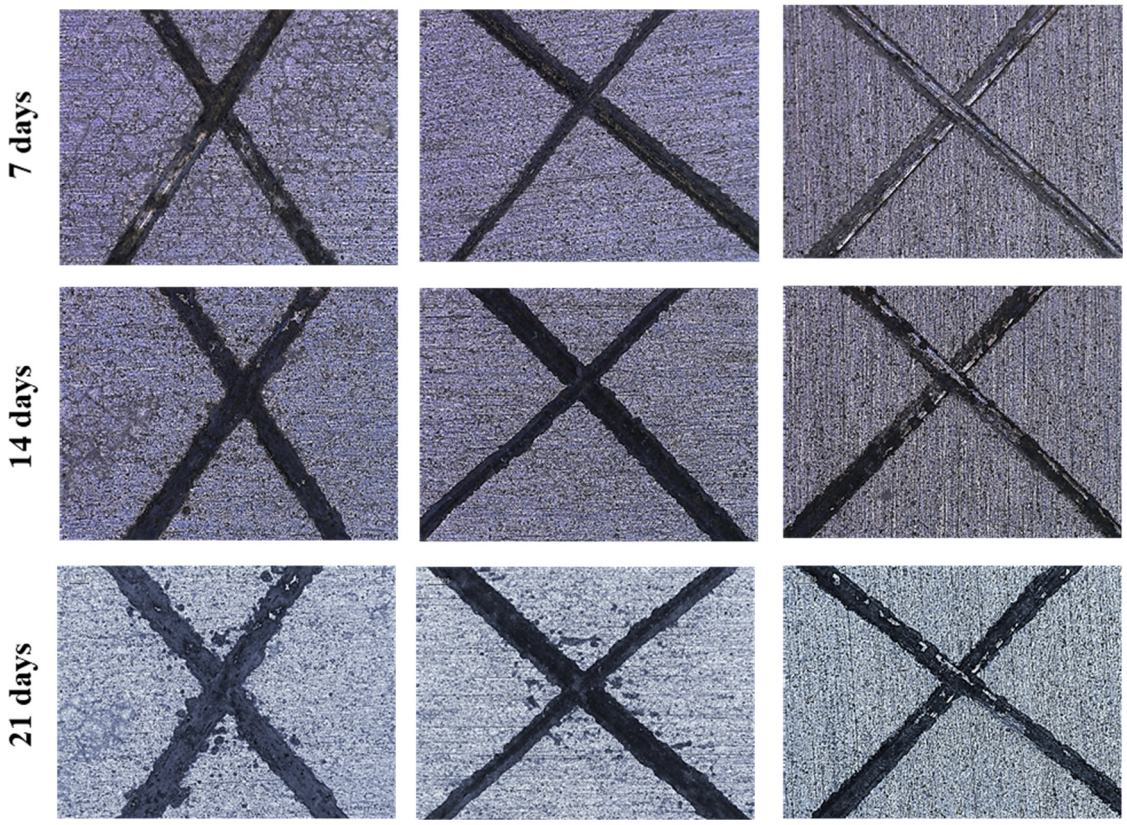

Figure 3.25*. Digital microscopy images of a) SCA-GTS, b) SCA-GTS-Li and c) SCA-GTS-Ce scribed coatings during an immersion test in 0.5 mol L^{-1} NaCl solution at room temperature. Red circles indicate the visually observable onset of significant corrosion damage.*

C1.2.4.2. Evaluation of the active corrosion protection of scribed specimens

Figure 3.26 shows the evolution of corrosion damage on scribed SCA-GTS, SCA-GTS-Li and SCA-GTS-Ce specimens up to 21 days of immersion in 0.5M NaCl solution. The EDS analysis of the studied GTS-coated specimens surface (**Table 3.14**) reveals the simultaneous coating degradation and the formation of Al oxide/hydroxide compounds at the scribe [242]. In both SCA-GTS and SCA-GTS-Li coatings, the concentration of Si from the sol-gel part decreased as a function of immersion time due to the progressive GTS coating dissolution [242, 259].

Regardless of the inhibitor, the addition of Li or Ce delays the coatings cracking and peeling in these scribed specimens (**Figure 3.26b**). For instance, SCA-GTS coating reveals a cracked surface and partial peeling after 3 days of immersion (**Figure 3.26a**) due to its low stability when the damage occurs. Conversely, SCA-GTS-Li coatings reveal a less cracked surface than SCA-GTS coating after 3 days of immersion, and the partial peeling did not occur till after 14 days of immersion (**Figure 3.26b**).

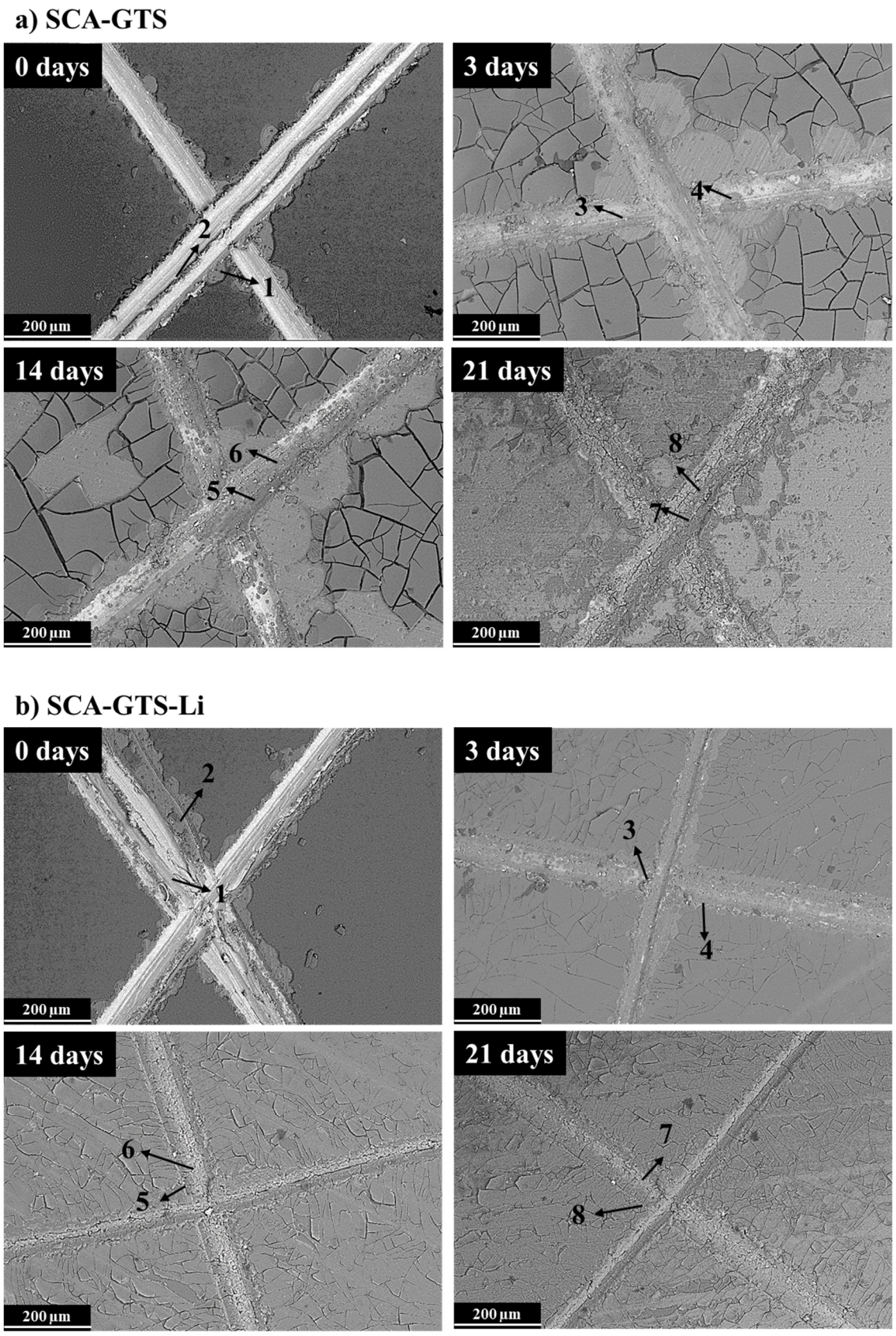

Figure 3.26. *Continuation.*

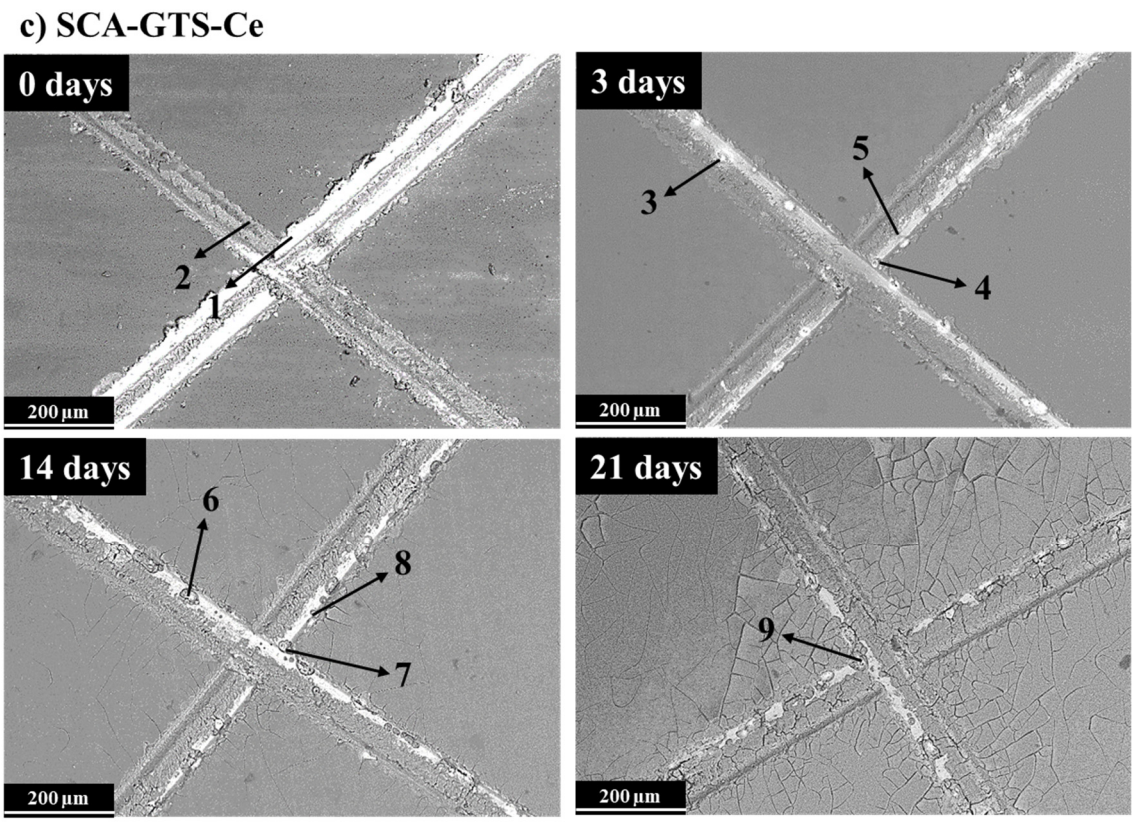

Figure 3.26. *Scanning electron micrographs corresponding to the scribed plan views of a) SCA-GTS, b) SCA-GTS-Li and c) SCA-GTS-Ce coatings, after 28 days immersion in 0.5 mol L^{-1} NaCl solution.*

Table 3.14. *EDS analysis of the entire scribed coatings surface of 2024 coated with SCA-GTS, SCA-GTS-Li and SCA-GTS-Ce coatings as a function of the immersion time.*

Coating	Days	C	O	Mg	Al	S	Si	Ce
SCA-GTS	0	36.5	40.9	0.3	11.6	-	10.7	-
	3	30.2	49.2	-	9.5	-	11.1	-
	14	20.8	57.6	0.2	13.6	1.1	6.7	-
	21	20.4	58.6		14.6	1.3	5.1	
SCA-GTS-Li	0	32.1	42.2	0.4	13.7	0.4	11.2	-
	3	29.7	52.3	-	4.6	-	13.4	-
	14	27.0	52.8	0.1	7.9	0.7	11.5	-
	21	23.7	57.4		8.8		10.1	
SCA-GTS-Ce	0	32.1	45.1	-	10.9	0.6	11.3	-
	3	32.2	48.1	-	7.5	-	12.2	0.3
	14	31.8	49.8	-	6.0	-	12.4	0.3
	21	27.31	55.17		5.74		11.54	0.24

The less cracked surface is attributed to the presence of Li in the GTS structure. This is in agreement with previous studies where the self-healing ability of Li-containing HSG, polyurethane and epoxy coatings have been demonstrated due to Li ions leaching to the damaged zone, hampering the Cl^- ions penetration through the coating [250, 251, 260]. According to these studies, the Li-ions leaching from Li salts (e.g. Li_2CO_3, LiOH) is highly favoured by the alkaline environment in the defect-scribe, thus forming a protective layer of lithium-containing species at local defects [261, 262].

For SCA-GTS-Ce coating, only slight surface cracking was observed after 14 days of immersion (**Figures 3.26c**). Also, coating peeling next to the scribe was not observed till 21 days. Besides, the Si concentration was practically constant during all immersion times, confirming the higher stability of this coating (**Table 3.14**).

To ascertain the compositional changes in the scribed area, **Table 3.15** represents the EDS analysis on the scribes of the different GTS-coated specimens (**Figure 3.26**) as a function of the immersion time.

In all studied SCA-GTS coatings, Si and C were detected only outside the scribe, which is consistent with the undamaged HTS coating. In the scribe Al and Cu from 2024 substrate were identified. The Cu signal vanishes by the formation of overlaying Al oxide/hydroxides during immersion as revealed by the increased O content in the scribed area. S corresponding to the SCA film was detected in regions were the HSG top layer was delaminated.

In the particular case of SCA-GTS-Ce coating, a considerable amount of Ce (~5 at.%) was detected in the scribe after 3 days of immersion which remained relatively constant at longer immersion times (**Table 3.15**). The amount of Ce found in the deposits is much higher than that previously reported by Tiringer *et al.* [242] using the same sol-gel coating on a non-anodized 7075-T6 alloy (0.1-0.3 at. %), indicating that the presence of the SCA underlayer is an efficient Ce reservoir that facilitates its liberation.

The presence of Ce-rich deposits is associated with an active corrosion protection mechanism where Ce species leach from the coating and precipitate on the surface of cathodic sites.

Table 3.15. *EDS analysis at the scribe at various locations (marked in* ***Figure 3.26****) of 2024 coated with SCA-GTS, SCA-GTS-Li and SCA-GTS-Ce coatings as a function of the immersion time.*

Coating	Days	Location	C	O	Al	S	Cu	Si	Ce
SCA-GTS	0	1	15.0	55.2	23.8	2.1		3.9	
		2	37.4	29.5	24.3		1.0	7.8	
	3	3	15.6	41.5	32.3		3.9	6.7	
		4	17.0	33.0	45.4		1.0	3.6	
	14	5	21.3	56.9	11.2			10.6	
		6	37.1	59.5	1.1			2.3	
	21	7		66.8	24.7	3.1		5.4	
		8		74.7	20.7			4.6	
SCA-GTS-Li	0	1		15.0	79.7		1.7	3.6	
		2	18.9	57.7	17.3	1.6		4.5	
	3	3	18.6	36.8	38.2			6.4	
		4	15.5	60.9	13.6			10.0	
	14	5	24.7	51.5	16.7			7.1	
		6	13.1	62.7	19.4			4.8	
	21	7	8.8	69.3	16.4			5.5	
		8	14.7	65.2	12.8			7.3	
SCA-GTS-Ce	0	1	22.7	9.3	64.2		1.5	2.3	
		2	15.6	55.5	22.7	2.6	0.6	3.0	
	3	3	16.6	48.6	23.2			7.4	4.2
		4	17.5	47.8	21.0			8.6	5.1
		5	20.8	54.4	13.7			7.4	3.7
	14	6	15.5	60.0	18.0			4.4	2.1
		7	12.9	63.5	16.3			4.9	2.4
		8	15.5	56.4	18.2			6.2	3.7
	21	9	18.7	53.6	15.4			8.0	4.3

Figure 3.27 depicts a schematic illustration of the SCA-GTS-Ce coating and its corrosion protection mechanism. This mechanism is based on the obtained results in this work and those obtained by Lakshmi [263].

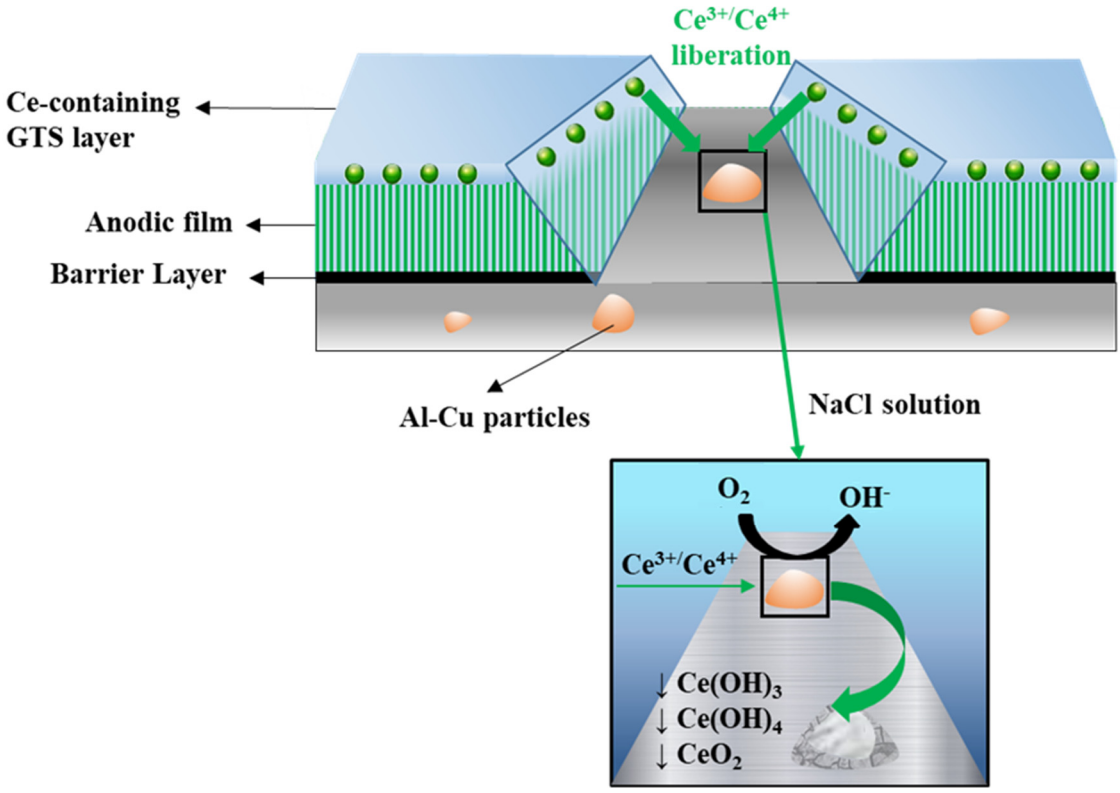

Figure 3.27. *Schematic illustration for active protection mechanism of SCA-GTS-Ce coating.*

According to this mechanism, Ce soluble species leach from the coating. At this stage the majority of Ce is released as Ce^{3+}, however some Ce(IV) aqueous species are likely to be present as suggested by the pale yellow colour observed during the Ce-containing sol-gel synthesis (the use of HNO_3 during the synthesis may oxidize some Ce(III) into Ce(IV) [263]. Then, precipitation of Ce oxides/hydroxides takes place at the locations of intermetallic particles where the cathodic reaction is occurring (**Equation 3.3**). In a neutral environment and in the presence of oxygen the dominant precipitates should be $Ce(OH)_3$ and $Ce(OH)_4$ [264] formed by the reactions indicated in **Equation 3.4** and **3.5**. Note that the precipitation of $Ce(OH)_4$ may occur either directly from the Ce(IV) present in the solution or from oxidation of Ce^{3+} as shown in (**Equation 3.6**) [264].The precipitation of some CeO_2 is also possible according to (**Equation 3.7**), although the amount of this product should be negligible for the studied conditions [264].

$$O_2 + 2\,H_2O + 4e^- \rightarrow 4OH^- \qquad \textit{Equation (3.3)}$$

$$Ce^{3+} + 3OH^- \rightarrow Ce(OH)_3 \qquad \textit{Equation (3.4)}$$

$$Ce^{4+} + 4OH^- \rightarrow Ce(OH)_4 \qquad \textit{Equation (3.5)}$$

$$4Ce^{3+} + O_2 + 14\,H_2O \rightarrow 4Ce(OH)_4 + 12\,H^+ \qquad \textit{Equation (3.6)}$$

$$Ce^{3+} + O_2 + 6H_2O \rightarrow 4CeO_2 + 12\,H^+ \qquad \textit{Equation (3.7)}$$

According to several studies, there is the risk that Ce salts are quickly released from HSG coatings into the damaged area, thereby leading to short-term inhibition followed by fast system degradation [242, 263, 265, 266]. This issue is not observed in the SCA-GTS-Ce since Ce concentration on the cathodic sites was still high even after long immersion times (**Table 3.15**). Also, the coating remained intact in the unscribed regions without signs of degradation

C1.2.5. Concluding remarks on GTS sealing of SCA anodic film

The main conclusions regarding the synthesis and application of inhibitor-free, Li- and Ce-loaded hybrid sol-gel coatings on anodized 2024 alloy can be summarized as follows:

- The *in situ* incorporation of organic inhibitors into conventional TSAA and TSA films (15 V, 25 min) was evaluated. A citric-containing TSAA film (SCA, 0.25 M citric acid) of 4.5 μm showed the highest short-term corrosion resistance/thickness ratio. It was suggested that the beneficial effect of citric acid is related to the formation of aluminium citrate within the pores.
- Inhibitor-free, Li- and Ce-containing HSG coatings were successfully developed on the SCA film formed on 2024 alloy.
- The corrosion performance of SCA film was improved by at least one order of magnitude after the HSG sealing. *In situ* incorporations of Ce and Li improved the coating stability and resulted in lesser degradation of the coatings in comparison to the SCA-GTS coating. According to EIS experiments, Li-containing HSG coating showed worse performance than the Ce-containing formulation.
- Corrosion testing with scribed specimens revealed an improved performance of inhibitor-containing HSG coatings. The mechanism of Li inhibition was not elucidated due to the difficulties associated with the detection of this element. In case of Ce, it was demonstrated that the self-healing ability of the coating was due to the release of Ce species from the coating and the subsequent formation of Ce-oxides/hydroxides at defective areas.

C1.3. Conclusions of Chapter 1

In situ incorporation of corrosion inhibitors into thin anodic films and hybrid sol-gel sealings was evaluated on 2024 alloy. The main conclusions are summarized as follows:

- Anodizing at 1.5 mA cm^{-2} for 25 minutes produced TSAA and TSA films of ~ 0.5-1.5 μm thickness with high corrosion resistance. In situ incorporation of Ce was beneficial for TSAA, but not for TSA. Among the studied conditions, the best corrosion performance was achieved for SC1.6 film (7.5 g L^{-1} of $Ce(SO_4)_2$). Ce incorporation in the outer film was confirmed by RBS. TEM examination revealed that the addition of $Ce(SO_4)_2$ reduced the lateral porosity of the anodic film and slightly increased the barrier layer thickness. It is suggested that the precipitation of Ce(IV) oxides/hydroxides in the anodic film pores is responsible for the improved corrosion resistance. For TSA selected film (T2), long-term corrosion resistance was mainly attributed to the reduced lateral porosity and the buffering effect provided by tartrate ions. Selected T2 and SC1.6 films showed optimal paint adhesion, similar fatigue strength and corrosion resistance in NSST and EIS tests. By way of comparison, scratched SC1.6 film showed enhanced corrosion resistance in NSST in comparison to T2 and similar to CAA film.

- Among different corrosion inhibitors, 0.25M citric acid demonstrated to be an effective additive for improving the corrosion performance of TSAA films (15 V, 25 min). The precipitation of aluminium citrate within the pores is believed to be responsible for this enhancement. The citric-containing TSAA film (SCA) was successfully combined with inhibitor-free, Li- and Ce-containing HSG coatings. The Ce-containing film (SCA-GTS-Ce) showed the best corrosion results due to its self-healing ability associated with the precipitation of Ce-oxides/hydroxides at defective areas.

Chapter 2: Development of flash-PEO coatings

As it has been mentioned in the Introduction (**Section 1.3.3**), flash-PEO could become a feasible alternative to CAA if the energy consumption were kept to a minimum and other coating characteristics such as thickness, corrosion resistance, fatigue life and paintability met the stringent requirements of the aircraft industry. Previous studies have shown that the porous structure of PEO coatings is ideal for the application of sealing post-treatments and paints, whereas it compromises the long-term corrosion performance of stand-alone coatings due to the easy access of aggressive species [109, 267].

In this sense, Chapter 2 is focused on the development of flash-PEO coatings with improved corrosion resistance for painted and non-painted applications. The structure of the chapter is divided into four sections or strategies: (i) preliminary studies on LDH post-treatments of flash-PEO coatings on commercially pure aluminium; (ii) *in situ* incorporation of inorganic corrosion inhibitors into flash-PEO coatings for painted components; (iii) LDH post-treatment of a flash-PEO coating on a commercial Al-Cu alloy for non-painted components; and (iv) lauric acid post-treatment of a flash-PEO coating for improved hydrophobicity. The ultimate goal is to produce, in very short treatment times, thin PEO coatings that combine low energy consumption and improved corrosion performance for either stand-alone or painted components. **Figure 4.1** shows the graphical abstract of Chapter 2.

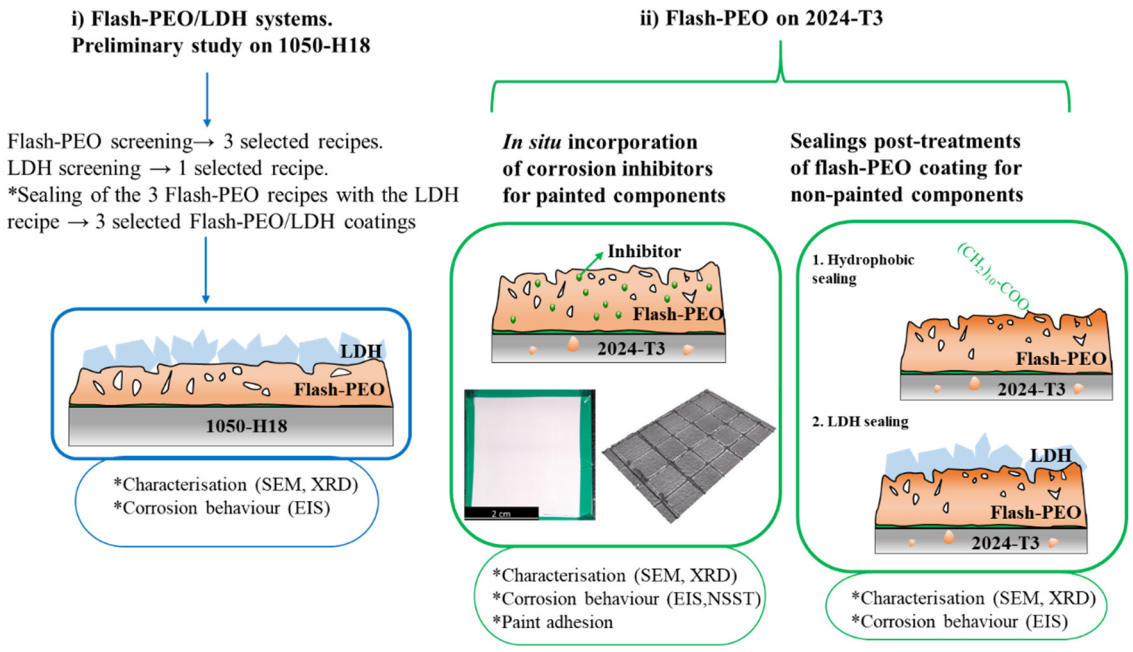

Figure 4.1. *General scheme of Chapter 2.*

Chapter 2

C2.1. Flash-PEO coatings and LDH post-treatment on 1050 alloy

C2.1.1. Introduction

The application of sealing post-treatments on flash-PEO coatings is a relatively unexplored field. Among the different options described in **Section 1.3.3.3**, LDH has been receiving increasing attention in recent years due to its potential for combining passive and active corrosion protection. The concept of LDH-based sealings on PEO coatings has been recently proven [132, 133, 268], although many variables require further study such as the effect of coating composition. Also, it needs to be demonstrated that thin PEO coatings are suitable for LDH post-treatment.

In this section, several eco-friendly electrolytes based on aluminate, silicate and phosphate species are evaluated for the development of flash-PEO coatings. Then, several LDH recipes are explored on the bulk alloy before LDH post-treatment of selected PEO coatings. Finally, the best flash-PEO/LDH systems are characterized and evaluated in terms of corrosion resistance. A commercially pure aluminium substrate (1050 alloy) is used in these preliminary studies in order to avoid interference from alloying elements.

C2.1.2. Screening of flash-PEO coatings

Flash PEO coatings were obtained on 1050 alloy in 31 different dilute (<50 g L^{-1}) electrolytes under low current densities (100-200 mA cm^{-2}) and short treatment times (180-200 s) (**Table 4.1**).

Table 4.1. *Flash PEO conditions of 1050 alloy.*

Coating	Electrolyte (g L^{-1})		Coating	Electrolyte (g L^{-1})		Coating	Electrolyte (g L^{-1})	
	$NaAlO_2$	KOH		$(Na_3P_3O_6)_3$	KOH		Na_2SiO_3	KOH
A1.1	4	1.0	P1.1	30	1	S1.1	10.5	2.8
A1.2	4	3.3	P1.2	30	3	S1.2	10.5	3.5
A1.3	4	5.6	P1.3	30	5	S1.3	10.5	4.6
A2.1	7	1.0	P2.1	40	1	S2.1	15.0	2.8
A2.2	7	3.3	P2.2	40	3	S2.2	15.0	3.5
A2.3	7	5.6	P2.3	40	5	S2.3	15.0	4.6
A3.1	10	1.0	P3.1	50	1	S2.4	15.0	6.0
A3.2	10	3.3	P3.2	50	3	S2.5	15.0	8.0
A3.3	10	5.6	P3.3	50	5	S2.6	15.0	10.0
			P4*	$Na_4P_2O_7$: 20	2.8	S4*	$Na_2SiO_3 \cdot 5H_2O$: 25	2.8
			P5*	$Na_3PO_4 \cdot 12H_2O$: 20	2.8	S5*	$Na_2SiO_3 \cdot 5H_2O$: 5	8.4

Notes: - PEO treatment conditions: V (V): 400; j (mA cm^{-2}): 100; t (s): 180.
- *PEO treatment conditions: V (V): 350; j (mA cm^{-2}): 50; t (s): 200.

All the developed flash-PEO coatings were formed under DC anodizing conditions in order to quickly develop thin coatings without excessive energy consumption [108, 118]. AC PEO is known to produce more uniform coatings, but it requires longer treatment times than the ones used in this work.

The growth of PEO coatings takes place under the presence of short-lived and numerous discharges on the surface. These discharges continuously initiate and quench in the entire coating surface. Sparking regime is easily achieved due to the high polarization of the aluminium in the studied electrolytes (**Table 4.1**), which means that relatively small current densities can cause a dielectric breakdown. Higher breakdown voltages (associated with the spark-regime commencement during the PEO process) are related to higher coating thickness and consequently, higher energy consumption [109, 111, 114]. Based on this, the first screening stage was conducted considering the combination of uniform surface appearance and low breakdown voltage (**Figure 4.2)**. The latter was estimated from the time that discharges were visible with the naked eye.

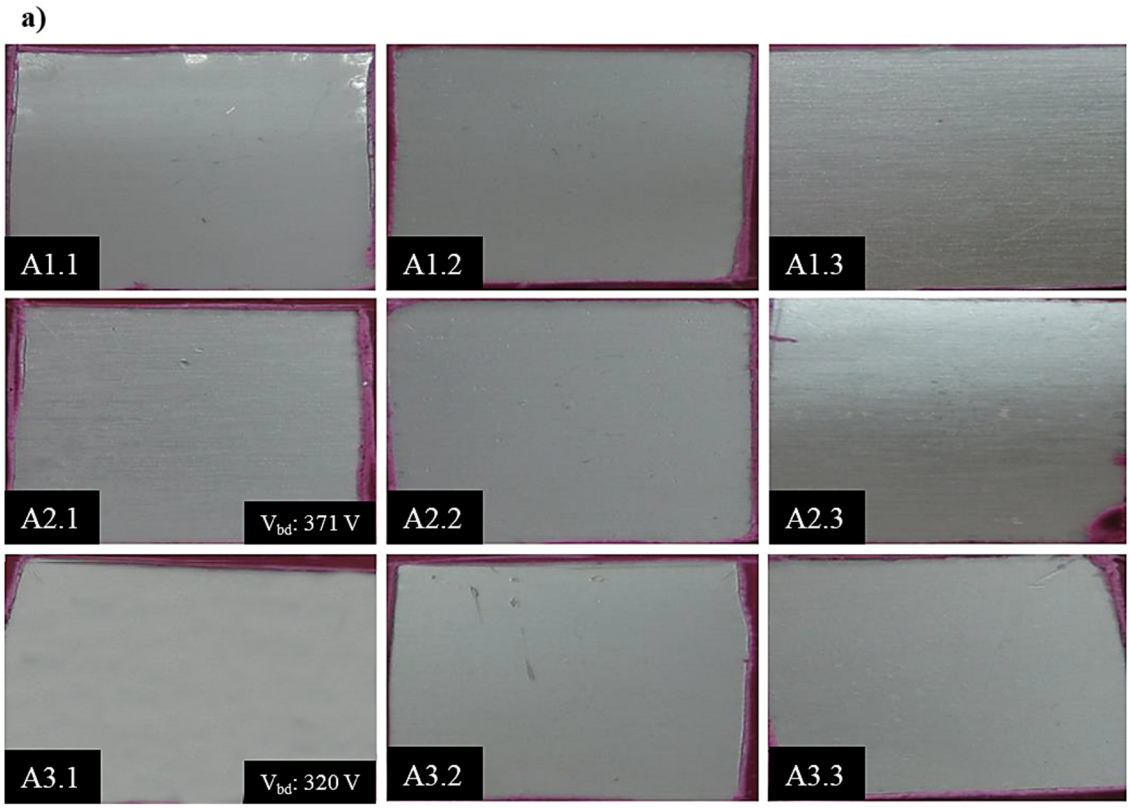

Figure 4.2. *Continuation*

b)

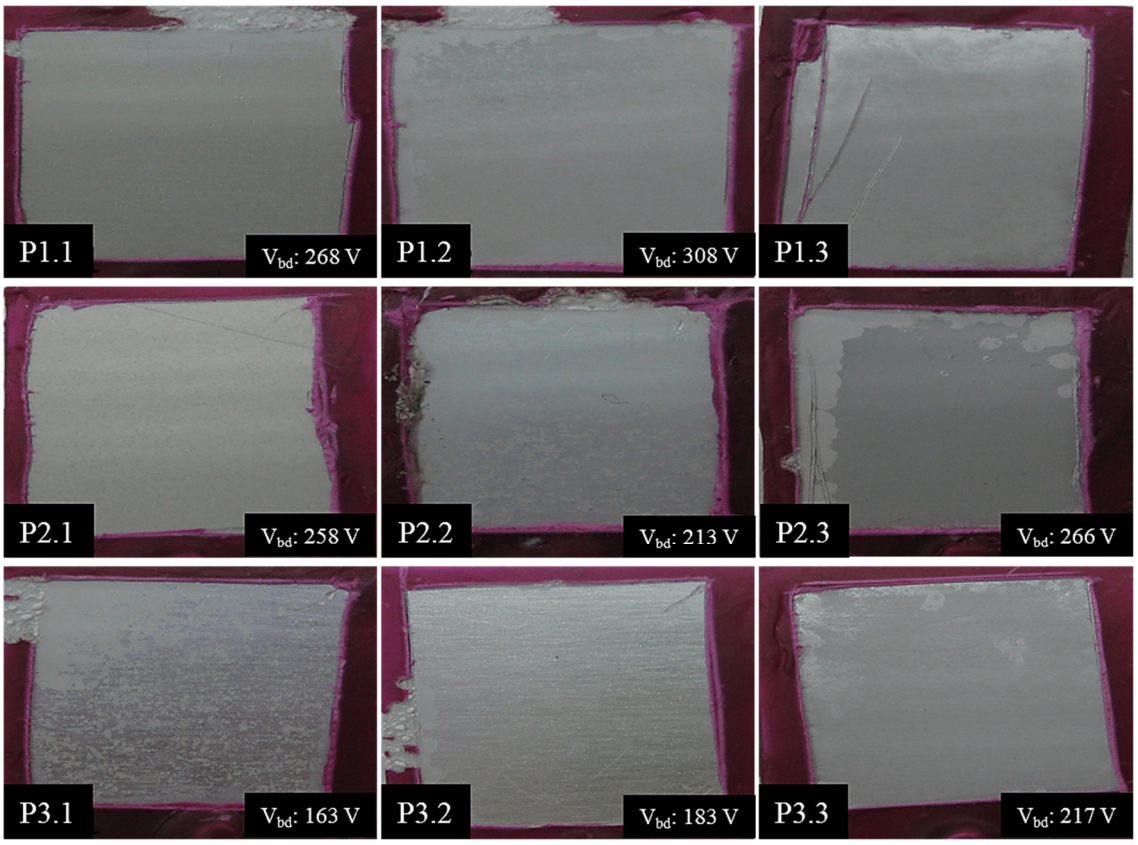
P1.1
V_{bd}: 268 V
P1.2
V_{bd}: 308 V
P1.3
P2.1
V_{bd}: 258 V
P2.2
V_{bd}: 213 V
P2.3
V_{bd}: 266 V
P3.1
V_{bd}: 163 V
P3.2
V_{bd}: 183 V
P3.3
V_{bd}: 217 V

c)

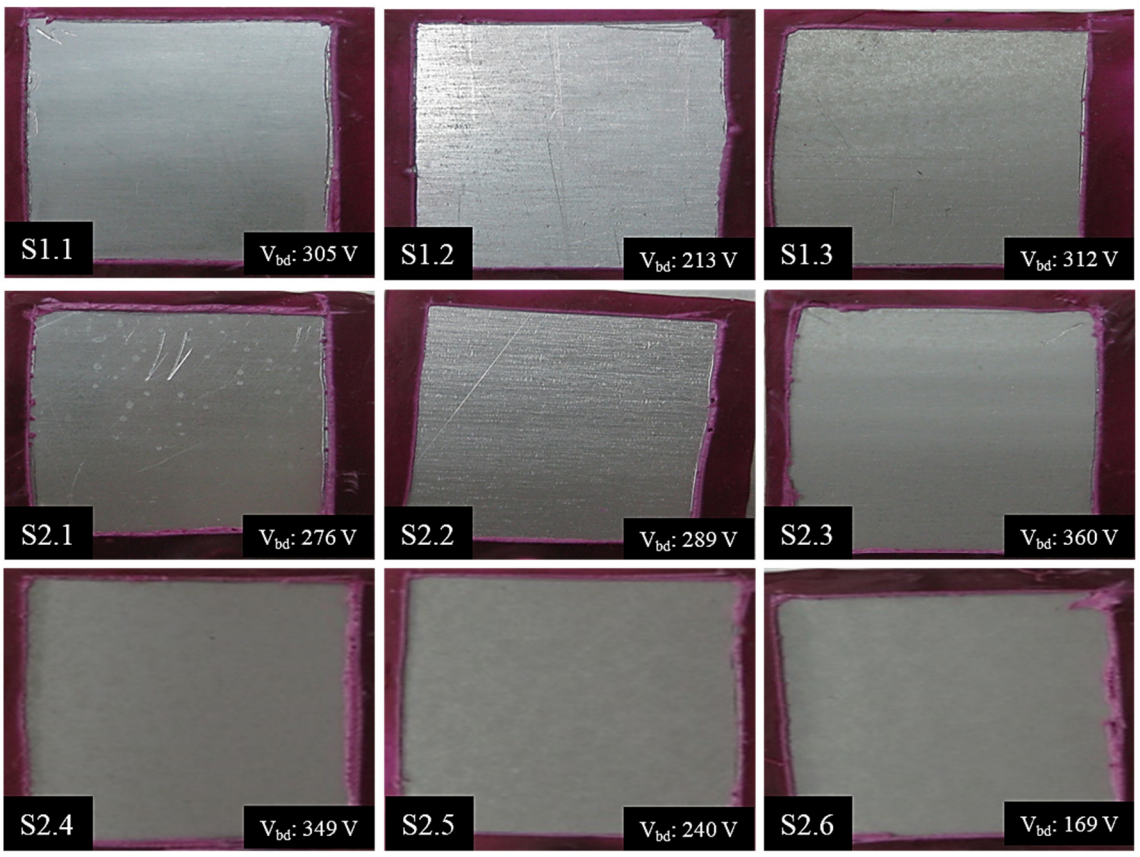
S1.1
V_{bd}: 305 V
S1.2
V_{bd}: 213 V
S1.3
V_{bd}: 312 V
S2.1
V_{bd}: 276 V
S2.2
V_{bd}: 289 V
S2.3
V_{bd}: 360 V
S2.4
V_{bd}: 349 V
S2.5
V_{bd}: 240 V
S2.6
V_{bd}: 169 V

c) Continuation

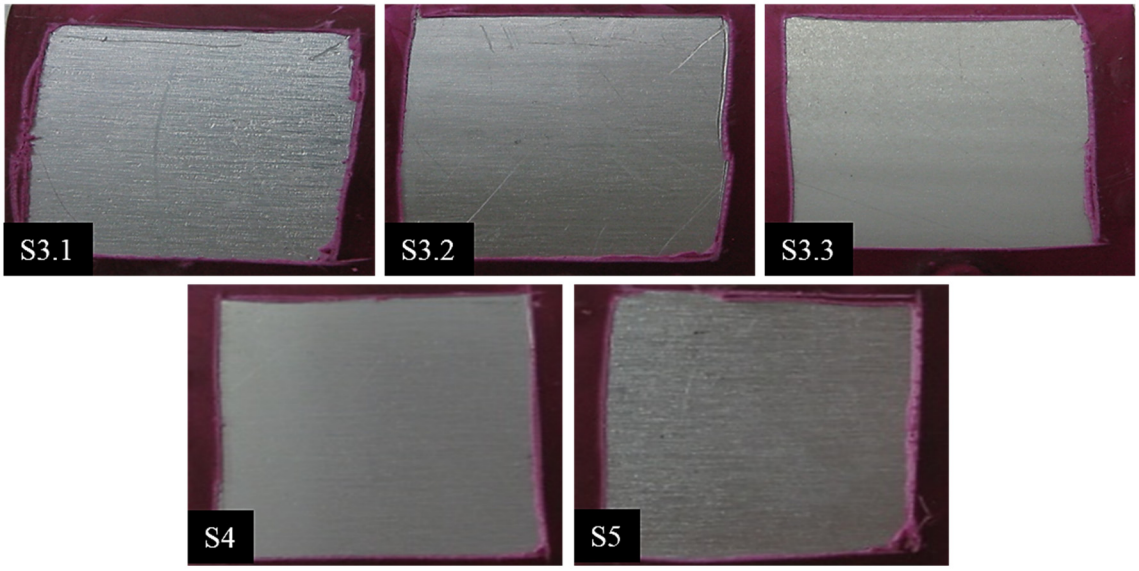

Figure 4.2. *Surface appearance and breakdown voltage values of studied flash-PEO coatings in (a) aluminate-, (b) phosphate- and (c) silicate-based electrolytes. Specimens without indicated* V_{bd} *values did not show visible discharges.*

As it can be seen in **Figure 4.2**, only the flash-PEO coatings identified as A3.1, P2.1, S2.6 and S4 showed uniform surfaces due to establishment of a stable sparking, or discharge, regime. Breakdown voltages for these specimens were 320 V, 258 V, 169 V and 108 V, respectively. These coatings were selected for the second screening stage, which consisted of EIS testing in 3.5 wt.% NaCl solution following 1h of immersion.

Figure 4.3a shows a comparison of the thicknesses of the A3.1, P2.1, S2.6 and S4 coatings. The impedance modulus, |Z|, at 10^{-2} Hz is plotted in **Figure 4.3b**.

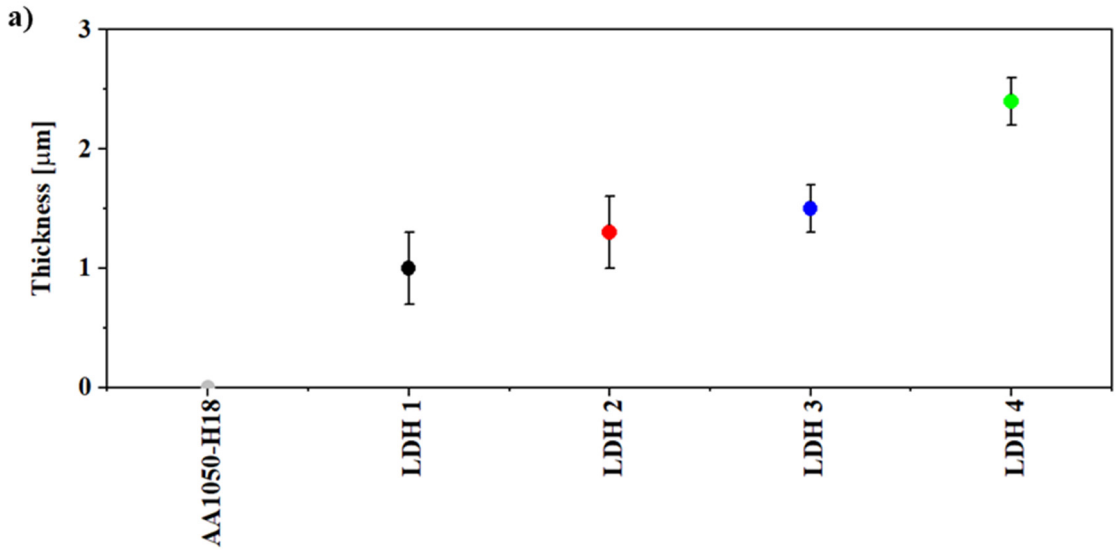

Figure 4.3. *Continuation*

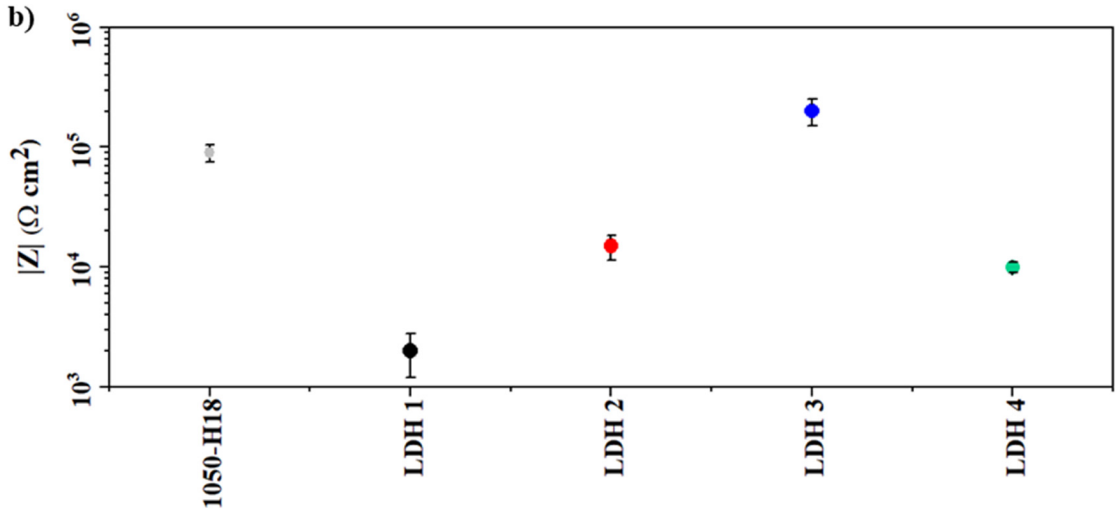

Figure 4.3. *Scatter diagram of (a) thickness and (b) impedance modulus at 10^{-2} Hz in 3.5 wt.% NaCl of the selected flash-PEO coatings on 1050 alloy.*

Following the EIS results, three PEO coatings were selected to study the influence of coating composition on LDH growth (i.e. one per each electrolyte composition: aluminate A3.1, phosphate P2.1 and silicate S4). The PEO coating growth rate and specific energy consumption of the selected coatings are shown in **Table 4.2**. Energy values were obtained from integration of the voltage- and current-time transients (**Figure 4.4**) recorded during the PEO process.

Table 4.2. *Conductivities, breakdown voltages, thicknesses, coating growth rates and specific energy consumption values of selected flash-PEO coatings on 1050 alloy.*

Coating	σ (mS cm^{-1})	V_{bd} (V)	Thickness (µm)	Coating growth rate (µm min^{-1})	Energy consumption (kW h m^{-2} µm^{-1})
A3.1	13.1 ±0.1	320±6	1.1±0.3	~0.37	3.8±0.3
P2.1	11.1±0.1	257±15	2.4±0.4	~1.31	4.7±0.2
S4	32.9±0.2	108±7	2.1±0.5	~0.39	2.2±0.1

As it can be seen in **Figure 4.4**, a current drop is observed in aluminate and silicate electrolytes when the set-limits 400 V and 350 V were reached after 40 s and 75 s of treatment, respectively. It is worth noting that microdischarges almost extinguished for current density values below 20 mA cm^{-2}, but the treatments were carried on till the set time in order to repair microdefects in the oxide material [269]. This also explains the relatively low coating growth rates measured for these two electrolytes [111, 113].

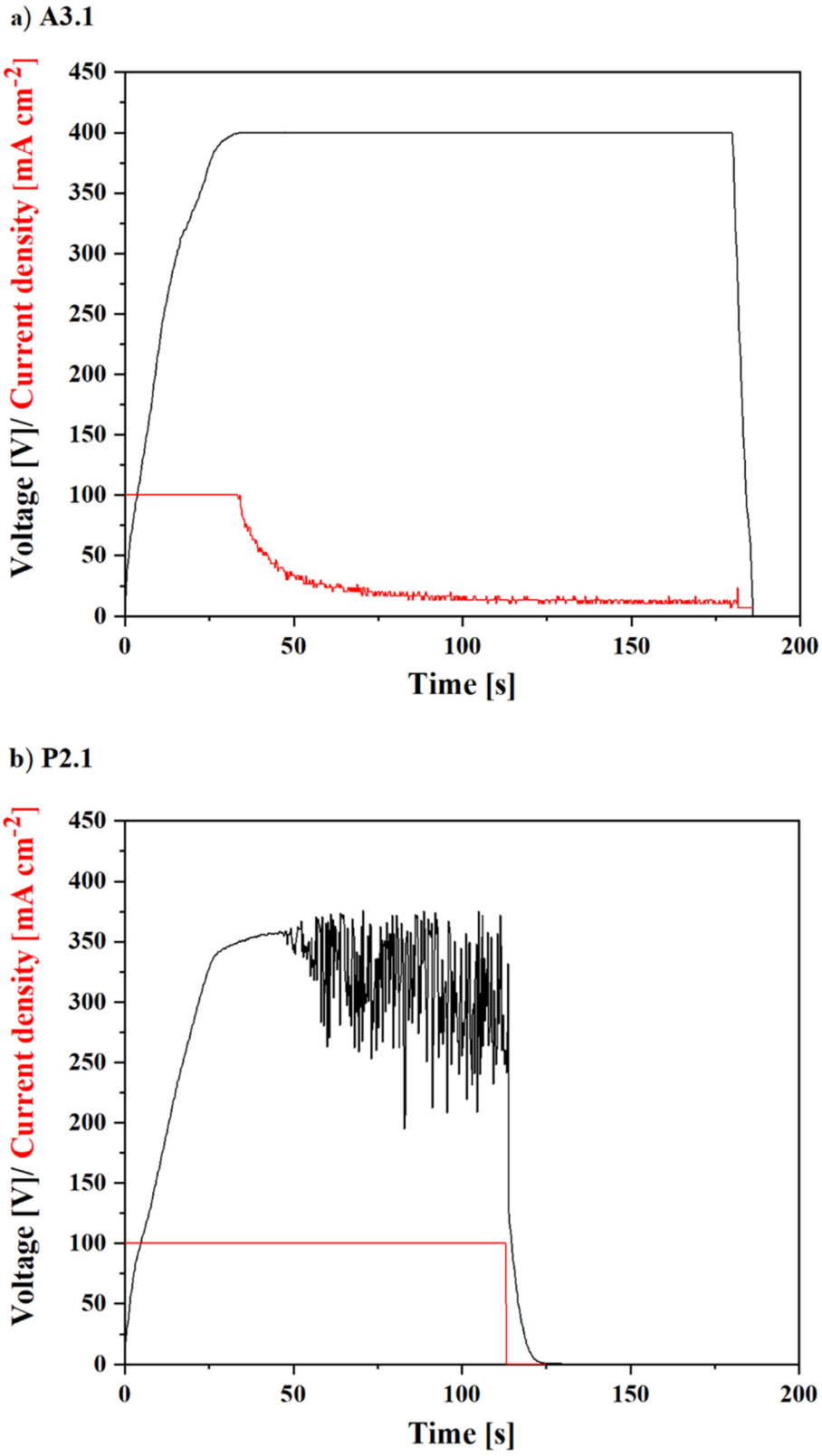

Figure 4.4. *Continuation*

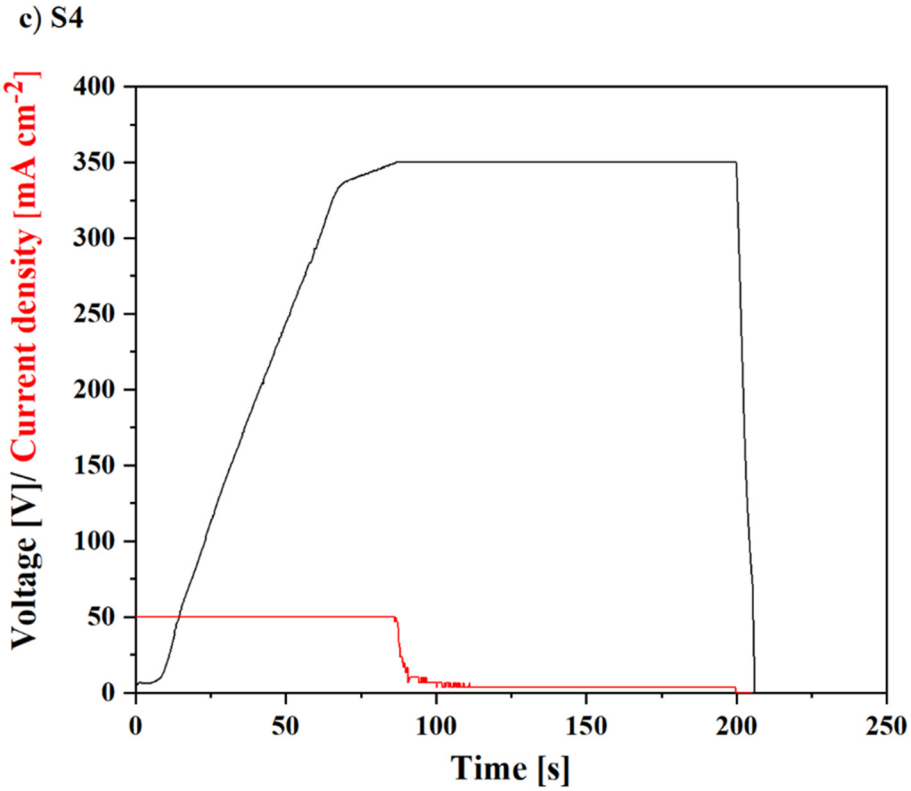

Figure 4.4. *Voltage-current time curves for (a) A3.1, (b) P2.1 and (c) S4 flash-PEO coatings on 1050 alloy.*

The fact that the limiting voltage is reached (hence the current drop) could be explained by the formation of a more compact and, consequently, more resistant coating [123]. A high value of energy consumption in the case of aluminate is mainly due to the fact that aluminate species in the electrolyte gave rise to the formation of a coating composed of nearly pure alumina, which has very low electron conductivity (i.e., the current flows mainly by ion and not by electron transfer) [270]. Further, the high breakdown voltage (320 V) in the aluminate electrolyte compelled the use of a higher voltage limit (400 V) to ensure a long enough period of sparking in order to achieve a uniform coating of a significant thickness; this yielded a higher specific energy consumption value.

The high values of energy consumption and coating growth rate in the case of phosphate electrolyte (**Table 4.2**), where sparking was observed until the end of the treatment, was due to the absence of current drop, because the limiting value of 350 V was never reached (**Figure 4.4b**). In this case, intense microdischarges and voltage variations were observed after 60 s and, therefore, the treatment was stopped at 115 s to maintain coating uniformity.

The lowest energy consumption of 2.2 kW h m^{-2} μm^{-1} was achieved in the case of silicate electrolyte. This was mainly the result of its high conductivity and, therefore, low breakdown voltage. The onset of microdischarges early in the treatment and the relatively long sparking period before current decay resulted in an intermediate coating growth rate value compared to the other electrolytes (**Table 4.2**). The specific energy consumption values obtained under DC conditions in the present work are similar to those reported in studies carried out under AC conditions. For example, Matykina *et al*. developed a PEO coating on pure aluminium using silicate electrolyte and obtained a growth rate of 1.3 μm min^{-1} and energy consumption values of 4.77 kW h m^{-2} μm^{-1} [123]. Cheng *et al.* reported a growth rate of 11.3 μm min^{-1} and energy consumption values of 5 kW h m^{-2} μm^{-1} for an Al-Cu alloy in concentrated aluminate electrolyte [113]. It is well known that DC conditions promote low energy consumption in comparison with AC conditions [111, 123]; however, in this study the values obtained were considerably lower compared with the available data for different PEO treatments on commercial Al alloys, which can be as high as 26.7 kW h m^{-2} μm^{-1} [123].

The present findings demonstrate that in order to reduce specific energy consumption under DC conditions it is necessary to (i) limit the final forming voltage to ensure a current drop, and (ii) use electrolytes with high conductivity, which ensures low microdischarges onset voltages and extended sparking periods, as in the case of the S4 electrolyte.

C2.1.3. Characterization of flash-PEO coatings

Figure 4.5 reveals the XRD patterns of the studied A3.1, P2.1 and S4 PEO coatings. The presence of γ-Al_2O_3 as the main constituents of all selected PEO coatings is typical for PEO coatings on Al alloys developed in the studied electrolytes [118, 271].

Typically, conventional PEO coatings also show the presence of α-Al_2O_3 enriched oxide layers, although the flash-PEO conditions used in the present study only allow the formation of γ-Al_2O_3, which is usually formed at lower voltage values (350–400 V) [128, 272-274].

An additional peak of γ-Al_2O_3 was detected in A3.1 coating. It is due to the presence of aluminate species in the electrolyte, thereby increasing the presence of this phase over the coating surface.

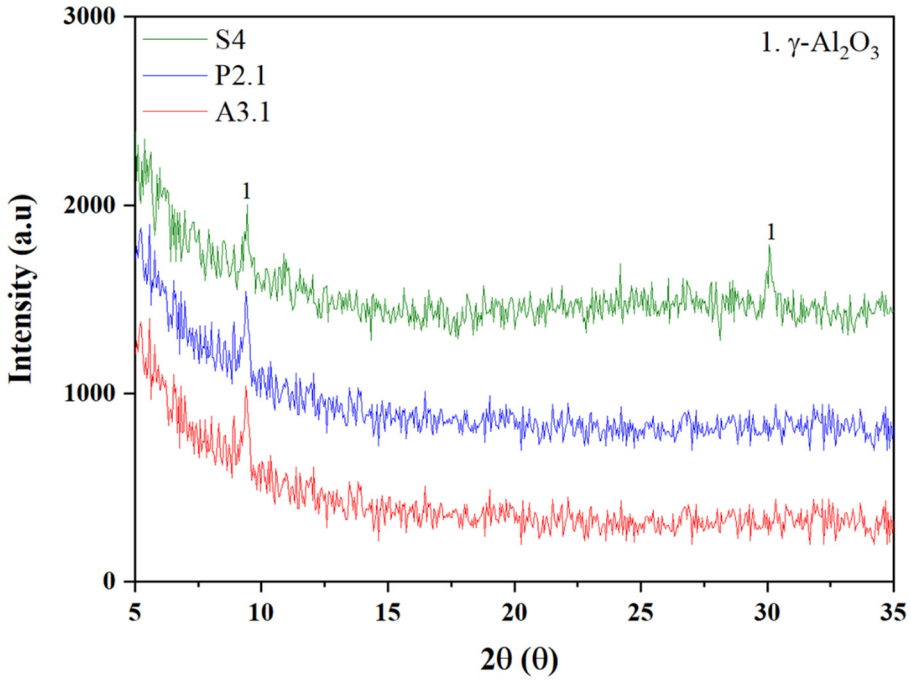

Figure 4.5. *Grazing angle XRD patterns of A3.1, P2.1 and S4 PEO coatings on 1050 alloy.*

Figure 4.6 show the plan views and cross-section scanning electron micrographs of 1050 alloy with the selected PEO coatings along with the corresponding EDS analysis (**Table 4.3**).

All the specimens show a thin oxide layer of 1–2.5 μm (**Figures 4.6b,d,f**). This is particularly evident in the aluminate-based A3.1 coating, where the Al-Fe intermetallic compounds from the substrate are still visible in the coating (**Figure 4.6a**, **inset**) due to its low thickness. This coating is also more heterogeneous (**Figure 4.6b**) than the other ones, which is attributable to its higher breakdown voltage [133, 275, 276] and its low coating growth rate.

Phosphate-based P2.1 coating shows a homogeneous surface appearance (**Figure 4.6c**), and the highest thickness value (**Figure 4.6d**). This was mainly due to the presence of polyphosphate species that participated in PEO coating formation and favoured its high coating growth rate [115].

Silicate-based S4 coating, with the lowest breakdown voltage, showed a homogeneous surface morphology with very sparse submicrometric pores (**Figure 4.6e**). The latter may be attributable to the formation of a thin superficial glassy layer of SiO_2, which can be surmised from the EDS analysis where the presence of 1.5 at.% Si in the coatings and greater content of oxygen than in the other two coatings was confirmed (**Table 4.3**).

The corrosion resistance of studied PEO coatings is related to PEO coating thickness and porosity. The lack of pores and higher coating thickness restricts the Cl^- penetration and

prevents its detrimental effect on corrosion resistance [277]. For this reason, the corrosion resistance of P2.1 and S4 PEO coatings is higher than that of the A3.1 PEO coating.

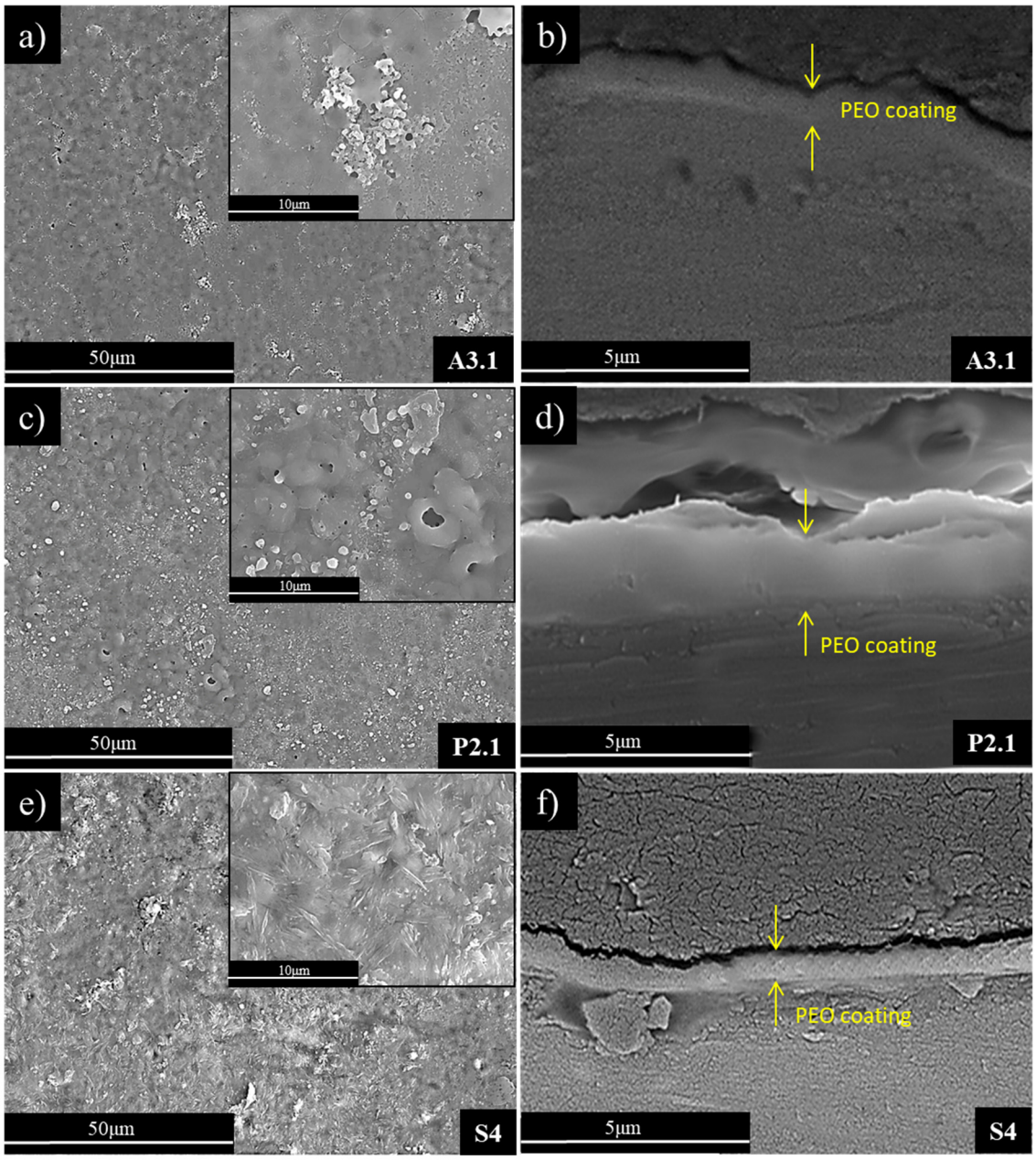

Figure 4.6. *Plan views (a,c,e) and cross-sections (b,d,f) of secondary electron images of A3.1, P2.1, S4 coatings.*

Table 4.3. *EDS area analysis of A3.1, P2.1, S4 coatings.*

Coating	EDS (at.%)				
	O	Al	Fe	P	Si
A3.1	45.7	52.8	1.1	-	-
P2.1	53.3	46.6	-	1.1	-
S4	64.3	33.6	-	-	1.5

C2.1.4. Screening of LDH treatments

Prior to post-treatment of the selected PEO coatings, the effects of nitrate source and treatment time on the growth of LDH coatings on the bare aluminium substrate were investigated (**Table 4.4**).

Table 4.4. *Studied LDH synthesis conditions for surface modification of 1050 alloy.*

LDH treatment	Chemical composition (M)	Immersion time (min)
LDH 1	$Zn(NO_3)_2 \cdot 6H_2O$: 0.1 NH_4NO_3: 0.06	30
LDH 2	$Zn(NO_3)_2 \cdot 6H_2O$: 0.1 NH_4NO_3: 0.06	60
LDH 3	$Zn(NO_3)_2 \cdot 6H_2O$: 0.1 $NaNO_3$: 0.06	30
LDH 4	$Zn(NO_3)_2 \cdot 6H_2O$: 0.1 $NaNO_3$: 0.06	60

Note: All treatments were developed in 250 mL aqueous solution at 95 ºC. pH values were adjusted to 6.5 using 1 vol.% ammonia.

As it can be seen in **Figure 4.7**, LDH 1 and LDH 2 coatings exhibited a colourless surface appearance in comparison to LDH 3 and LDH 4. It could be related to the use of NH_4NO_3 reagent instead of $NaNO_3$. In the case of LDH 3 and LDH 4 coatings, the presence of $NaNO_3$ reagent in the solution promoted the formation of coloured LDH coatings, possibly due to the presence of sodium ions in the LDH 3 and LDH 4 coatings structure; although longer treatment times lead to a heterogeneous LDH growth (LDH 4).

Regarding the coating homogeneity, NH_4NO_3 promoted the formation of homogeneous LDH coatings (**Figure 4.7**) at both short and long treatment times, which is in agreement with other studies [155, 159, 162, 278].

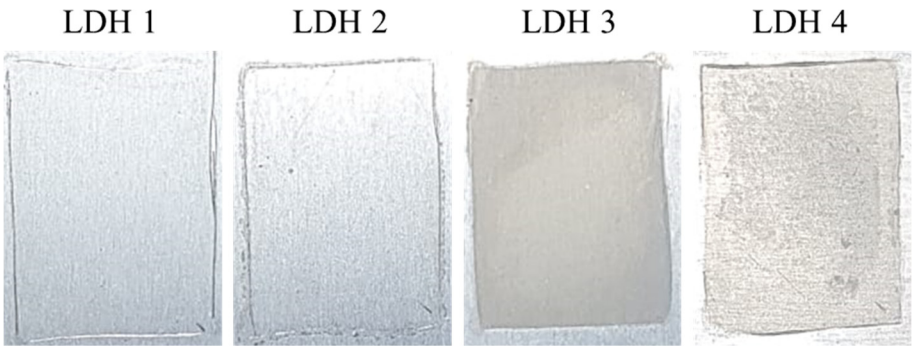

Figure 4.7. *Surface appearance of studied LDH coatings formed on the bare 1050 alloy.*

Figure 4.8 depicts the XRD patterns of the studied LDH treatments grown on the bare material, where the diffraction peaks at 9.6º and 19.9º, corresponding to the characteristic (003) and (006) reflections of LDHs intercalated with NO_3^- [279-281], indicate satisfactory formation of the LDH layer.

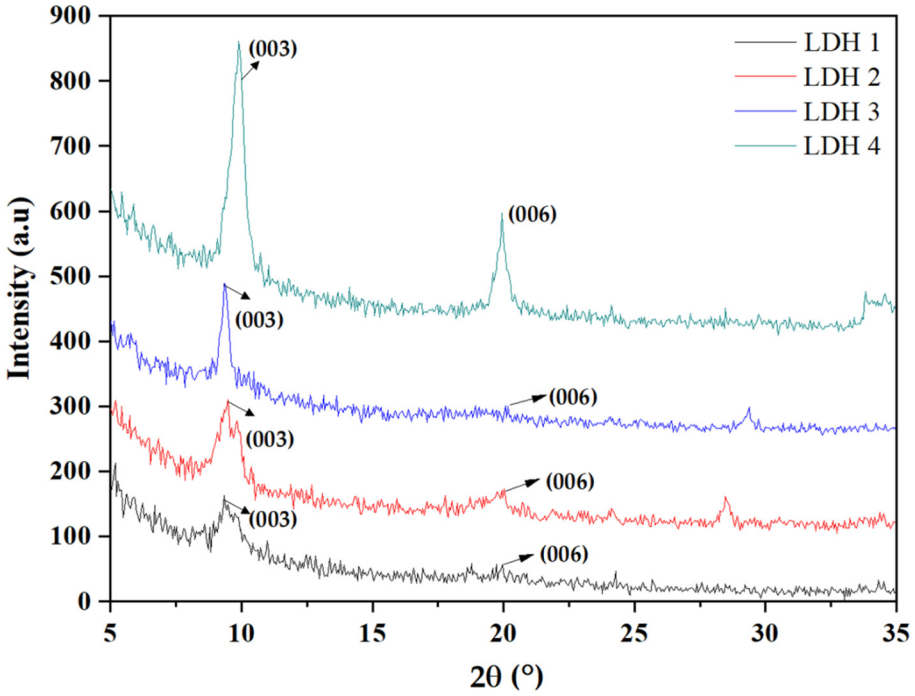

Figure 4.8. *XRD patterns of Zn-Al-LDH 1-4 coatings on 1050 alloy.*

LDH recipes containing $NaNO_3$ in the solution (LDH 3 and LDH 4) yield a more defined and intense (003) peak, probably due to the presence of sodium ions in the LDH structure [282]. On the other hand, the presence of NH_4NO_3 drove the formation of broadened peaks [283] and also prompted an additional small peak at 9.9º that could be associated with an LDH phase intercalated with carbonate arising from atmospheric CO_2 [155]. LDHs formed under long treatment times (LDH 2 and LDH 4) showed peaks of higher intensity in comparison to LDHs formed under short treatment times (LDH 1 and LDH 3), indicating an increment in the degree of crystallinity [283].

Figure 4.9 shows secondary electron images of the LDH coatings (**Table 4.4**) grown on the bare aluminium substrate, where their typical flake-like structure can be observed, particularly in specimens LDH 1 and LDH 4.

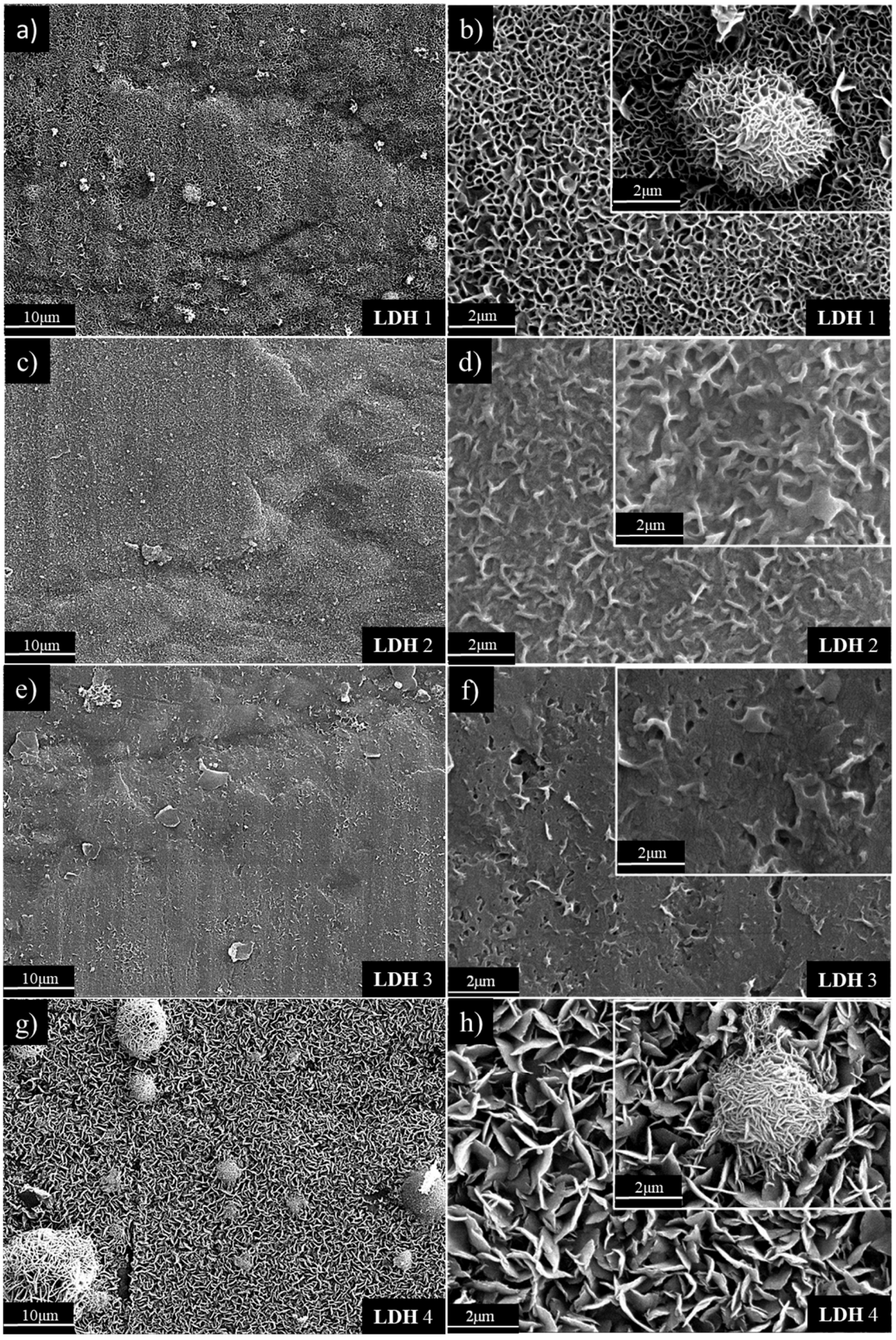

Figure 4.9. *Secondary electron images of the (a,b) LDH 1 (c,d) LDH 2, (e,f)LDH 3 and (g,h) LDH 4 coatings on the bare 1050 alloy.*

The highly open structure revealed by the LDH 1 specimen, formed in the presence of NH_4NO_3, is in good agreement with the broad XRD peaks previously mentioned (**Figure 4.9a**).

In case of the LDH 2 specimen, the flake-like structure is not so well-defined, which is usually attributed to the incorporation of carbonate ions (from atmospheric CO_2) into the LDH gallery [279]. This is consistent with the peak found at 9.9º in the XRD pattern (**Figure 4.9b**).

The LDH coating developed during immersion for 60 min in the solution containing $NaNO_3$ (LDH 4) showed relatively large and curved plate-like LDH microcrystals, which is consistent with the high intensity (003) peak observed in the XRD pattern. However, these microcrystals were not yet defined after 30 min treatment (LDH 3), which is also consistent with the smaller intensity peaks in the XRD pattern (**Figures 4.8c,d**).

In order to evaluate the correlation between corrosion protection and the structure of studied LDHs, a screening process based on corrosion performance (EIS) was carried out. **Figure 4.10** depicts the thickness and |Z| at 10^{-2} Hz values of the studied LDH coatings. As it can be seen in **Figure 4.10a**, LDH 2 and LDH 4 coatings developed at longer treatment times showed a slight thickness increase with respect to the LDH1 and LDH 3. This is in agreement with several studies reporting that longer treatment times produce thicker LDH layers [279, 281].

Regarding the corrosion resistance, the presence of spheroidal particles in flake-like LDH 1 and LDH 4 specimens (**Figure 4.9**) is typically associated with the presence of secondary phases [133, 284, 285] that favour aluminium cation dissolution from the surrounding matrix due to their cathodic behaviour [279]. The porous structure of these spheroidal particles could favour Cl^- penetration and explain the lower corrosion protection offered by LDH 1 and LDH 4 coatings (**Figure 4.10b**) [286-288]. The LDH 2 specimen showed a better corrosion response in comparison to LDH 1 and LDH 4, although its performance was worse than that of the untreated alloy. It is possibly associated with the longer treatment time for LDH 2, thus forming a less-porous coating [289, 290].

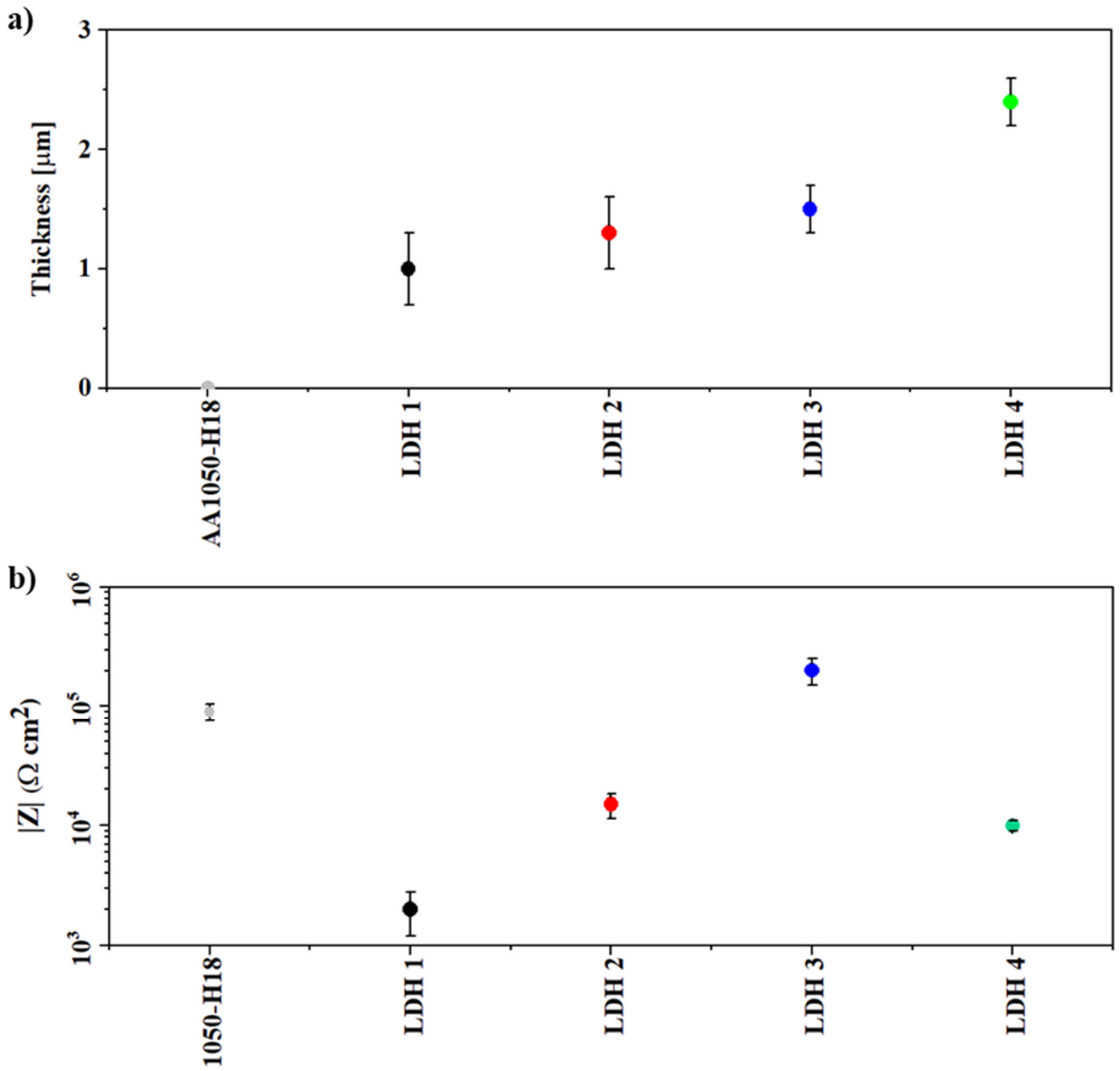

Figure 4.10. *Scatter diagram of (a) thickness and (b) impedance modulus at 10^{-2} Hz in 3.5 wt.% NaCl of the selected LDH coatings on 1050 alloy.*

The only LDH treatment that showed a beneficial effect was LDH 3. This may be due to the presence of sodium ions in the LDH gallery, which facilitated the formation of non-porous and compact corrosion-protective LDH coating. For this reason, LDH 3 was the treatment selected for post-treatment of the PEO coatings.

C2.1.5. Characterization of PEO/LDH systems

Figure 4.11 depicts the homogeneous LDH formation on selected PEO coatings. The different PEO coating thickness and surface compositions caused several colour differences after sealing with LDH. These colour changes are related to the different morphological and microstructural features of the studied PEO/LDH systems, as will be further disclosed.

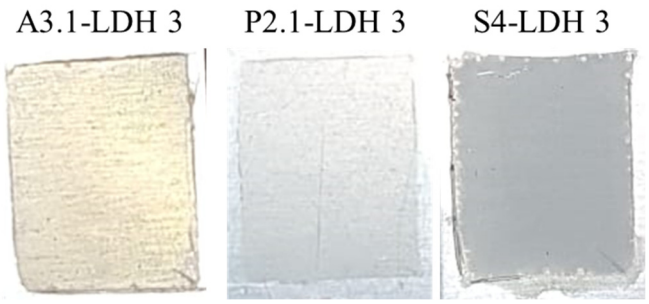

Figure 4.11. *Surface appearance of Zn-Al-LDH-coated A3.1, P2.1 and S4 PEO coatings on 1050 alloy.*

Figure 4.12 shows the XRD patterns of A3.1, P2.1 and S4 PEO coatings with the LDH 3 post-treatment, where it can clearly be seen that the composition of the PEO coating has an effect on LDH growth.

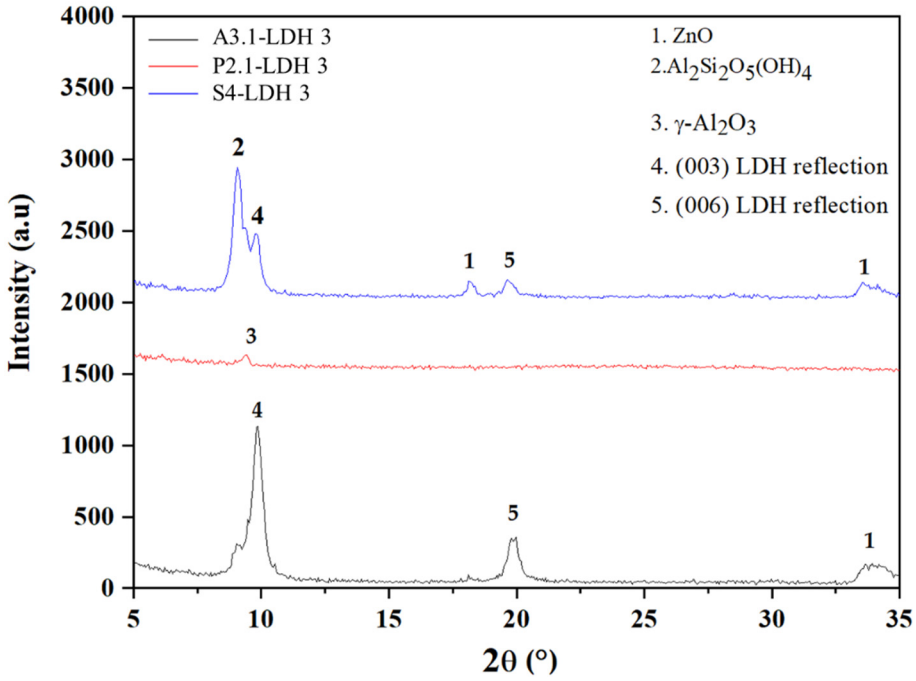

Figure 4.12. *XRD patterns of Zn-Al-LDH-coated A3.1, P2.1 and S4 PEO coatings.*

PEO/LDH coatings based on aluminate and silicate electrolytes showed the typical peaks at 9.6º and 19.9º, which corresponded to the characteristic (003) and (006) reflections of LDH intercalated with NO_3^- [279-281]. Additionally, the presence of ZnO and $Al_2Si_2O_5(OH)_4$ characteristic peaks were observed in the A3.1-LDH and S4-LDH specimens, which originate from the interaction between the LDH solution and the γ-Al_2O_3 phase in the coating.

In the particular case of PEO coating developed in P2.1-LDH coating, there was only a γ-Al_2O_3 peak detected in that range. This could be attributed to the formation of non-

crystalline phases, or to only a small amount that could not be detected at the selected scan rate (**Figure 4.12**).

Figure 4.13 shows the morphology of the PEO/LDH systems. It is evident that the composition of the PEO coating has a strong influence over the LDH morphology.

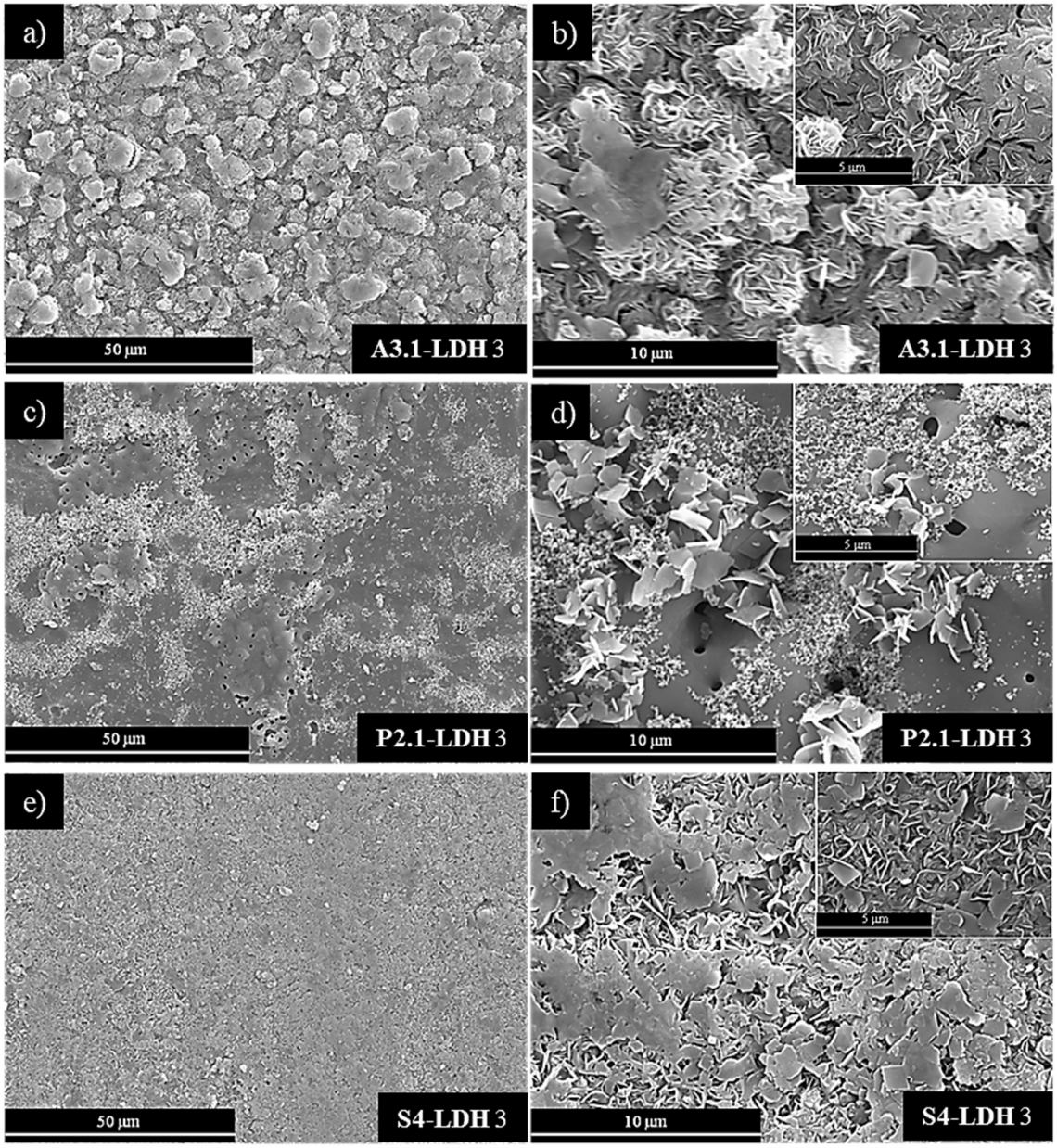

Figure 4.13. *Secondary electron images of the plan views of the PEO/LDH systems on 1050 alloy: (a,b) A3.1/LDH, (c,d) P2.1/LDH, and (e,f) S4/LDH.*

The characteristic flake-like LDH structure can be clearly observed on the entire surface of the A3.1-LDH coating (**Figures 4.13a,b**). In case of the S4-LDH coating, the LDH coverage is more heterogeneous (**Figures 4.13e,f**). In both cases, however, surface morphology agrees with the XRD patterns that showed the presence of the characteristic

LDH reflections. The P2.1-LDH system, on the other hand, shows a much lesser number of LDH flakes and large areas of unmodified PEO coating (**Figures 4.13c,d**) which is also in accordance with the XRD results.

According to previous studies [133, 156, 291], $Al(OH)_2^+$ cations are an essential requirement to form the LDH layers. Due to the porous structure of PEO coatings and their compositions, two sources can provide $Al(OH)_2^+$ cations: (i) aluminium from the substrate (due to the electrochemical interactions with LDH solutions), and (ii) aluminium from the PEO coating (due to chemical dissolution) [292].

As can be seen in **Figure 4.13**, the amount of well-defined LDH flakes was highest for A3.1 and lowest for the P2.1 and S4 coatings. Further, the P2.1 coating surface revealed a highly heterogeneous LDH distribution with substantial areas free of LDH material (**Figure 4.13d**). By contrast, the S4 surface was entirely covered by LDH conversion coating, but featured a mostly flattened, featureless material rather than flakes. These differences in LDH coverage and morphology are related to the PEO coating thickness and chemical composition.

The low thickness of the A3.1 PEO coating (~1 μm) (**Figures 4.6a,b**), ensured the $Al(OH)_2^+$ cations migration from the aluminium metal matrix towards the coating surface. Concerning the chemical composition of PEO coating surfaces, the aluminium content decreased in the order A3.1 > P2.1 > S4 (**Figure 4.6; Table 4.3**), since only A3.1 electrolyte contained aluminate species. Unlike A3.1, the S4 coating, although having low thickness suitable for facilitated cation migration, lacked the additional source of aluminium cations in the coating itself.

The sparse formation of LDH on P2.1 coating is related to the greater charge passed during the P2.1 treatment and intense sparking until the end of the treatment (**Figure 4.6b**), thus resulting in greater thickness which hampered the migration capacity of $Al(OH)_2^+$ cations. This justifies the absence of LDH reflection peaks in XRD patterns of the P2.1-LDH (**Figure 4.13**).

C2.1.6. Corrosion resistance of PEO/LDH systems

The effect of LDH post-treatment on the thickness and corrosion resistance of selected PEO coatings was evaluated by EIS testing in 3.5 wt.% NaCl for 1 h immersion (**Figure 4.14**).

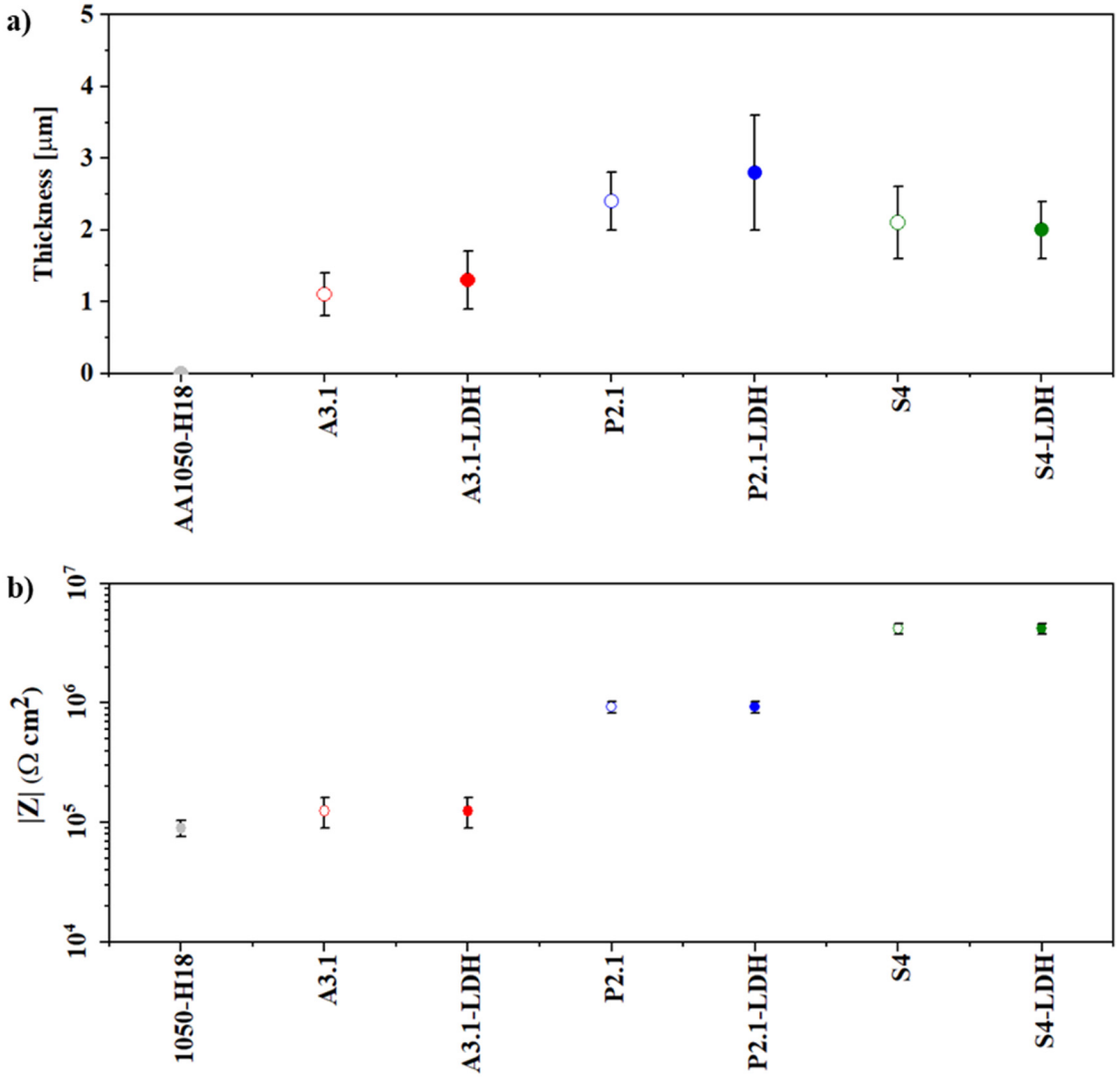

Figure 4.14. *Scatter diagram of (a) thickness and (b) impedance modulus at 10^{-2} Hz of PEO/LDH systems on 1050 alloy.*

As shown in **Figure 4.14**, PEO coatings with and without LDH treatment showed similar coating thickness and impedance modulus. This could be attributed to two factors: (i) LDH flake resistance is negligible compared with that of the PEO coating, and (ii) part of the PEO coating dissolved and lost some of its barrier properties during the formation of LDH (under conditions described in the experimental part), retracting from the possible small beneficial effect of the LDH layer.

This effect can be related to the trapping of Cl^- ions by the LDH structure, thus preventing fast development of chloride-induced corrosion processes. For instance, when an LDH layer is not loaded with inhibitors, the corrosion resistance remains unchanged or degrades slightly, as has been shown in [133]. On the other hand, when LDH is intercalated with an inhibitor (e.g. vanadate ions), an improvement in corrosion resistance is observed with immersion time due to an active protection effect [133, 293].

The present findings highlight that the development of LDH-container layers did not deteriorate the corrosion resistance of flash PEO coatings, which has a potential for added active protection functionality.

C2.1.7. Concluding remarks on PEO/LDH systems on 1050 alloy

Some conclusions can be drawn regarding the effects of LDH post-treatments:

- Flash PEO coatings with ~1–2 μm thickness and ~2–5 kW h m^{-2} μm^{-1} energy consumption were generated on a commercially pure aluminium alloy. Low energy consumption was ensured through relatively high electrolyte conductivity.
- The first stage of the active protection system was successfully completed on flash PEO coatings via the development of an LDH layer. LDH coating is continuous and well defined when the PEO layer is thin (~1 μm), and the LDH formation is further facilitated when additional $Al(OH)_2^+$ cations are lixiviated from the coating.
- Corrosion resistance of inhibitor-free flash PEO/LDH coatings is mainly determined by the low porosity of the PEO layer. Formation of the LDH layer does not compromise the corrosion resistance of flash PEO coatings. Loading of the LDH scaffold with corrosion inhibitors is necessary in order to achieve an enhanced corrosion protection.

Therefore, the first stage of active protection system building can be considered successful. The second stage would consist of loading the LDH scaffold with corrosion inhibitors that would ensure enhanced corrosion protection.

In conclusion, these results are highly relevant for understanding the relation between coherent and uniform LDH layer formations on flash PEO coatings, which is the first step in achieving active protection systems through the incorporation of green corrosion inhibitors into the LDH layer.

C2.2. Flash-PEO coatings and hydrophobic sealing on 2024 alloy

C2.2.1. *In situ* incorporation of corrosion inhibitors

C2.2.1.1. Introduction

An intrinsic property that PEO technology offers is the easy incorporation of electrolyte species and additives (e.g. corrosion inhibitors) into the coating structure, thus providing a better corrosion performance. Up to date, only a few investigations have been reported on the microstructural and corrosion properties of inhibitor-loaded PEO coatings (**Table 1.16**). The coating thicknesses in these works were above 10 μm, which is much higher than that of CAA films (<5 μm) and, therefore, critical for fatigue sensitive applications. Another point to consider for CAA replacement is compatibility with sealing post-treatments and paints in multi-layer coating systems typically used on internal and external aircraft structures. However, literature data on paint adhesion and sealing post-treatments of flash-PEO coatings is almost non-existent (**Section 1.3.3.3**), making the assessment of the real worth of these developments very challenging.

In this section, three strategies based on flash-PEO in eco-friendly electrolytes are explored as an alternative to CAA films for painted and non-painted components based on the 2024 alloy: (i) flash-PEO coatings (~5 μm) with in situ inhibitor loading; (ii) LDH post-treatment of a phosphate/silicate-based flash-PEO coating; and (iii) sealing post-treatment with lauric acid in order to produce a hydrophobic surface for non-painted components.

C2.2.1.2. Screening of flash-PEO coatings

Preliminary screening of flash-PEO coatings on 2024 alloy under DC and AC anodizing regimes was carried out using several electrolytes (**Table 4.5**). The operating conditions, electrolyte composition and concentrations were established considering previous studies [113, 118, 294-297] and the findings from the previous section (**Section 2.1.2**).

Table 4.5. *Flash-PEO conditions for surface modification of 2024 alloy.*

DC conditions			AC conditions		
Coating	**Electrolyte ($g\ L^{-1}$)**	**V_{bd} (V)**	**Coating**	**Electrolyte ($g\ L^{-1}$)**	**V_{bd} (V)**
P2.1-2024	$(Na_3P_3O_6)_3$: 40 KOH : 1	250 ± 10	P2.1-2024-AC	$(Na_3P_3O_6)_3$: 40 KOH : 1	235 ± 12
PK	$(Na_3P_3O_6)_3$: 30 KOH : 1	320 ± 6	S4-2024-AC	$Na_2SiO_3{\cdot}5H_2O$: 25 KOH : 2.8	90 ± 5
PKSi	$(Na_3P_3O_6)_3$: 20 $Na_2SiO_3{\cdot}5H_2O$: 10 KOH : 1	230 ± 8	SiK-40s	$Na_2SiO_3{\cdot}5H_2O$: 12.5 KOH : 5	180 ± 20
PKSi-1	$Na_3PO_4{\cdot}12H_2O$: 20 $Na_2SiO_3{\cdot}5H_2O$: 10 KOH : 1	210 ± 35	SiK-60s	$Na_2SiO_3{\cdot}5H_2O$: 12.5 KOH : 5	180 ± 20
S4-2024	$Na_2SiO_3{\cdot}5H_2O$: 25 KOH : 2.8	120 ± 7	SiK-100s	$Na_2SiO_3{\cdot}5H_2O$: 12.5 g/L KOH : 5	180 ± 20
PKB	$(Na_3P_3O_6)_3$: 30 $Na_2B_4O_7{\cdot}10H_2O$: 10 KOH : 1	310 ± 32	PKB-60s	$(Na_3P_3O_6)_3$: 20 $Na_2B_4O_7{\cdot}10H_2O$: 10 KOH : 1	190 ± 35
PKSiB	$Na_3PO_4{\cdot}12H_2O$: 20 $Na_2SiO_3{\cdot}5H_2O$: 10 $Na_2B_4O_7{\cdot}10H_2O$: 5 KOH : 1	310 ± 15	PKB-100s	$(Na_3P_3O_6)_3$: 20 $Na_2B_4O_7{\cdot}10H_2O$: 10 KOH : 1	190 ± 35
PKSiB-1	$Na_3PO_4{\cdot}12H_2O$: 20 $Na_2SiO_3{\cdot}5H_2O$: 10 $Na_2B_4O_7{\cdot}10H_2O$: 10 KOH : 1	300 ± 25	A3.1-2024	$NaAlO_2$: 10 KOH : 1	270 ± 45
A3.1-2024	$NaAlO_2$: 10 KOH : 1	290 ± 55	PKAl-AC	$(Na_3P_3O_6)_3$: 20 $NaAlO_2$: 5 KOH : 1	135 ± 40
PKAl	$(Na_3P_3O_6)_3$: 20 $NaAlO_2$: 5 KOH : 1	150 ± 35	PKSi-AC	$Na_3PO_4{\cdot}12H_2O$: 5 Na_2SiO_3 (1.39 kg dm^{-3}): 10.5 KOH : 2.8	180 ± 50
- DC PEO treatment conditions: V (V): 400; I (A): 0.2; t (s): 100.			- AC PEO treatment conditions: $V_{+/-}$ (V): (+490/-110, 50% duty cycle); I (A): 0.2; f (Hz): 100; t (s): 100.		

First screening of the flash-PEO coatings (one per anodizing regime) was conducted considering both surface appearance and breakdown voltage. **Figure 4.15** depicts the surface appearance of developed coatings under DC and AC conditions.

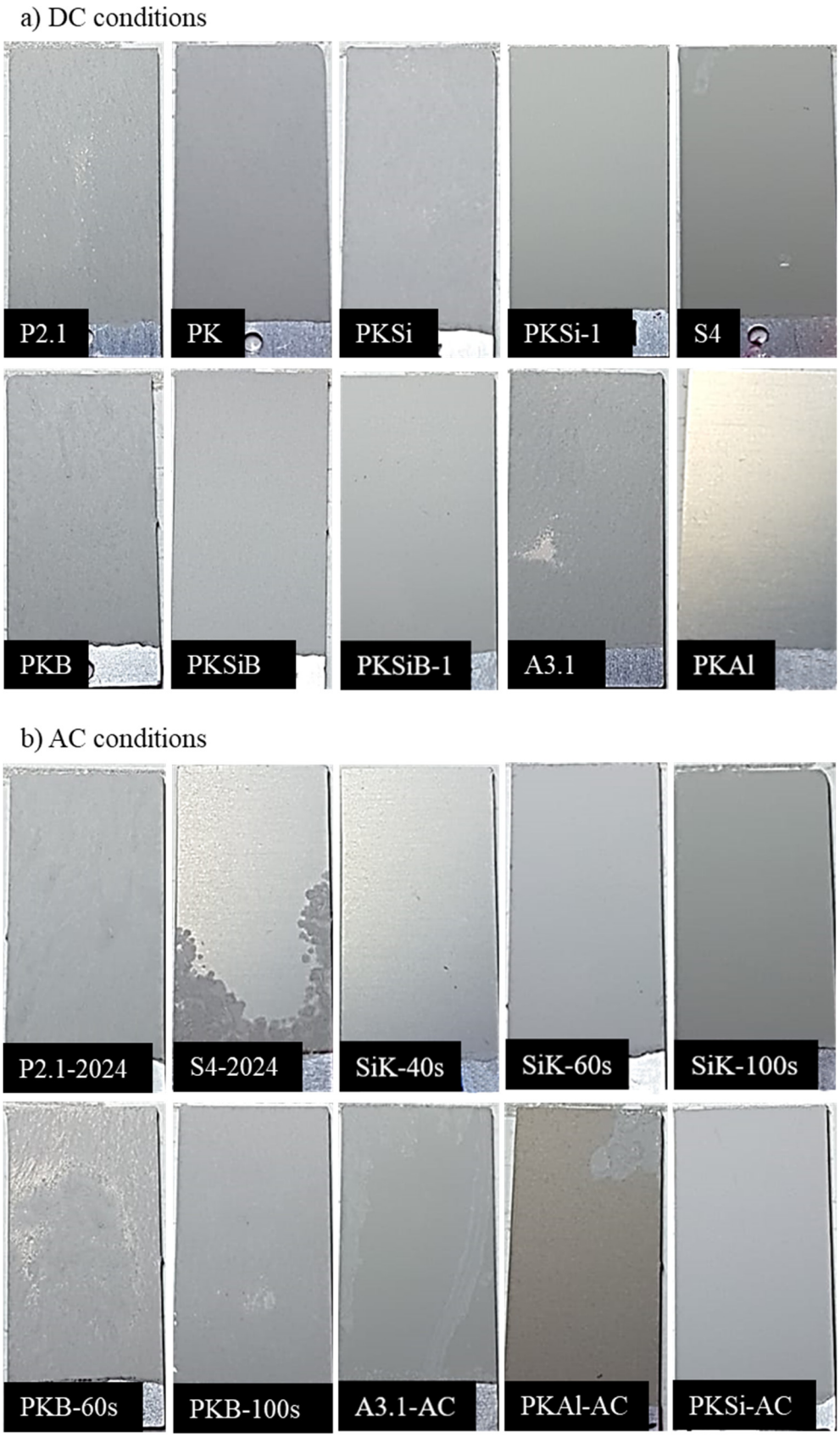

Figure 4.15. *Surface appearance of studied flash-PEO coatings under (a) DC conditions and (b) AC conditions on 2024 alloy.*

As it can be seen in **Figure 4.15a**, the majority of DC coatings showed a uniform surface appearance. By contrast, only SiK-based and PKSi-AC coatings showed an acceptable surface appearance for AC conditions (**Figure 4.15b**). PEO recipes that failed this screening stage displayed a non-homogeneous microdischarge regime and, consequently, a heterogeneous and burned surface. This effect was more noticeable in aluminate-based electrolytes, which is in agreement with the higher values for dielectric breakdown of aluminium in borate- [298, 299] and aluminate-containing [296, 300] solutions. The presence of sodium aluminate produces polymerization process and electrolyte instability over time, modifying the electrolyte ionic composition (aluminate complexes) [301, 302]. As a consequence, higher breakdown voltages, lower reproducibility and bad surface appearance was observed for coatings developed in aluminate-containing electrolytes (**Figure 4.15**).

On the other hand, flash PEO coatings developed in polyphosphate-, silicate- and polyphosphate/silicate-based electrolytes displayed better results in terms of surface appearance and sparking-regime (including the lowest breakdown voltages and uniformly distributed sparks). It is known that coating growth rate increases in the presence of silicate species [115, 303], promoting a homogeneous coating formation even for the lowest treatment times. Phosphates have been shown to promote the formation of α-Al_2O_3 and consequently, a slightly higher breakdown voltage was achieved for phosphate-containing coatings [115, 304].

The second screening stage was based on EIS testing. **Figure 4.16** gathers for the selected coatings the thickness and the impedance modulus at low frequency (10^{-2} Hz) after 1h of immersion time in 3.5 wt.% NaCl.

As can be seen in **Figure 4.16a**, with the exception of PKAl coating, all the flash-PEO coatings showed thicknesses around ~5 µm. Based on these results, the coating combining the highest and closely reproducible |Z| with the lowest thickness (~5 µm) was considered for further studies, i.e. PK coating.

It is worth noting that most of the studies concerned with *in situ* inhibitor incorporation use silicate-based electrolytes (**Table 1.16**). Therefore, there is a knowledge gap regarding the suitability of phosphates in this regard.

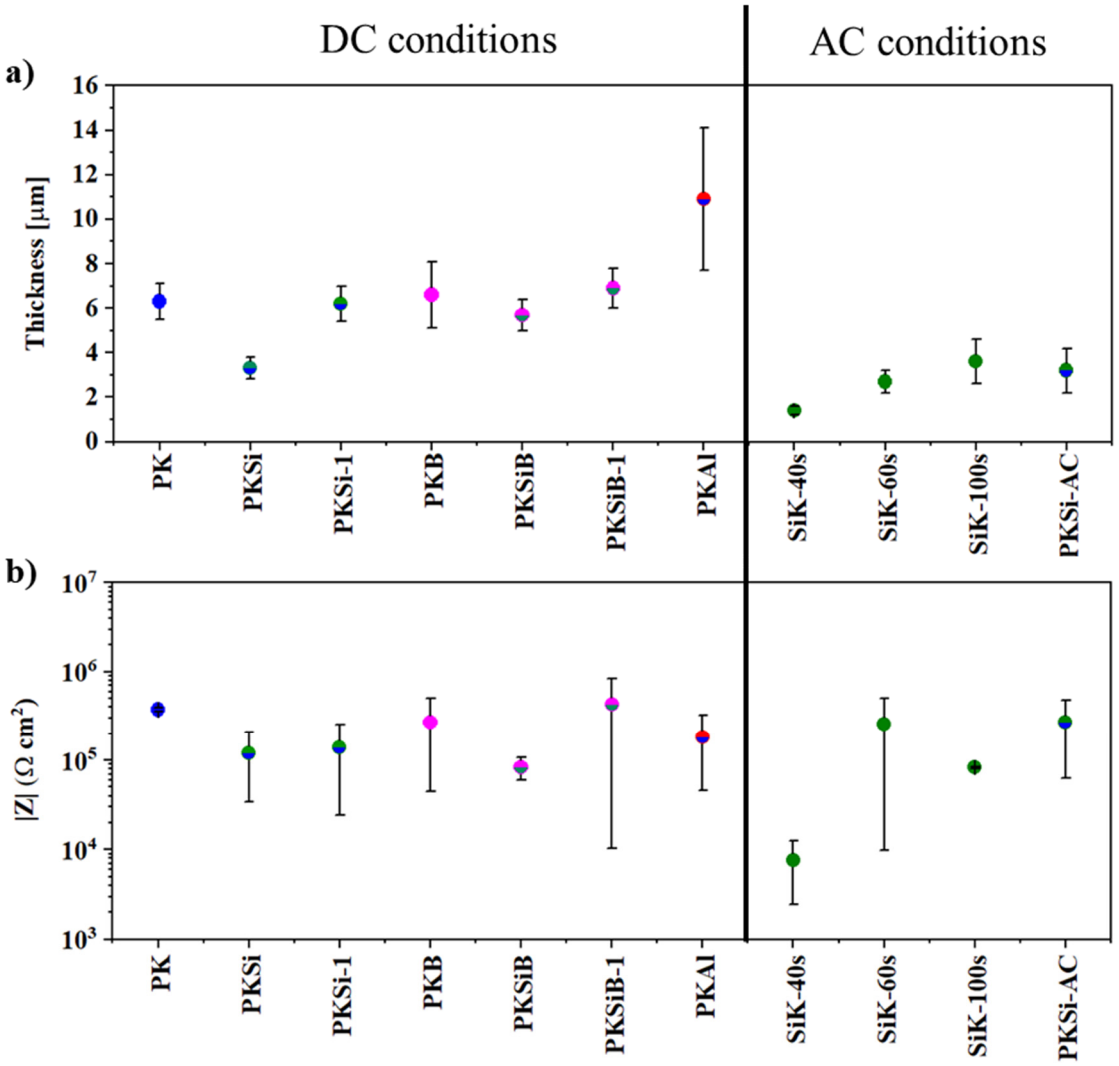

Figure 4.16. *Scatter diagram of (a) thickness and (b) impedance modulus at 10^{-2} Hz of the developed flash-PEO coatings on 2024 alloy. Colours: blue-phosphate (PK), green-silicate (SiK), red-aluminate (A) and pink-phosphate/borate. Mixed colours correspond to electrolytes mixtures.*

C2.2.1.3. Screening of inhibitors

Inhibitor-containing PEO coatings were obtained in 34 different combinations of electrolytes based on the PK electrolyte with and without the addition of EDTA (PKE) and 6 inhibitor species as summarised in **Table 4.6**.

Table 4.6. *Studied inhibitor concentrations in PK electrolyte.*

Base electrolyte	Inhibitors
PK (30 g L^{-1} $(Na_3P_3O_6)_3$ + 1 g L^{-1} KOH)	• $NaVO_3$: (0.5-3) mM • Na_2MoO_4 : (0.5-3) mM • $La_2(SO_4)_3$: (0.5-3) mM • Na_2SnO_3 : (0.5-3) mM • Na_2WO_4 : (0.5-12) mM • $Ce_2(SO_4)_3$: (0.5-3) mM

- DC PEO treatment conditions: V (V): 400; I (A): 0.2; t (s): 100.

- All corrosion inhibitors were incorporated with and without Na_2EDTA into the electrolyte. EDTA concentration was adjusted to a 1:1 molar ratio with respect to the active anion or cation of each compound.

Screening of the PEO coatings with inhibitors was conducted according to their thickness and modulus of impedance at low frequency (|Z| at 10^{-2} Hz) in 3.5 wt.% NaCl after 1 h of immersion. Surface appearances were similar to that of the PK base coating in all studied coatings (**Figure 4.15**). The best candidates (one cationic and one anionic inhibitor-containing coating) had to combine uniform surface appearance, the lowest possible thickness and the highest possible, closely reproducible modulus.

Inhibitor concentration for the first corrosion screening was 1.5 mM for the active anion or cation with and without EDTA. According to the corrosion resistance performance, 0.5 and 3 mM concentrations were also evaluated with or without EDTA (depending on the corrosion performance).

As it can be seen in **Figure 4.17a**, most inhibitor-containing coatings showed a slight increase in thickness (1-3 μm) with respect to the PK reference coating. This is in agreement with several studies reporting that inhibitors species in the electrolyte produce a coating growth rate increase with the formation of thicker oxide layers [125-127, 129, 183]. The addition of EDTA does not seem to play an important role in thickening of the oxide layer and small differences in the values can be ascribed to the alteration of the plasma discharges and the characteristic electrical field [305].

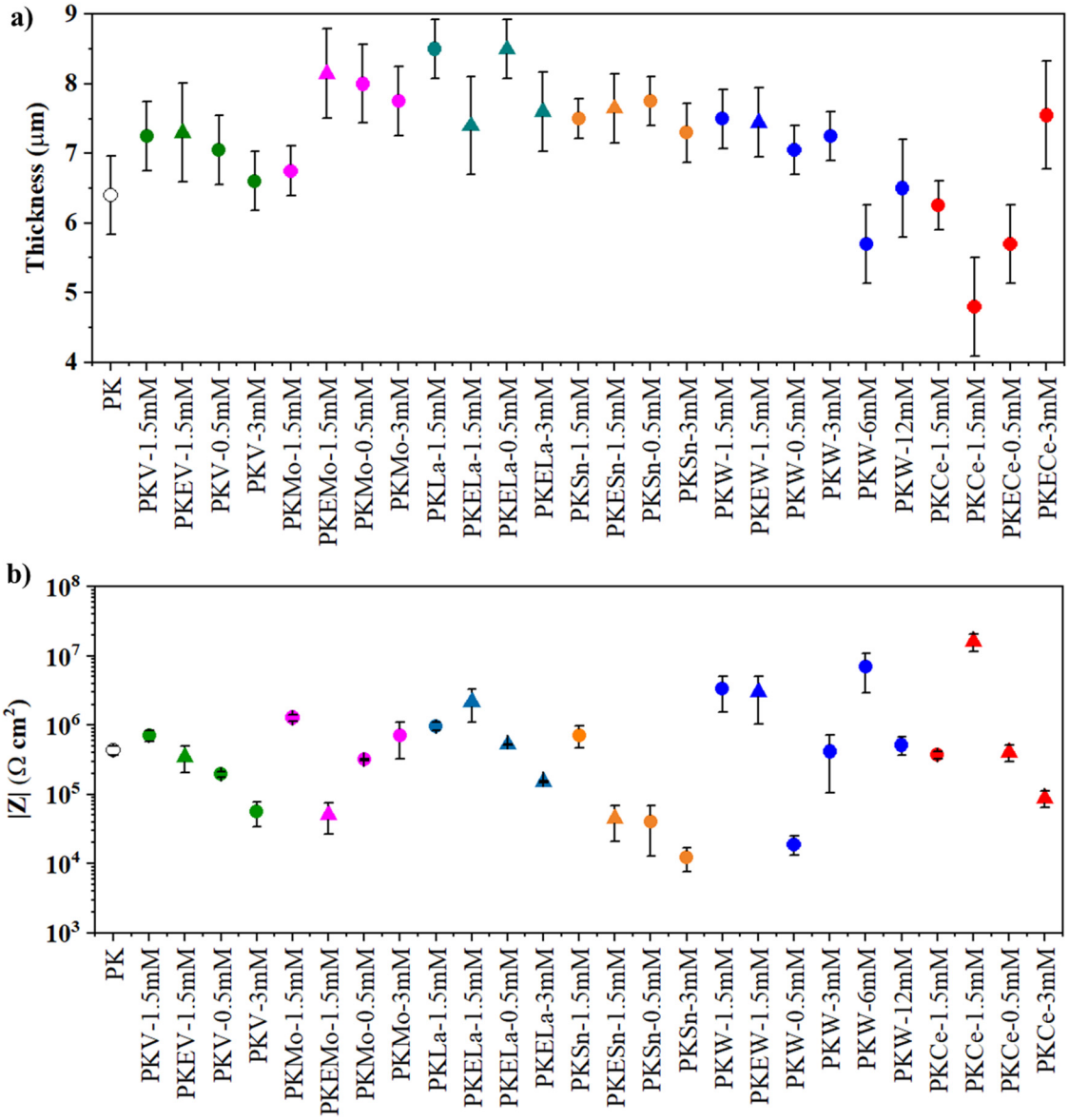

Figure 4.17. *Scatter diagram of (a) thickness and (b) impedance modulus at 10^{-2} Hz of the developed inhibitor-containing flash-PEO coatings on 2024 alloy. The empty symbol indicates the PK reference coating; filled circles indicate the addition of inhibitor and triangles are used for inhibitor-EDTA combinations. Colours: green- $NaVO_3$ (V), pink- Na_2MoO_4 (Mo), dark blue- $La_2(SO_4)_3$ (La), orange-stannate Na_2SnO_3 (Sn), blue- Na_2WO_4 (W) and red- $Ce_2(SO_4)_3$ (Ce).*

Different corrosion responses were obtained depending on the nature of the inhibitor and its combination with EDTA (**Figure 4.17b**). Additions of $NaVO_3$, Na_2MoO_4 and Na_2SnO_3 showed only a slight improvement, whereas their combination with EDTA led to significant deterioration compared with the reference coating. This may be due to the inability of anionic inhibitors to form stable complexes with EDTA in alkaline media and the resultant competition of free $EDTA^{4-}$ with oxyanions and polyphosphate in their

migration towards the anode, thereby diminishing the amount of passivating species entering the plasma micro-discharge and adsorbing onto the surface [306]. The only anion inhibitor that produced a clear improvement in corrosion resistance was Na_2WO_4. Again, in this case, the addition of EDTA was not beneficial.

The higher impedance of the PEO coating formed in the presence of WO_4^{2-} could be related to numerous factors, including coating compactness, stability of the oxides that may form during PEO (e.g. WO_3, $Al_2(WO_4)_3$), inhibitor concentration at the location of coating defects and inhibitor effects on the kinetics of anodic and cathodic reactions. WO_3 is less soluble in water and hence more protective than MoO_3 or V_2O_5 [307] (the presence of WO_3 has been reported in a previous study on PEO of an Al alloy [308]). The mixed oxide $Al_2(WO_4)_3$ could also be formed (no solubility data was found for it by the authors). In case of coating dissolution, WO_4^{2-} ions are likely to be released. These are known to behave as anodic inhibitors that adsorb on the surface at flawed areas [309]. MoO_4^{2-} ions are also efficient anodic inhibitors that adsorb on the surface, forming a barrier layer which impedes the adsorption of Cl^- ions [310].

These anions could arise from the dissolution of oxides such as MoO_3 or $Al_2(MoO_4)_3$. However, it seems that a relatively high critical concentration of MoO_4^{2-} ions are needed for efficient inhibition [311]. This could explain the lower impedance modulus found in this study for MoO_4^{2-} in comparison with WO_4^{2-}. VO_4^{3-} ions, which could originate from dissolution of V_2O_5 and $AlVO_4$, can be considered as mixed inhibitors, suppressing both anodic and cathodic reactions [312], although their efficiency is typically lower than that of WO_4^{2-} and MoO_4^{2-} ions [208]. The Al-Sn-O system does not form mixed oxides like $Al_2(WO_4)_3$, $AlVO_4$ or $Al_2(MoO_4)_3$. Therefore, Sn is likely to be incorporated in the PEO coating as SnO_2 only. This oxide is amphoteric and therefore fairly stable under neutral conditions, however it could serve as a source of inhibitor anions (SnO_3^{2-}) at cathodic regions where high pH may develop [313, 314].

$La_2(SO_4)_3$ and $Ce_2(SO_4)_3$ only revealed noticeable effects when combined with EDTA. This is related to EDTA forming stable negatively-charged complexes with La^{3+} and Ce^{3+}, thus enabling their easier incorporation into the coating [305, 315]. The presence of rare earths (RE) in oxide films formed on Al substrates is known to enhance their corrosion resistance [316]. The enhanced protection is typically related to the formation of RE-rich compounds and modification of coating morphology (i.e. reduced porosity) [128, 137, 317]. The higher impedance modulus provided by the addition of Ce(III) in comparison

with La(III) is most likely related to the oxidation of Ce(III) to Ce(IV) during PEO. Ce(IV) is typically superior to La(III) and Ce(III) in terms of corrosion protection because Ce(IV) forms more stable oxides and hydroxides in neutral environments. For instance, $Ce(OH)_4$ is insoluble at pH>3 whereas $Ce(OH)_3$ and $La(OH)_3$ are insoluble for pH values above 8 [222].

PKECe and PKW coatings were selected for further optimisation, varying the inhibitor species concentration between 0.5 and 12 mM. For PKECe the optimum concentration was 1.5 mM Ce^{3+}, whereas 6 mM WO_4^{2-} provided the best results for the PKW electrolyte (2×10^7 Ω cm^2 and ~5 µm for PKECe-1.5 mM and 10^7 Ω cm^2 and ~5 µm for PKW-6 mM). The PKECe-1.5 mM and PKW-6 mM coatings were further subjected to characterization, detailed corrosion performance study and paintability testing. The inhibitor-free PK coating was also analysed for comparison.

Figure 4.18 depicts the voltage-time responses under current-controlled mode for the optimized coatings. **Table 4.7** gathers the obtained values of thickness, specific energy consumption, breakdown voltage and electrolyte conductivity.

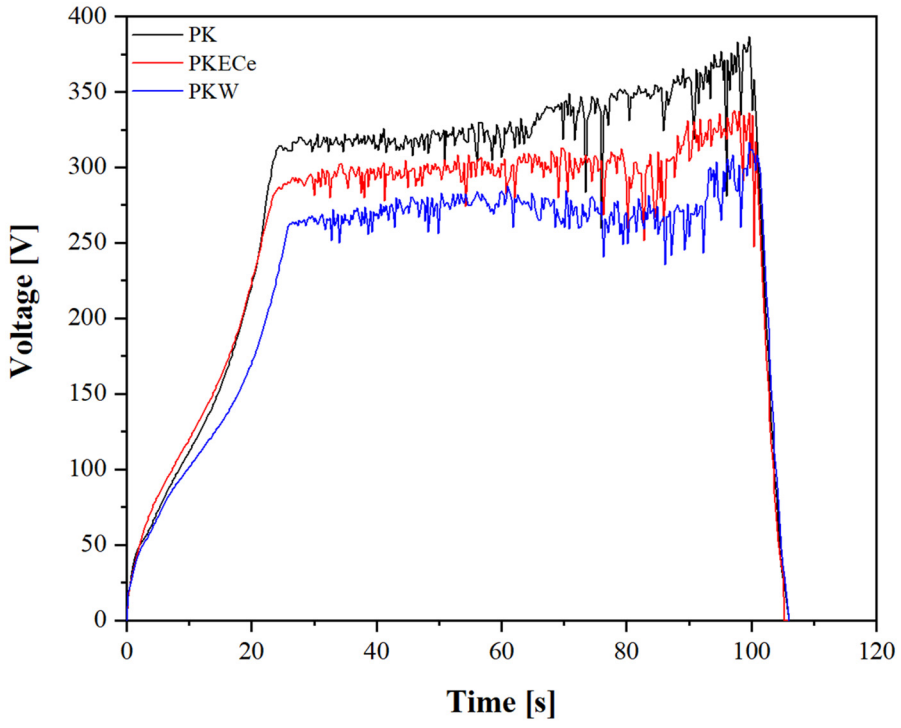

Figure 4.18. *Voltage-time responses during PEO treatment of 2024 alloy at 100 mA cm^{-2} in PK, PKW and PKECe electrolytes.*

Table 4.7. *Conductivity, breakdown voltage (U_{bd}), thicknesses and specific energy consumption values of selected flash-PEO coatings.*

Coating	σ (mS cm^{-1})	U_{bd} (V)	Thickness (µm)	Energy consumption (kW h m^{-2} µm^{-1})
PK	10.0 ±0.1	320±6	6.3±0.8	1.3±0.2
PKECe	10.3±0.1	280±8	4.8±0.3	1.2±0.1
PKW	10.7±0.1	260±4	5.7±0.6	1.1±0.1

Voltage-time trends were similar with and without inhibitor species with slight differences in the final voltage values. An initial voltage surge is observed as the barrier film develops on the surface. Sparking initiates at ~25 s. Then, voltage increased at a much lesser rate with visible oscillations as sparking progressed during the formation of the PEO coatings. The presence of inhibitors in the electrolyte decreases the voltage in comparison to the PK electrolyte, the decrease being more significant in the case of PKW (**Table 4.7**). This is in agreement with the conductivity values of the electrolyte.

The selected flash-PEO coatings show energy consumption values in the high range of those typically observed for conventional anodizing in acidic electrolytes (e.g. 0.1-1 kW h m^{-2} µm^{-1}), although the treatment time is much shorter (100 s for flash-PEO vs. ~900-3000 s for anodizing) [123, 318].

C2.2.1.4. Characterization of inhibitor-containing flash-PEO coatings

Figure 4.19 depicts the plan view and cross-sectional scanning electron micrographs of the selected coatings containing Ce and W species. PK coating is also included as a reference.

All the studied coatings reveal a porous morphology due to oxygen evolution and electrolyte vaporization at the location of micro-discharges [105, 273, 319]. Some of the pores correspond to the remnants of the discharge channels as seen in the cross-section in **Figure 4.19b**. PK and PKW coatings reveal similar pore population density, whereas PKECe showed the lowest value, suggesting a lower number or less mobile micro-discharges (**Table 4.8**).

In terms of average pore size and porosity (area fraction), the lowest values were found for the PKW coating. This is attributed to the higher inhibitor concentration (i.e. higher conductivity) promoting longer lasting micro-discharges and smoother flow of molten oxide over the surface [308, 320, 321]. It is interesting to note that PKECe shows a slightly greater pore size than the other two coatings. This may be due to the decomposition of Ce-EDTA complexes and the formation of CO_2 [315].

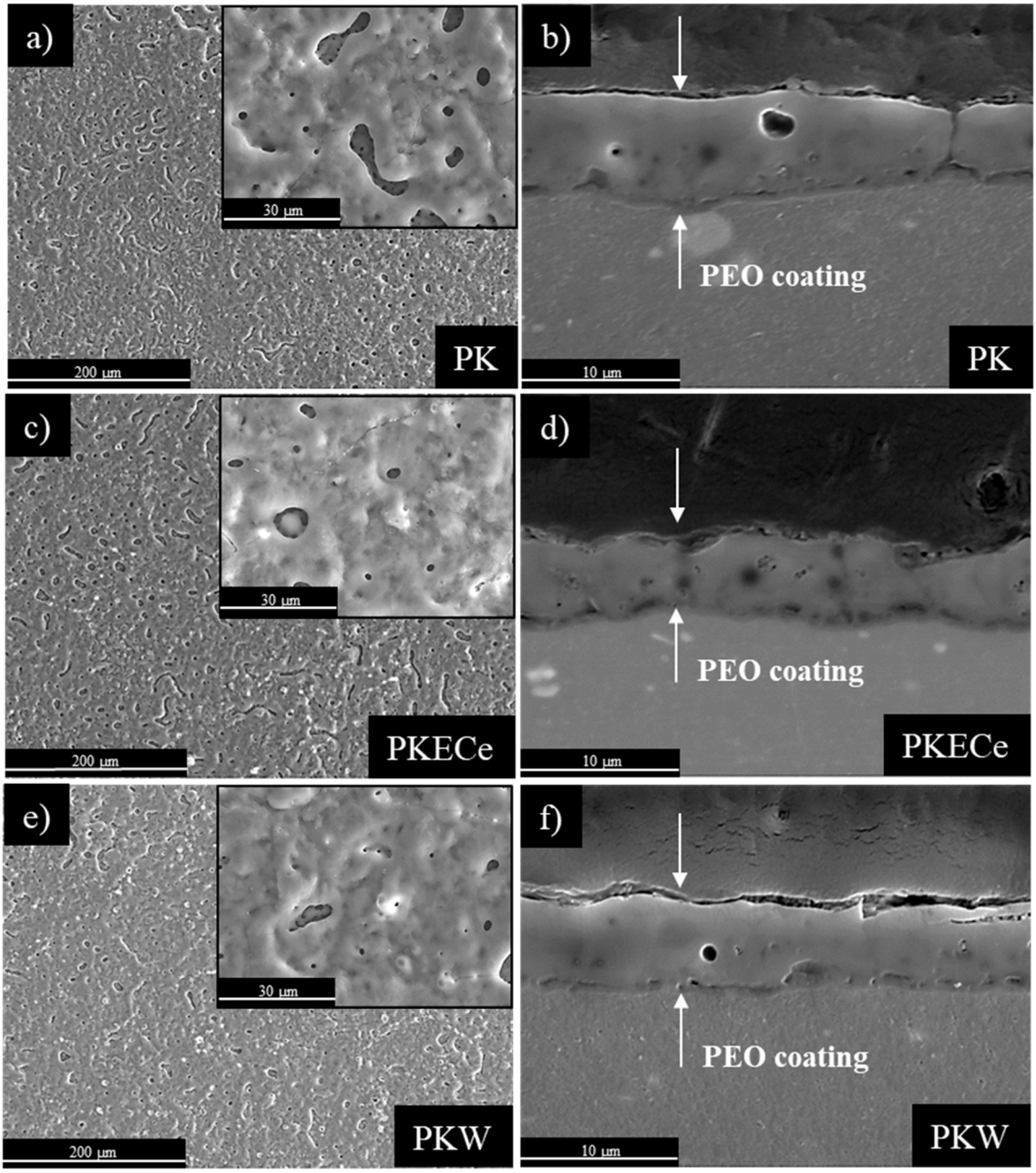

Figure 4.19. *Scanning electron micrographs corresponding to the (a,c,e) plan views and (b,d,f) cross-section views of PK, PKECe and PKW coatings on 2024 alloy.*

Table 4.8. *Surface characteristics of the studied coatings.*

PEO coating/characteristics	PK	PKECe	PKW
Population density of pores (10^3 pores mm^{-2})	15±2	12±1	15±2
Average pore area (μm^2)	3.4±0.2	3.8±0.3	2.8±0.3
Area fraction	5.0±0.7	4.8±0.4	4.1±0.5
Contact angle (º)	38±2.7	17±1.6	78±3.7

Contact angle measurements demonstrate the hydrophilic nature (i.e. < 90º) of all studied coatings mainly due to their inherent porosity. PK and PKECe coatings were significantly more hydrophilic compared with the PKW coating which could be explained by their greater pore size [322], being higher in the case of PKECe coating (**Table 4.8**). The incorporation of Ce into bulk Al_2O_3 is supposed to increase the hydrophobicity of the surface [323]. Therefore, the obtained results suggest that coating porosity overrules surface chemistry in relation to wettability.

Cross-sectional micrographs of the studied PEO coatings reveal similar thickness values for PK (~6.3 ± 0.8 μm) and PKW (~5.7 ± 0.6 μm) coatings and slightly lower for PKECe (~4.8 ± 0.3 μm) (**Figures 4.19b,d,f**). The latter could be explained by its lower pore population density, which could be due to lesser microdischarge mobility associated with the increased resistance of Ce-rich oxide material. However, there are other factors that may have an influence on the coating thickness such as (i) EDTA-enhanced Al solubility and (ii) the competition between the ingress of Ce-EDTA and polyphosphate complexes. The latter should account for a greater volume of newly formed material in the discharge channel.

For all studied coatings, a two-layered structure typical of DC pulse electrical regime was observed [133]: an outer layer with penetrating discharge channels and a compact inner barrier layer. This structure is therefore missing the intermediate layer decorated with microcracks and numerous submicrometric pores of thick PEO coatings produced under AC regimes [104, 105].

As shown in **Table 4.9**, the coatings are mainly composed of species derived from the polyphosphate-based electrolyte and the substrate (O, Na, Al and P), with negligible differences. Modified electrolytes yielded coatings with either incorporation of Ce or W species. W was uniformly distributed throughout the coating thickness, whereas Ce was mainly enriched in the outer region of the coating.

Table 4.9. *EDS analysis of the selected PEO coatings (at. %).*

PEO coating/Location		O	Na	Al	P	Cu	Ce	W
PK	Surface	62.2	0.3	26.1	11.4	0.1		
	Outer	60.6	0.1	23	16.1	0.2		
	Inner	55.8	-	37.6	6.5	0.1		
PKECe	Surface	63.2	0.3	26.1	9.9	0.2	0.3	
	Outer	41.6	0.7	41.4	15.7	0.2	0.4	
	Inner	52.1		36.2	11.3	0.3	0.1	
PKW	Surface	61.6	0.5	28.7	8.6	0.1		0.5
	Outer	61.5	0.5	28.8	8.6	0.1		0.5
	Inner	47.5	0.1	45.5	6.3	0.1		0.5

XRD analysis reveals the presence of $AlPO_4$ and γ-Al_2O_3 as the main constituents of all studied PEO coatings. This is typical for PEO coatings on Al alloys developed in phosphate electrolytes [128, 308, 324, 325] (**Figure 4.20**).

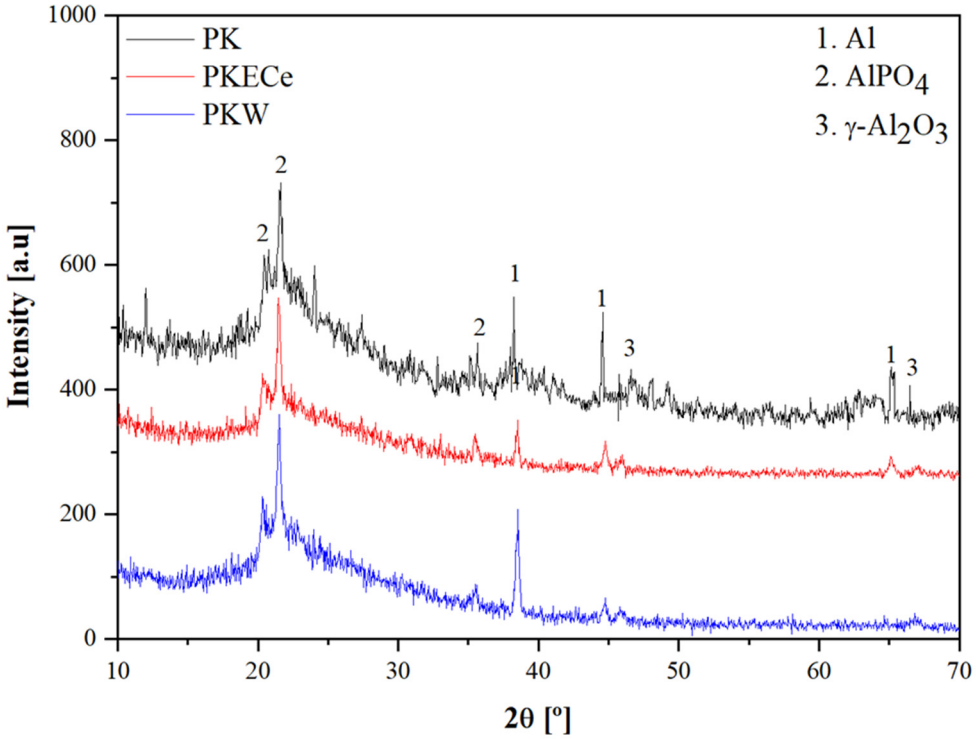

Figure 4.20. *XRD patterns of the selected PEO coatings on 2024 alloy.*

The presence of $AlPO_4$ arises from the decomposition of $P_6O_{18}^{6-}$ hexamer anions into PO_4^{3-} under plasma conditions [304]. In comparison with conventional PEO coatings, the oxide layers developed in the present work do not show α-Al_2O_3 (characteristic peak at 25.6°) [132, 133]. This is due to lower applied voltage and intensity of discharges

during the process [128, 272-274]. No crystalline Ce or W containing phases were identified, possibly due to their low amount. Peaks of Al, corresponding to the substrate, were also detected due to the low thickness of the coatings.

C2.2.1.5. Corrosion behaviour of inhibitor-containing flash-PEO coatings

Figure 4.21 depicts the Bode and Nyquist diagrams for PK, PKECe and PKW coatings after immersion in 3.5 wt.% NaCl solution for 1 h and 28 d.

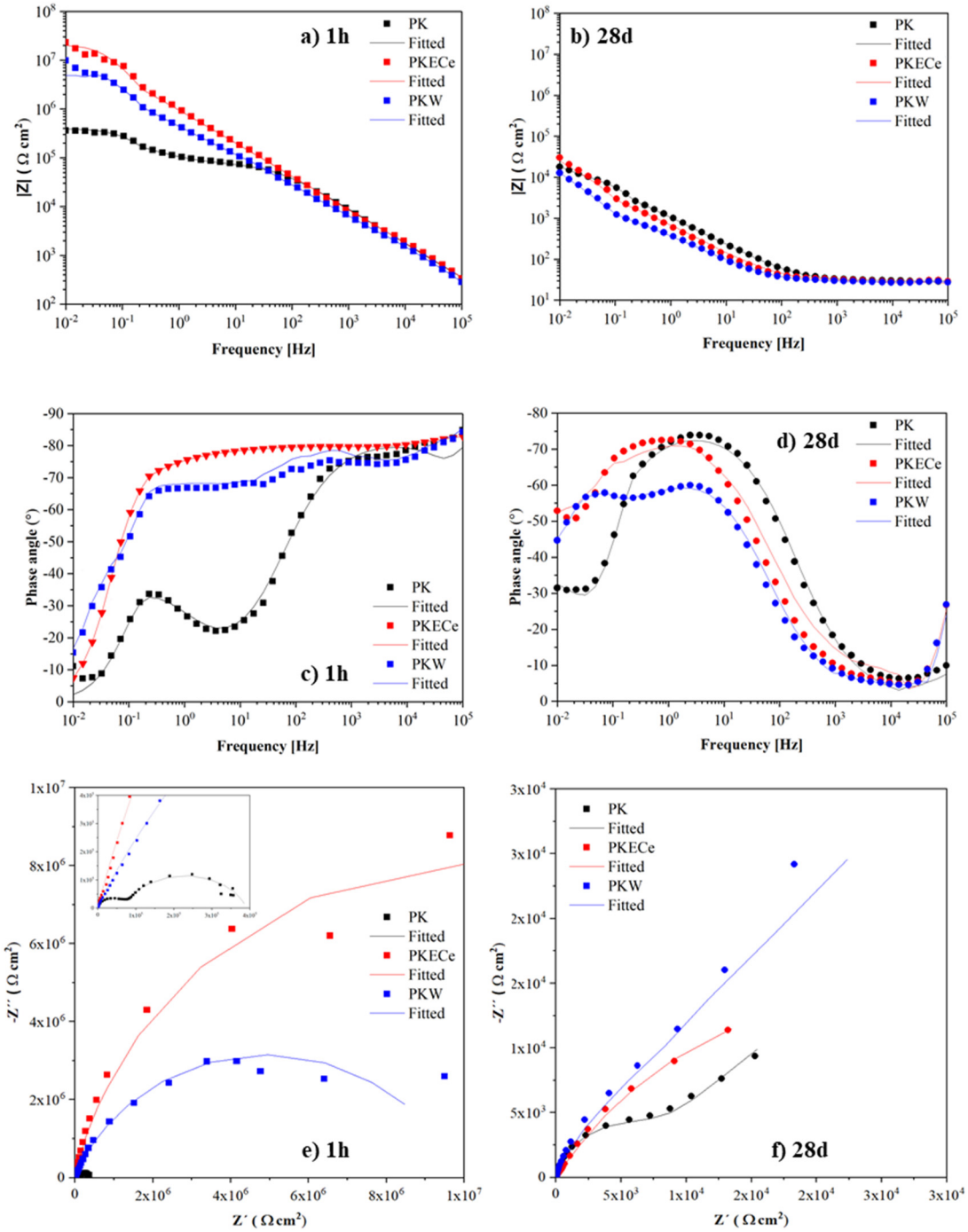

Figure 4.21. *(a-d) Bode (e,f) and Nyquist plots of the PK, PKECe and PKW coatings after 1 hour and 28 days of immersion time in 3.5 wt.% NaCl solution.*

For short immersion time, the two relaxation processes are related to the responses of the outer porous and inner barrier layers of the coatings at high and low frequencies, respectively. After 28 days of immersion, the time constant at high frequencies disappears almost completely due to the penetration of the electrolyte and degradation of the outer porous layer. The relaxation process observed at intermediate frequencies is related to the overall behaviour of the coating dominated by the inner barrier response, whereas the time constant at low frequencies is related to corrosion processes [324-326].

In the equivalent circuits used to interpret the EIS results (**Figure 4.22**) constant phase elements (CPE) were used instead of capacitances in order to account for the non-ideal behaviour of the system.

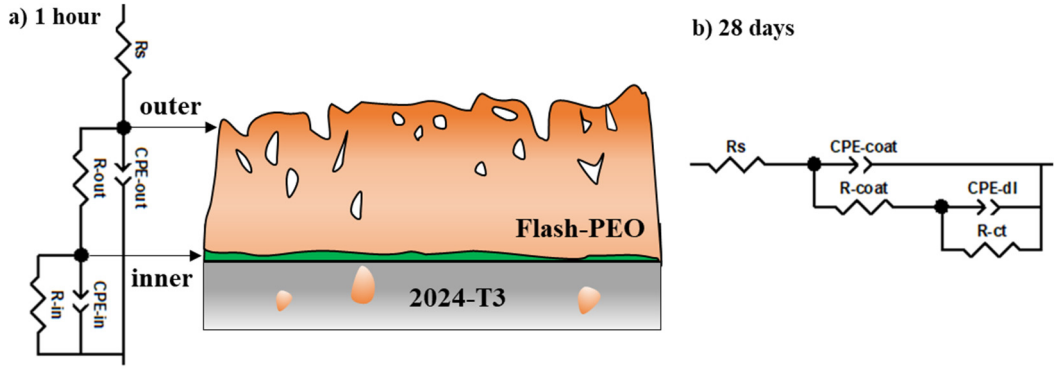

Figure 4.22. *Equivalent circuits used to fit the EIS data after (a) 1 hour and (b) 28 days of immersion in 3.5 wt.% NaCl solution.*

For short immersion time (1 h) the elements in the equivalent circuit (**Figure 4.22a**) include Rs (solution resistance), CPE-out/R-out (ascribed to the capacitive and resistive behaviour of the outer layer) and CPE-in/R-in (ascribed to the capacitive and resistive behaviour of the inner layer). After 28 d of immersion (**Figure 4.22b**), the outer and inner part of the PEO coating behave as a single layer giving an overall response of the coating (R-coat/CPE-coat) at intermediate frequencies. The time constant at low frequencies can be ascribed in this case to the corrosion activity at the metal surface defined by the charge transfer resistance (R-ct) and the capacitive behaviour of the double layer at the metal/electrolyte interface (CPE-dl). The electrical parameters obtained by fitting of the equivalent circuits are given in **Table 4.10** for 1 hour and **Table 4.11** for 28 days.

Table 4.10. *Equivalent circuit data for the PK, PKECe and PKW PEO coatings for 1h of immersion time in 3.5 wt.% NaCl solution.*

Coating	CPE-out, ($F\ s^{(n-1)} \cdot cm^{-2}$)	n_{out}	R-out, ($\Omega\ cm^2$)	CPE-in, ($F\ s^{(n-1)} \cdot cm^{-2}$)	n_{in}	R-in, ($\Omega\ cm^2$)
PK	$4.2 \cdot 10^{-8}$	0.92	$7.7 \cdot 10^{4}$	$1.5 \cdot 10^{-6}$	0.78	$1.2 \cdot 10^{5}$
PKECe	$1.2 \cdot 10^{-7}$	0.85	$4.4 \cdot 10^{5}$	$1.7 \cdot 10^{-6}$	0.89	$1.0 \cdot 10^{7}$
PKW	$2.2 \cdot 10^{-7}$	0.96	$1.3 \cdot 10^{5}$	$3.3 \cdot 10^{-6}$	0.80	$9.4 \cdot 10^{6}$

Table 4.11. *Equivalent circuit data for the PK, PKECe and PKW coatings for 28 days of immersion time in 3.5 wt.% NaCl solution.*

Coating	CPE-coat, ($F\ s^{(n-1)} \cdot cm^{-2}$)	n_{coat}	R-coat, ($\Omega\ cm^2$)	CPE-dl, ($F\ s^{(n-1)} \cdot cm^{-2}$)	n_{dl}	R-ct, ($\Omega\ cm^2$)
PK	$5.6 \cdot 10^{-5}$	0.87	$9.1 \cdot 10^{3}$	$5.3 \cdot 10^{-4}$	0.78	$1.8 \cdot 10^{4}$
PKECe	$8.3 \cdot 10^{-5}$	0.79	$1.1 \cdot 10^{4}$	$9.8 \cdot 10^{-5}$	0.76	$4.9 \cdot 10^{4}$
PKW	$1.7 \cdot 10^{-5}$	0.88	$1.3 \cdot 10^{4}$	$7.2 \cdot 10^{-5}$	0.81	$3.3 \cdot 10^{4}$

For short immersion time, a beneficial effect of the inhibitors is evident from the higher R-out and R-in values in comparison with the PK coating. This protective barrier effect was likewise confirmed by the near-capacitive behaviour of the inner layers of PKECe and PKW coatings (CPE-out, CPE-in), hampering the electrolyte penetration (**Table 4.10**) [319, 327]. In all cases, the overall coating resistance is mainly provided by the inner layer, although PKECe also shows a significant contribution from the outer layer (greater R-out). This is likely to be related to the less soluble Ce-rich compounds in the outer layer, which are known to provide short-term protection [128, 221, 317].

For longer immersion times all coatings show a decrease of the low-frequency impedance modulus, typical for non-sealed porous coatings, associated with the loss of the protective barrier properties and the start of the electrochemical activities at the substrate/coating interface. After 28 days of immersion, the beneficial effect of inhibitor incorporation into the coating is no longer observed (**Table 4.11**). This could be related to the accumulation of corrosive ions, including Cl^-, inside the pores and their gradual penetration towards the substrate [317, 319, 324].

C2.2.1.6. Paintability of inhibitor-containing flash-PEO coatings

Paint adhesion tests revealed the best performance for the PKECe coating followed by PKW and PK (**Figure 4.23**). All the coatings are hydrophilic and their pore size and area fraction porosity are at similar levels. Therefore, the observed differences in paint adhesion must be related to changes in surface chemistry following the *in situ* incorporation of inhibitors.

The literature data on paint adhesion to PEO coatings is scarce but, in general, good results are achieved due to the porous ceramic-like morphology of the surface [130, 328]. The present results show that inhibitor loading, in addition to improved corrosion performance, can also be used for tailoring wettability and paint adhesion of flash-PEO coatings.

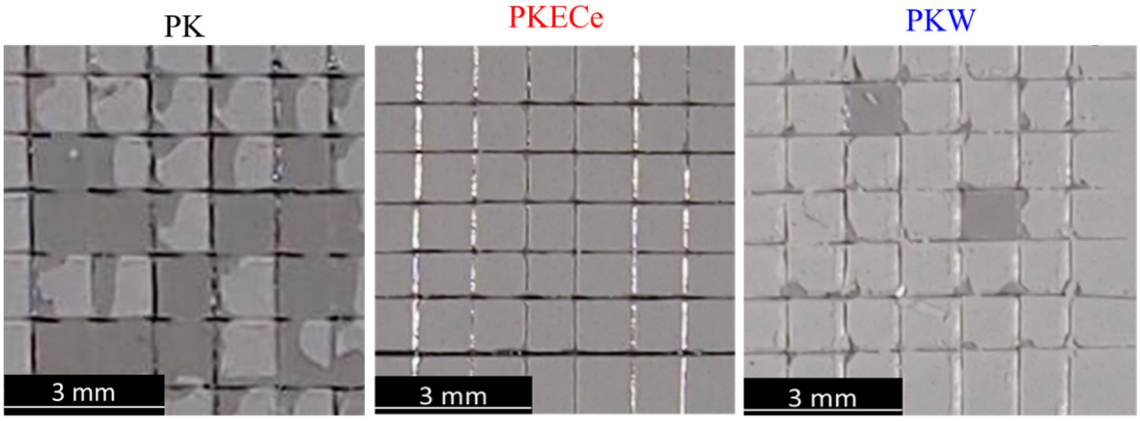

Figure 4.23. *Appearance of painted PEO surfaces after the adhesion test. PK-rating 4, PKECe-rating 0 and PKW-rating 2.*

C2.2.1.7. NSST of inhibitor-containing flash-PEO coatings

Square panels (40 x 40 mm) with PKECe and PKW painted coatings were evaluated in NSST up to 1000 h (**Figure 4.24**). PK coating was excluded from this batch due to its inferior corrosion resistance and paint adhesion.

None of the specimens revealed pitting or paint blistering. Although to the author's best knowledge, there are no other studies available in the literature concerning the paint adhesion and salt spray testing of flash-PEO coatings, these results are comparable with those reported for some sealed (e.g. with sol-gel or polymers) patented PEO coatings on aluminium alloys [329, 330] and painted anodic films utilized in the aerospace industry [50, 209].

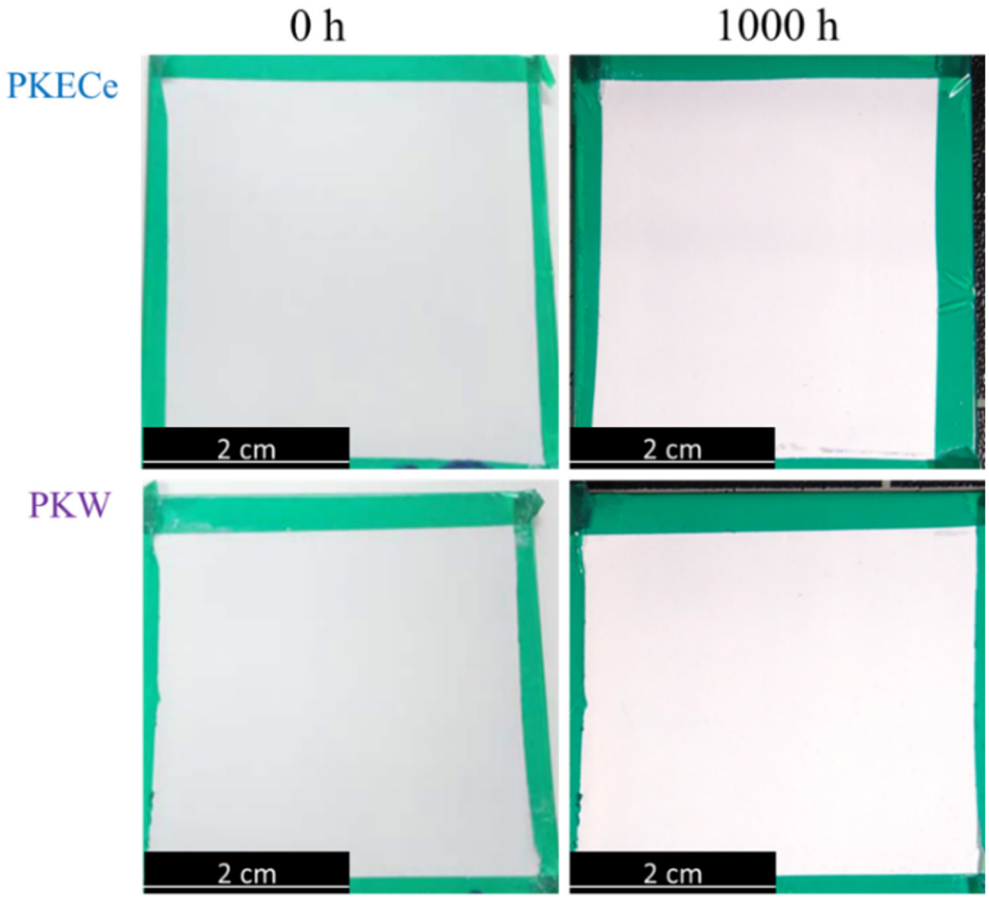

Figure 4.24. *Macrographs of PKECe and PKW painted coatings before and after 1000 h of NSST.*

C2.2.1.8. Concluding remarks on in situ incorporation of corrosion inhibitors on flash-PEO coatings on 2024 alloy

The main conclusions regarding the *in situ* incorporation of corrosion inhibitors on flash-PEO coatings can be summarized as follows:

- PKECe-1.5 mM and PKW-6.0 mM flash-PEO coatings with ~5 μm thickness and ~1–2 × 10^7 Ω cm^2 impedance modulus in 3.5% NaCl were selected after screening of several *in situ* added inhibitors including La, molybdate, vanadate and stannate.
- From a corrosion point of view, the addition of $EDTA^{4-}$ in the electrolytes has a positive effect only for cationic inhibitors.
- The energy consumption for the selected flash-PEO coatings is considerably lower compared to conventional PEO treatments on Al alloys and comparable to the high range values of conventional anodizing processes.
- Inhibitor species are incorporated in a small amount (< 0.5 at.%) preferentially in the outer part for Ce and homogeneously distributed in the case of W.
- The addition of Ce^{3+} and WO_4^{2-} into the coatings leads to an improvement in short-term corrosion behaviour.

- PKECe reveals the best results in terms of both paint adhesion and corrosion behaviour after 1000 h of exposure time in NSST.

Key performance characteristics of the PKECe and PKW coatings in comparison with CAA reference film are summarized in **Table 4.12.**

Table 4.12. *Comparison of PKECe and PKW key properties of PKECe and PKW coatings with CAA reference film.*

Coating	Thickness (µm)	|Z| (10^{-2} Hz) (Ω cm^2)-1 hour/28 days	Paintability rating
CAA	0.7 ± 0.1	$8.0 \times 10^6/3.0 \times 10^4$	0
PKECe	4.8 ± 0.3	$2.0 \times 10^7/3.0 \times 10^4$	0
PKW	5.7 ± 0.6	$1.0 \times 10^7/1.0 \times 10^4$	2

By way of comparison between both PEO coatings, PKECe shows better corrosion resistance, lower thickness and better paint adhesion. Besides, corrosion and paintability performance of PKECe coating is similar to those of the CAA reference film. The layer thickness of PKECe coating fulfills the CAA requirement (2-7 µm) although, a significant reduction in fatigue strength in comparison to the present CAA reference film may be expected.

Further research of fatigue behavior of flash-PEO coatings is needed in order to reveal their full potential for key fatigue-sensitive applications since in painted conditions, PKECe may be able to replace CAA for corrosion-sensitive applications.

C2.2.2. Sealing post-treatments of flash-PEO coated 2024 alloy

C2.2.2.1. Introduction

The porous morphology of PEO coatings offer an opportunity of sealing of the pores by different post-treatments, thus providing a better corrosion performance [267]. On that basis, in order to increase the functionality of flash PEO coatings, new sealing post-treatments are in constant research for non-painted components in the aircraft industry. Among the different sealing strategies stated in **Section 1.3.3.3**, the formation of hydrophobic coatings has been pointed due to its easy operation and higher potential for corrosion protection. Another sealing alternative, already explored in **Section 2.1** is the formation of an LDH coating and the research of novel eco-friendly corrosion inhibitors for loading into an LDH scaffold.

In this section, two sealing strategies for a flash-PEO coating are explored as an alternative to Cr-based sealing for non-painted components on the 2024 alloy: (i) hydrophobic sealing post-treatment with lauric acid; and (ii) LDH post-treatment with inhibitor loading. Both sealing strategies were performed over the PKSi-AC (from now on PKSi) coating selected from the previous section since it was identified as the most suitable for LDH post-treatment in terms of corrosion protection and thickness.

C2.2.2.2. Hydrophobic sealing

Lauric acid is a relatively cheap acid and allows the formation of a hydrophobic layer on the surface of anodic alumina film. Lauric acid-based sealing of PKSi coating surface was investigated in four different lauric acid-based solutions (**Table 2.8**). The lauric acid concentration and treatment times were established considering previous studies based on long-chain carbon fatty acids [138, 331-334].

Screening of the operating conditions was conducted according to their modulus of impedance at low frequency (|Z| at 10^{-2} Hz) in 3.5 wt% NaCl after 1 h of immersion (**Figure 4.25**). The best condition had to combine uniform surface appearance and the highest possible modulus.

In all cases, after lauric acid sealing, the surface appearance and the coating thickness were the same as those of the stand-alone PKSi coating (**Figures 4.15**, **4.16b**). However, different corrosion responses were obtained depending on the lauric acid concentration and treatment time (**Figure 4.25**).

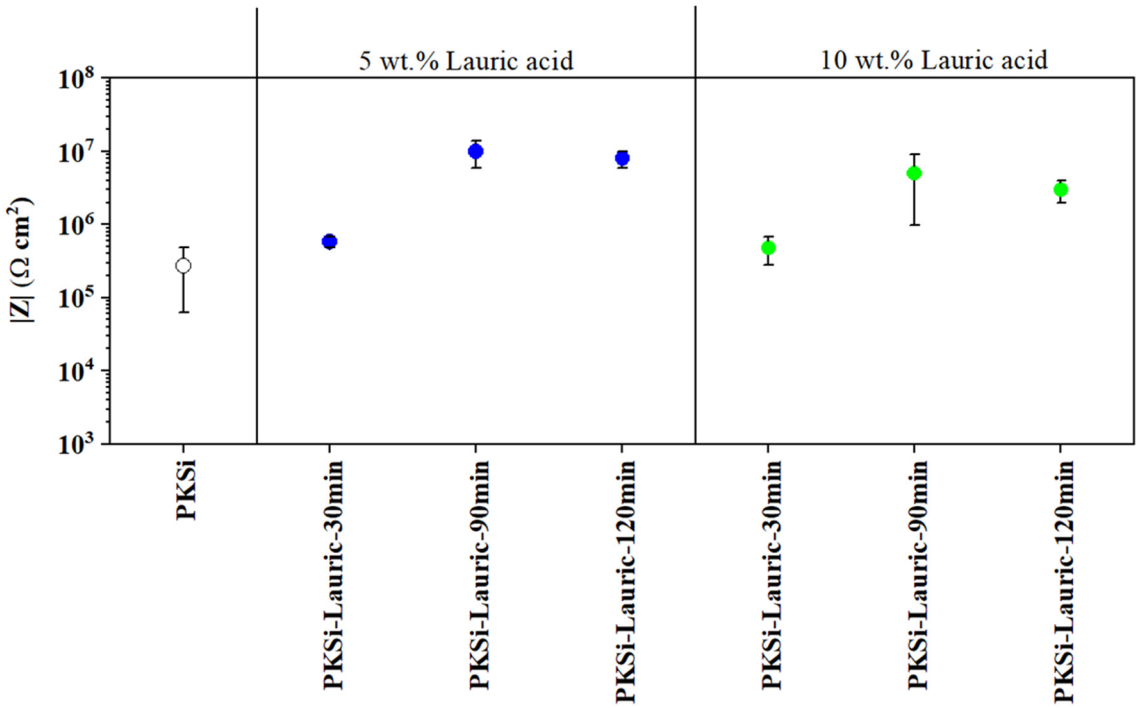

Figure 4.25. *Scatter diagram of impedance modulus at 10^{-2} Hz of the lauric acid-based sealing operating conditions on PKSi coating. The empty symbol indicates the PKSi-AC reference coating; filled circles indicate the lauric acid sealing combinations. Colours: blue-5 wt.% of lauric acid and green-10 wt.% of lauric acid.*

Additions of lauric acid at both concentrations showed only a slight improvement for 30 min treatment, whereas longer treatment times led to a significant improvement compared with the PKSi reference coating. It may be due to the ability of anionic laureate to form stable complexes with PKSi coating surface at long treatment times, thereby increasing the amount of laureate-based species adsorbed onto the PKSi coating surface [333, 334]. The best and most reproducible corrosion performance was obtained by PKSi coating immersion in a 5 wt.% lauric acid in an ethanol-based solution for 90 minutes (at 25ºC). PKSi and Lauric-treated PKSi (from now on, PKSi-Lauric) coatings were selected for further detailed characterization and corrosion performance studies.

C2.2.2.3. Characterization of hydrophobic flash-PEO coatings

XRD analysis reveals the presence of SiO_2 and γ-Al_2O_3 as the main constituents of PKSi coating. This is typical for PEO coatings on Al alloys developed in silicate-phosphate electrolytes (**Figure 4.26**) [131, 294, 335]. The formation of SiO_2 arises from the decomposition of SiO_3^{2-} anions of the electrolyte under plasma discharge conditions during the PEO process; SiO_2 is typically located in the outer region of the coating [336, 337].

Another constituent of the PKSi coating is γ-Al_2O_3. This is consistent with previous studies and it is typically associated with relatively low voltages and, thereby, less intense discharges during the process [267, 338, 339]. Peaks of Al, corresponding to the substrate, were also detected due to the low thickness of the coating.

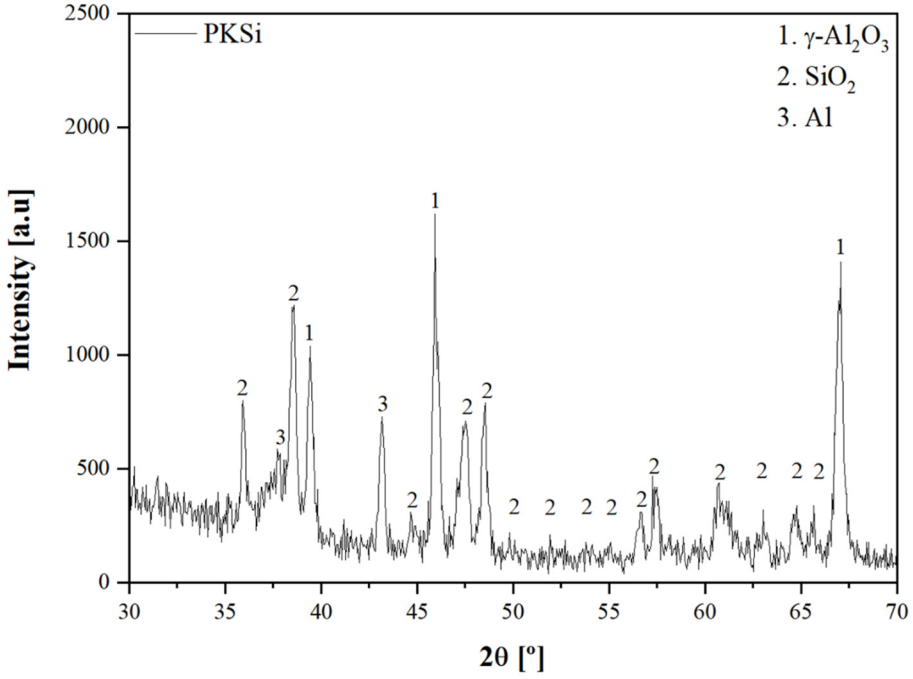

Figure 4.26. *XRD patterns of selected PKSi coating on 2024 alloy.*

Figure 4.27 depicts the plan view and cross-sectional scanning electron micrographs of the PKSi and PKSi-Lauric coatings. Due to a very short process duration and, therefore, small size and short life-time of the discharges, PKSi coating (**Figures 4.27a,b**) revealed a low-porous structure. The apparent surface porosity is ~3 % and the average pore size is about 2 μm. It can be related to the electrolyte composition since according to previous studies, a higher concentration of phosphate anions in the electrolyte promotes the formation of larger pores, whereas silicate anions favours the formation of less-porous PEO surfaces [131, 294, 335]. For this reason, the combination of silicate with phosphate anions resulted in the formation of a compact and low-porous PKSi coating.

Interestingly, the surface microstructure of PKSi-Lauric coating (**Figures 4.27c,d**) is quite similar to that of PKSi coating, i.e. the micropores formed during the PEO process did not appear sealed by lauric acid treatment.

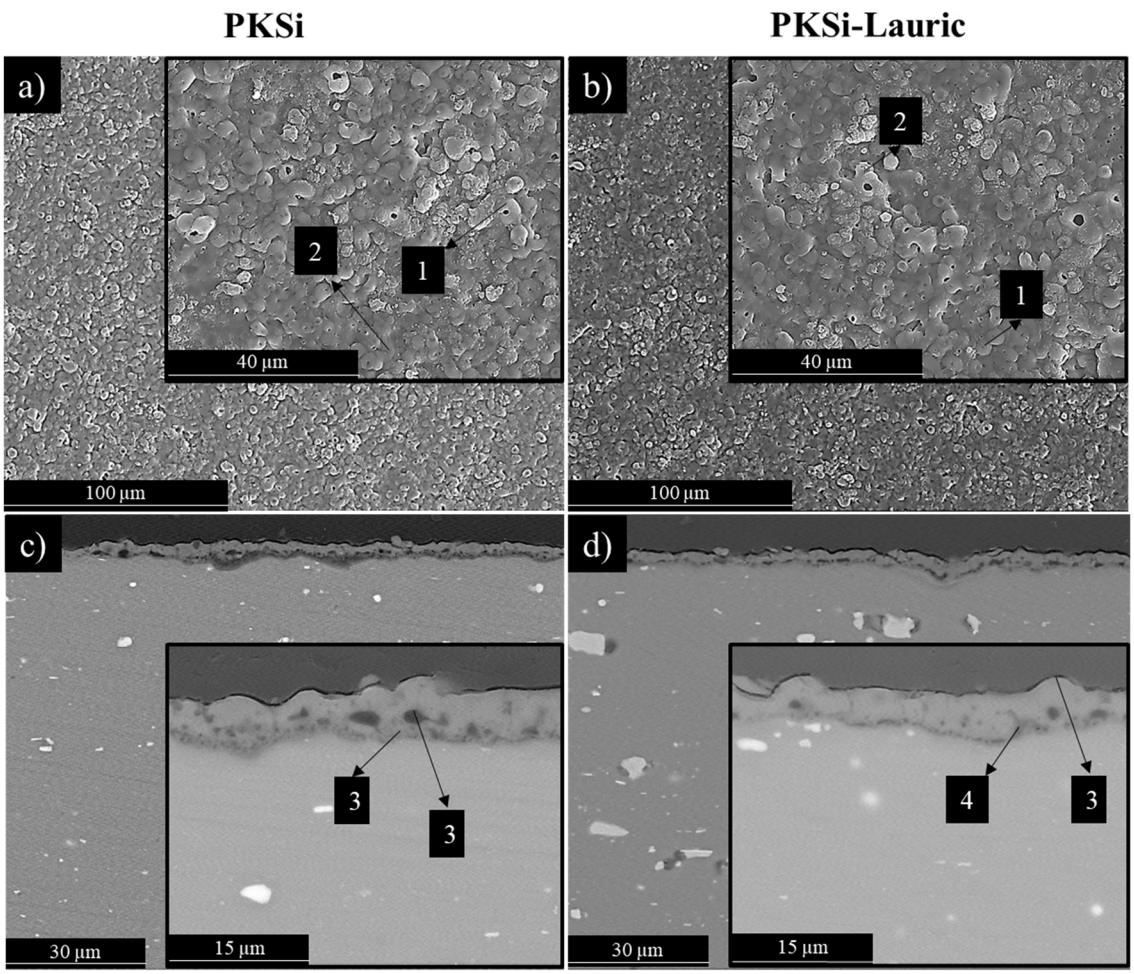

Figure 4.27. *Scanning electron micrographs corresponding to the (a-d) plan views and (e,f) cross-section views of PKSi and PKSi-Lauric coatings on 2024 alloy.*

Table 4.13 shows the effect of lauric acid-based post-treatment on the coating thickness, roughness and contact angle value of PKSi and PKSi-Lauric coatings.

Table 4.13. *Surface characteristics of the studied PKSi and PKSi-Lauric coatings.*

PEO coating/characteristics	PKSi	PKSi-Lauric
Thickness (µm)	3.2±1.0	3.4±1.1
Roughness (R_a/R_z)	0.2/0.9	0.2/0.9
Contact angle (°)	31±1	122±5

Evidently, lauric acid post-treatment did not significantly affect the roughness and thickness of the PKSi coating. The low contact angle value of non-treated PKSi coating demonstrates its hydrophilic nature. Considering the low surface porosity of PKSi coating, the later feature was related to the PKSi surface composition since the high presence of γ-Al_2O_3 and SiO_2 are known to behave as hydrophilic surfaces [340, 341].

Nevertheless, the hydrophilic properties of the PKSi coating were significantly decreased after the application of lauric acid post-treatment, thereby indicating its adsorption and interaction with the oxide material [334].

Cross-sectional micrographs of the PKSi coating revealed a two-layered structure (**Figures 4.27e,f**): a relatively dense outer layer with microcracks and pores, constituting most of the coating thickness and pore band in the inner region of the coating. Typically, a thin (<500 nm) barrier layer adjacent to the coating/substrate interface is present in the PEO coatings, however it was not resolved at the chosen magnifications. The pore band may be caused by the evolution of gas bubbles (mainly O_2 and H_2) entrapped during the rapid solidification of molten material in the discharge channels [109, 188].

As shown in **Table 4.14**, the coatings are mainly composed of species derived from the phosphate/silicate-based electrolyte and the substrate (O, Al, Si and P), with minor differences.

Table 4.14. *EDS analysis of the PKSi and PKSi-Lauric coatings (at. %).*

PEO coating	location	O	Al	Si	P	C
PKSi	1	46.6	23.1	1.4	0.1	28.8
	2	42.1	24.4	1.4	-	32.1
	3	37.0	33.7	0.9	-	28.4
	4	39.9	29.1	0.8	0.9	29.3
PKSi-Lauric	1	31.0	21.6	0.9		46.5
	2	30.0	21.1	2.4		46.5
	3	23.1	10.8	0.7	0.1	65.3
	4	29.4	14.5	1.1		55.0

According to EDS results, the PKSi-Lauric surface yielded both uniform incorporation and distribution of C species. According to previous studies [331, 342, 343], long-chain carboxylic acids can be chemisorbed onto the surface of γ- Al_2O_3 forming a hydrophobic hydrocarbon chain on the PKSi coating surface.

C2.2.2.4. Corrosion behaviour of hydrophobic flash-PEO coatings

Figure 4.28 depicts the Bode and Nyquist diagrams for PKSi and PKSi-Lauric coatings after immersion in 3.5 wt.% NaCl solution for 1 hour and 28 days.

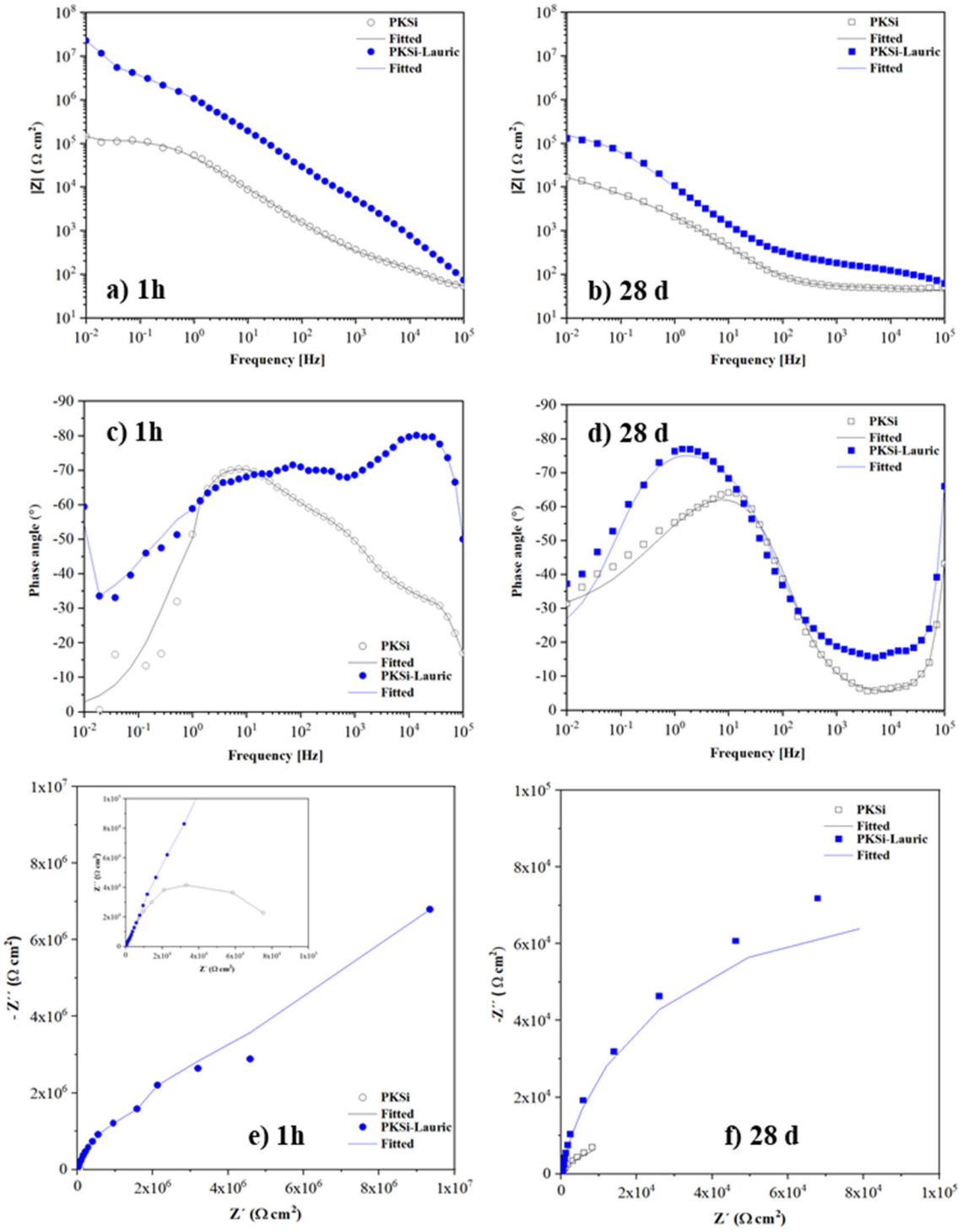

Figure 4.28. *Bode (a-d) and Nyquist (e,f) plots of the PKSi and PKSi-Lauric coatings after 1 hour and 28 days of immersion time in 3.5 wt.% NaCl solution.*

After 1 hour of immersion, the impedance value of the PKSi-Lauric coating is approximately two orders of magnitude higher than that of PKSi in the whole frequency range (**Figure 4.28a**), confirming the beneficial effect of lauric acid post-treatment on corrosion resistance.

Figure 4.28c shows the Bode phase angle plots for PKSi and PKSi-Lauric coatings for 1 hour. The higher frequency angles describe the external layer properties of PKSi and PKSi-Lauric coatings. The higher phase angle values (~75º) of PKSi-lauric coating in medium and high-frequency range after 1 hour of immersion confirms highly capacitive behaviour (typical for organic coating layers) and the difficulties of the corrosive media to penetrate the lauric-based hydrophobic layer [331, 344]. Accordingly, the reduced semicircle diameter in the Nyquist plot also confirmed the lower corrosion resistance of PKSi coating in comparison to PKSi-Lauric (**Figure 4.28e**).

After 28 days of immersion, the Bode impedance plots (**Figure 4.28b**) demonstrated the improved long-term corrosion resistance of the PKSi coating after hydrophobic modification by lauric acid treatment.

In both coatings, the time constant at high frequencies (~10^4 Hz) disappears almost completely due to the penetration of Cl^- anions throughout the external coating structure. Nevertheless, the semicircle diameter in the Nyquist diagram (**Figures 4.28f**) was still larger for PKSi-Lauric coating than PKSi coatings, denoting the constantly lower permeability of PKSi-Lauric coating at longer immersion times.

Figure 4.29 depicts the equivalent circuits used to interpret the EIS results for PKSi and PKSi-Lauric coatings. Note that laureate anions (green) are bonded with the PEO substrate. The PKSi equivalent circuit includes R_s (solution resistance), CPE_{-out}/R_{-out} (ascribed to the capacitive and resistive behaviour of the outer layer) and CPE_{-in}/R_{-in} (ascribed to the capacitive and resistive behaviour of the inner layer) (**Figure 4.29a**). For PKSi-Lauric coating (**Figure 4.29b**), the equivalent circuit is quite similar to PKSi coating except for CPE_{-h}/R_{-h} elements that are ascribed to the superficial hydrophobic modification [138].

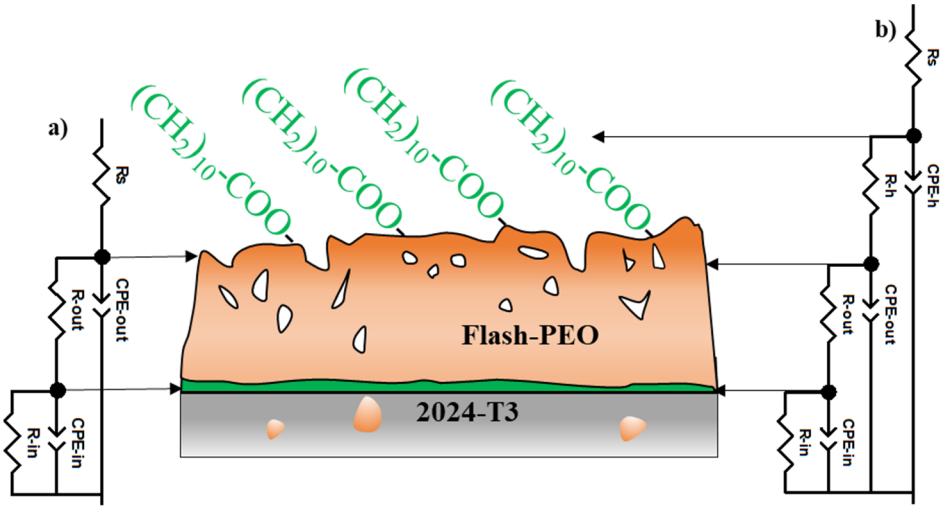

Figure 4.29. *Equivalent circuits used to fit the EIS data for (a) PKSi and (b) PKSi-Lauric coatings after 1h and 28 days of immersion in 3.5 wt.% NaCl solution.*

The electrical parameters obtained by fitting of the equivalent circuits are given in **Table 4.15** for 1 hour and **Table 4.16** for 28 days.

Table 4.15. *Equivalent circuit data for the PKSi and PKSi-Lauric coatings for 1 hour of immersion time in 3.5 wt.% NaCl solution.*

Coating	CPE-h ($F\ s^{(n-1)}\cdot cm^{-2}$)	n_h	R-h ($\Omega\ cm^2$)	CPE-out ($F\ s^{(n-1)}\cdot cm^{-2}$)	n_{out}	R-out ($\Omega\ cm^2$)	CPE-in ($F\ s^{(n-1)}\cdot cm^{-2}$)	n_{in}	Rb ($\Omega\ cm^2$)
PKSi				$1.1\cdot10^{-5}$	0.88	270	$2.8\cdot10^{-5}$	0.88	$1.3\cdot10^{5}$
PKSi-lauric	$1.8\cdot10^{-6}$	0.94	$1.8\cdot10^{3}$	$3.3\cdot10^{-7}$	0.93	$4.1\cdot10^{6}$	$2.5\cdot10^{-7}$	0.92	$2.4\cdot10^{7}$

Table 4.16. *Equivalent circuit data for the PKSi and PKSi-Lauric coatings for 28 days of immersion time in 3.5 wt.% NaCl solution.*

Coating	CPE-h ($F\ s^{(n-1)}\cdot cm^{-2}$)	n_h	R-h ($\Omega\ cm^2$)	CPE-out ($F\ s^{(n-1)}\cdot cm^{-2}$)	n_{out}	R-out ($\Omega\ cm^2$)	CPE-in ($F\ s^{(n-1)}\cdot cm^{-2}$)	n_{in}	Rb ($\Omega\ cm^2$)
PKSi				$1.2\cdot10^{-4}$	0.87	53	$6.4\cdot10^{-4}$	0.88	$1.5\cdot10^{4}$
PKSi-lauric	$2.6\cdot10^{-5}$	0.82	$3.5\cdot10^{2}$	$1.5\cdot10^{-6}$	0.82	$1.1\cdot10^{3}$	$8.5\cdot10^{-6}$	0.82	$1.4\cdot10^{5}$

For short and long immersion time, a beneficial effect of the lauric acid post-treatment in PKSi-Lauric coating is evident from the higher R_{-h}, R_{-out} and R_{-in} values in comparison with the PKSi coating. This protective barrier effect was likewise confirmed by the near-capacitive behaviour of the external and inner layers of PKSi-Lauric coating (CPE-h,

CPE_{-out}, CPE_{-in}), hampering the electrolyte penetration (**Tables 4.15, 4.16**). It is likely to be related to the organic matter presence on the PKSi-Lauric surface since the contact area between the immersed surface and water decreases. By this approach, the probability of the Cl^- species absorbed or retained in the PKSi-Lauric surface is decreased [138, 334, 344].

It is particularly evident for longer immersion times since PKSi coating shows a decrease of the R_{-out} and R_{-in} values which are typical for non-sealed PEO coatings (**Table 4.16)** [137, 267]. However, for PKSi-Lauric coating, the presence of organic matter on the PKSi surface decreased the ion transfer (CPE_{-h}, CPE_{-out}, CPE_{-in}) (**Table 4.16**) from the electrolyte solution to the sample surface and as a result, electrolyte ions can hardly pass the coating layer, i.e. mass transfer of aggressive species towards the substrate is limited [333, 345]. These results are in concordance with the higher values of contact angles obtained for PKSi-Lauric coating, confirming reduced permeability of the coatings by corrosive media.

C2.2.2.5. Concluding remarks on flash-PEO/hydrophobic system on 2024 alloy

Key performance characteristics of the PKSi coating in comparison with CAA reference film are summarized in **Table 4.17**.

Table 4.17. *Comparison of PKSi key properties with CAA reference film.*

Coating	Thickness (µm)	|Z| (10^{-2} Hz) (Ω cm^2)-1 hour/28 days
CAA	0.7 ± 0.1	$8.0 \cdot 10^6/3.0 \cdot 10^4$
PKSi	3.2 ± 1.0	$2.0 \cdot 10^5/2.0 \cdot 10^4$
PKSi-Lauric	3.4 ± 1.1	$1.0 \cdot 10^7/1.0 \cdot 10^5$

By way of comparison between both coatings, PKSi shows worse short-term corrosion resistance and higher thickness. However, long-term corrosion performance of PKSi coating is similar to that of the CAA reference film. The layer thickness of PKSi coating fulfils the CAA requirement (2-7 µm), although a slight reduction in fatigue strength in comparison to the present CAA reference film may be expected.

Regarding the effect of hydrophobic surface modification, lauric acid post-treatment was successfully developed for PKSi coating. Therefore, the first step of the hydrophobic corrosion protection system for non-painted components can be considered successful. Further research would consist of studies of fatigue behaviour of flash-PEO coatings and

up-scaling process in order to reveal their full potential for key fatigue-sensitive applications. As for the corrosion-sensitive applications, PKSi-Lauric may be able to replace CAA for use in non-painted conditions.

C2.2.3. LDH sealing on 2024 alloy

Among all flash-PEO coatings evaluated in **Section 2.2.1.2**, PKSi-AC is a promising candidate for LDH post-treatment as it is relatively thin (~3 µm) and shows a high corrosion resistance.

LDH sealings have been developed for the PKSi-AC coating surface (**Table 4.18**) using selected LDH recipes that were investigated in **Section 2.1.4** (LDH 3) (**Table 4.4**) and **3.1.2** (Ca-Al-LDH) (**Table 5.1**). Further modification of the LDH layer was carried by immersion in solutions containing corrosion inhibitors (**Table 4.19**).

Table 4.18. *LDH synthesis conditions of PKSi-AC coating.*

LDH treatment	Chemical composition (M)	Immersion time (min)
Zn-Al-LDH	$Zn(NO_3)_2 \cdot 6H_2O$: 0.1 $NaNO_3$: 0.06	30
Ca-Al-LDH	$Ca(NO_3)_2 \cdot 4H_2O$: 0.1 NH_4NO_3: 0.3	60

Note: All treatments were developed in 250 mL of aqueous solution at 95 ºC. pH values were adjusted to 6.5 using 1 vol.% ammonia for Zn-LDH. For Ca-LDH, pH values were adjusted to 10 using 2 M NaOH.

Table 4.19. *Reaction conditions for inhibitor intercalation.*

Corrosion inhibitor	pH
$CeNO_3$	8
$KMnO_4$	10
$LiNO_3$	10
$NaVO_3$	9
$Na_2MoO_4 \cdot 4H_2O$	8
$Na_2WO_4 \cdot H_2O$	10

- All corrosion inhibitors were incorporated after the LDH formation (post-treatment). The concentration of all corrosion inhibitors was 0.1M. The inhibitors intercalation was carried out at 45 ºC for 2 hours. All pH values were adjusted to 10 using 2 M NaOH.

Screening of the PKSi-AC/LDH coatings was conducted considering their surface appearance (**Figure 4.30**) and short-term corrosion resistance in 3.5 wt.% NaCl solution by EIS testing (**Figure 4.31**). Base LDH coatings denominated as Zn-Al-LDH and Ca-Al-LDH showed uniform surfaces due to a homogeneous LDH coating growth over the

PKSi-AC coating surface. For that, both LDH coatings were selected for the inhibitor loading stage.

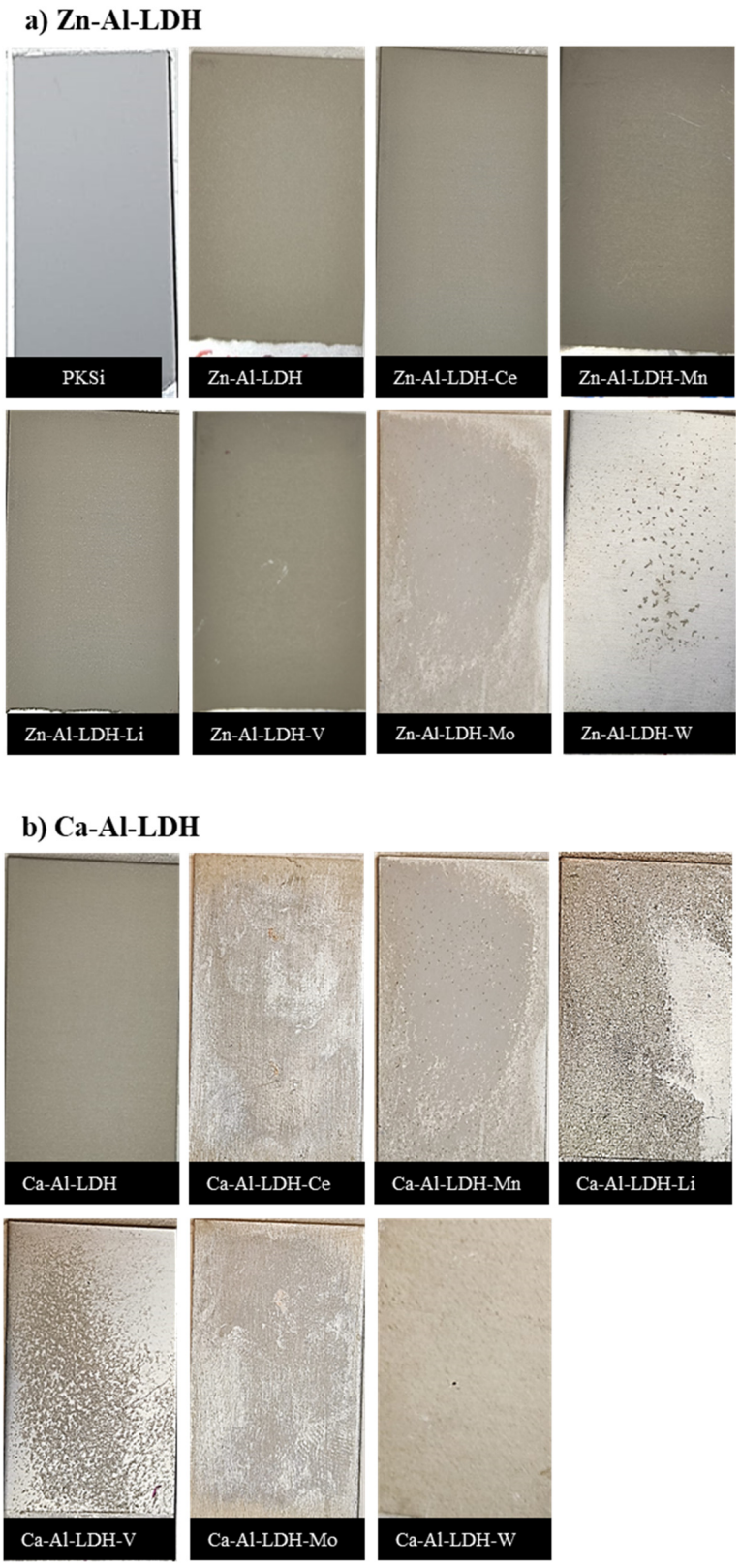

Figure 4.30. *Surface appearance of studied (a) Zn-Al-LDH and (b) Ca-Al-LDH coatings on 2024 alloy before and after inhibitor-loading process.*

As it can be seen in **Figure 4.30a**, the majority of Zn-Al-LDH coatings showed a uniform surface appearance. By contrast, only base Ca-Al-LDH coating showed an acceptable surface appearance (**Figure 4.30b**).

The inhibitor-loading process into the LDH structure depends on several factors such as the LDH gallery size (i.e. interplanar distance) and the size/charge ratio of the incoming anion. The anion-exchange process occurs by ionic exchange of a NO_3^- for a similar anion in terms of size and charge.

The use of cations (i.e. Ce^{3+}, Li^+) as corrosion inhibitors has been only reported for their *in situ* incorporation during the LDH synthesis process, when they combine with aluminium and form a Zn/M^{3+}-Al-LDH structure [159, 287]. However, there is a gap of knowledge regarding the use of cationic elements as corrosion inhibitors since only a few studies relate their loading into the LDH coating surface during post-treatment [346-348].

In the present study, the inhibitor loading into Zn-Al-LDH coating has produced an acceptable coating appearance in case of Ce^{3+}, Li^+, MnO_4^-, and VO_3^- ions and negative for MoO_4^{2-} and WO_4^- anions. It should be noted that the only anionic inhibitor that have been sufficiently studied in literature is VO_3^-. It is worth noting that most of the studies concerned with VO_3^- inhibitor incorporation use NH_4NO_3-based electrolytes and longer treatment times [133, 159, 162, 268, 349]. Therefore, VO_3^- inhibitor incorporation into the LDH structure is mainly known to occur with the open and well-defined Zn-Al-LDH structure. In the present work, on the other hand, the Zn-Al-LDH coating was developed in $NaNO_3$ media and, although exhibiting an adequate corrosion protection, it did not have a well-defined flaky morphology. This may explain the poor surface appearance after MoO_4^{2-} and WO_4^- post-treatment since both anions are similar to VO_3^- in terms of size and charge and it would be reasonable to expect that they need an open flaky LDH structure as well.

Following the post-treatment in Ce^{3+}, Li^+, MnO_4^- and VO_3^- solutions, practically no change in surface appearance of the specimens in comparison to Zn-Al-LDH was observed. This could be an indication of the insufficient incorporation of these species into the LDH structure since the low-porous and non-defined LDH structure may have hampered their incorporation.

In the case of Ca-Al-LDH, there are no studies available regarding its formation on aluminium alloys by *in situ* growth method. The inhibitor-loading process was

detrimental since the surface appearance was heterogeneous in all studied inhibitors (**Figure 4.30b**). This may be related to the non-defined and non-porous Ca-Al-LDH structure (studied in **Section 3.2.3**) which present difficulties for inhibitor intercalation. Further modifications of the the inhibitor-loading process in Ca-Al-LDH coating (**Table 4.14)** by varying the inhibitor species concentration (0.05 and 0.15 M) and pH range (6-12) produced similarly heterogeneous surface appearance.

According to the obtained results (**Figure 4.30**), Zn-Al-LDH coating post-treated with Ce^{3+}, Li^{+}, MnO_4^- and VO_3^- solutions were subjected to second screening stage based on EIS testing. **Figure 4.31** gathers the thickness and the impedance modulus at low frequency (10^{-2} Hz) for the selected coatings after 1 h of immersion in 3.5 wt.% NaCl. The inhibitor-free Zn-Al-LDH and Ca-Al-LDH coatings were also tested for comparison.

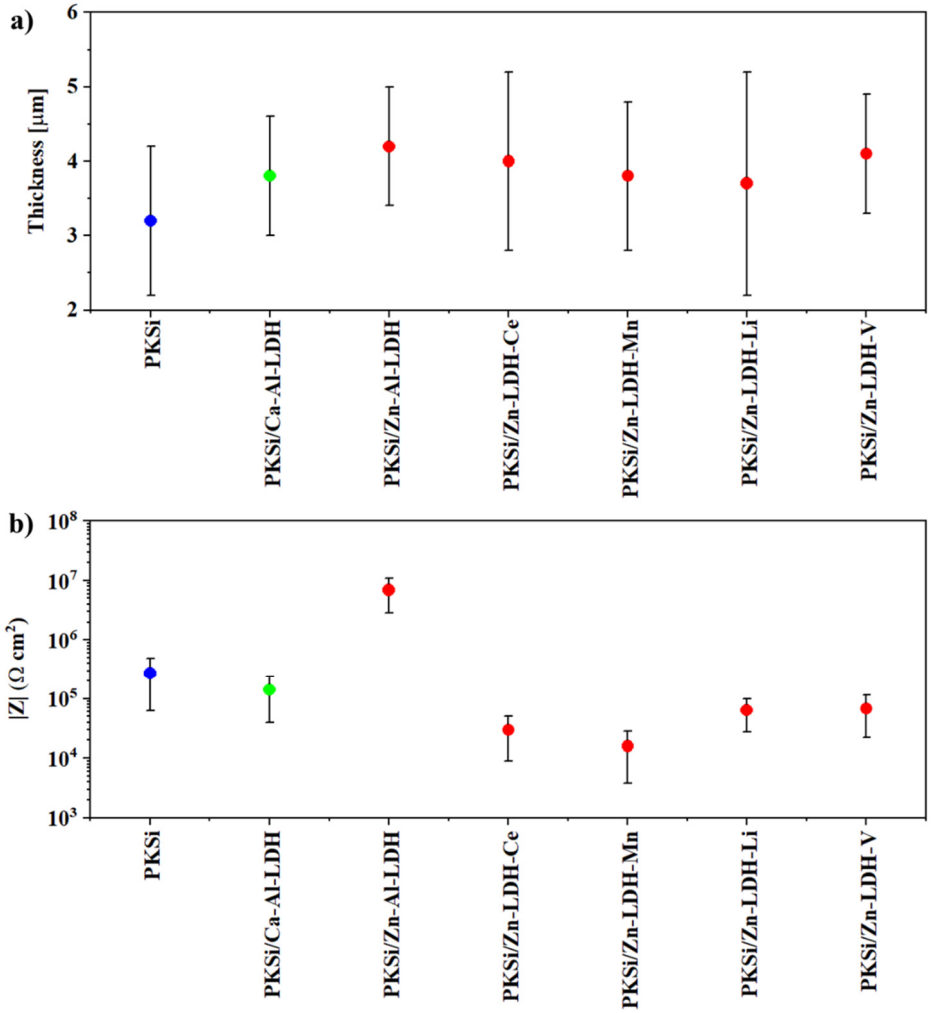

Figure 4.31. *Scatter diagram of (a) thickness and (b) impedance modulus at 10^{-2} Hz of the developed PKSi-AC/LDH-based coatings on 2024 alloy after 1 hour and 28 days of immersion in 3.5 wt.% NaCl solution.*

As can be seen in **Figure 4.31**, the coating combining the highest and closely reproducible |Z| with the lowest thickness variation with respect to PKSi coating was the base Zn-Al-LDH.

As stated in **Section 2.1**, LDH coating is continuous and well defined when the PEO layer is thin (~1 μm). However, in case of such thin PEO layers, no benefit from LDH in terms of improved corrosion resistance is achieved due to partial dissolution of the PEO coating itself. On the other hand, a thicker PKSi coating (~3 μm) on 2024 alloy appears to be more suitable for the formation of LDH without an apparent loss of PEO integrity and enables the increase of the corrosion resistance of PEO/LDH system by about one order of magnitude. This success can possibly be attributed to two factors: (i) the pore band present in the inner region of the PKSi coating facilitated the supply of Al^{3+} cations from the substrate for growth of LDH layer; (ii) the low surface porosity of PKSi coating [131, 133, 293].

The most likely reason for the reduced corrosion resistance of the coatings following the inhibitor-loading post-treatments is the poorly-defined, flat morphology of LDH that forms on thicker PEO coatings. Such morphologies do not present sufficient interplanar distance for ion exchanges, in which case the prolonged immersion in the inhibitor solutions only destabilizes the PEO/LDH system.

C2.2.3.1. Concluding remarks on flash-PEO/LDH system on 2024 alloy

In conclusion, the corrosion resistance of a ~3 μm-thick flash-PEO coating on 2024 alloy sealed with LDH layer was notably increased to the level similar to that of the CAA following 1 h of immersion in 3.5% NaCl (**Table 4.20**).

Table 4.20. *Comparison of PKSi/Zn-Al-LDH key properties with CAA reference film.*

Coating	Thickness (μm)	|Z| (10^{-2} Hz) (Ω cm^2)-1 hour
CAA	0.7 ± 0.1	$8.0 \cdot 10^6$
PKSi/Zn-Al-LDH	4.0 ± 1.0	$1.0 \cdot 10^7$

This can be considered as a remarkable advance since for thinner PEO coatings on 1050 alloy, no change in corrosion performance was observed following LDH sealing.

Therefore, the next step in achieving the PEO/LDH active protection systems would be a search for base LDH coatings that enable the growth of open flaky structures on flash-PEO coatings and support intercalation of new eco-friendly corrosion inhibitors.

C2.3. Conclusions of Chapter 2

The Flash-PEO and LDH strategies were successfully optimized on pure aluminium (1050 alloy) and 2024 alloy. The main conclusions can be summarized as follows:

- On 1050 alloy, thin flash-PEO coatings (~1–2 μm) in aluminate, silicate and phosphate electrolytes with lower energy consumption (~2–5 kW h m^{-2} μm^{-1}) than conventional PEO treatments were developed. Silicate-based PEO coating showed the best corrosion performance. Zn-Al-LDH coating was formed in bare and PEO treated 1050 alloy. The formation of the Zn-Al-LDH layer on selected PEO coatings does not compromise their corrosion resistance and is further facilitated when additional $Al(OH)_2^+$ cations are lixiviated from the coating.
- On 2024 alloy, the *in situ* incorporation of different corrosion inhibitors into a selected phosphate-based PEO coating (PK) was studied as a functionalization strategy for painted components. Among the studied coatings, PKECe and PKW coatings (~5 μm) showed the highest short-term corrosion resistance/thickness ratio. Both coatings showed similar long-term corrosion resistance in EIS and NSS tests. By way of comparison, PKECe has been targeted as the most promising coating since it showed the best paint adhesion and similar corrosion resistance to that of CAA reference film.
- On 2024 alloy, hydrophobic surface modification by lauric acid post-treatment was performed in a selected phosphate-silicate flash-PEO coating (PKSi, ~3 μm) for non-painted components. Lauric acid was chemisorbed on the PKSi coating surface increasing its hydrophobicity. Based on EIS results, PKSi-Lauric coating revealed similar long-term corrosion to that of CAA reference film.
- On 2024 alloy, different LDH post-treatments were performed on PKSi coating for non-painted components. Zn-Al-LDH coating was selected as the most promising one for inhibitor-loading post-treatments, although no improvement was observed. PKSi/Zn-Al-LDH coating revealed similar short-term corrosion to that of the CAA reference film.

Chapter 3: LDH conversion coatings on 2024 alloy

As mentioned in the Introduction (**Section 1.3.4.2**), LDH films can be a feasible alternative to provide a Cr-free conversion coating. So far, Zn-Al-LDH loaded with vanadate has been identified as the most promising candidate to substitute CCCs. However, vanadate and chromate are considered equally toxic. On that basis, new strategies based on LDH coatings include the development of other LDH coatings and the incorporation of eco-friendly corrosion inhibitors as post-treatment.

Chapter 3 is focused on the development of LDH coatings on 2024 alloy for improved corrosion resistance of painted components. The structure of the chapter is divided into two sections: (i) preliminary study on basic LDH synthesis; and (ii) *in situ* incorporation of eco-friendly corrosion inhibitors into the LDH structure. The ultimate goal is to synthesize thin LDH coatings that combine eco-friendly chemicals and improved corrosion performance and paint adhesion. **Figure 5.1** shows the graphical abstract of Chapter 3.

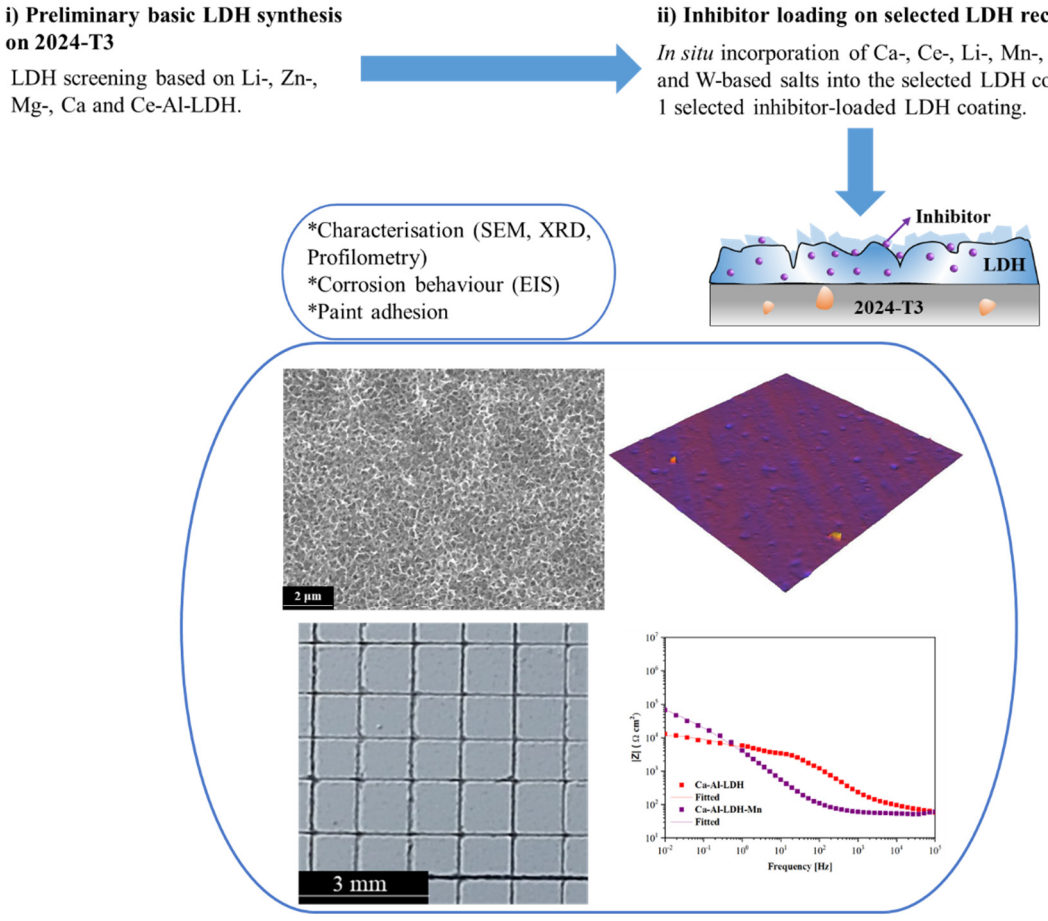

Figure 5.1. *General scheme of Chapter 3.*

Chapter 3

C3.1. LDH synthesis

C3.1.1. Introduction

Among the different combinations of divalent and trivalent cations stated in the introduction (**Section 1.3.2.3**), the one based on the formation of Zn-Al-LDH stands out due to its high stability and ion-exchange capacity for incorporation of corrosion inhibitors. Nevertheless, there are many other LDH structures whose performance on Al-Cu alloys remains unknown, e.g. Ca-Al-LDH.

In this section, several eco-friendly cations with different charges and ratios are evaluated for the development of LDH conversion coatings by *in situ* growth method. The best LDH coatings in terms of surface appearance and short-term corrosion resistance were selected for further inhibitor loading, detailed characterization and long-term corrosion performance study.

C3.1.2. Screening of LDH conversion coatings

So far, most studies have focused on the corrosion properties of mono- (Li^{+}), di- (Zn^{2+}, Mg^{2+}) and trivalent (Ce^{3+}) Al-LDH coatings. On that basis, Zn-Al-NO_3 [155, 159, 162, 278], Zn/Ce-Al-LDH [159, 348, 350, 351] and Mg-Al-LDH [280, 349, 352, 353] are the most widely studied LDH coatings for the Al-Cu system. On the other hand, Li-Al-LDH coatings [354-357] have been studied in AZ31 magnesium alloy and some aluminium alloys (e.g. Al-Li and Al-Si systems) by *in situ*, co-precipitation and electrochemical deposition. Most of the used conditions included different nitrate anion sources (e.g. NH_4NO_3 and CH_4N_2O), treatment times (20 min-24 h), temperatures (60-100 ºC), pH values (~6.5-11) and M^{x+} concentrations (5-500 mM). All the reported Li-LDH coatings were homogeneous and well-defined, enabling a corrosion resistance improvement of one order of magnitude in comparison to the cited non-coated alloys.

Moreover, there are numerous studies concerning the use of divalent cations (e.g. Co^{2+} [358, 359], Cu^{2+} [360, 361], Fe^{2+} [362, 363], Ni^{2+}[351], Sn^{2+}[364], etc.) to form M^{2+}-Al-LDH coatings by co-precipitation and electrochemical methods. Among the different reported LDH coatings, the one based on the formation of Ca-Al-NO_3 LDH coating stands out due to the excellent anionic-exchange ability of NO_3^- in the LDH structure with several anionic species (e.g. CO_3^{2-}, PO_4^{3-} and short-chain carboxylic acids) [289, 365, 366]. Recently, Ahsan *et al.* [367] reported a beneficial effect on the corrosion resistance of AA6082 alloy after the formation of Ca-Al-LDH by *in situ* growth methodology.

Nevertheless, there are no available studies on the *in situ* growth of Ca-Al-LDH on 2024 substrate.

On that basis, there is a knowledge gap in regards to how the combination of different synthesis conditions and the use of other cations influence LDH morphology, corrosion, and paint adhesion performances on the 2024 substrate by *in situ* growth methodology.

The operation conditions in the present study have been established considering previous findings in **Section 2.1.4** and the latest mentioned studies based on Li-, Zn-, Mg-, Ca- and Ce-Al-LDH. The studied LDH coatings were obtained on 2024 alloy in 32 different electrolytes under different treatment times (30-360 min), pH values (6-10), temperature (70-95ºC) and different anions (NO_3^-, CO_3^{2-} and PO_4^{3-}) by *in situ* growth methodology (**Table 5.1**).

Table 5.1. *Operation conditions used in the synthesis of studied LDH coatings on 2024 alloy.*

LDH coating	Chemical composition	Treatment time (min)	Temperature (ºC)	pH
Li-Al-LDH*-1	0.01M LiOH 0.03M $LiNO_3$	60	95	6.5
Li-Al-LDH*-2	0.01M LiOH 0.03M $Li_2(CO_3)$	20	95	6.5
Li-Al-LDH*-3	0.01M LiOH 0.03M $Li_2(CO_3)$	60	95	6.5
Li-Al-LDH*-4	0.01M LiOH 0.03M $Li_3(PO_4)$	20	95	6.5
Li-Al-LDH*-5	0.01M LiOH 0.03M $Li_3(PO_4)$	60	95	6.5
Zn-Al-LDH-1	0.05M $Zn(NO_3)_2{\cdot}6H_2O$ 0.3M NH_4NO_3	15	95	6.5
Zn-Al-LDH-2	0.05M $Zn(NO_3)_2{\cdot}6H_2O$ 0.3M NH_4NO_3	30	95	6.5
Zn-Al-LDH-3	0.05M $Zn(NO_3)_2{\cdot}6H_2O$ 0.3M NH_4NO_3	60	95	6.5
Zn-Al-LDH-4	0.05M $Zn(NO_3)_2{\cdot}6H_2O$ 0.3M NH_4NO_3	30	70	6.5
Zn-Al-LDH-5	0.05M $Zn(NO_3)_2{\cdot}6H_2O$ 0.3M NH_4NO_3	360	70	6.5
Zn-Al-LDH-6	0.05M $Zn(NO_3)_2{\cdot}6H_2O$ 0.3M $NaNO_3$	30	95	6.5
Mg-Al-LDH-1	0.05M $Mg(NO_3)_2{\cdot}6H_2O$ 0.3M NH_4NO_3	15	95	6.5
Mg-Al-LDH-2	0.05M $Mg(NO_3)_2{\cdot}6H_2O$ 0.3M NH_4NO_3	30	95	6.5
Mg-Al-LDH-3	0.05M $Mg(NO_3)_2{\cdot}6H_2O$ 0.3M NH_4NO_3	60	95	6.5
Mg-Al-LDH-4	0.05M $Mg(NO_3)_2{\cdot}6H_2O$	30	95	6.5

	0.3M NH_4NO_3			
Mg-Al-LDH-5	0.05M $Mg(NO_3)_2 \cdot 6H_2O$ 0.3M NH_4NO_3	360	70	6.5
Mg-Al-LDH-6	0.05M $Mg(NO_3)_2 \cdot 6H_2O$ 0.3M $NaNO_3$	30	95	6.5
Ca-Al-LDH-1	0.05M $Ca(NO_3)_2 \cdot 6H_2O$ 0.3M NH_4NO_3	60	95	6.5
Ca-Al-LDH-2	0.01M $Ca(NO_3)_2 \cdot 6H_2O$ 0.3M NH_4NO_3	60	95	6.5
Ca-Al-LDH-3	0.1M $Ca(NO_3)_2 \cdot 6H_2O$ 0.3M NH_4NO_3	60	95	6.5
Ca-Al-LDH-4	0.1M $Ca(NO_3)_2 \cdot 6H_2O$ 0.3M NH_4NO_3	15	95	10
Ca-Al-LDH-5	0.1M $Ca(NO_3)_2 \cdot 6H_2O$ 0.3M NH_4NO_3	30	95	10
Ca-Al-LDH-6	0.1M $Ca(NO_3)_2 \cdot 6H_2O$ 0.3M NH_4NO_3	60	95	10
Ca-Al-LDH-7	0.1M $Ca(NO_3)_2 \cdot 6H_2O$ 0.3M NH_4NO_3	60	70	6.5
Ca-Al-LDH-8	0.1M $Ca(NO_3)_2 \cdot 6H_2O$ 0.3M NH_4NO_3	360	70	10
Ca-Al-LDH-9	0.15M $Ca(NO_3)_2 \cdot 6H_2O$ 0.3M NH_4NO_3	60	95	10
Ca-Al-LDH-10	0.2M $Ca(NO_3)_2 \cdot 6H_2O$ 0.3M NH_4NO_3	60	95	10
Ce-Al-LDH-1	0.05M $Ce(NO_3)_3 \cdot 6H_2O$ 0.3M NH_4NO_3	30	95	6.5
Ce-Al-LDH-2	0.05M $Ce(NO_3)_3 \cdot 6H_2O$ 0.3M NH_4NO_3	60	95	6.5
Ce-Al-LDH-3	0.05M $Ce(NO_3)_3 \cdot 6H_2O$ 0.3M $NaNO_3$	30	95	6.5
Ce-Al-LDH-4	0.05M $Ce(NO_3)_3 \cdot 6H_2O$ 0.3M $NaNO_3$	60	95	6.5

Notes:
- All treatments were performed under continuous stirring in 250 mL solution.
- pH values were adjusted by NaOH (1M)/Ammonia solution (1 vol.%)
*pH value was adjusted with concentrated HNO_3

The first screening stage was performed focussing on the uniform surface appearance (**Figure 5.2**). As can be seen in **Figure 5.2a**, Li-Al-LDH coatings showed a uniform surface appearance, demonstrating their suitability for *in situ* growth on the 2024 substrate (**Table 5.1**). The *in situ* method was likewise fit for Zn-Al-LDH coatings which were modified in the present investigation by using shorter treatment times and $NaNO_3$ as NO_3^- anion source, in contrast to previous studies on the 2024 substrate [155, 159, 162, 278].

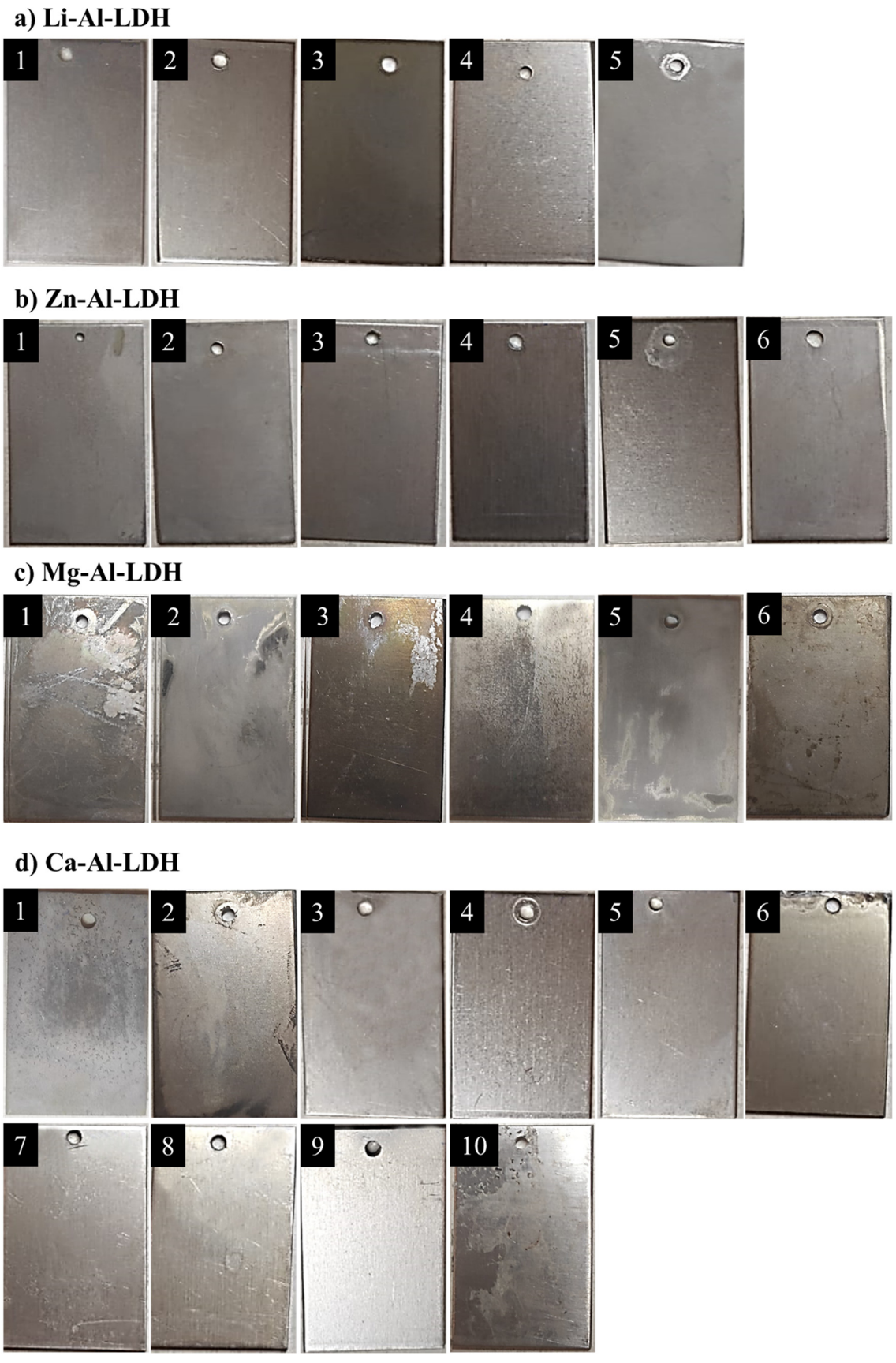

Figure 5.2. *Continuation.*

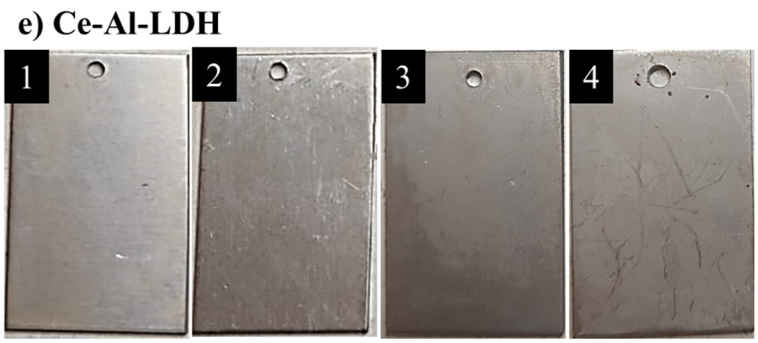

Figure 5.2. *Surface appearance of developed LDH coatings in (a) Li-, (b) Zn-, (c) Mg-, (d) Ca- and (e) Ce-based solutions.*

On the contrary, Mg-Al-LDH coatings showed a heterogeneous surface appearance (**Figure 5.2c**). This may be related to the uncompleted reaction between the base material and the Mg-based solutions since most of the published studies were performed at longer treatment times (4-12 h) to form a homogeneous and thicker LDH layer (6-13 μm) [280, 349, 352, 353] than those employed in this work. This demonstrates that *in situ* growth methodology is not suitable for the formation of Mg-Al-LDH coatings in short treatment times at studied compositions (**Table 5.1**).

In the case of Ca-Al-LDH coatings, the homogeneous surface appearance was achieved when using 0.1M $Ca(NO_3)_2$ under different treatment times and pH values (Ca-Al-LDH (3-9)) (**Figure 5.2d**). In contrast, in most of the other published studies, Ca-Al-LDH formation was performed in concentrated $Ca(NO_3)_2$ solutions (0.1-1.4 M) at much longer treatment times (4-12 h) by co-precipitation method [289, 365, 366]. On that basis, the results obtained in the present work confirm the suitability of *in situ* growth methodology to form in a short term homogeneous Ca-Al-LDH coatings on 2024 substrate.

Among the studied Ce-based recipes, Ce-Al-LDH-1 and Ce-Al-LDH-2 coatings showed uniform surface appearance (**Figure 5.2e**), even though the used treatment times were much shorter (30 min-1h) than those employed in other studies (e.g. 24 h) [159, 348, 350, 351]. By contrast, the heterogeneous surface appearance of Ce-Al-LDH-3 and Ce-Al-LDH-4 coatings may be due to the use of $NaNO_3$ as a source of NO_3^- anions. This could be related to the hampering effect of sodium ions on the formation of homogeneous Ce-Al-LDH.

The group of homogeneous LDH coatings including Zn-Al-LDH (1-6), Ce-Al-LDH (1,2), Li-Al-LDH (1-5) and Ca-Al-LDH (3-9) were subjected to EIS testing in 3.5 wt.% NaCl

after 1h of immersion in order to identify the best candidates that combined the lowest possible thickness with the highest possible impedance modulus (**Figure 5.3**).

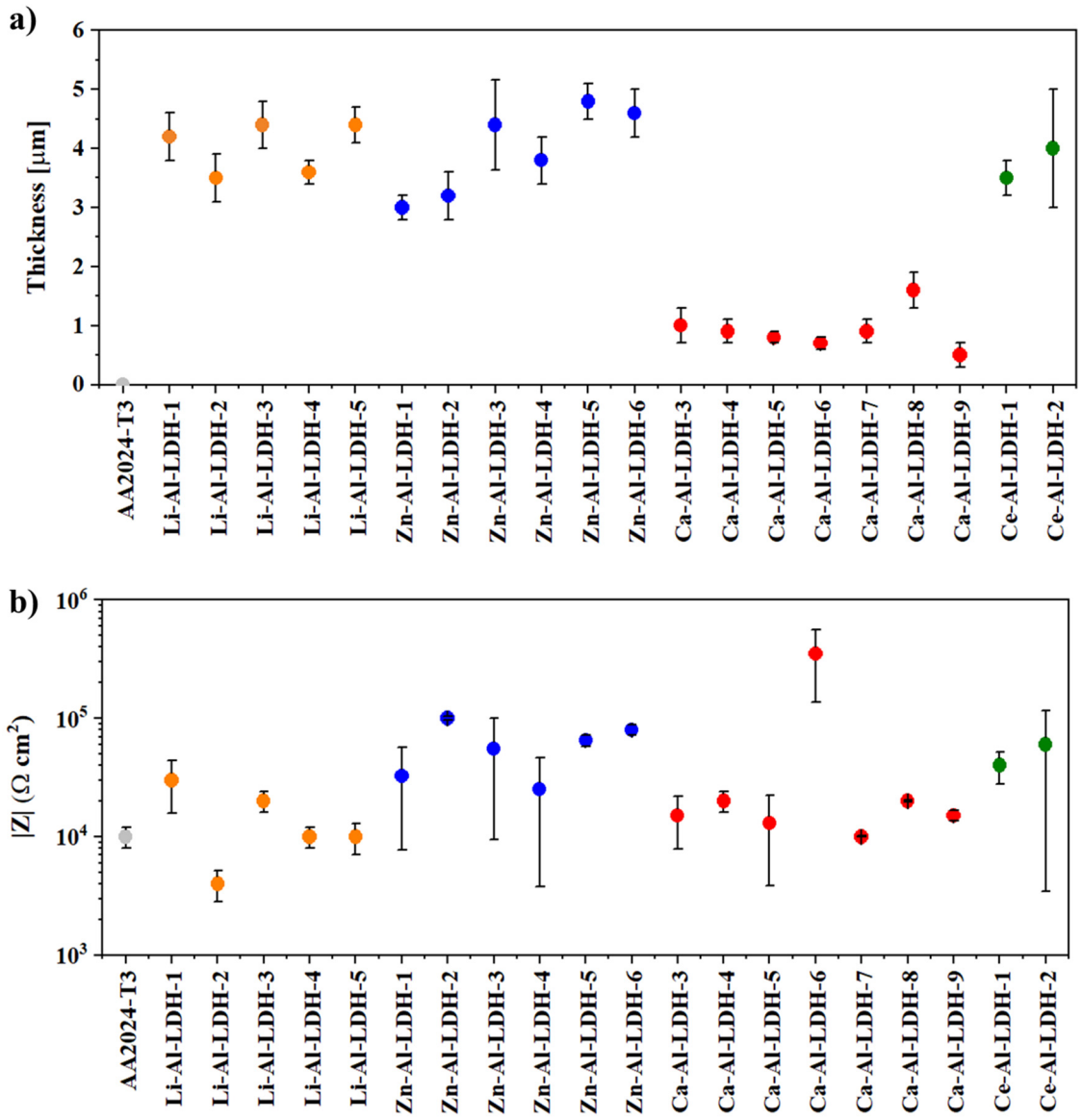

Figure 5.3. *Scatter diagram of (a) thickness and (b) impedance modulus at 10^{-2} Hz in 3.5 wt.% NaCl of the selected LDH coatings on 2024 substrate. Colours: Blue-Zn-Al-LDH, Green-Ce-Al-LDH, Orange-Li-Al-LDH and Red-Ca-Al-LDH.*

As can be seen in **Figure 5.3a**, except for Ca-Al-LDH coatings (~1 µm), Zn-, Li- and Ce-Al-LDH coatings showed thicknesses around 3-5 µm. More specifically, most studied LDH coatings showed a slight thickness increase at longer treatment times which is in agreement with previous studies [368, 369]. However, other factors may influence the coating thickness such as the cation concentration in the electrolyte and the temperature.

The latter variables are known to account for a greater concentration of available cations for the newly LDH structure crystallization on the whole 2024 substrate [368-371].

Regarding the corrosion resistance, different responses were obtained depending on the M^{x+} nature and the operating conditions (**Figure 5.3b**). Li-Al-LDH (1,3,5) coatings showed a slight increase in corrosion resistance with respect to the 2024 substrate (**Figure 5.3b**). A recent study on the *in situ* formation of Li-Al-NO_3 LDH on A601-T5 (Al-Si alloy) reported a corrosion improvement of one magnitude order in comparison to the un-coated alloy [357]. The lower corrosion performance achieved in the present study may be related to the low ability of the studied Li-based formulations to form LDH coatings with enhanced corrosion protection on Al-Cu alloy, which is possibly related to the specific composition of the intermetallic particles in the Al-Cu system. Besides, prior studies have demonstrated that the intercalation of NO_3^-, CO_3^{2-} and PO_4^{3-} on Li-Al-LDH formed by co-precipitation showed an adequate anion-exchange with Cl^- anions [372, 373]. In the present work, however, the effect of the studied anions (NO_3^-, CO_3^{2-} and PO_4^{3-}) (**Table 5.1**) on the surface appearance, coating thickness and corrosion resistance was negligible (**Figure 5.3**), suggesting that these anions have low anion-exchange ability with Cl^- anions in the Li-Al-LDH coatings formed by *in situ* growth methodology.

Ce-Al-LDH-1 coating showed only a slight improvement in corrosion resistance with respect to the non-treated alloy, whereas a longer treatment time led to a non-reproducible Ce-Al-LDH-2 coating (**Figure 5.3b**). The latter may be due to the low concentration of Ce^{3+} ions in Ce-Al-LDH-2 solution and the resultant difficulty to form a stable and corrosion protective LDH coating [374]; most of the studies of Ce-based LDH coatings on 2024 substrate only reported the successful LDH layer formation in the presence of Zn^{2+} cations, as combined Zn/Ce-Al-LDH [159, 350, 375].

The two LDH coatings that produced a most significant improvement in corrosion resistance were Zn-Al-LDH-2 and Ca-Al-LDH-6 coatings. Among the Zn-Al-LDH treatments, a noticeable corrosion protection was revealed only in case of the coatings produced at short treatment times, i.e. Zn-Al-LDH-2 and Zn-Al-LDH-6. That is probably due to the noticeable barrier effect of the non-defined morphology of these LDH coatings, as evaluated in **Section 2.1.4,** which is in agreement with several studies [155, 159, 162, 278]. Unlike for the Zn-Al-LDH coatings formed in the 1050-H18 alloy (**Section 2.1.4**), the use of different nitrates (NH_4NO_3 and $NaNO_3$, respectively) as NO_3^- anion source

resulted in closely similar corrosion behaviour of Zn-Al-LDH-2 and Zn-Al-LDH-6 coatings.

For Ca-Al-LDH coatings a negligible corrosion improvement was observed in all cases, with the exception of Ca-Al-LDH-6 coating. The higher response of the latter can be related to the synthesis conditions, since successful Ca-Al-LDH formation and the Ca^{2+} intercalation into the Al-LDH structure has been associated in the literature with the use of long treatment times (5-24 h), high temperatures (80ºC) and alkaline pH values (9-11) [289, 365, 366]. The higher temperature and longer treatment time compared to the other studied LDH formulations were required to facilitate the formation of Ca-Al-LDH [365]. The use of alkaline pH is related to the chemical reactions involved in dissolution of the aluminium substrate to form Ca-Al-LDH-based structures [289, 365].

It should be noted that Ca-Al-NO_3 LDH coating properties could be also associated with the adsorption of CO_3^{2-} onto the interlayer space. This is in accordance with Radha *et al.* [289], who reported that the LDH interlayer becomes more stable with the increasing charge of the anion, thus assisting the easy exchange of NO_3^- by higher valent anions such as CO_3^{2-} which tend to bond strongly with the hydroxide layer. According to the absence of an inert atmosphere during the synthesis conditions, the CO_3^{2-} incorporation into the positively charged Ca-Al-LDH structure occurs from atmospheric CO_2 [289, 376]. This suggests that the higher corrosion response may be also associated with the efficiency of the anionic exchange reaction between CO_3^{2-} and Cl^- anions into the Ca-Al-NO_3 structure.

The present findings highlight that *in situ* growth methodology can be successfully implemented for the development of a Ca-Al-LDH coating. Based on these results, the coatings combining the highest and closely reproducible |Z| with the lowest thickness (~1-3 μm), i.e. Zn-Al-LDH-2 and Ca-Al-LDH-6, were utilized for inhibitor loading studies.

C3.2. Inhibitor loading

C3.2.1. Introduction

An intrinsic property of LDH coatings is their easy functionalization by inhibitor-based post-treatments. Depending on the corrosion inhibitor charge, two possible interactions with the LDH structure are possible: (i) incorporation and of corrosion inhibitors in the interlayer space (anionic inhibitors) and (ii) adsorption on the LDH surface (cationic inhibitors), thus providing a smart and superior long-term corrosion protection. On that

basis, the incorporation of corrosion inhibitors produces slight morphological changes that positively affect corrosion resistance.

Another point to consider for the inhibitor-loading screening is the compatibility of the resultant system with paints in multi-layer coating systems. In this section, these aspects have been investigated using EIS screening after *in situ* incorporation of eco-friendly corrosion inhibitors into selected Zn-Al- and Ca-Al-LDH films (**Section 3.1**) on 2024 alloy. Then, the best inhibitor-loaded LDH coating has been characterized and evaluated in terms of detailed long-term corrosion performance study and paint adhesion in comparison to inhibitor-free LDH coating. The ultimate goal is to develop a thin LDH conversion coating that provides enhanced long-term corrosion resistance for painted components.

C3.2.2. Screening of inhibitor-loaded LDH coatings

Inhibitor-containing LDH screening has been carried out on Zn-Al-LDH and Ca-Al-LDH coatings with the incorporation of Ca-, Ce-, Li-, Mn-, Mo-, Ni- and W-based species in 14 electrolytes under different pH values (6.5-12), as summarised in **Table 5.2**.

Table 5.2. *Studied inhibitor-loading conditions on selected Zn-Al-LDH and Ca-Al-LDH coatings.*

Inhibitor (M)	pH value
$Ca(NO_3)_2$ (Ca)	10
$CeNO_3 \cdot 6H_2O$ (Ce)	6.5/12
$LiNO_3$ (Li)	6.5/10
$KMnO_4$ (Mn)	6.5/10
$Na_2MoO_4 \cdot 4H_2O$ (Mo)	6.5/9
$Ni(CH_3COO)_2 \cdot 4\ H_2O$ (Ni)	10
$Na_2WO_4 \cdot H_2O$ (W)	10

-In all cases, the inhibitor loading conditions were: Concentration (M): 0.1; T(ºC): 45; t (h): 2.

The inhibitor loading process and its operating conditions have been determined considering the Pourbaix diagram of each inhibitor and previous studies based on the abovementioned inhibitors [155, 158, 159, 208, 346, 377].

The surface appearance of inhibitor post-treated Zn-Al-LDH-2 and Ca-Al-LDH-6 coatings are disclosed in **Figure 5.2**. The inhibitor loading process in some cases produced a slight coating thickness increase (0.5-1 μm), which may be due to the modification of the LDH structure and inhibitor adsorption on the LDH surface [158,

288]. The first screening stage involved a comparison of the coating modulus of impedance at low frequency (|Z| at 10^{-2} Hz) determined in 3.5 wt.% NaCl after 1 h of immersion (**Figure 5.4**).

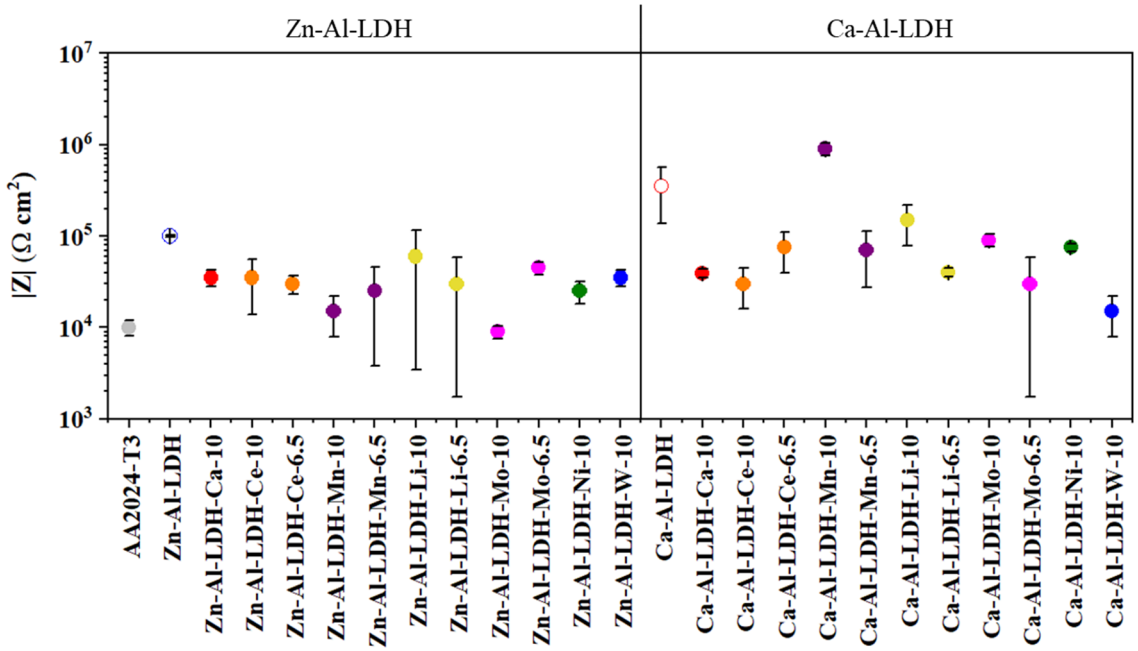

Figure 5.4. *Scatter diagram of impedance modulus at 10^{-2} Hz of the developed inhibitor-containing LDH coatings on 2024. The empty blue and red circles indicate the Zn-Al- and Ca-Al-LDH reference coatings, respectively. The filled circles indicate the inhibitor incorporation. Colours: red-$Ca(NO_3)_2$ (Ca), orange- $Ce_2(SO_4)_3$ (Ce), purple- $KMnO_4$ (Mn), yellow-$LiNO_3$ (Li), pink- Na_2MoO_4 (Mo), green-$Ni(CH_3COO)_2$ (Ni) and blue- Na_2WO_4 (W).*

The lower impedance of the Zn-Al- and Ca-Al-LDH reference coatings treated with Ca^{2+} Ce^{3+}, Li^{+} and Ni^{2+} cations may be related to the inability of these to be adsorbed onto or incorporated in the studied LDH structure under specified conditions in **Table 5.2**. Although the available literature concerning the incorporation of these corrosion inhibitors is scarce, it may be hypothesized that an excess of the positive charge on LDH structure impeded the intercalation of these cations. The observed decrease in corrosion performance in comparison to base Zn-Al-LDH and Ca-Al-LDH coatings (**Figure 5.4**) may be associated with partial dissolution of the LDH coatings and changes in their morphology during the inhibitor-loading treatment.

Regarding the anionic inhibitors, MoO_4^{2-} anion is known to behave as an efficient anodic inhibitor that has previously been successfully intercalated into Zn-Al-LDH using the same loading conditions (**Table 5.2**) [158, 378]. However, the corrosion performance of Zn-Al-LDH and Ca-Al-LDH coatings after post-treatment with MoO_4^{2-} anion resulted in

lower impedance response. This may be related to the different synthesis conditions of base Zn-Al-LDH and Ca-Al-LDH coatings (**Table 5.1**), since the incorporation of MoO_4^{2-} was only reported in well-defined Zn-Al-LDH structures developed at a lower temperature (~60ºC) and longer treatment times (6 h) [158, 378]. Likewise, the incorporation of WO_4^{2-} was only reported in Zn-and Mg-Al-NO_3 LDH structures formed by co-precipitation method at longer treatment times (3-168 h) and higher temperatures (~70-100 ºC) [378-381] than the used in the present study (**Table 5.2**). Again, in this case, the synthesis conditions may have caused lower anion-exchange efficiency between WO_3^{2-} anions with NO_3^- from the Zn-Al-LDH and Ca-Al-LDH structures and the reduction of total impedance moduli compared with those of the base LDH coatings.

The higher impedance modulus provided by the post-treatment of Ca-Al-LDH coating in MnO_4^--based solution suggests that intercalation of MnO_4^- anion into the LDH structure have successfully occurred. For this reason, Ca-Al-LDH-Mn-10 (from now on Ca-Al-LDH-Mn) coating was selected for further characterization and for detailed corrosion and paintability testing. The inhibitor-free Ca-Al-LDH coating was also analyzed for comparison.

C3.2.3. Characterization of selected LDH coatings

The Mn-based post-treatment on the Ca-Al-LDH coating promoted colour and topographic changes as shown in **Figure 5.5** and **Table 5.3**. In that regard, surface roughness and texture are known to influence the paint adhesion, wettability and corrosion resistance of the coatings [382]. Ca-Al-LDH-Mn shows a golden colour and slightly higher Ra and Sa values than Ca-Al-LDH coating. This is likely associated with Mn incorporation since compounds of this element are known to have a brown/yellow.

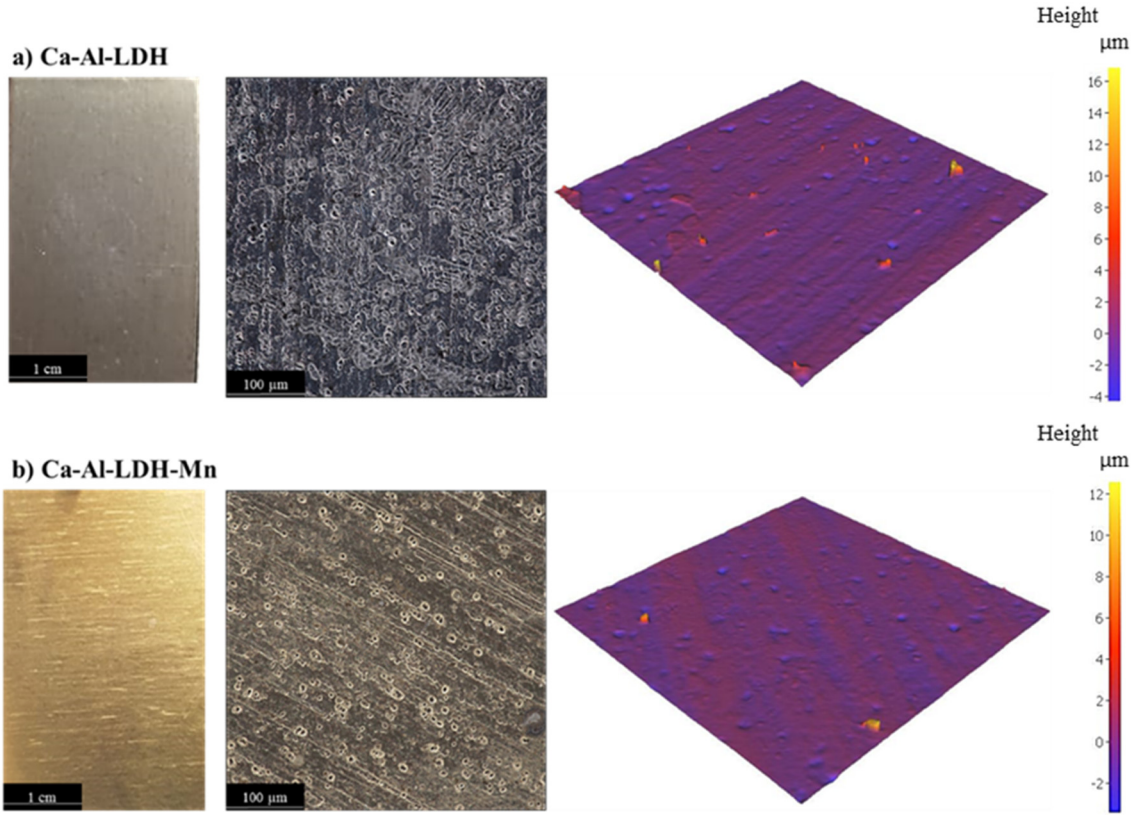

Figure 5.5. *Surface and Optical profilometry micrographs of the (a) Ca-Al-LDH and (b) Ca-Al-LDH-Mn studied LDH coatings, including the 3D-rendered images and 3D-topographical maps.*

Table 5.3. *Roughness values of studied Ca-Al-LDH-based coatings on 2024 alloy.*

Roughness (µm)	Ca-Al-LDH	Ca-Al-LDH-Mn
Ra	0.10±0.01	0.30±0.02
Sa	0.30±0.02	0.40±0.02

XRD patterns of the selected Ca-Al-LDH and Ca-Al-LDH-Mn coatings formed on 2024 substrate are shown in **Figure 5.6.** Peaks of Al and secondary phases (IMCs) proceeding from the substrate are identified as a consequence of the low thickness of the studied LDH coatings. A small diffraction peak at ~12 º was observed for the Ca-Al-LDH specimen. This was insufficient for a sound identification, but it is in the typical region of LDH phases, particularly near the (001) diffraction of Ca-Al-LDH [383]. No additional Ca-containing phases were identified, probably due to the short treatment time (1h). For instance, according to other studies like that from Ahsan *et al.* [367], who developed a Ca-Al-LDH coating on 6082 alloy at treatment times between 12 and 72 h, Ca-containing phases such as $Ca(OH)_2$ (~17.5º) and tricalcium aluminate (~27.5º) were more evident only after long treatment times. $CaCO_3$ is another phase that is sometimes observed in LDH synthesis. This is mainly associated with the limited amount of calcium that can be

stabilized in the LDH structure since the ionic size of calcium (1.10 Å) is higher than that of aluminium (0.54 Å). This is the reason why $CaCO_3$ is often found when high Ca:Al are used [384].

In the case of Ca-Al-LDH-Mn coating no LDH diffractions were observed. This could be associated with the intercalation of Mn into the Ca-Al-LDH structure and broadening of the diffraction peaks [385-387], making them indistinguishable. The colour change after the Mn-based post-treatment is in line with this hypothesis. An additional peak at 28º indicates that some of the Mn is also deposited as α-MnO_2. It is known that reduction of Mn(VII) to Mn(IV) is highly favoured in alkaline media (pH: ~9-12) [387-389]; in this study the Mn-loading process was carried out at pH 10.

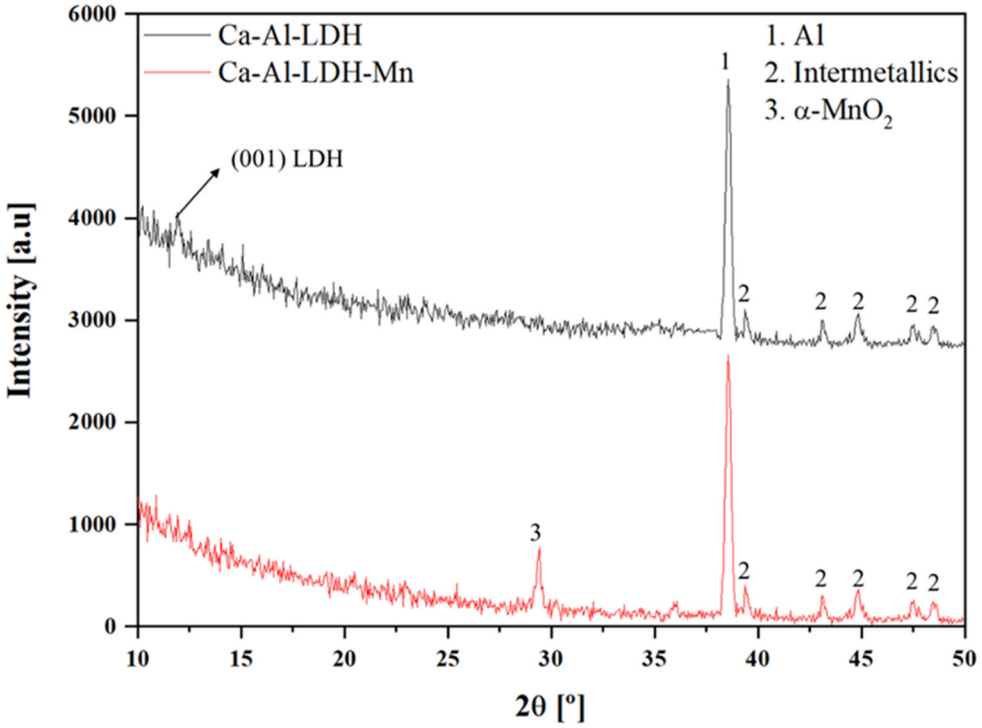

Figure 5.6. *XRD patterns of Ca-Al-LDH and Ca-Al-LDH-Mn coatings on 2024 alloy.*

Figure 5.7 shows the plan views secondary electron images of the Ca-Al-LDH and Ca-Al-LDH-Mn coatings grown on the 2024 substrate. These images reveal homogeneous and compact Ca-Al-LDH and Ca-Al-LDH-Mn layers with their typical flaky morphology. It is important to note that flakes were not very well defined due to operating conditions used in this study (1 h and 95ºC). In other studies, with higher treatment times (>12 h) and temperatures (140 ºC), flakes are better defined [367]. Cross-sectional micrographs of Ca-Al-LDH (**Figure 5.7d**) and Ca-Al-Mn-LDH (**Figure 5.7f**) reveal a slightly higher thickness value for Ca-Al-LDH (0.6 ± 0.1 µm) than for Ca-Al-Mn-LDH

(0.5 ± 0.1 μm), suggesting that some dissolution of the film occurred during post-treatment, although the thickness difference was negligible. These thickness values are considerably lower in comparison to the available literature related to Ca-Al-LDH coating formed by *in situ* growth methodology [367]. Again, in this case, it is mainly related to the low temperature and treatment times used in this study.

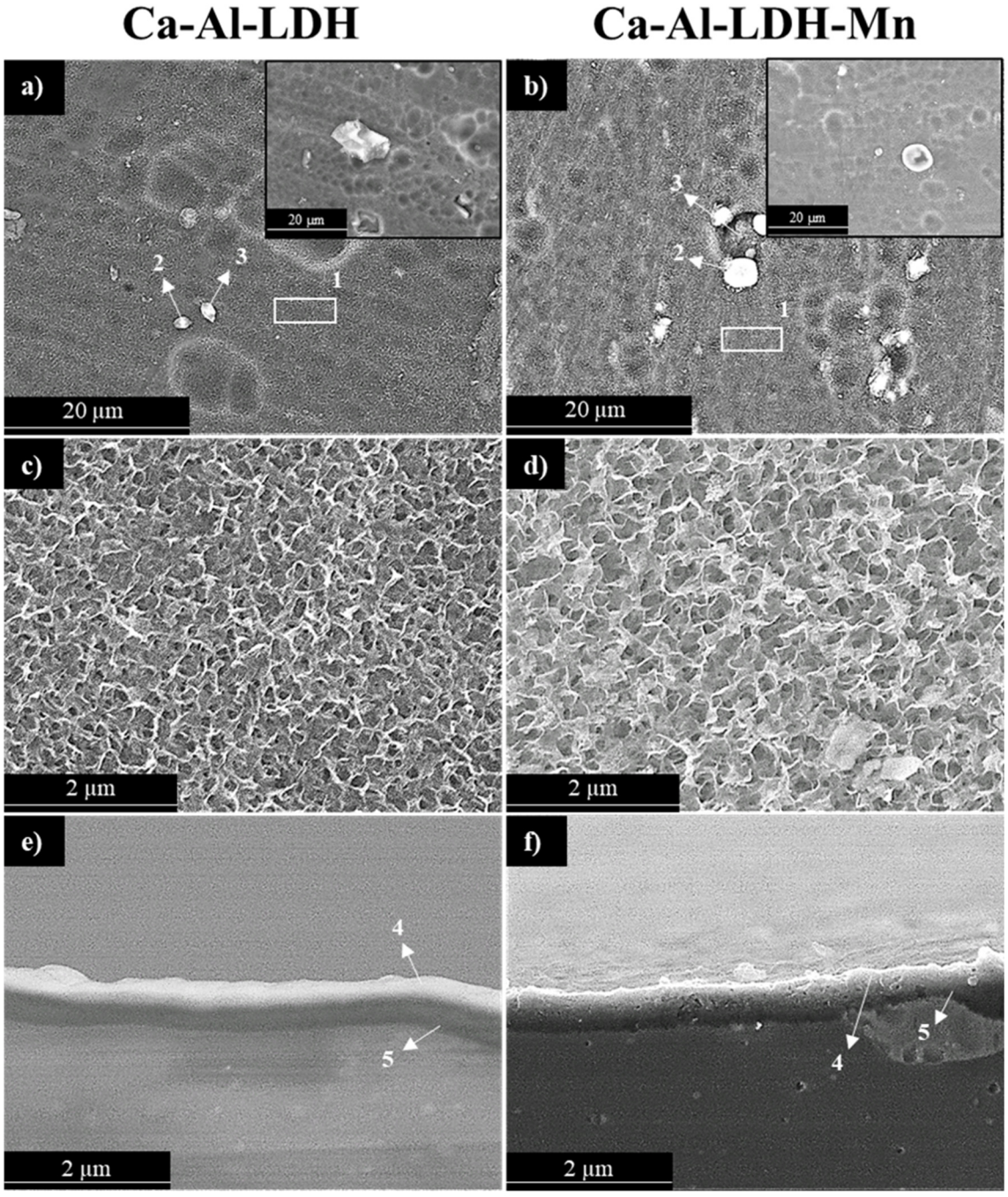

Figure 5.7. *Scanning electron micrographs of (a, c, e) Ca-Al-LDH and (b, d, f) Ca-Al-LDH-Mn coatings on 2024 alloy.*

According to the EDS results presented in **Table 5.4**, the content of Al, Cu and Mg, derived from the substrate was similar in both Ca-Al-LDH and Ca-Al-LDH-Mn coatings (marked as area 1).

Table 5.4. *EDS (at.%) area analysis of Ca-Al-LDH and Ca-Al-LDH-Mn coatings on 2024 alloy.*

Coating	Location		O	Al	Ca	Mn	Cu	Mg	Fe
Ca-Al-LDH	Longitudinal view	1	55.6	43.1	-	-	0.3	1.0	0.03
		2	65.2	33.4	0.1	-	0.6	0.4	0.3
		3	70.0	29.2	0.1	-	0.3	0.3	0.2
	Cross-section view	4	52.8	45.3	0.1	-	1.0	0.8	-
		5	56.2	43.0	-	-	0.2	0.6	-
Ca-Al-LDH-Mn	Longitudinal view	1	46.4	52.0	-	0.4	0.4	0.8	-
		2	83.9	5.5	0.5	9.2	-	0.3	0.5
		3	69.4	21.0	0.2	2.0	5.3	1.8	0.2
	Cross-section view	4	68.1	29.8	0.3	1.0	0.14	0.5	0.1
		5	24.6	64.7	-	1.0	6.5	0.2	3.0

Ca was only detected (~0.3 at.%) in the Ca-Al-LDH-Mn specimen, preferentially in the outer layer and within white-round deposits. These results suggest that the initial LDH coating contains Ca, as shown in the XRD pattern, although in very small amounts (non-detectable by EDS). Later, during the post-treatment, there is release of Ca ions and redeposition on the surface. After post-treatment, it is evident that some permanganate is incorporated (~0.3 at.%) into the LDH structure (area 1, Ca-Al-LDH-Mn), confirming the hypothesis previously mentioned.

The EDS analysis of large white particles in Ca-Al-LDH revealed that these were highly enriched in Al and O, possibly in the form of $Al(OH)_3$ (points 2 and 3, Ca-Al-LDH). Contrarily, white-round deposits in the Ca-Al-LDH-Mn specimen show high amounts of Mn and O, which is consistent with the detection of MnO_2 by XRD. It is important to mention that these deposits are surrounding intermetallic particles as deduced from the significant amount of Mg, Fe and Cu in point 3 for Ca-Al-LDH-Mn. This is probably due to the cathodic nature of secondary phases facilitating the reduction of Mn(VII) [284, 353, 389, 390].

C3.2.4. Corrosion behaviour of selected LDH coatings

Figure 5.8 depicts the Bode and Nyquist diagrams after immersion in 3.5 wt.% NaCl solution for 1 h and 28 d of studied Ca-Al-LDH and Ca-Al-LDH-Mn coatings.

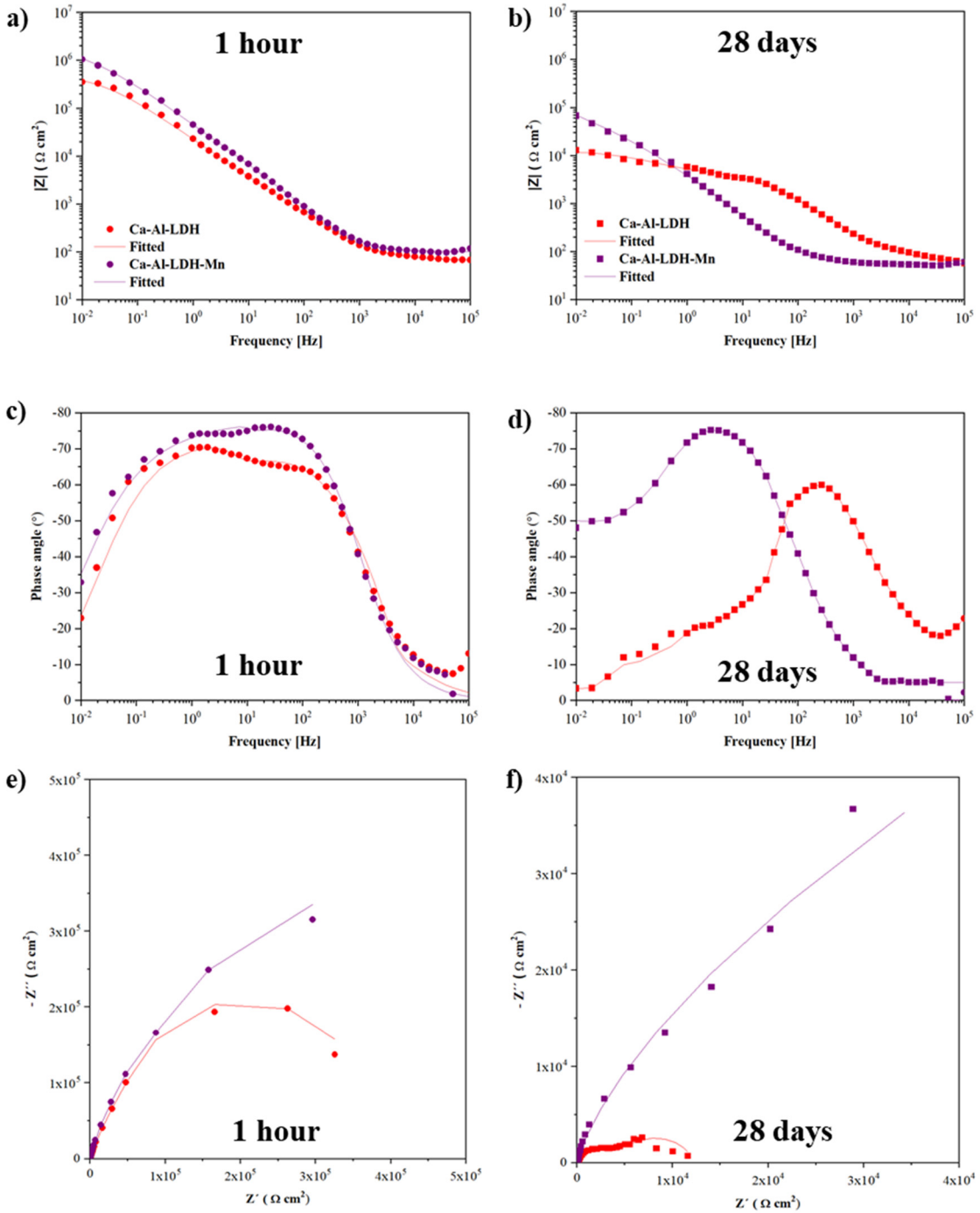

Figure 5.8. *(a-d) Bode and (e,f) Nyquist plots of the selected Ca-Al-LDH and Ca-Al-LDH-Mn coatings after 1 hour and 28 days of immersion time in 3.5 wt.% NaCl solution.*

The different electrochemical processes observed in Bode diagrams can be associated with three distinct parts of the coatings: (i) the external LDH layer (10^3-10^5 Hz), (ii) the

intermediate LDH part associated with the middle frequency response of the system (10^1–10^2 Hz) and (iii) the metal/LDH layer interface (10^0-10^{-2} Hz). The external and intermediate parts of LDH are difficult to differentiate at the beginning of testing.

It should be noted that the impedance modulus of the Ca-Al-LDH-Mn coating was approximately one order of magnitude higher than that of the Ca-Al-LDH coating after 28 days of immersion time. It is a greater difference compared with the difference that existed between the two coatings at the initial period of immersion (**Figures 5.8a,b**). It demonstrates the positive effect of MnO_4^- incorporation and the deposition of α-MnO_2 on the coating surface since the loss of protection is lesser with time in the Ca-Al-LDH-Mn coating.

The phase angle-frequency response for the LDH coated substrates indicates the presence of several relaxation processes. A broad peak shown at intermediate frequencies (**Figure 5.8c**) for Ca-Al-LDH and Ca-Al-LDH-Mn coatings is a result of the overlapping of two phase angle peaks. The fact that the peak at 10^1–10^2 Hz is more pronounced for Ca-Al-LDH-Mn coating is ascribed to the presence of Mn-containing species in the coating.

Following 28 days of immersion, higher impedance and phase angle values at intermediate/low frequencies were observed for Ca-Al-LDH-Mn, indicating its higher stability compared to Ca-Al-LDH coating (**Figure 5.8d**). The observed drastic decrease of phase angle for Ca-Al-LDH at 10^{-1}–10^1 Hz indicates an acceleration of the kinetics of the overall corrosion process due to the penetration of Cl^- ions.

The elements in the equivalent circuit (**Figure 5.9**) include R_s (solution resistance), CPE_{-LDH}/R_{-LDH} (ascribed to the capacitive and resistive behaviour of the outer LDH layer), CPE_{-ox}/R_{-ox} (ascribed to the capacitive and resistive behaviour of the inner LDH layer) and CPE_{-dl}/R_{-dl} (ascribed to the double layer at the metal/electrolyte interface) [155, 278, 279, 349].

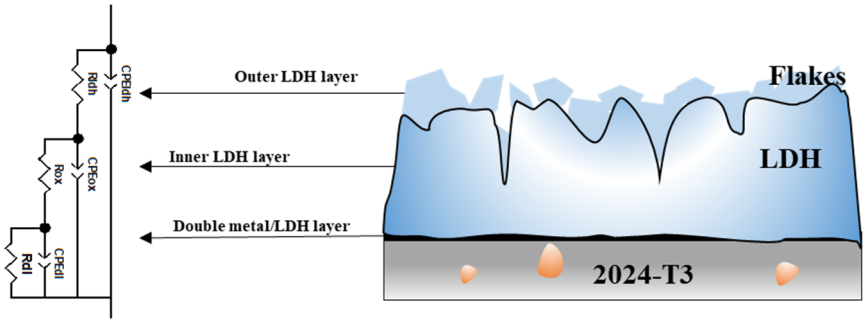

Figure 5.9. *Equivalent circuit used to fit the EIS data of Ca-Al-LDH and Ca-Al-LDH-Mn coatings grown on 2024 substrate after 1 hour and 28 days of immersion in 3.5 wt.% NaCl solution.*

The electrical parameters obtained by fitting of the equivalent circuits are given in **Table 5.5** for 1 hour and for 28 days.

Table 5.5. *Equivalent circuit data for the selected Ca-Al-LDH and Ca-Al-LDH-Mn coatings grown on 2024 for 1 h and 28 days of immersion time in 3.5 wt.% NaCl solution.*

Coating	CPE_{LDH} ($F\ s^{(n-1)}\cdot cm^{-2}$)	n_{LDH}	R_{LDH} ($\Omega\ cm^2$)	CPE_{ox} ($F\ s^{(n-1)}\cdot cm^{-2}$)	n_{ox}	R_{ox} ($\Omega\ cm^2$)	CPE_{dl} ($F\ s^{(n-1)}\cdot cm^{-2}$)	n_{ox}	R_{dl} ($\Omega\ cm^2$)
1 hour									
Ca-Al-LDH	$3.7\cdot10^{-5}$	0.90	160	$3.7\cdot10^{-5}$	0.87	$3.5\cdot10^{4}$	$3.8\cdot10^{-5}$	0.83	$6.7\cdot10^{5}$
Ca-Al-LDH-Mn	$7.0\cdot10^{-6}$	0.89	$4.3\cdot10^{4}$	$5.5\cdot10^{-6}$	0.90	$1.2\cdot10^{3}$	$2.5\cdot10^{-6}$	0.74	$5.9\cdot10^{5}$
28 days									
Ca-Al-LDH	$6.4\cdot10^{-6}$	0.80	600	$1.6\cdot10^{-5}$	0.88	$4.0\cdot10^{3}$	$1.6\cdot10^{-5}$	0.85	$7.7\cdot10^{3}$
Ca-Al-LDH-Mn	$9.8\cdot10^{-6}$	0.82	530	$7.1\cdot10^{-6}$	0.91	$4.6\cdot10^{4}$	$2.9\cdot10^{-7}$	0.74	$4.3\cdot10^{5}$

For 1 hour of immersion, Ca-Al-LDH-Mn shows a higher value of the LDH layer resistance (R_{-LDH}) than Ca-Al-LDH (**Table 5.5**). The improved resistance of the outer LDH coating part is associated with the corrosion protection effect of the Mn incorporation. This enhanced corrosion resistance was equally confirmed by the lower values of CPE of Ca-Al-LDH-Mn coating compared to Ca-Al-LDH coating.

After 28 days of immersion time, a decrease in the overall corrosion resistance and CPE parameters is observed (**Table 5.5**). This indicates that the electrolyte has penetrated through the LDH coating and given rise to the electrochemical activities at the substrate/coating interface. Interestingly, the resistance of the inner LDH layer (R_{-ox}) of Mn-intercalated LDH increased with immersion time and became greater than that of the Mn-free coating by one order of magnitude, whereas the opposite was true for 1 h immersion: the inner part of Mn-containing LDH was less resistant than that of Mn-free LDH. This indicates that the Ca-Al-LDH-Mn shows a much better long-term corrosion performance than stand-alone Ca-Al-LDH coating thereby, thus restraining the mass transport of aggressive species towards the electrolyte/metal interface [155, 349]. The improved corrosion resistance of the Mn-containing coating was attributed to two factors:

the liberation of MnO_4^- from the coating, which act as an mixed inhibitor [389], and the hampered cathodic activity of the IMCs due to the formation of α-MnO_2 deposits.

C3.2.5. Paintability of selected LDH coatings

The flaky nature of LDH coatings explains the high hydrophilicity (i.e. low contact angle) of Ca-Al-LDH (4 ± 1º) and Ca-Al-LDH-Mn (26± 6º) coatings. Thus, the water droplet is largely absorbed by the flakes and, therefore, spreads easily, although the inhibitor intercalation process appears to decrease the coating hydrophilicity. This effect is likely to contribute to the higher corrosion resistance of the Ca-Al-LDH-Mn coating.

Paint adhesion tests revealed similar performance for the Ca-Al-LDH and Ca-Al-LDH-Mn coatings (**Figure 5.10**). Therefore, the presence of Mn-containing species in the LDH surface chemistry does not compromise paint adhesion. The literature data on paint adhesion to LDH coatings is practically non-existent, save for a single work where good results were achieved [391].

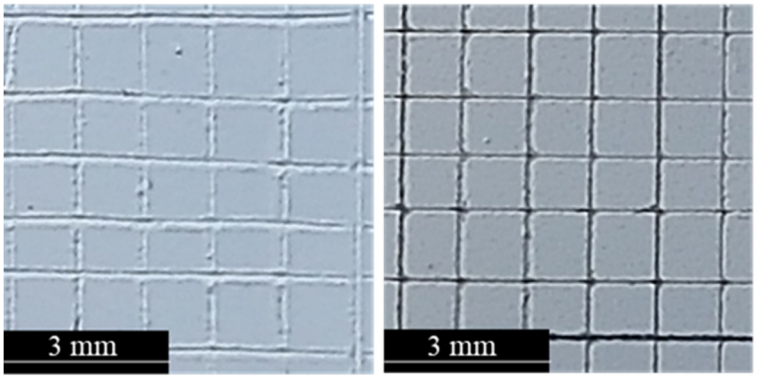

Figure 5.10. *Appearance of painted LDH coatings surfaces after the paint adhesion test. Rating 0 for both (a) Ca-Al-LDH and (b) Ca-Al-LDH-Mn.*

C3.3. Conclusions of Chapter 3

For the first time, *in situ* growth of a Ca-Al-LDH coating and its successful modification with a corrosion inhibitor was achieved on the 2024 alloy. The main conclusions can be summarized as follows:

- Among the different LDH coatings, Zn-Al-LDH and Ca-Al-LDH showed the highest corrosion resistance/thickness ratio and were selected for further inhibitor-loading post-treatments using Ni-, Li-, Mn-, W-, Ce- and Mo-species.
- MnO_4^--loading of the Ca-Al-LDH coating (0.5 µm) gave the best results in terms of corrosion resistance. Mn was detected in the coating both in the flakes and as MnO_2 precipitated at the location of secondary phases.
- MnO_4^--loading decreased the hydrophilicity of the coating without compromising its excellent paintability.

Taking into account the results presented in this chapter, Ca-Al-LDH-Mn could be used as Cr-free conversion coating for painted components in the aircraft industry. However, further tests concerning active corrosion protection ability, up-scaling and mechanical properties should be implemented in the future.

Chapter 4: PEO and HA of AM Al10SiMg alloy

Recent developments in additive manufactured Al alloys are mostly focused on the Al-Si systems as they are the easiest to process due to their low melting point and fluidity. However, there remains a knowledge gap regarding their suitability for surface treatment and tribological performance following anodizing treatments. In conventional Al alloys, anodic films for wear-sensitive applications can be obtained by either hard anodizing (HA) or plasma electrolytic oxidation (PEO). Note that conventional anodizing lacks the required hardness or thickness for such applications. Recently, several studies confirmed that AM Al alloys can be anodized [185, 189], although no data is available on their wear properties. Also, there is no straight-forward comparison regarding the morphology, composition and wear performance of HA and PEO coatings on these new alloys.

On that basis, Chapter 4 is aimed to provide information on HA and PEO coatings on an Al10SiMg AM alloy and to compare the process and coating characteristics with respect to those on a A361 cast alloy. The structure of the chapter is divided into three sections: (i) metallographic study of cast A361 and AM Al10SiMg alloys; (ii) characterization of HA and PEO coatings and; (iii) tribological properties of non-coated, HA- and PEO-coated alloys. In case of the AM alloy, the anisotropy between XY and XZ planes is evaluated. **Figure 6.1** shows the graphical abstract of Chapter 4.

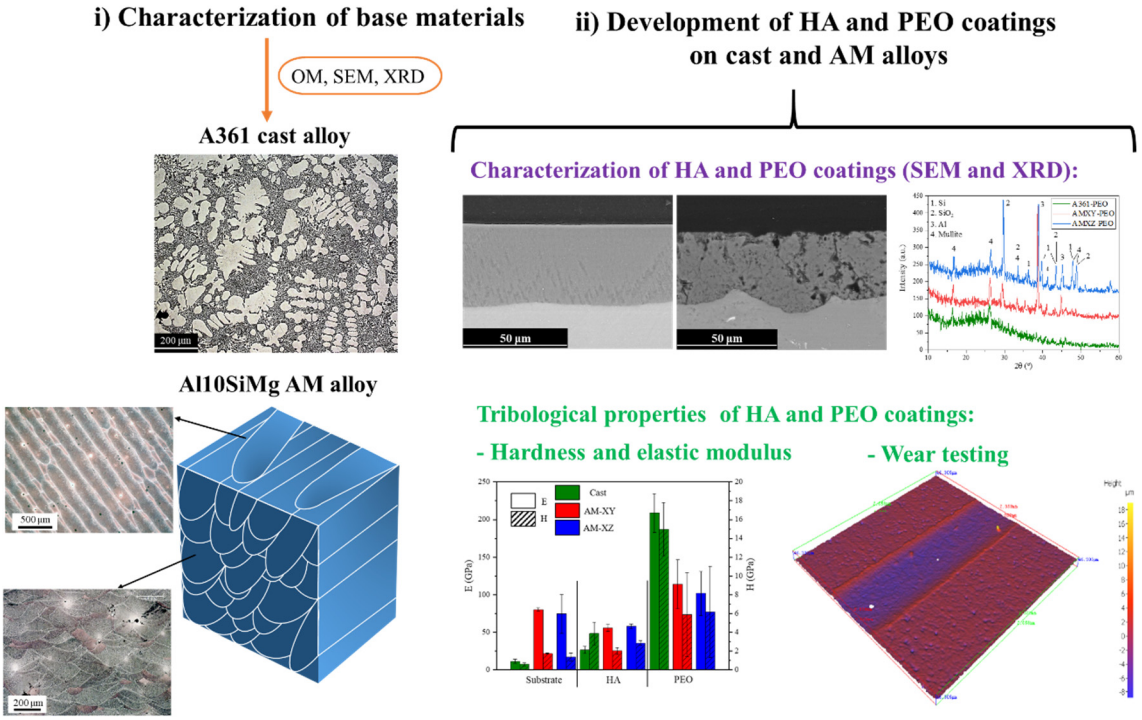

Figure 6.1. *General scheme of Chapter 4.*

C4.1. Characterization of A361 and Al10SiMg alloys

Figure 6.2 shows optical micrographs of the studied A361 alloy and both XY- and XZ-planes of the AM alloy. The A361 cast alloy reveals the characteristic α-Al dendrites and the eutectic Al-Si at the interdendritic spaces (**Figures 6.2a,b**). β-AlFeSi intermetallic needle-shaped particles are also observed due to the presence of Fe impurity [392].

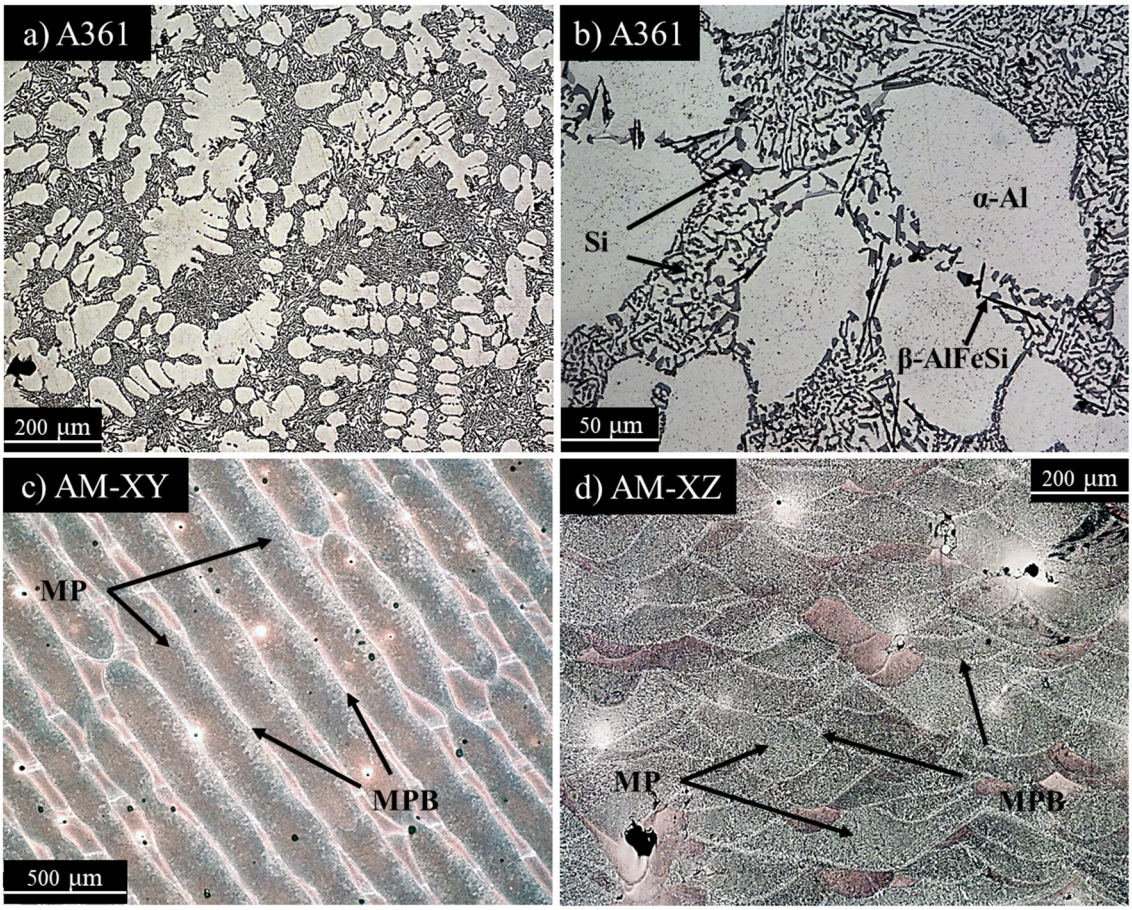

Figure 6.2. *Optical micrographs of the studied cast and AM alloys: (a-b) A361 cast alloy, (c) XY plane and (d) XZ plane of Al10SiMg AM alloy.*

In the AM alloy, the melt pools (MPs) formed by the laser path during the SLM procedure in both AM-XY (parallel to the building platform, **Figure 6.2c**) and AM-XZ (perpendicular to the building platform, **Figure 6.2d**) planes were visible due to the coarser microstructure of the melt pool borders (MPBs). Their formation is associated with the thermal gradient during the laser pass, being the cooling rate lower in the MPBs [393, 394]. The MPs appeared elongated along the laser path in the XY plane and a semicircular-like shape in the XZ plane [185].

To study the microstructure in more detail, scanning electron microscopy examination of the A361 and Al10SiMg alloys was carried out (**Figure 6.3**). Apart from the β-AlFeSi

needles, EDS maps also revealed the segregation of Mg (**Figure 6.3c**), suggesting the formation of other intermetallics such as π-AlFeSiMg and Mg_2Si [203].

Figures 6.3d,f disclose the microstructural anisotropy in both AM planes within the MPs and the coarse microstructure formed at the MPBs (**Figure 6.3e**). The brighter Si 3D network enclosed the α-Al cells, rounded in the XY plane and elongated towards the lower part of the MPs in the XZ plane. This anisotropy arises from the direction of the thermal gradient during the pass of the laser [185, 393].

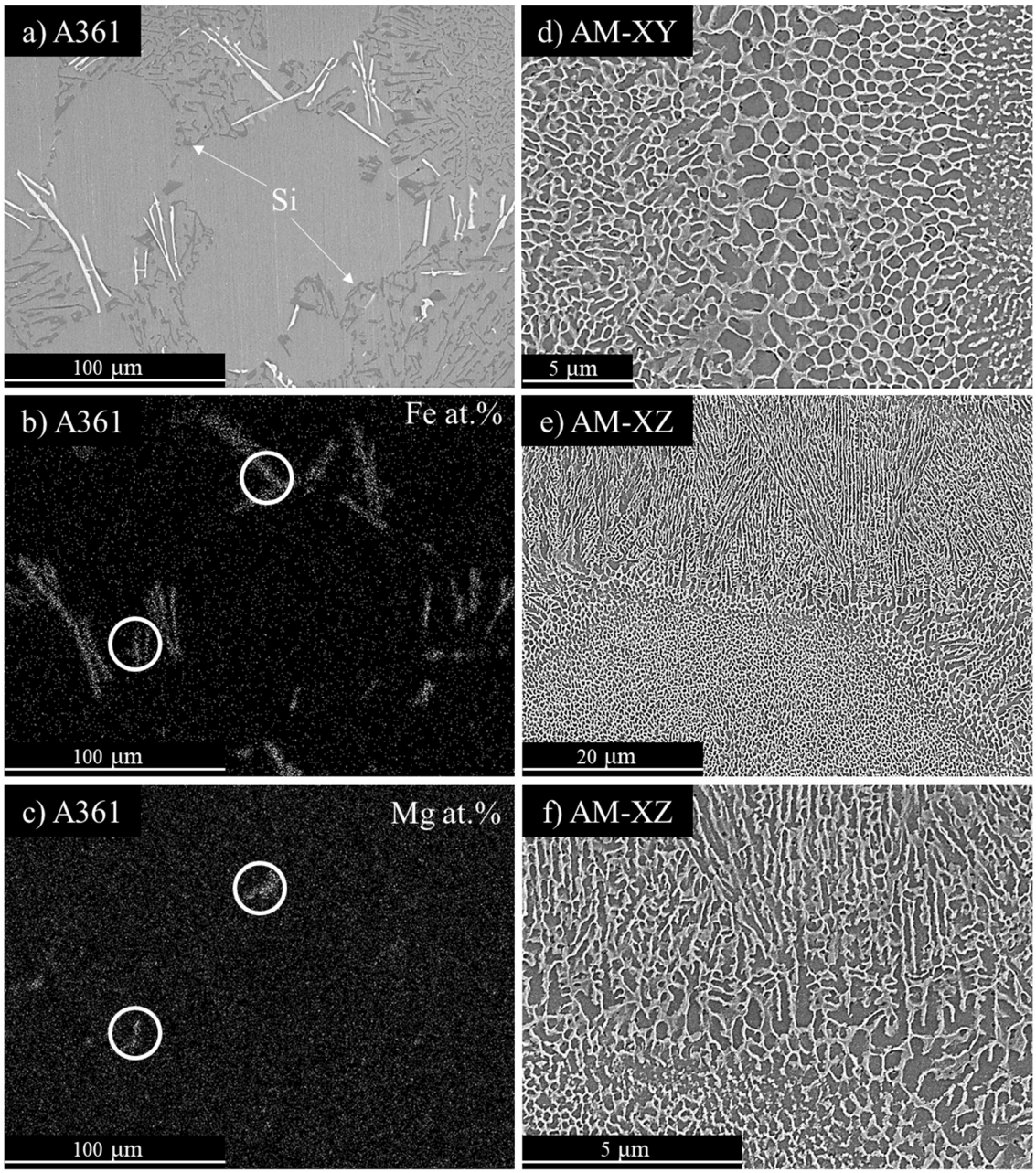

Figure 6.3. *Secondary electron micrographs of the studied cast and AM alloys: (a-c) A361 cast alloy, (d) XY plane and (e-f) XZ plane of Al10SiMg AM alloy.*

C4.2. Characterization of HA and PEO coatings

C4.2.1. Voltage-time curves

Figure 6.4 depicts the voltage-time curves recorded during the HA and PEO processes. The presented curves for the HA treatment correspond to the treatment times optimized to obtain ~50 µm-thick coatings. The treatment times for PEO, on the other hand, were adjusted in order to obtain ~80 µm-thick coatings in all the specimens.

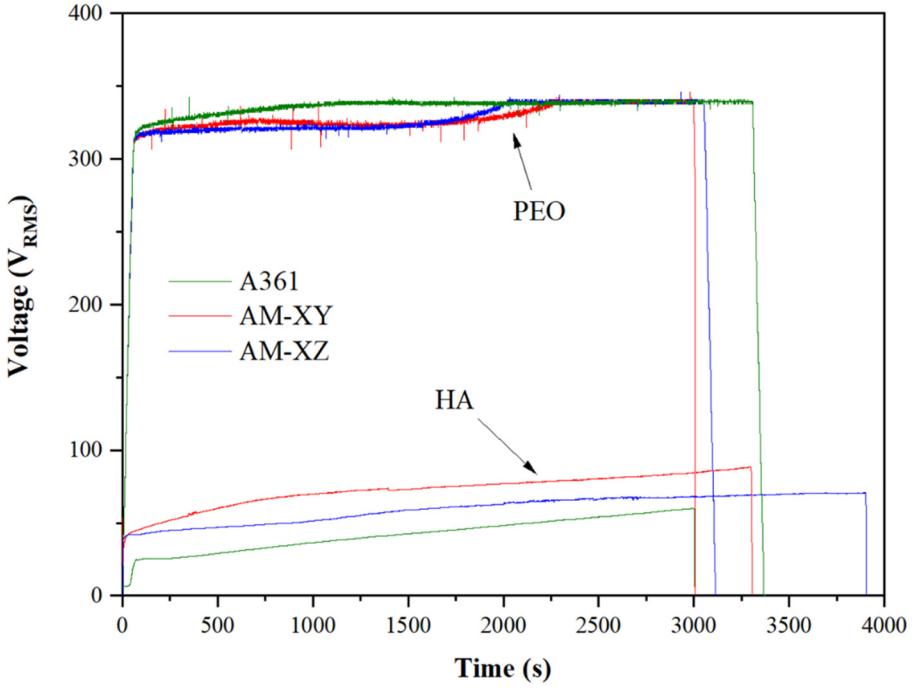

Figure 6.4. *Voltage-time responses during HA and PEO treatments of A361 and XY- and XZ-planes of Al10SiMg AM alloy.*

During the PEO process, the A361 reached the formation voltage of 340 V after ~1200 s, while the AM samples reached this voltage at ~2250 s after maintaining for an extended period a constant segment at ~324 V (**Figure 6.4**). The higher voltage of the A361 specimen at the early stages indicated a higher coating resistance, which is due to an increased thickness and density of the coating over the entire specimen surface [189, 395]. In the AM alloy, voltage-time trends were similar in both XY and XZ planes, i.e. the different orientation of MPs does not have any effect on the PEO process.

During the HA process, on the other hand, the voltage and treatment time of the AM planes were higher than the ones of the A361 cast alloy. At the same time, while the AMXY plane required a higher voltage than the AMXZ plane (~25 V), longer treatment times (by ~750 s longer) for the AMXZ were needed (**Figure 6.4**).

Previous studies by Revilla *et al.* [172, 185] reported the anisotropic anodizing behaviour

of AM alloys. According to them, this was attributed to the fact that during anodizing of the XY plane, the anodization front periodically encounters a barrier in form of MPBs, whereas in the XZ plane the anodizing front moves parallel to the MBPs.

To clarify this, **Figure 6.5** represents a simplified view of the AM microstructure. White lines represent coarser MPBs, whereas red and green arrows represent the anodic front that advances in the directions normal to the XY and XZ planes, respectively.

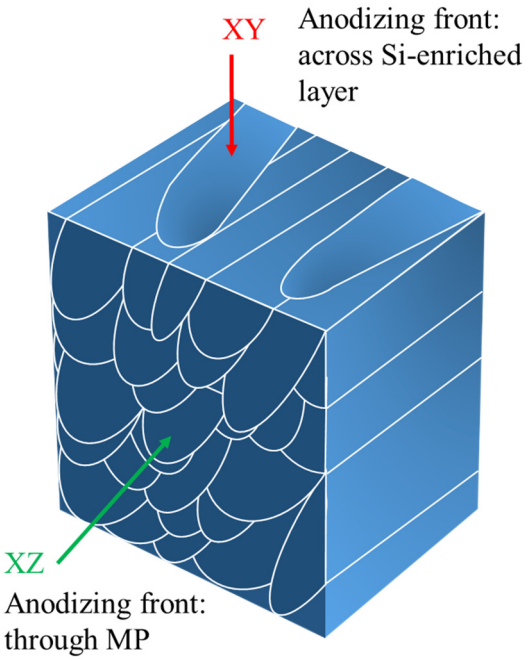

Figure 6.5. *Schematic view of anodizing fronts for both XY and XZ planes in Al10SiMg AM alloy.*

The anodizing front would encounter two different situations: XZ) moving through the MPs, thus coming across rounded (but long in-depth) Al cells and the fine Si network; XY) moving across the bottom of the MPs where it would face a Si-rich layer in the MBPs. The anodic front would alternate more resistive Si-rich layers when moving across the XY planes where the required anodizing voltage would be greater than at the MPs when moving across the XZ planes (**Figure 6.4**). On the other hand, the anodizing of the XZ plane would encounter MPs and perpendicular MPBs rather than alternate resistive layers.

C4.2.2. HA and PEO coatings microstructure

Figure 6.6 depicts the cross-sectional scanning electron micrographs and EDS Si maps (third column, corresponding to the area in the second column) of the HA (a-f) and PEO (g-l) coatings, prepared for the subsequent wear tests.

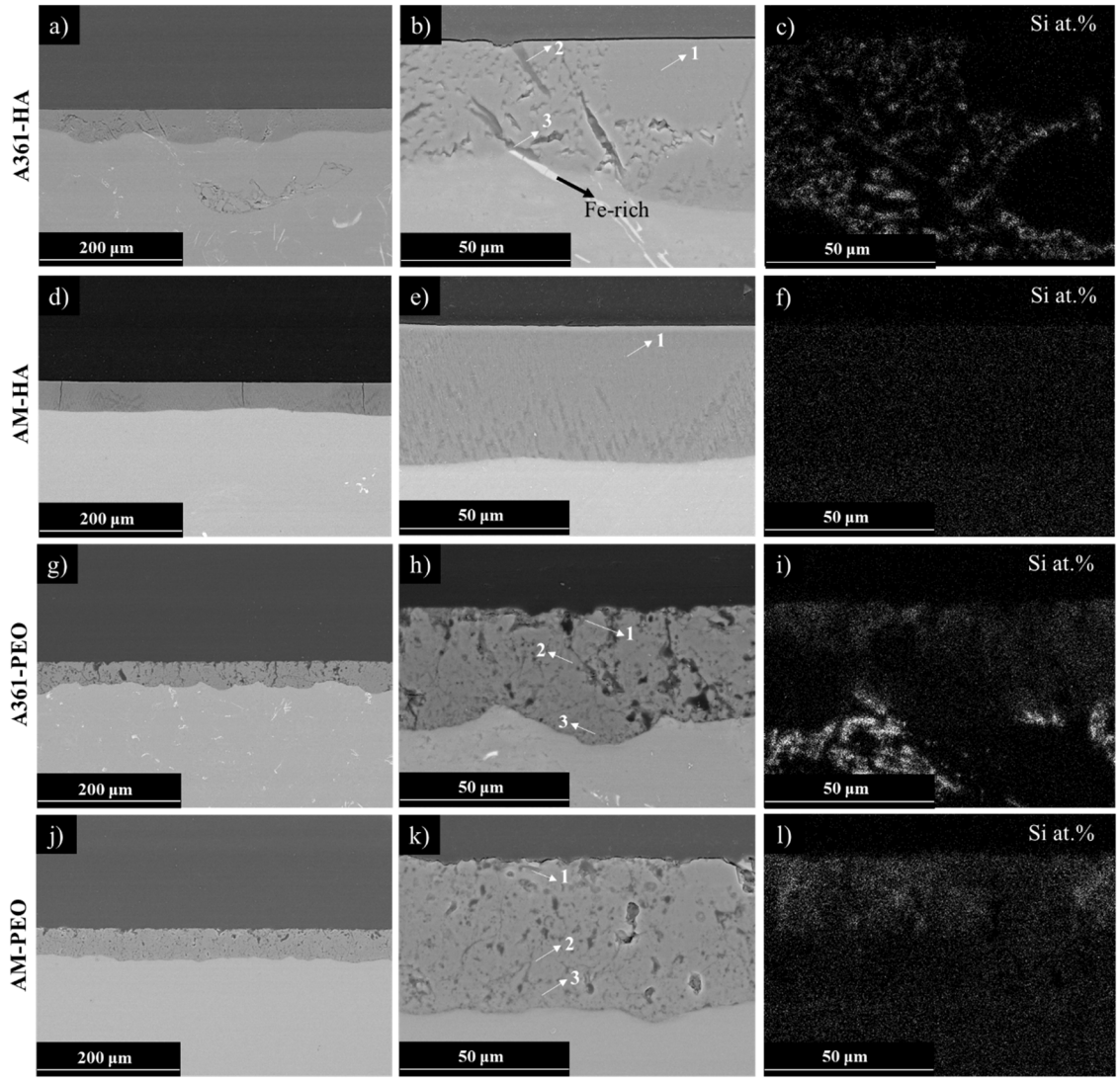

Figure 6.6. *Scanning electron micrographs of the studied (a-c) HA-coated A361 cast and (d-f) AM-XY alloys and PEO-coated (g-i) A361 cast and (j-l) AM-XY alloys.*

Apart from the Si distribution, EDS maps (**Table 6.1**) also revealed that studied coatings were mainly composed of species derived from the electrolytes (O, Na, Si, S and K) and from the substrate (Al, Si and Fe).

The A361-HA coating presented signs of partially oxidized Si crystals and intermetallics within the coating (marked as 2 and 3 in **Table 6.1**; **Figure 6.6b**) and a hampered interface at the Si-rich eutectic regions of the material. The large size of the Si crystals at these eutectic regions impeded the complete anodization of the substrate and shielded the material beneath them. As a result, these sections of the coating were thinner and heterogeneous [393]. Porosity at these sections was linked to the formation of cavities by oxygen gas evolution during Si oxidation [276]. Further cavities might be formed via release of localised thermal and/or volume expansion stresses around the Si particle [172,

396]. Detachment of large particles could also take place during metallographic preparation. In contrast, thicker and compact regions of the A361-HA coating corresponded to anodized α-Al dendrites (marked as 1 in **Table 6.1**; **Figure 6.6b**).

Table 6.1. *EDS analysis of the selected HA- and PEO-coated A361 cast and AM-XY alloys (at. %).*

Coating	Location	O	Na	Al	Si	S	K	Fe
A361-HA	1	60.2	-	34.1	0.7	5.0	-	-
	2	57.1	-	21.8	17.4	3.2	-	0.5
	3	50.4	-	25.0	19.0	2.9	-	2.8
AM-HA	1	54.6	-	35.3	5.3	4.8	-	-
A361-PEO	1	57.1	-	30.4	10.5	1.0	1.0	-
	2	58.2	-	38.2	3.0	0.2	0.4	-
	3	58.9	-	38.1	1.9	0.6	0.5	-
AM-PEO	1	54.2	0.8	26.0	15.8	-	3.1	-
	2	52.0	0.2	41.9	4.8	-	1.1	-
	3	48.9	0.6	39.1	8.6	-	2.8	-

The AM-HA coatings were more compact (i.e. less porosity) and had a flat coating-substrate interface. Si at. % maps (**Figure 6.4f**) showed the homogeneous distribution of Si with an average content of 5.3 at. % (**Table 6.1**; **Figure 6.6e**). These morphological and chemical features were the result of the fine Si-network that led to the complete oxidation of Si [172, 185]. MPBs produced certain heterogeneities in the morphology and retraced interface due to the coarser size of Si crystals.

The PEO coatings on both A361 and AM alloys showed a high density of micro and sub-micro pores and thermal cracks associated with gas evolution and to the action of micro-discharges during the PEO process (**Figures 6.4g-l**) [189]. The A361-PEO coating appeared to have finer porosity than the AM-PEO coatings, although scattered and relatively large pores are visible in some areas. The coating-substrate interface was found flatter in the AM-PEO samples probably due to the fine distribution of Si (**Figure 6.4k**), while the shielding effect of large Si crystals thinned the PEO coating over the eutectic regions of the cast alloy (**Figures 6.4h,i**).

Nevertheless, the retrace of the coating-substrate interface in the A361-PEO specimen was less accentuated than in the case of the A361-HA probably due to the more aggressive character of plasma discharges. For both A361-PEO and AM-PEO coatings, Si was found to be preferentially incorporated at the upper part of the coating due to the incorporation of electrolyte Si-rich species (**Figures 6.4i,l**; **Table 6.1**). According to the EDS results presented in Table 1, the content of Si in the AM-PEO specimens was slightly higher than in the case of the A361-PEO coating, increasing the formation of SiO_2 [397].

To ascertain the nature of Si and Al in the studied coatings, XRD patterns of the substrates, HA-coated and PEO-coated specimens are represented in **Figure 6.7**. The XRD patterns of the substrates (**Figure 6.7a**) revealed the Al diffraction peaks at ~38º and ~45º and weaker diffraction at ~28º corresponding to Si, which was observed as a defined peak in the A361 sample and as a broadened band in the AM samples. This was in agreement with the size of the Si particles in both types of material since no substantial differences between both AM planes were observed.

The XRD patterns of the HA-coated samples (**Figure 6.7b**) revealed the presence of Al from the substrate and a wide band between 20 and 35º, suggesting the presence of ordered amorphous alumina [187, 227, 398, 399]. The latter is in good agreement with the general amorphous character of anodic Al films [46, 187, 227, 400].

The marked Si diffraction peak in the A361-HA coating was probably due to a combined contribution from the Si in the substrate and the un-oxidized particles within the coating. However, no SiO_2 diffraction peaks were identified. This could be related to the hampered oxidation of the large Si particles from the substrate.

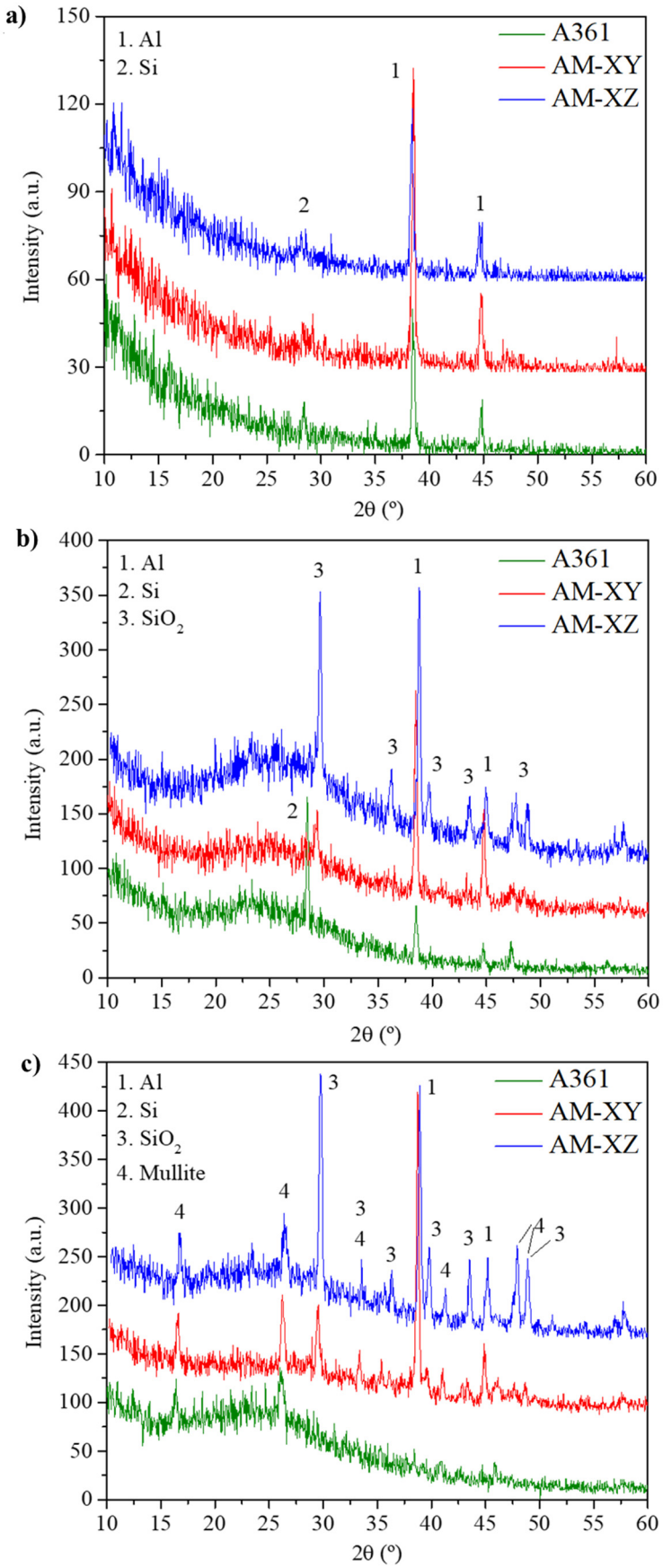

Figure 6.7. *XRD patterns of (a) un-coated, (b) HA-coated and (c) PEO-coated A361 and AM planes.*

For AM-HA coatings, the presence of SiO_2 was detected (**Figure 6.7b**). Several studies reported that the finer and homogeneous distribution of Si in the AM samples eased its oxidation, thus leading to the formation of SiO_2 during the anodizing process [276, 396]. Nevertheless, a significant difference regarding the relative intensity of SiO_2 between the HA coatings formed in both AM planes was identified; the AMXZ-HA presenting a higher SiO_2 content than the AMXY-HA. This difference may be related to a decreased fraction of oxidized Al and Si in the AMXY-HA coating resulting from the higher density of MPBs and their quasi-parallel disposition with respect to the anodizing front.
In that regards, Revilla *et al.* demonstrated that as the size of Si crystals increased, the percentage of oxidized Si decreased [170]. Henceforth, these Si-rich layers could have increased the content of un-oxidized material in the AMXY-HA. On the other hand, Zhu *et al.* showed that when large plate-like Si crystals were parallel to the anodizing front (XY plane), the portion of non-oxidized Si increased and Al became shielded [396]. The bottom of the MPBs could have had a similar effect, thereby preserving the Al underneath them.

The mechanism of coating formation during PEO was significantly different from the HA growth mechanism, since the dielectric breakdown of the anodic oxide and generation of microdischarges gave rise to formation of high temperature crystalline phases. As stated for AM HA-coated specimens, the XZ plane promoted the formation of a less resistive film mostly due to the coating developed at the MPs. Likewise, the PEO on the XZ plane would present a higher density of discharges, thus promoting the incorporation of electrolyte elements (Si) and the formation of crystalline phases such as SiO_2 and mullite ($Al_2O_3 \cdot SiO_2$) (**Figure 6.7c**).

C4.3. Mechanical properties

C4.3.1. Hardness and Elastic modulus

Figure 6.8 depicts the hardness (H) and the elastic modulus (E) of the non-coated, HA-coated and PEO-coated specimens determined in nanoindentation experiments on the cross-section.

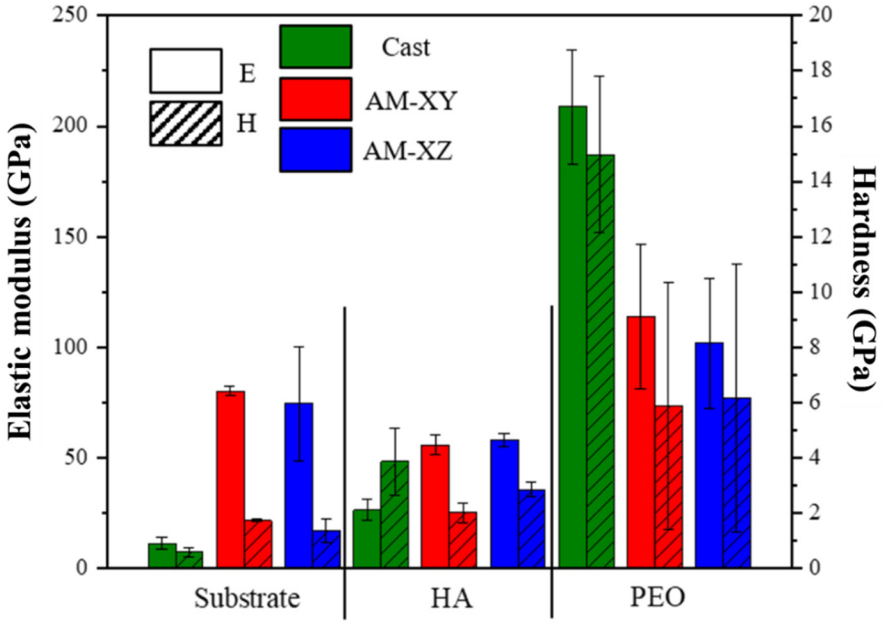

Figure 6.8. *Hardness (H) and the elastic modulus (E) values of un-coated, HA-coated and PEO-coated A361 and AM planes.*

AM substrates were slightly harder (1 – 2 GPa) and approximately seven times stiffer (~75 GPa) than the A361 specimen (0.5 and 10 GPa, respectively). Regarding the response of the HA treated specimens, it appeared that the 3D SiO_2 network developed within the AM-HA led to higher E (~55 GPa) than in the A361-HA (26 GPa). On the other hand, the H of the AM-HA coatings was found between 2 and 3 GPa while the one of the A361-HA specimen was ~ 4GPa.

These results indicated that, either in the metallic or oxide state, the 3D network distribution of Si provided higher elastic recovery than the bulk α-Al/alumina dendrites and eutectic regions of the A361 alloy [401]. On the other hand, the lower H of the AM-HA specimens could be also related to the homogeneous formation of SiO_2, which is known to be softer than alumina (~2 GPa, [402]). The H measured for the A361-HA specimen was in agreement with other H values reported for amorphous hard anodic alumina film (~5 GPa, [403]). The softer silica network and the size of harder alumina cells could be considered as a source of plastic deformation, i.e. decreasing the H of the AM-HA. Fracture of the SiO_2 network and/or intra-granular cracking might lead to relative movements of the alumina cells (i.e. rotation and sliding) during the indentations increasing the plasticity and, in turn, reducing the measured H [227, 396].

In comparison with the bare substrates and amorphous HA coatings, the PEO coatings showed higher H and E. The A361-PEO specimen showed higher H and E (15 GPa and

~180 GPa, respectively) than the AM-PEO specimens (6 GPa and ~105 GPa, respectively).

The obtained H values were in good agreement with previous reports on PEO coatings composed by crystalline α- and γ-Al_2O_3, mullite ($Al_2O_3 \cdot SiO_2$) and amorphous alumina obtained in silicate or alumina-silicate electrolytes on Al-Si alloys (~9 – 16 GPa) [267, 397].

It is worth recalling that the AM-PEO specimens were found to have a homogeneous outer Si-rich layer where crystalline SiO_2 would have formed. This phase distribution was in contrast to the heterogeneous distribution of the phases in A361-PEO which had higher Si (and therefore, presumably, mullite) contents above eutectic regions of the alloy where the Si content is higher. Gulec *et al.* [397] confirmed that the micro-hardness of the PEO coatings, as well as the contents of γ-Al_2O_3 and mullite, decreased with the content of Si in the cast alloy. The authors reported a 1000 HV micro-hardness (~9.8 GPa) for the PEO coating fabricated on the Al-12Si alloy. The lower H of the AM-PEOs (~ 6GPa) compared with A361-PEO (15 GPa) may be assigned to the homogeneous formation of softer SiO_2. Slonova and co-workers [404] used a silicate electrolyte for the PEO treatment of an hypereutectic AK21 alloy (20-22 Si wt.%). The authors reported high Si content in the PEO coating and wide-spread formation of amorphous SiO_2 together with α-Al_2O_3, γ-Al_2O_3 and mullite. The resulting H of the coating was about 4.5-5 GPa. Recently, Rogov *et al*. [405] fabricated a PEO coating in a silicate electrolyte after a pre-anodizing stage on an SLM Al-12Si alloy. The authors reported the formation of an amorphous silica coating with 520 $HV_{0.2}$, which is equivalent of 5.1 GPa. Henceforth, the softer mechanical response and large dispersion of the H values of the AM-PEO coating (**Figure 6.7**) compared to the A361-PEO coating could be due to the homogeneous formation of softer SiO_2.

C4.3.2. Wear testing

C4.3.2.1. Friction coefficients

The friction coefficients (F_c) measured for the non-coated, HA-coated and PEO-coated A361 and AM alloys are shown in **Figure 6.9**. It is worth pointing out that the friction coefficients were measured every 2 m and the first data point of the series corresponded to the second meter.

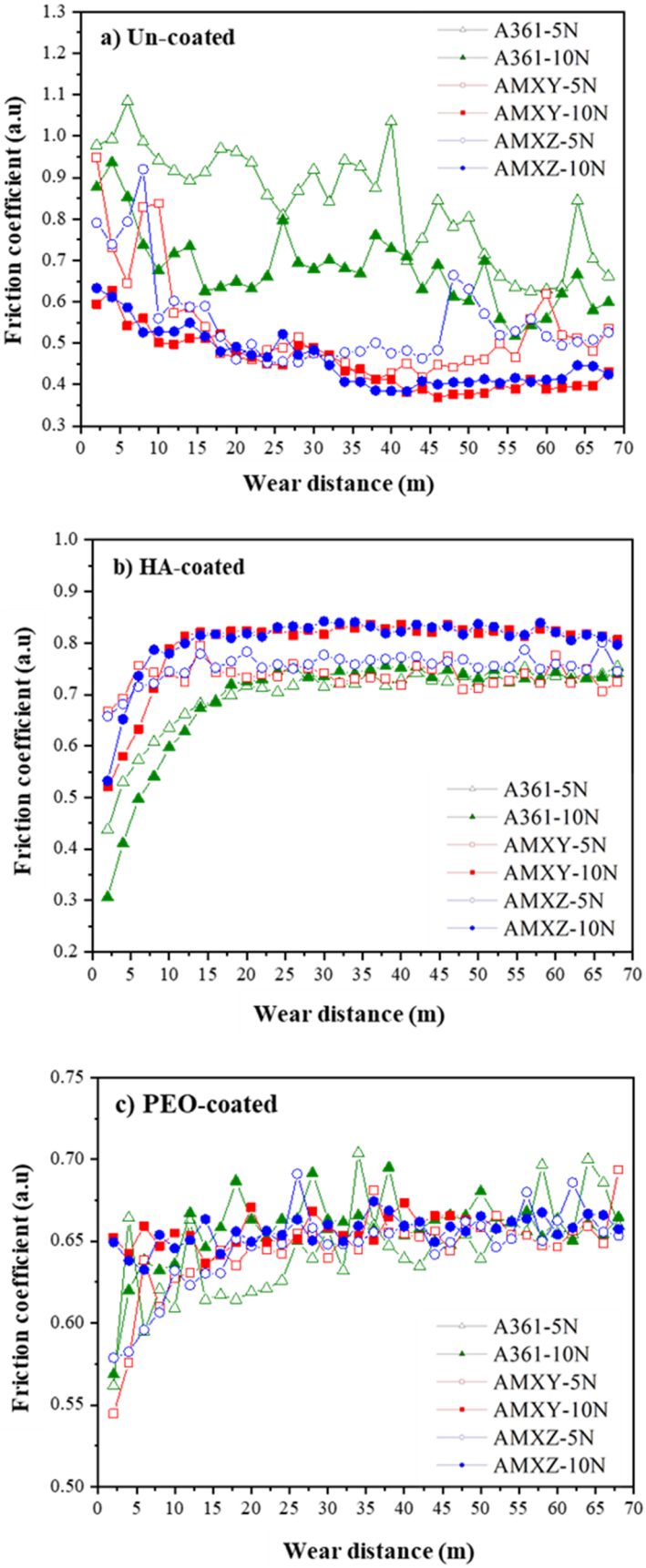

Figure 6.9. *Friction coefficients for the (a) un-coated, (b) HA-coated and (c) PEO-coated A361 and AM alloys.*

The F_c of the substrates decreased with the wear distance (**Figure 6.9a**). For both A361 and AM alloy (XY- and XZ-planes), the initial values were 0.8-1 at 5 N and 0.6 for 10 N. The values of the cast alloy decreased almost linearly to ~0.65 at the end of the tests. For the AM alloy, the F_c reached a steady-state beyond 30 m. The final F_c of the AM samples at 10 N was lower (0.4) than the ones at 5 N (~0.55). The cast alloy presented large oscillations in contrast to the smoother evolution of the AM samples, which may be related to the more homogeneous AM microstructure.

The friction coefficients of the HA-coated specimens (**Figure 6.9b**) reached a plateau after a running-in period. The running-in period was longer for the A361-coated sample at both loads, thus achieving a plateau at ~0.75 after a wear distance of 25 m. The AM-coated samples presented a significantly shorter running-in period reaching the steady-state at approximately 10 m for both loads. These samples showed a clear load dependence, the friction coefficients being 0.75 at 5 N and 0.8 at 10 N. The PEO-coated specimens experimented a steady-state at about 0.65 for almost the entire tests at both loads (**Figure 6.9c**).

C4.3.2.2. Wear rates

The calculated wear rates (W_r) for the non-coated, HA-coated and PEO-coated A361 and AM alloys are shown in **Figure 6.10**. W_r were calculated by measuring the wear volume produced by the tests. Wear surfaces and the cross-section of the tests were examined in a SEM.

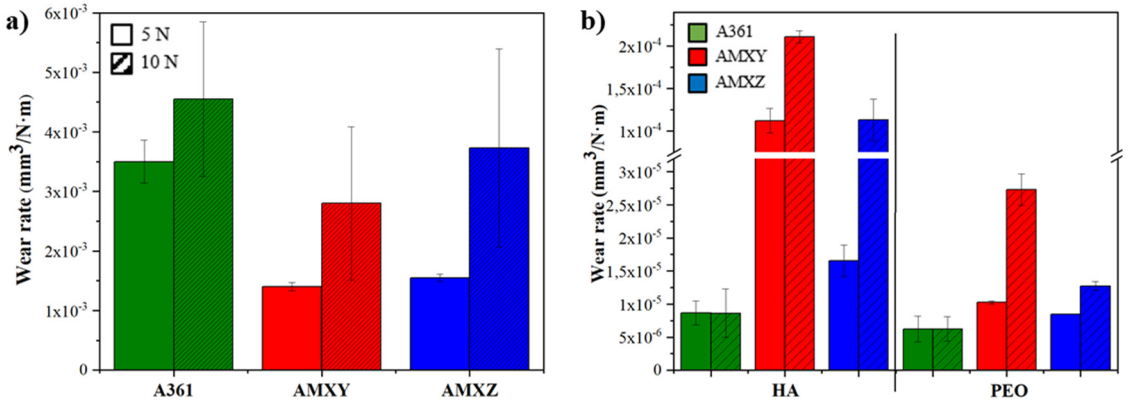

Figure 6.10. *Wear rates for the (a) non-coated and (b) HA-coated and PEO-coated A361 and AM alloys at 5N and 10N.*

These results proved the beneficial effect of HA and PEO treatments in the wear performance of the studied alloys, reducing W_r at both loads in comparison to the non-coated specimens (~10^{-3} mm^3 N^{-1} m^{-1}) (**Figure 6.10a**) by up to one magnitude order for

AM-HA (~10^{-4} mm^3 N^{-1} m^{-1}) and two orders for AM-PEO, respectively (from ~10^{-5} mm^3 N^{-1} m^{-1}) (**Figure 6.10b**). The W_r reduction was also significant in the case of the cast alloy, being reduced from ~$4 \cdot 10^{-3}$ mm^3 N^{-1} m^{-1} to $7.5 \cdot 10^{-6}$ mm^3 N^{-1} m^{-1} for both treatments and loads.

The W_r of the coated specimens were in good agreement with the hardness measurements indicating that the hardness of the constituents of the coating dominated the wear behavior. It should be noted that the AM-PEO specimens showed slightly higher W_r than the A361-HA specimens, which could be assigned to the hardness dispersion of the AM-PEO (**Figure 6.7**).

The A361 cast alloy subjected to both surface treatments showed the best wear performance ($0.75 \cdot 10^{-5}$ mm^3 N^{-1} m^{-1}). Also, for both treatments, the W_r did not change with the applied load. This behaviour and the W_r values for these specimens were in good agreement with previous reports and demonstrated a great load-bearing capacity of the coatings due to their enhanced hardness and stiffness compared with the underlying substrate [187, 406].

Similarly to the friction coefficients (F_c), the HA-coated AM specimens showed a clear load dependence, the W_r being higher at 10 N. For both surface treatments and loads, XZ-plane showed lower W_r than the XY-plane at both loads. On the other hand, the PEO-coated AM specimens showed a better performance than the HA coatings, with lesser anisotropy at lower load. This behavior was in contrast to that of the non-coated planes, where the AMXZ plane showed higher W_r values.

The AM-HA specimens presented noticeable anisotropy. It have probably arisen from the enhanced crystallinity of the AMXZ-coated samples compared with the AMXY-coated ones (**Figure 6.7**). For the HA coatings, the anisotropy stemmed from the slightly lower hardness of the AMXY-HA, which was richer in SiO_2 [187]. More specifically, coated specimens showed better wear performance in the following order: A361-PEO > A361-HA > AMXZ-PEO > AMXY-PEO > AMXZ-HA > AMXY-HA.

C4.3.2.3. Wear mechanism for HA-coated specimens

The SEM images of the wear tracks on the HA-coated specimens at 10 N are shown in **Figure 6.11**. **Table 6.2** shows the EDS results at various locations on wear tracks of HA-coated specimens

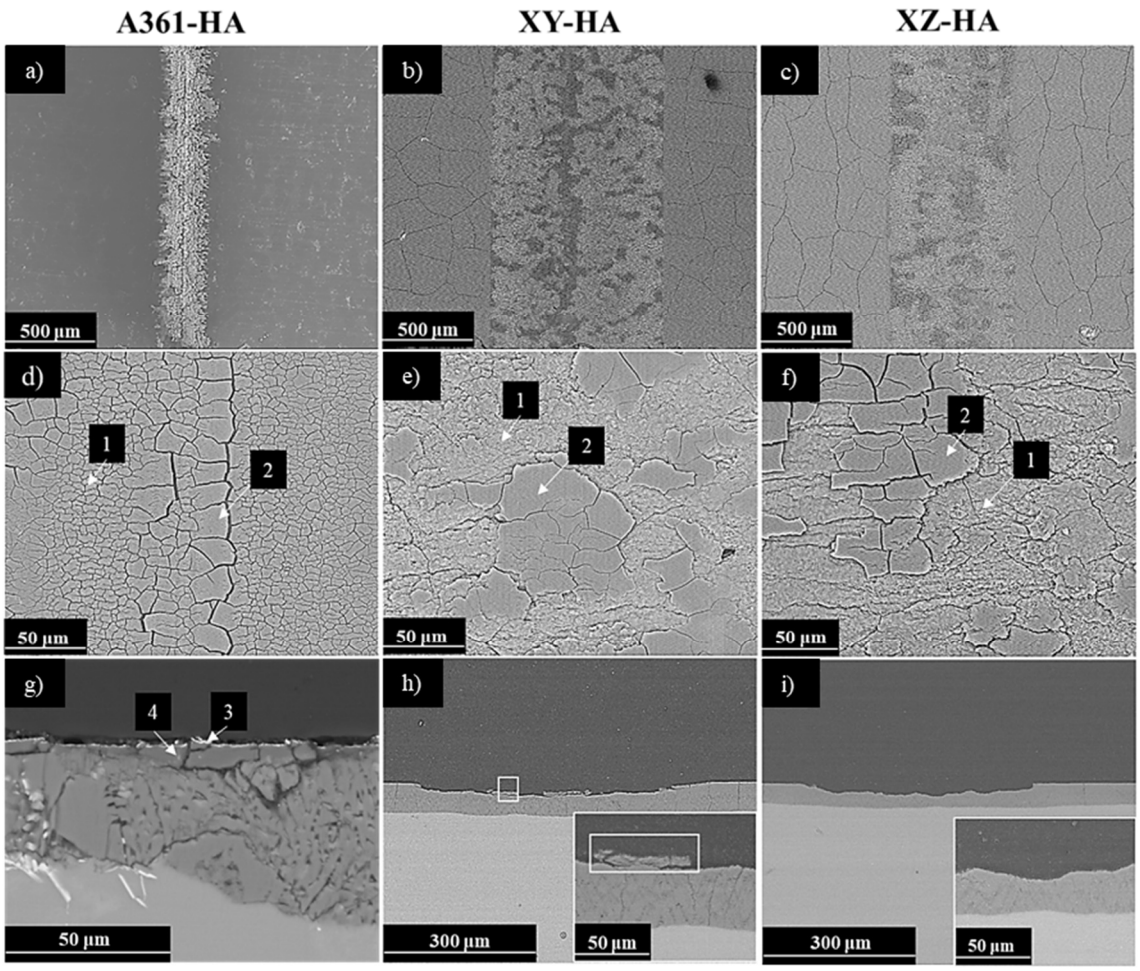

Figure 6.11. *(a-f)Plan views and (g-i) cross-sections of the wear tracks at 10 N after 70 m of HA coated A361 and AM alloys (XY and XZ planes).*

Table 6.2. *Concentrations (at. %) of elements obtained by EDS analysis at various locations on wear tracks of HA-coated A361 and AM alloys. Locations are denoted in the SEM micrographs in* ***Figure 6.11****.*

Coating	Location	C	O	Al	Si	S
A361-HA	1	33.8	38.7	19.9	4.1	3.5
	2	18.5	49.9	24.9	2.4	4.3
	3	55.4	37.6	5.3	1.1	0.7
	4	23.4	62.5	10.6	2.4	1.1
XY-HA	1	-	58.4	35.0	6.0	0.6
	2	15.9	54.1	23.1	3.3	3.6
XZ-HA	1	25.5	34.8	30.6	4.0	5.1
	2	18.4	44.8	28.4	4.2	4.2

The evident differences between HA-coated alloys in the wear track width (**Figure 6.11**) were in good agreement with the W_r shown in the previous section: AMXY-HA > AMXZ-HA > A361-HA. At higher magnification (**Figure 6.11a**), the wear surface in the A361-HA sample consisted entirely of a smooth and cracked tribolayer (**Figure 6.11d**).

For the AM-coated samples, the wear track showed a rougher surface and isolated tribolayer islands with sharp edges (**Figures 6.11e-f,** corresponding to darker areas in **Figures 6.11b,c**). The F_c data suggests that the tribolayer in AM HA-coated samples rapidly formed during the first meters of the tests (running-in period) and progressively wore off during the steady-state segment. Similarly to the A361-HA specimen, cracks were observed in both detached areas and tribolayer islands (**Figure 6.11a**). The chemical composition of the tribolayer is practically the same as for the HA-coatings (**Table 6.2**). The sharp edges corresponded to the fractures of the isolated tribolayer islands, thus indicating that cracking was formed during the test before detachment.

Cross-section images showed the curved surface of the coatings after the wear tests (**Figures 6.11g-i**). The top part of the AM-coated specimens at the wear track had a saw-like surface corresponding to the detached areas. At the top of the AMXY-HA cross-section, a plate-like particle from the tribolayer islands was identified (**Figure 6.11h**).

Coating cracks marked with a white square in **Figure 6.11h** were found in the AMXY-HA sample. Horizontal cracks under the tribolayer plate suggested that these would have grown beneath the tribolayer via shear forces producing the subsequent detachment by tension due to the stylus passing-over. No through-thickness cracks in the AMXZ-HA were identified, which could indicate that for this specimen, flaws were sub-superficial.

The AM-HA coatings failure was found to consist of the detachment of the superficial tribolayer via cracking underneath the tribolayer, as observed in **Figures 6.11h,i**, due to maximum shear stresses. The AMXY-HA specimen may have suffered notable damage due to the action of these maximum shear stresses at softer SiO_2-enriched locations (**Figure 6.11h**).

C4.3.2.4. Wear mechanism for PEO-coated specimens

The SEM images of the wear tracks on the PEO-coated specimens at 10 N are shown in **Figures 6.12**. The width of the wear tracks maintained the same tendency observed with the W_r results for the PEO-coated samples: AMXY-PEO > AMXZ-PEO > A361-PEO. All the specimens presented the same smooth and sharp flake-like wear surface without significant detachment (**Figures 6.12a-c**). At higher magnifications, the SEM

images revealed some contrast within the track. EDS measurements (marked in **Figures 6.12d-f**) showed traces of W, in higher content at the brighter areas, indicating the damage of the WC counterpart and its transfer to the tribolayer (**Table 6.3**). Fine bright speckles with a slightly higher content of W were also observed in AMXY-PEO coating (**Figure 6.12e**). Cross-section SEM images did not reveal significant surface curvature at the wear locations. However, a thin brighter layer was found at the top of these regions (**Figures 6.12g-i**) corresponding to the W-rich tribolayer (**Table 6.3**). The higher elastic recovery of the PEO coatings and their ceramic-protective nature prevented the cracking as it provided enough deformation ability.

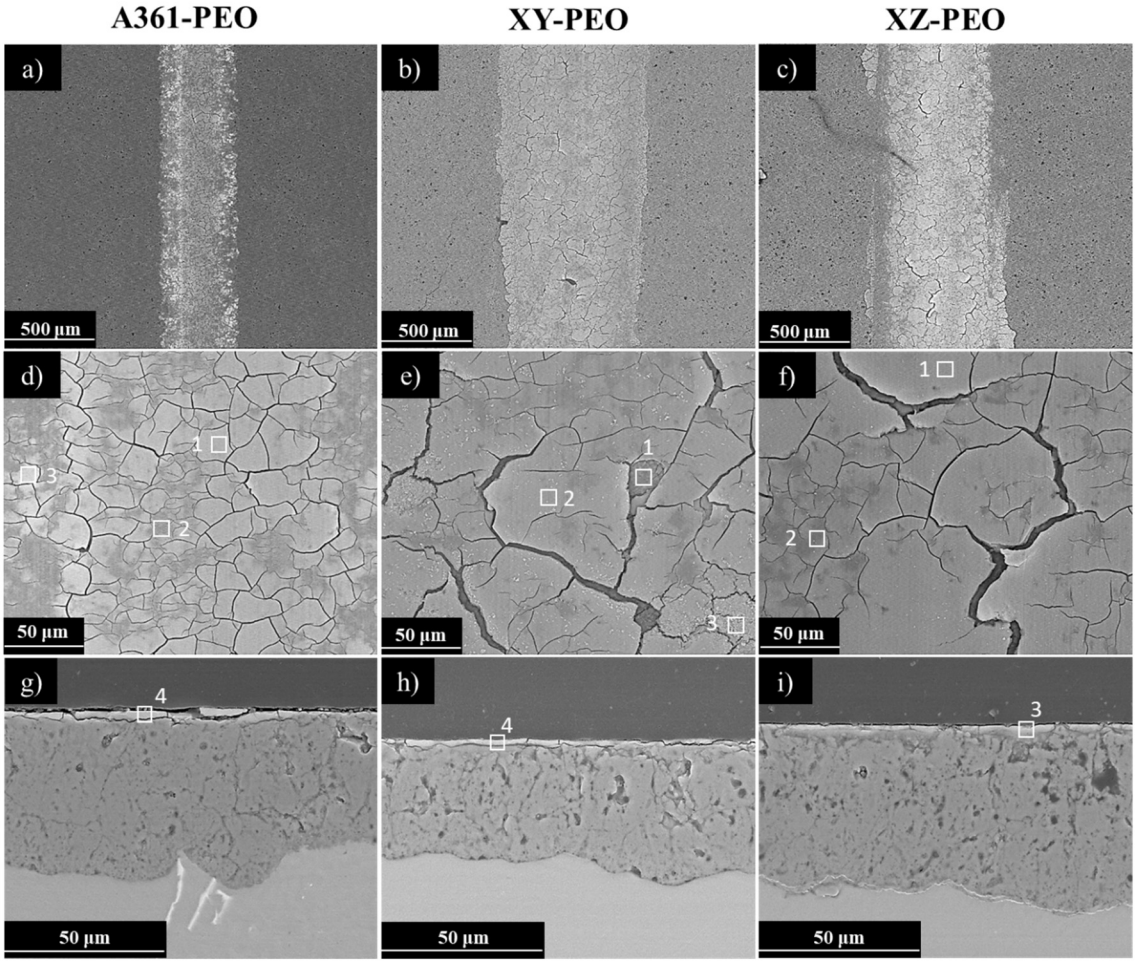

Figure 6.12. *(a-f) Plan views and (g-i) cross-sections of the wear tracks at 10 N after 70 m of PEO coated A361 and AM alloys (XY and XZ planes).*

Table 6.3. *Concentrations (at. %) of elements obtained by EDS analysis at various locations on wear tracks of PEO-coated A361 and AM alloys. Locations are denoted in SEM micrographs in* ***Figure 6.12****.*

Coating	Location	O	Al	Si	K	W
A361-PEO	1	54.0	27.9	11.9	3.4	2.8
	2	51.2	33.0	13.6	1.6	0.6
	3	56.6	24.6	10.5	3.70	4.6
	4	74.3	17.7	5.9	0.8	1.3
XY-PEO	1	50.1	32.5	14.2	2.8	0.4
	2	56.6	25.1	13.4	3.1	1.8
	3	55.6	23.4	14.5	4.3	2.2
	4	69.4	17.4	10.3	1.6	1.3
XZ-PEO	1	65.0	21.1	9.3	2.0	2.6
	2	52.1	27.0	18.3	2.6	-
	3	65.2	20.7	10.9	1.8	1.4

C4.4. Conclusions of Chapter 4

Some conclusions can be drawn regarding the effects of Al10SiMg AM alloy microstructure on HA and PEO processes and tribological performance of the resultant coatings:

- In the A361 cast alloy large eutectic silicon structures are present, while in the Al10SiMg AM alloy the eutectic silicon was more finely and uniformly distributed. This influenced the coatings growth kinetics in both HA and PEO treatments, resulting in significant differences with respect to the A361 counterpart in terms of morphology, composition and phases formation. Moreover, the anisotropic microstructure between the XY and XZ orientations of the AM alloy was also reflected in the HA and PEO treatments.
- The fine 3D Si network was fully oxidized during the HA treatment producing compact and homogeneous coatings consisting on amorphous alumina cells enclosed in a crystalline 3D silica network. The Si network provided the most homogeneous PEO coatings and the widespread incorporation of Si, providing the predominant formation of crystalline SiO_2, in contrast to its absence within the coatings on the A361 cast alloy. The anisotropic microstructure of the AM alloy led to higher contents of crystalline SiO_2 within the coatings fabricated on the XZ plane for both treatments.
- Wear resistance was strongly influenced by the ceramic nature of the studied HA and PEO coatings, which in turn is strongly influenced by the Si distribution. The PEO treatment effectively improved the wear resistance of the AM alloy. Nevertheless, the widespread formation of SiO_2, preferentially near to the surface of the PEO coatings, was detrimental for wear resistance in comparison to the cast PEO treated A361 alloy. Significant anisotropy after PEO treatment in the wear performance between the XY and XZ planes was only observed with a normal applied force of 10 N during the wear tests. These results indicate that further PEO treatments of Al-Si AM alloys should be aimed to reduce the content of SiO_2 in favor of mullite or alumina phases. The wear performance was: A361-PEO > A361-HA > AMXZ-PEO > AMXY-PEO > AMXZ-HA > AMXY-HA.

In conclusion, these results are highly relevant to understanding the relation between the Si distribution and the formation of HA and PEO coatings on Al-Si AM alloys, which is the first step in achieving wear protection systems for aircraft applications

5. Conclusions

The development of novel Cr-free protective surface treatments is one of the main challenges for aluminium in the aircraft industry. In this Thesis, several environmentally friendly alternatives to Cr-based treatments are investigated. In Chapters 1, 2 and 3 strategies based on conventional anodizing, plasma electrolytic oxidation, conversion treatments, sealings and their combination with corrosion inhibitors have been tested and tuned on 2024 Al-Cu alloy. In Chapter 4, wear resistant films produced by hard anodizing and plasma electrolytic oxidation have been investigated for an additive manufactured Al10SiMg alloy. The main conclusions of this work are summarized as follows:

Chapter 1.

Anodic films with enhanced corrosion resistance have been developed on 2024 Al alloy. After a screening stage where multiple parameters were evaluated, it was concluded that anodizing at relatively low current density (1.5 mA cm^{-2}) produced thin (<3 μm) anodic films with high corrosion resistance. The addition of $Ce(SO_4)_2$ into sulphuric acid bath (SC1.6 treatment) resulted in Ce incorporation in the outer part of the anodic film, increased barrier layer thickness and reduced lateral porosity with a positive effect on corrosion resistance. The stand-alone anodic film produced in tartaric-sulphuric mixture (T2 treatment) revealed a high corrosion resistance and did not benefit from the addition of Ce. Selected T2 and SC1.6 films showed optimal paint adhesion and fatigue strength. Full-system evaluation with painted-and-scratched specimens revealed that the SC1.6 treatment was the best candidate for the replacement of chromic acid anodizing for painted applications.

Duplex coatings consisting of an anodic film and a hybrid sol-gel (HSG) layer have been developed for non-painted components. An anodic film with enhanced corrosion resistance and good compatibility with the top sol-gel layer was developed in a sulphuric-citric acid mixture (SCA). Li- and Ce-containing HSG coatings revealed better stability than inhibitor-free reference. The Ce-containing film (SCA-GTS-Ce) was identified as the best candidate for non-painted applications due to its self-healing ability.

Chapter 2.

Flash-plasma electrolytic oxidation (Flash-PEO) coatings with enhanced corrosion resistance and minimal energy consumption have been optimized on 1050 and 2024 alloys. Screening of flash-PEO process parameters for 1050 alloy in aluminate-, silicate-

and phosphate-based electrolytes revealed that low current densities (100-200 mA cm^{-2}) and short treatment times (100-200 s) produced thin, energy-efficient and corrosion protective coatings (A3.1, P2.1, S4).

Layered double hydroxide coatings based on Zn and Al (Zn-Al-LDH) were synthesized and screened on bare 1050 alloy and the abovementioned flash-PEO coatings (1-3 μm). It was found that aluminate-based coatings facilitated LDH growth. Results revealed that inhibitor-free LDH sealings do not compromise the corrosion resistance of studied coatings. The S4-LDH system showed the best corrosion performance.

After evaluation of several flash-PEO recipes, including those previously optimized on the 1050 alloy, a polyphosphate-based coating (PK, 100 mA cm^{-2}, 100 s, 5 μm) has been identified as the best candidate for further studies using *in situ* incorporation of inorganic corrosion inhibitors such as vanadate, permanganate, molybdate, tungstate, cerium and lanthanum. Coatings formed with additives $Ce_2(SO_4)_3$ and Na_2WO_4, PKECe and PKW respectively, showed superior corrosion protection. The Ce-containing coating revealed an excellent paint adhesion and salt-spray test performance when painted, therefore should be considered as an option for the replacement of chromic acid anodizing for painted applications.

For non-painted applications, a flash-PEO phosphate-silicate coating (PKSi) with appropriate thickness (~3 μm) was developed on 2024 alloy for further sealing post-treatments with Zn-Al-LDH or lauric acid. Studied LDH formulations improved the short-term corrosion protection but showed a limited response to inhibitor-loading. Hydrophobic lauric acid sealing of the flash-PEO coating yielded similar long-term corrosion to that of a reference CAA film.

Chapter 3.

LDH coatings formed by *in situ* growth method have been investigated on 2024 alloy. After a screening stage based on surface appearance and short-term corrosion resistance, it was concluded that Zn-Al- and Ca-Al-based LDH coatings formed at 95ºC during 1 hour produced thin (< 3 μm) coatings with high corrosion resistance. The incorporation of Mn in the Ca-Al-LDH structure was confirmed and resulted in enhanced long-term corrosion performance and excellent paint adhesion. For this reason, Ca-Al-LDH-Mn was pinpointed as a promising candidate for Cr-based conversion coatings for painted applications.

Chapter 4.

Hard anodizing (HA) and PEO coatings were successfully developed on additively manufactured (AM) Al10SiMg alloy and compared to those produced on A361 cast alloy. The AM Al10SiMg alloy consisted of α-Al cells enclosed in a fine 3D Si network. This microstructure yields homogeneous HA and PEO coatings with higher content of crystalline SiO_2 in comparison to the A361 cast alloy. HA and PEO treatments demonstrated an improved wear resistance compared to the bare substrates, although the AM coated alloy revealed inferior wear performance compared to the coated cast alloy due to its high SiO_2 content, particularly in the coatings formed on the XY plane.

To sum up, the findings of this Thesis reveal that it is possible to develop Cr-free coatings on aluminium alloys that could become an alternative to the state-of-the-art surface technologies employed by the aircraft industry, particularly in regards to Cr(VI)-containing formulations. Results from **Chapters 1-3** demonstrate that is possible to develop thin and corrosion resistant Cr-free surface treatments based on conventional anodizing, PEO and LDH on 2024 alloy that are compatible with environmentally friendly paints and sealings. **Chapter 4** proves that is possible to obtain uniform and hard coatings on an AM Al-Si alloy through HA and PEO processes, which is a step towards the design of wear-resistant AM components in aircraft applications.

6. Bibliography

1. Dursun, T., *Recent developments in advanced aircraft aluminium alloys.* Materials & Design, 2014. 56: p. 862-871.

2. Campbell, F.C., *Chapter 2 - Aluminum*, in *Manufacturing Technology for Aerospace Structural Materials*. 2006, Elsevier Science: Oxford. p. 15-92.

3. Ghali, E., *Fundamentals of Electrochemical Corrosion*. Corrosion Resistance of Aluminum and Magnesium Alloys. 2010: Wiley. 1-48.

4. Zhang, X., Y. Chen, and J. Hu, *Recent advances in the development of aerospace materials.* Progress in Aerospace Sciences, 2018. 97: p. 22-34.

5. *Advanced Research Projects Agency - Energy. Visited 29/11/2020*. Available from: https://arpa-e.energy.gov/?q=arpa-e-programs/metals.

6. Ashby, M.F. and D.R.H. Jones, *Chapter 11 - Light Alloys*, in *Engineering Materials 2 (Fourth Edition)*. 2013, Butterworth-Heinemann: Boston. p. 189-204.

7. *Material property data. Visited: 02/12/2020*. Available from: http://matweb.com/index.aspx.

8. *The Aluminium association. Visited: 20/10/2020*. Available from: https://www.aluminum.org/industries/production/recycling.

9. Mouritz, P.A., *8 - Aluminium alloys for aircraft structures*, in *Introduction to Aerospace Materials*, P.A. Mouritz, Editor. 2012, Woodhead Publishing: Boston. p. 173-201.

10. Abd El-Aty, A., et al., *Strengthening mechanisms, deformation behavior, and anisotropic mechanical properties of Al-Li alloys: A review.* Journal of Advanced Research, 2018. 10: p. 49-67.

11. Wanhill, R.J.H. and G.H. Bray, *Chapter 2 - Aerostructural Design and Its Application to Aluminum–Lithium Alloys*, in *Aluminum-lithium Alloys*, R.J.H. Wanhill, Editor. 2014, Butterworth-Heinemann: Boston. p. 27-58.

12. Bellonte, M. *Composite Materials in the Airbus A380 - From History to Future* -. in *ICCM13 proceedings*. 2001.

13. Rambabu, P., et al., *Aluminium Alloys for Aerospace Applications*, N.E. Prasad, Editor. 2017, Springer Science. p. 29-52.

14. LANXESS, *Surface treatment for applications in the aeronautics and aerospace industries.* 2018. p. 137. Visited: 17/08/2020. Available from: https://echa.europa.eu/es/support/substance-identification. .

15. *Cutaway Drawings. Cutaway Illustrations and Images of Vehicles for artists. Visited: 28/10/2019*. Available from: https://conceptbunny.com/airbus-a380/.

16. Snihirova, D., S.V. Lamaka, and M.F. Montemor, *4 - Smart composite coatings for corrosion protection of aluminium alloys in aerospace applications*, in *Smart Composite Coatings and Membranes*, M.F. Montemor, Editor. 2006, Woodhead Publishing: Boston. p. 85-121.

17. Warren, A.S. *Developments and Challenges for Aluminum - A Boeing Perspective*, in *Proceedings of the 9th International Conference on Aluminium Alloys*. 2004.

18. Guan, R.-g. and D. Tie, *A Review on Grain Refinement of Aluminum Alloys: Progresses, Challenges and Prospects.* Acta Metallurgica Sinica (English Letters), 2017. 30.

19. Gus Trompiz, A.S., *Aluminium makers fight plastic planes with new alloys*, in *Reuters*. 2013. Visited 21/05/2020. Available form: https://www.reuters.com/article/air-show-aluminium-idUSL5N0EQ2DJ20130620.

20. Wanhill, R.J.H., *Chapter 15 - Aerospace Applications of Aluminum–Lithium Alloys*, in *Aluminum-lithium Alloys*, N. Eswara Prasad, A.A. Gokhale, and R.J.H. Wanhill, Editors. 2014, Butterworth-Heinemann: Boston. p. 503-535.

21. Estrin, Y., M. Murashkin, and R. Valiev, *Ultrafine-Grained Aluminium Alloys: processes, Structural Features and Properties*, in *Fundamentals of Aluminium Metallurgy: Production, Processing and Applications*, R. Lumley, Editor. 2010. p. 468-503.

22. Das, A. and Z.Y. Fan, *7 - Semi-solid processing of metallic alloys*, in *The Deformation and Processing of Structural Materials*, Z. Xiao Guo, Editor. 2005, Woodhead Publishing: Boston. p. 252-283.

23. DebRoy, T., et al., *Additive manufacturing of metallic components – Process, structure and properties.* Progress in Materials Science, 2018. 92: p. 112-224.

24. Electrics, A.M.G., *Industry overview*, in *Additive Manufacturing Machines & Materials*. 2019. Visited: 2/10/2019. Available from: https://www.ge.com/additive/.

25. Kapranos, P., et al., *Advanced Casting Methodologies: Investment Casting, Centrifugal Casting, Squeeze Casting, Metal Spinning, and Batch Casting.* Comprehensive Materials Processing, 2014. 5: p. 39-67.

26. Sher, D., *SmarTech Analysis' latest report highlights top metal AM patent holder companies*, in *3D Printing Media Network*. 2019. Visited 21/05/2020. Available form: https://www.3dprintingmedia.network/top-metal-am-patent-holder-companies/.

27. ADDISPACE, *Diagnóstico y estudio de las oportunidades de fabricación aditiva metálica en el sector aeroespacial de la región del SUDOE*. 2017. Visited: 25/11/2019. Availbale from: https://www.3dprintingmedia.network/top-metal-am-patent-holder-companies/.

28. Wahlström, T., *Additive Manufacturing in Production for the Automotive Industry (Master Thesis)*, in 2016, Lund University.

29. Lowther, M., et al., *Clinical, industrial, and research perspectives on powder bed fusion additively manufactured metal implants.* Additive Manufacturing, 2019. 28: p. 565-584.

30. Ngo, T.D., et al., *Additive manufacturing (3D printing): A review of materials, methods, applications and challenges.* Composites Part B: Engineering, 2018. 143: p. 172-196.

31. Czaban, M., *Aircraft corrosion - Review of corrosion processes and its effects in selected cases.* Fatigue of Aircraft Structures, 2018: p. 5-20.

32. Authority, C.A., *Corrosion and Inspection of General Aviation Aircraft, CAP 1570.* 2017. Visited: 2/10/2018. Available from: https://publicapps.caa.co.uk/docs/33/CAP1570_Corrosion.pdf.

33. Taylor, D., *Understanding the Corrosion Threat to Ageing Aircraft* 2015. Paper 012, UK Goverment. Visited: 02/02/2018. Available from: https://assets.publishing.service.gov.uk/government/uploads/system/uploads/attachment_data/file/516201/AAPWG_Paper_012.pdf.

34. Domingo, R., *Corrosion Control for Aircraft*. 2018. Visited: 04/05/2019. Available from: https://www.faa.gov/documentLibrary/media/Advisory_Circular/AC_43-4B.pdf. p. 1-26.

35. Ferreira, M.G.S., M.L. Zheludkevich, and J. Tedim, *Advanced protective coatings for aeronautical applications*, in *Nanocoatings and Ultra-Thin Films: Technologies and Applications*, A. Salam, Editor. 2011. p. 235-279.

36. Visser, P., H. Terryn, and J.M.C. Mol, *12-Aerospace coatings*, in *Active protective coatings*, A. E. Hughes, et al., Editors. 2016, Springer Netherlands. p. 315-372.

37. ECHA, E.C.A. *List of substances included in Annex XIV of REACH ("Authorisation List"). Visited: 28/02/2020. Available from: https://reachonline.eu/reach/en/annex-xiv.html.*

38. Hawksworth, D.K., *19 - Fluxless brazing of aluminium*, in *Advances in Brazing*, D.P. Sekulić, Editor. 2013, Woodhead Publishing: Boston. p. 566-585.

39. Sukiman, N.L., et al., *Durability and Corrosion of Aluminium and Its Alloys: Overview, Property Space, Techniques and Developments.*, in *Aluminium Alloys - New Trends in Fabrication and Applications*, Z. Ahmad, Editor. 2012, IntechOpen.

40. Cramer, S.D., *ASM Handbook, Volume 13A - Corrosion: Fundamentals, Testing, and Protection*, ed. B.S. Covino. 2010: ASM International.

41. Hughes, A.E., et al., *High Strength Al-Alloys: Microstructure, Corrosion and Principles of Protection*, in *Recent Trends in Processing and Degradation of Aluminium Alloys*, Z. Ahmad, Editor. 2011, IntechOpen.

42. Zhang, X., et al., *Investigation of the de-alloying behaviour of θ-phase (Al2Cu) in AA2024-T351 aluminium alloy.* Corrosion Science, 2016. 108: p. 85-93.

43. Hughes, A.E., et al., *Corrosion of AA2024-T3 Part II: Co-operative corrosion.* Corrosion Science, 2011. 53(1): p. 27-39.

44. King, R.G., *Chapter 2 - Cleaning*, in *Surface Treatment and Finishing of Aluminium*, R.G. King, Editor. 1988, Pergamon: Oxford. p. 13-25.

45. King, R.G., *Chapter 3 - Chemical Finishing*, in *Surface Treatment and Finishing of Aluminium*, R.G. King, Editor. 1988, Pergamon: Oxford. p. 26-33.

46. Runge, J., *The Metallurgy of Anodizing Aluminum*. Springer Nature. 2018: Springer International Publishing.

47. Kulinich, S.A. and A.S. Akhtar, *On conversion coating treatments to replace chromating for Al alloys: Recent developments and possible future directions.* Russian Journal of Non-Ferrous Metals, 2012. 53(2): p. 176-203.

6. Bibliography

48. Qi, J., et al., *Trivalent chromium conversion coating formation on aluminium.* Surface and Coatings Technology, 2015. 280: p. 317-329.

49. Hughes, A., *Chromate Conversion Coatings on 2024 Al Alloy.* Surface and Interface Analysis, 1997. 25(4): p. 223-234.

50. Beneke M. and N. S., *Chromate free surface pre-treatments for aluminium alloys, AIRBUS*. 2016. Visited: 05/08/2018. Available from: https://serdp-estcp.org/.

51. Williams, M., *An alternative to chromates for corrosion protection for aluminum alloys (Master Thesis)* in 2011, University of Rhode Island.

52. Yingbiao, L., et al., *Optimized anodization setup for the growth of TiO2 nanotubes on flat surfaces of titanium based materials.* MATEC Web of Conferences, 2017. 137: p. 2011.

53. Zhou, F., *Growth mechanism of porous anodic films on aluminium (PhD Thesis)*, in 2011, The University of Manchester

54. Patermarakis, G., *The origin of nucleation and development of porous nanostructure of anodic alumina films.* Journal of Electroanalytical Chemistry, 2009. 635(1): p. 39-50.

55. Thompson, G.E., *Porous anodic alumina: fabrication, characterization and applications.* Thin Solid Films, 1997. 297(1): p. 192-201.

56. Garcia-Vergara, S.J., et al., *A flow model of porous anodic film growth on aluminium.* Electrochimica Acta, 2006. 52(2): p. 681-687.

57. Garcia-Vergara, S., et al., *Formation of porous anodic alumina in alkaline borate electrolyte.* Thin Solid Films, 2007. 515: p. 5418-5423.

58. Le Coz, F., L. Arurault, and L. Datas, *Chemical analysis of a single basic cell of porous anodic aluminium oxide templates.* Materials Characterization, 2010. 61(3): p. 283-288.

59. Iglesias-Rubianes, L., et al., *Cyclic oxidation processes during anodizing of Al–Cu alloys.* Electrochimica Acta, 2007. 52(24): p. 7148-7157.

60. Arenas-Vara, M., P. Skeldon, and S. García-Vergara, *Effect of copper-enriched layers on localized corrosion of aluminium-copper alloys.* Revista Facultad de Ingeniería, 2018. 27: p. 7-15.

61. García-Rubio, M., et al., *Influence of molybdate species on the tartaric acid/sulphuric acid anodic films grown on AA2024 T3 aerospace alloy.* Corrosion Science, 2009. 51(9): p. 2034-2042.

62. Garcia-Vergara, S.J., et al., *Influence of copper on the morphology of porous anodic alumina.* Corrosion Science, 2006. 48(10): p. 2937-2946.

63. Mingo, B., et al., *Efficiency of anodising of Al–Cu alloy in sulphuric acid at low potentials.* Transactions of the IMF, 2015. 93: p. 18-23.

64. Abrahami, S., et al., *Towards Cr(VI)-free anodization of aluminum alloys for aerospace adhesive bonding applications: A review.* Frontiers of Chemical Science and Engineering, 2017: p. 1-18.

65. Cohen, S. and S. Spadafora, *A Comparison of Thin Film Sulfuric Acid Anodizing and Chromic Acid Anodizing Processes*. 1995. Visited: 02/05/2018. Available from: https://apps.dtic.mil/dtic/tr/fulltext/u2/a298250.pdf.

66. Curioni, M., et al., *Role of Tartaric Acid on the Anodizing and Corrosion Behavior of AA 2024 T3 Aluminum Alloy.* Journal of the Electrochemical Society, 2009. 156: p. C147-C153.

67. Boeing, *Boric Acid-Sulfuric Acid Anodizing. WO200402712lA2.* 2004.

68. Domingues, L., et al., *Anodising of Al 2024-T3 in a modified sulphuric acid/boric acid bath for aeronautical applications.* Corrosion Science, 2003. 45: p. 149-160.

69. Abrahami, S., et al., *The Effect of Anodic Aluminum Oxide Chemistry on Adhesive Bonding of Epoxy.* The Journal of Physical Chemistry C, 2016. 120: p. 19670–19677.

70. Bouchama, L., et al., *Enhancing aluminum corrosion resistance by two-step anodizing process.* Surface and Coatings Technology, 2013. 235: p. 676-684.

71. Girginov, C., et al., *Impact of the anodizing duration on the surface morphology and performance of A2024-T3 in a model corrosive medium.* Materials Chemistry and Physics, 2017. 198: p. 137-144.

72. Priet, B., et al., *Effect of new sealing treatments on corrosion fatigue lifetime of anodized 2024 aluminium alloy.* Surface and Coatings Technology, 2016. 307: p. 206-219.

73. Hakimizad, A., K. Raeissi, and F. Ashrafizadeh, *Characterization of aluminum anodized layers modified in sulfuric and phosphoric acid baths and their effect on conventional electrolytic coloring.* Surface & Coatings Technology, 2012. 206.

74. Torrescano-Alvarez, J.M., M. Curioni, and P. Skeldon, *Effects of oxygen evolution on the voltage and film morphology during galvanostatic anodizing of AA 2024-T3 aluminium alloy in sulphuric acid at −2 and 24 °C.* Electrochimica Acta, 2018. 275: p. 172-181.

75. Ding, Z., et al., *Morphology perspective on chromic acid anodizing replacement by thin film sulfuric acid anodizing.* Surface and Coatings Technology, 2018. 350: p. 31-39.

76. Balaraju, J.N., et al., *Effect of Mn/Mo incorporated oxide layer on the corrosion behavior of AA 2024 alloy.* Corrosion Science, 2011. 53(12): p. 4084-4092.

77. Li, Y.-d., et al., *Influence of adipic acid on anodic film formation and corrosion resistance of 2024 aluminum alloy.* Transactions of Nonferrous Metals Society of China, 2016. 26(2): p. 492-500.

78. Boisier, G., et al., *FESEM and EIS study of sealed AA2024 T3 anodized in sulfuric acid electrolytes: Influence of tartaric acid.* Journal of The Electrochemical Society, 2008. 155(11): p. 521-529.

79. García-Rubio, M., et al., *Effect of postreatment on the corrosion behaviour of tartaric–sulphuric anodic films.* Electrochimica Acta, 2009. 54(21): p. 4789-4800.

80. Capelossi, V.R., et al., *Corrosion protection of clad 2024 aluminum alloy anodized in tartaric-sulfuric acid bath and protected with hybrid sol–gel coating.* Electrochimica Acta, 2014. 124: p. 69-79.

6. Bibliography

81. Shen, Y., et al., *Effect of anodic films on corrosion resistance and fatigue crack initiator of 2060-T8 Al-Li alloy.* International Journal of Electrochemical Science, 2015. 10: p. 938-946.

82. Zhang, J.-s., et al., *The bonding strength and corrosion resistance of aluminum alloy by anodizing treatment in a phosphoric acid modified boric acid/sulfuric acid bath.* Surface and Coatings Technology, 2008. 202(14): p. 3149-3156.

83. Koczera, A.E., *The effects of carboxylic acids in aluminum anodizing (Master Thesis),* in 2017, University of New Hampshire.

84. Smith, C., *Research into Chromate-Free Treatments for the Protection of Aluminum Alloys, AGARD report*. 1997.

85. Moutarlier, V., et al., *EIS characterisation of anodic films formed on 2024 aluminium alloy, in sulphuric acid containing molybdate or permanganate species.* Corrosion Science, 2005. 47(4): p. 937-951.

86. Moutarlier, V., et al., *An electrochemical approach to the anodic oxidation of Al 2024 alloy in sulfuric acid containing inhibitors.* Surface and Coatings Technology, 2002. 161: p. 267-274.

87. Smith, C., *Environmentally Compliant Surface Treatments of Materials for Aerospace Applications. AGARD Report.* 1997.

88. Giovanardi, R., C. Fontanesi, and W. Dallabarba, *Adsorption of organic compounds at the aluminium oxide/aqueous solution interface during the aluminium anodizing process.* Electrochimica Acta, 2011. 56(9): p. 3128-3138.

89. Jalal, H., Y. Saoud, and F. Karabet, *Effect of organic additives on AA6066 anodization.* Journal of Chemical Technology and Metallurgy, 2019. 54(2): p. 447-453.

90. BOMBARDIER, *SOCOSURF TCS. Technical Data Sheet.* 2017. Visited: 02/06/2018. Available from: https://www.socomore.com/shop/surface-treatment/finishing-treatment/socosurf-tcs-scop/.

91. Henkel, *Technical Data Sheet, BONDERITE M-CR 1200* 2014. Visited: 07/09/2018. Available from: https://www.henkel-adhesives.com/es/es/producto/conversion-coatings/bonderite_m-cr_1200saero.html

92. *Haas Group International SCM Ltd. Use of potassium dichromate for sealing after anodizing applications by aerospace companies and their suppliers.* 2018. p. 65. Visited in: 02/01/2019. Avilable from: https://echa.europa.eu/documents/10162/d6c88cd1-ef18-460b-8493-e1d59211a888.

93. Ono, S., *Sealing Mechanism of Anodic Porous Oxide Films Formed on Aluminum in Lithium Hydroxide Solution*, in *Proceedings of the 12th International Conference on Aluminium Alloys*. 2010. p. 1463-1468.

94. Hao, L. and B.R. Cheng, *Sealing processes of anodic coatings—Past, present, and future.* Metal Finishing, 2000. 98(12): p. 8-18.

95. Zarras, P. and J.D. Stenger-Smith, *Chapter 3 - Smart Inorganic and Organic Pretreatment Coatings for the Inhibition of Corrosion on Metals/Alloys*, in *Intelligent Coatings for Corrosion Control*, A. Tiwari, Editor. 2015, Butterworth-Heinemann: Boston. p. 59-91.

96. Hughes, A.E., et al., *Coatings for corrosion prevention based on rare earths*, in *Rare Earth-Based Corrosion Inhibitors*, M. Forsyth, Editor. 2014, Woodhead Publishing Series in Metals and Surface Engineering. p. 186-232.

97. Zheng, S. and J. Li, *Inorganic–organic sol gel hybrid coatings for corrosion protection of metals.* Journal of Sol-Gel Science and Technology, 2010. 54: p. 174-187.

98. Yasakau, K., M.L. Zheludkevich, and M. Ferreira, *Role of intermetallics in corrosion of aluminum alloys. Smart corrosion protection*, in *Intermetallic Matrix Composites*, R. Mitra, Editor. 2018, Woodhead Publishing: Boston. p. 425-462.

99. Forano, C., et al., *Chapter 13.1 Layered Double Hydroxides*, in *Developments in Clay Science*, F. Bergaya, Editor. 2006, Elsevier B.V. p. 1021-1095.

100. Guo, L., et al., *Layered double hydroxide coatings on magnesium alloys: A review.* Journal of Materials Science & Technology, 2018. 34(9): p. 1455-1466.

101. Mohamed, A.M.A., et al., *Corrosion behavior of superhydrophobic surfaces: A review.* Arabian Journal of Chemistry, 2015. 8(6): p. 749-765.

102. Yinghao, W., et al., *Fabricating binary anti-corrosion structures containing superhydrophobic surface and sturdy barrier layer for Al alloys.* RSC Advances, 2016. 6: p. 10-24.

103. Luo, Y., J. Wei, and Z. Jiao, *Review on anodizing technologies for the fabrication of superhydrophobic aluminum-based surfaces.* Cailiao Daobao/Materials Review, 2016. 30: p. 89-96.

104. Walsh, F., et al., *Plasma electrolytic oxidation (PEO) for production of anodised coatings on lightweight metal (Al, Mg, Ti) alloys.* Transactions of the Institute of Metal Finishing, 2009. 87: p. 122-135.

105. Yerokhin, A., et al., *Plasma electrolysis for surface engineering.* Surface and Coatings Technology, 1999. 122(2): p. 73-93.

106. Davies, R.A. and A. Hickling, *Glow-discharge electrolysis. Part I. The anodic formation of hydrogen peroxide in inert electrolytes.* Journal of the Chemical Society, 1952(0): p. 3595-3602.

107. Dehnavi, V., *Surface Modification of Aluminum Alloys by Plasma Electrolytic Oxidation (PhD Thesis)*. 2014, The University of Western Ontario.

108. Jiang, B.L. and Y.M. Wang, *5 - Plasma electrolytic oxidation treatment of aluminium and titanium alloys*, in *Surface Engineering of Light Alloys*, H. Dong, Editor. 2010, Woodhead Publishing: Boston. p. 110-154.

109. Mohedano, M., et al., *Plasma electrolytic oxidation (PEO) of metals and alloys*, in *Encyclopedia of Interfacial Chemistry: Surface Science and Electrochemistry*. 2018. p. 423-438.

110. Xia, L., et al., *Investigation of the Scanning Microarc Oxidation Process.* Advances in Materials Science and Engineering, 2017. 2017: p. 1-12.

111. Matykina, E., et al., *Recent advances in energy efficient PEO processing of aluminium alloys.* Transactions of Nonferrous Metals Society of China (English Edition), 2017. 27(7): p. 1439-1454.

6. Bibliography

112. Yerokhin, A., et al., *Oxide ceramic coatings on aluminium alloys produced by a pulsed bipolar plasma electrolytic oxidation process.* Surface and Coatings Technology, 2005. 199: p. 150-157.

113. Cheng, Y., et al., *Key factors determining the development of two morphologies of plasma electrolytic coatings on an Al–Cu–Li alloy in aluminate electrolytes.* Surface and Coatings Technology, 2016. 291: p. 239-249.

114. del Olmo, R., et al., *LDH post-treatment of flash PEO coatings.* Coatings, 2019. 9(6): p. 354.

115. Guo-Hua, L., et al., *Microstructure and Corrosion Performance of Oxide Coatings on Aluminium by Plasma Electrolytic Oxidation in Silicate and Phosphate Electrolytes.* Chinese Physics Letters, 2006. 23(12): p. 3331-3333.

116. Doolabi, D., M. Ehteshamzadeh, and M. Mirhosseini, *Effect of NaOH on the Structure and Corrosion Performance of Alumina and Silica PEO Coatings on Aluminum.* Journal of Materials Engineering and Performance, 2012. 21: p. 2195–2202.

117. Polat, A., M. Makaraci, and M. Usta, *Influence of sodium silicate concentration on structural and tribological properties of microarc oxidation coatings on 2017A aluminum alloy substrate.* Journal of Alloys and Compounds, 2010. 504(2): p. 519-526.

118. Famiyeh, L. and X. Huang, *Plasma Electrolytic Oxidation Coatings on Aluminum Alloys: Microstructures, Properties, and Applications.* Modern Concepts in Material Science, 2018. 2(1): p. 526-539.

119. Snizhko, L.O., et al., *Anodic processes in plasma electrolytic oxidation of aluminium in alkaline solutions.* Electrochimica Acta, 2004. 49(13): p. 2085-2095.

120. Snizhko, L.O., et al., *Excessive oxygen evolution during plasma electrolytic oxidation of aluminium.* Thin Solid Films, 2007. 516(2): p. 460-464.

121. Asquith, D., et al., *Effect of combined shot-peening and PEO treatment on fatigue life of 2024 Al alloy.* Thin Solid Films, 2006. 515(3): p. 1187-1191.

122. Lonyuk, B., I. Apachitei, and J. Duszczyk, *The effect of oxide coatings on fatigue properties of 7475-T6 aluminium alloy.* Surface and Coatings Technology, 2007. 201(21): p. 8688-8694.

123. Matykina, E., et al., *Energy-efficient PEO process of aluminium alloys.* Materials Letters, 2014. 127: p. 13-16.

124. Fattah-alhosseini, A., S. Gashti, and M. Molaei, *Effects of Disodium Phosphate Concentration (Na2HPO4·2H2O) on Microstructure and Corrosion Resistance of Plasma Electrolytic Oxidation (PEO) Coatings on 2024 Al Alloy.* Journal of Materials Engineering and Performance, 2018. 27.

125. Yang, W., et al., *Effects of KMnO4 on microstructure and corrosion resistance of microarc oxidation coatings on 2024 aluminum alloy.* Journal of Central South University of Technology, 2010. 17(2): p. 223-227.

126. Pezzato, L., K. Brunelli, and M. Dabalà, *Corrosion properties of plasma electrolytic oxidation coated AA7075 treated using an electrolyte containing lanthanum-salts.* Surface and Interface Analysis, 2016. 48: p. 102-114.

127. Mann, R., W. Hansal, and S. Hansal, *Effects of pulsed current on plasma electrolytic oxidation.* Transactions of the IMF, 2014. 92: p. 297-304.

128. Wang, P., et al., *Effects of Ce(SO4)2 concentration on the properties of micro-arc oxidation coatings on ZL108 aluminum alloys.* Materials Letters, 2016. 182: p. 093-102.

129. Hwang, I.J., et al., *Formation of uniform passive oxide layers on high Si content Al alloy by plasma electrolytic oxidation.* Journal of Alloys and Compounds, 2010. 504: p. S527-S530.

130. Arrabal, R., et al., *Assessment of duplex coating combining plasma electrolytic oxidation and polymer layer on AZ31 magnesium alloy.* Surface and Coatings Technology, 2012. 206(22): p. 4692-4703.

131. Bouali, A.C., et al., *Layered double hydroxide based active corrosion protective sealing of plasma electrolytic oxidation/sol-gel composite coating on AA2024.* Applied Surface Science, 2019. 494: p. 829-840.

132. Serdechnova, M., et al., *Role of phase composition of PEO coatings on AA2024 for in-situ LDH growth.* Coatings, 2017. 7. 190.

133. Mohedano, M., et al., *Active protective PEO coatings on AA2024: Role of voltage on in-situ LDH growth.* Materials & Design, 2017. 120: p. 36-46.

134. Egorkin, V., et al., *Evaluation of Electrochemical Properties of the PEO-Coatings Treated with Hydrophobic Agent Solution on Aluminium Alloy.* Solid State Phenomena, 2015. 245: p. 116-120.

135. Gnedenkov, S.V., et al., *Wettability and electrochemical properties of the highly hydrophobic coatings on PEO-pretreated aluminum alloy.* Surface and Coatings Technology, 2016. 307: p. 1241-1248.

136. Rudnev, V.S., et al., *Polytetrafluoroethylene-oxide coatings on aluminum alloys.* Surface and Coatings Technology, 2016. 307: p. 1249-1254.

137. Mohedano, M., et al., *PEO of pre-anodized Al–Si alloys: Corrosion properties and influence of sealings.* Applied Surface Science, 2015. 346: p. 57-67.

138. Arunnellaiappan, T., et al., *Fabrication of corrosion resistant hydrophobic ceramic nanocomposite coatings on PEO treated AA7075.* Ceramics International, 2018. 44(1): p. 874-884.

139. Pezzato, L., et al., *Plasma Electrolytic Oxidation (PEO) as pre-treatment for sol-gel coating on aluminum and magnesium alloys.* Surface and Coatings Technology, 2019. 366: p. 114-123.

140. Ye, Z., et al., *Application of Plasma Electrolytic Oxidation to the Novel Aircraft Aluminum Alloy for Enhancing Corrosion Resistance.* Lecture Notes in Electrical Engineering, 2014. 297: p. 265-274.

141. Barik, R.C., et al., *Corrosion, erosion and erosion–corrosion performance of plasma electrolytic oxidation (PEO) deposited Al2O3 coatings.* Surface and Coatings Technology, 2005. 199(2): p. 158-167.

6. Bibliography

142. Schuman, T.P., *Chapter 17 - Protective coatings for aluminum alloys*, in *Handbook of Environmental Degradation of Materials*, M. Kutz, Editor. 2005, William Andrew Publishing: Norwich, NY. p. 345-366.

143. Qi, J., *Trivalent chromium conversion coatings on Al and Al-Cu alloys (PhD Thesis)*. 2015, The University of Manchester.

144. Liu, Y., et al., *Influence of copper on chromate conversion coating of aluminium alloys.* Transactions of The Institute of Metal Finishing, 2005. 83: p. 125-129.

145. Beelen, D.C., et al., *Aviox CF Primer: A new generation primer for aircraft maintenance.* Pigment & Resin Technology, 1998. 27: p. 28-33.

146. Mitton, D., et al., *Selected Cr(VI) replacement options for aluminum alloys: A literature survey.* Corrosion Reviews, 2017. 35(6): p. 365-381.

147. Hughes, A.E., *Conversion Coatings*, in *Encyclopedia of Interfacial Chemistry*, A.E. Hughes, Editor. 2017, Elsevier.

148. Matzdorf, C., *Preparation of coating aluminum substrates for protection against corrosion. US6375726B1.* 2012.

149. Guo, Y. and G.S. Frankel, *Characterization of trivalent chromium process coating on AA2024-T3.* Surface and Coatings Technology, 2012. 206(19): p. 3895-3902.

150. Ferreira, M.G.S., et al., *9 - Self-healing nanocoatings for corrosion control*, in *Corrosion Protection and Control Using Nanomaterials*, V.S. Saji and R. Cook, Editors. 2012, Woodhead Publishing: Boston. p. 213-263.

151. Yasakau, K.A., M.L. Zheludkevich, and M.G.S. Ferreira, *Corrosion and Corrosion Protection of Aluminum Alloys*, in *Encyclopedia of Interfacial Chemistry*, K. Wandelt, Editor. 2018, Elsevier: Oxford. p. 115-127.

152. Guo, X., et al., *Layered double hydroxide films: Synthesis, properties and applications.* Chemical communications (Cambridge, England), 2010. 46: p. 5197-210.

153. Mishra, G., B. Dash, and S. Pandey, *Layered double hydroxides: A brief review from fundamentals to application as evolving biomaterials.* Applied Clay Science, 2018. 153: p. 172-186.

154. Li, T., H. Miras, and Y.-F. Song, *Polyoxometalate (POM)-Layered Double Hydroxides (LDH) Composite Materials: Design and Catalytic Applications.* Catalysts, 2017. 7: p. 260.

155. Tedim, J., et al., *Influence of preparation conditions of Layered Double Hydroxide conversion films on corrosion protection.* Electrochimica Acta, 2014. 117: p. 164-171.

156. Tedim, J., et al., *Zn-Al layered double hydroxides as chloride nanotraps in active protective coatings.* Corrosion Science, 2012. 55: p. 1-4.

157. Zheludkevich, M.L., et al., *Active protection coatings with layered double hydroxide nanocontainers of corrosion inhibitor.* Corrosion Science, 2010. 52(2): p. 602-611.

158. Zhang, Y., et al., *Fabrication of inhibitor anion-intercalated layered double hydroxide host films on aluminum alloy 2024 and their anticorrosion properties.* Journal of Coatings Technology and Research, 2015. 12(2): p. 293-302.

159. Zhang, Y., et al., *Double-doped LDH films on aluminum alloys for active protection.* Materials Letters, 2017. 192: p. 33-35.

160. Dennis, R., et al., *Hybrid nanostructured coatings for corrosion protection of base metals: a sustainability perspective.* Material Research Express, 2015. 2. 32001.

161. Ofoegbu, S., F. Fernandes, and A. Pereira, *The Sealing Step in Aluminum Anodizing: A Focus on Sustainable Strategies for Enhancing both Energy Efficiency and Corrosion Resistance.* Coatings, 2020. 10. 226.

162. Tedim, J., et al., *Nanostructured LDH-container layer with active protection functionality*. Vol. 21. 2011. 15464-15470.

163. Brice, C., et al., *Precipitation behavior of aluminum alloy 2139 fabricated using additive manufacturing.* Materials Science and Engineering: A, 2015. 648: p. 9-14.

164. Bartkowiak, K., et al., *New Developments of Laser Processing Aluminium Alloys via Additive Manufacturing Technique.* Physics Procedia, 2011. 12: p. 393-401.

165. Ding, Y., et al., *Microstructure and mechanical property considerations in additive manufacturing of aluminum alloys.* MRS Bulletin, 2016. 41(10): p. 745-751.

166. Shi, R., et al., *Microstructural control in metal laser powder bed fusion additive manufacturing using laser beam shaping strategy.* Acta Materialia, 2020. 184: p. 284-305.

167. Aktarer, S., et al., *Effect of friction stir processing on tribological properties of Al-Si alloys.* IOP Conference Series: Materials Science and Engineering, 2017. 174: p. 012061.

168. Rosenthal, I., A. Stern, and N. Frage, *Strain rate sensitivity and fracture mechanism of AlSi10Mg parts produced by Selective Laser Melting.* Materials Science and Engineering, 2017. 682: p. 509-517.

169. Vora, P., et al., *AlSi12 in-situ alloy formation and residual stress reduction using anchorless selective laser melting.* Additive Manufacturing, 2015. 7: p. 12-19.

170. Revilla, R., et al., *Local Corrosion Behavior of Additive Manufactured AlSiMg Alloy Assessed by SEM and SKPFM.* Journal of The Electrochemical Society, 2016. 164(2): p. 27-35.

171. Revilla, R.I., Y. Rojas, and I. De Graeve, *On the Impact of Si Content and Porosity Artifacts on the Anodizing Behavior of Additive Manufactured Al-Si Alloys.* Journal of The Electrochemical Society, 2019. 166(14): p. C530-C537.

172. Revilla, R. and I. Graeve, *Influence of Si Content on the Microstructure and Corrosion Behavior of Additive Manufactured Al-Si Alloys.* Journal of The Electrochemical Society, 2018. 165: p. C926-C932.

173. Zhang, H., et al., *Selective laser melting of high strength Al–Cu–Mg alloys: Processing, microstructure and mechanical properties.* Materials Science and Engineering: A, 2016. 656: p. 47-54.

174. Aboulkhair, N.T., et al., *Reducing porosity in AlSi10Mg parts processed by selective laser melting.* Additive Manufacturing, 2014. 1-4: p. 77-86.

6. Bibliography

175. Prashanth, K.G. and J. Eckert, *Formation of metastable cellular microstructures in selective laser melted alloys.* Journal of Alloys and Compounds, 2017. 707: p. 27-34.

176. Cabrini, M., et al., *Evaluation of corrosion resistance of Al–10Si–Mg alloy obtained by means of Direct Metal Laser Sintering.* Journal of Materials Processing Technology, 2016. 231: p. 326-335.

177. Leon, A. and E. Aghion, *Effect of surface roughness on corrosion fatigue performance of AlSi10Mg alloy produced by Selective Laser Melting (SLM).* Materials Characterization, 2017. 131: p. 188-194.

178. Fathi, P., et al., *On microstructure and corrosion behaviour of AlSi10Mg alloy with low surface roughness fabricated by direct metal laser sintering.* Corrosion Science, 2019. 157: p. 126-145.

179. Örnek, C., *Additive manufacturing – a general corrosion perspective.* Corrosion Engineering, Science and Technology, 2018. 53: p. 1-5.

180. Kong, D., et al., *Corrosion of metallic materials fabricated by selective laser melting.* npj Materials Degradation, 2019. 3(1). 24.

181. Lorusso, M., *Tribological and Wear Behavior of Metal Alloys Produced by Laser Powder Bed Fusion (LPBF)*, in *Friction, Lubrication and Wear*, M.A. Chowdhury, Editor. 2019, IntechOpen.

182. Aboulkhair, N.T., et al., *3D printing of Aluminium alloys: Additive Manufacturing of Aluminium alloys using selective laser melting.* Progress in Materials Science, 2019. 106. 100578.

183. Kang, N., et al., *Microstructure and wear behavior of in-situ hypereutectic Al–high Si alloys produced by selective laser melting.* Materials & Design, 2016. 99: p. 120-126.

184. Prashanth, K.G., et al., *Tribological and corrosion properties of Al-12Si produced by selective laser melting.* Journal of Materials Research, 2014. 29: p. 2044-2054.

185. Revilla, R., et al., *Galvanostatic Anodizing of Additive Manufactured Al-Si10-Mg Alloy.* Journal of The Electrochemical Society, 2017. 164: p. C1027-C1034.

186. Khaled, T., *A look at hard chrome replacement. Report.*, in *Federal aviation administration*. 2002.

187. Malayoglu, U., et al., *An investigation into the mechanical and tribological properties of plasma electrolytic oxidation and hard-anodized coatings on 6082 aluminum alloy.* Materials Science and Engineering: A, 2011. 528(24): p. 7451-7460.

188. Shrestha, S. and B.D. Dunn, *18 - Plasma electrolytic oxidation and anodising of aluminium alloys for spacecraft applications*, in *Surface Engineering of Light Alloys*, H. Dong, Editor. 2010, Woodhead Publishing: Boston. p. 603-641.

189. Pezzato, L., M. Dabalà, and K. Brunelli, *Microstructure and Corrosion Properties of PEO Coatings Produced on AM-Aluminum Alloys.* Key Engineering Materials, 2019. 813: p. 298-303.

190. *ISO 2360:2003, Non-conductive coatings on non-magnetic electrically conductive base metals - Measurement of coating thickness - Amplitude-sensitive eddy-current method.* 2017.

191. *ASTM B117-Standard Practice for Operating Salt Spray (Fog) Apparatus*. 2019.

192. *ISO 17872:2007, Paints and varnishes — Guidelines for the introduction of scribe marks through coatings on metallic panels for corrosion testing.* 2007.

193. *ASTM D1654-92-Standard Test Method for Evaluation of Painted or Coated Specimens Subjected to Corrosive Environments*. 2000.

194. *ASTM E466-Standard Practice for Conducting Force Controlled Constant Amplitude Axial Fatigue Tests of Metallic Materials.* 2015.

195. *ISO 2409:2013, Paints and varnishes — Cross-cut test.* 2013.

196. Li, D., et al., *Investigation of Cerium Salt/Sulfuric Acid Anodizing Technology for 1420 Aluminum Alloy.* Materials Science Forum, 2000: p. 1695-1700.

197. Curioni, M., et al., *Formation of protective anodic oxides on aluminium by low voltage anodising in sulphuric acid with cerium nitrate and tartaric acid additions.* Transactions of the IMF, 2012. 90(6): p. 290-297.

198. Rodič, P. and I. Milošev, *Corrosion inhibition of pure aluminium and alloys AA2024-T3 and AA7075-T6 by Cerium(III) and cerium(IV) salts.* Journal of Electrochemical Society, 2016. 163: p. C85-C93.

199. Wu, D.F., et al., *Effect of Ce(SO4)2 additive on coating formed by micro-arc oxidation process on casting aluminum-copper alloy*, in *Advanced Materials Research*. 2013. p. 424-428.

200. Carangelo, M.C., A. Acquesta, T. Monetta and F. Belluccia *Cerium-Based Sealing of Anodic Films on AA2024T3: Effect of Pore Morphology on Anticorrosion Performance.* Journal of The Electrochemical Society, 2016. 163(14): p. C907-C916

201. Sroor, F. and F.T. Edelmann, *Tetravalent Chemistry Inorganic*, F. Sroor, Editor. 2012, Wiley Online Library.

202. Paulenova, A., et al., *Redox potentials and kinetics of the Ce3+/Ce4+ redox reaction and solubility of cerium sulfates in sulfuric acid solutions.* Journal of Power Sources, 2002. 109: p. 431-438.

203. Ecco, L.G., et al., *Waterborne acrylic paint system based on nanoceria for corrosion protection of steel.* Progress in Organic Coatings, 2016. 96: p. 19-25.

204. Janjić, T.J., et al., *Study of equilibria in solutions of some protonated metal(II)-edta complexes.* Journal of Inorganic and Nuclear Chemistry, 1979. 41(1): p. 63-65.

205. Saenz de Miera, M., et al., *Preferential anodic oxidation of second-phase constituents during anodising of AA2024-T3 and AA7075-T6 alloys.* Surface and Interface Analysis, 2010. 42: p. 241-246.

206. Curioni, M., et al., *Macroscopic and Local Filming Behavior of AA2024 T3 Aluminum Alloy during Anodizing in Sulfuric Acid Electrolyte.* Journal of the Electrochemical Society, 2008. 155(8): p. C387-C395.

207. Moutarlier, V., et al., *An electrochemical approach to the anodic oxidation of Al 2024 alloy in sulfuric acid containing inhibitors.* Surface and Coatings Technology, 2002. 161(2): p. 267-274.

6. Bibliography

208. Vargel, C., *Chapter F.1 - Protection of aluminium*, in *Corrosion of Aluminium (Second Edition)*, C. Vargel, Editor. 2020, Elsevier: Amsterdam. p. 383-443.

209. Rubio, M.G., *Optimisation of a non-chromium-containing tartaric acid/sulphuric acid anodising bath for aluminium alloys for aerospace industry application (PhD Thesis)*. 2009, Autonomous University of Madrid.

210. Datt, N., R. Nagori, and R. Mehrotra, *Kinetics and mechanisms of oxidations by metal ions. Part VI. Oxidation of α-hydroxy acids by cerium(IV) in aqueous nitric acid.* Canadian Journal of Chemistry, 2011. 64: p. 19-23.

211. Mubarok, Z., et al., *Effects of Anodizing Parameters in Tartaric-Sulphuric Acid on Coating Thickness and Corrosion Resistance of Al 2024 T3 Alloy.* Journal of Minerals and Materials Characterization and Engineering, 2015. 03: p. 154-163.

212. Li, F., L. Zhang, and R.M. Metzger, *On the Growth of Highly Ordered Pores in Anodized Aluminum Oxide.* Chemistry of Materials, 1998. 10(9): p. 2470-2480.

213. Martínez-Viademonte, M.P., et al., *A review on anodizing of aerospace aluminum alloys for corrosion protection.* Coatings, 2020. 10(11): p. 1-30.

214. Iglesias-Rubianes, L., et al., *Cyclic oxidation processes during anodizing of Al–Cu alloys.* Electrochimica Acta, 2007. 52: p. 7148-7157.

215. Curioni, M., P. Skeldon, and G.E. Thompson, *5 - Anodized anti-corrosion coatings for aluminium using rare earth metals*, in *Rare Earth-Based Corrosion Inhibitors*, M. Forsyth and B. Hinton, Editors. 2014, Woodhead Publishing: Boston. p. 143-162.

216. Wang, H. and H.W. Wang, *Analysis on porous aluminum anodic oxide film formed in Re–OA–H3PO4 solution.* Materials Chemistry and Physics, 2006. 97(2): p. 213-218.

217. Smith, G.F. and C.A. Getz, *Cerate Oxidimetry.* Industrial & Engineering Chemistry Analytical Edition, 1938. 10(4): p. 191-195.

218. Khan, M.F., et al., *Achieving non-adsorptive anodized film on Al-2024 alloy: Surface and electrochemical corrosion investigation.* Surfaces and Interfaces, 2019. 15: p. 78-88.

219. Mohammadi, M., et al., *Corrosion behavior of 2024 aluminum alloy anodized in sulfuric acid containing inorganic inhibitor.* TMS Light Metals, 2013: p. 509-513.

220. Moutarlier, V., et al., *Electrochemical characterisation of anodic oxidation films formed in presence of corrosion inhibitors.* Applied Surface Science, 2001. 183(1-2): p. 1-9.

221. Yasakau, K.A., M.L. Zheludkevich, and M.G.S. Ferreira, *Lanthanide Salts as Corrosion Inhibitors for AA5083. Mechanism and Efficiency of Corrosion Inhibition.* Journal of The Electrochemical Society, 2008. 155(5): p. 169-177.

222. Liu, X., et al., *In-situ fabrication of Ce-rich CeO2 nanocatalyst for efficient CO oxidation.* Journal of Alloys and Compounds, 2019. 792: p. 644-651.

223. Moutarlier, V., et al., *Characterisation of the anodic layers formed on 2024 aluminium alloy, in tetraborate electrolyte containing molybdate ions.* Applied Surface Science, 2005. 252(5): p. 1739-1746.

224. Yin, B., et al., *Novel strategy in increasing stability and corrosion resistance for super-hydrophobic coating on aluminum alloy surfaces.* Applied Surface Science, 2011. 258(1): p. 580-585.

225. Savas, T.P. and J.C. Earthman, *Fatigue Crack Nucleation Studies on Sulfuric Acid Anodized 7075-T73 Aluminum.* Journal of Materials Engineering and Performance, 2014. 23(6): p. 2131-2138.

226. Rateick, R.G., et al., *Relationship of microstructure to fatigue strength loss in anodised aluminium–copper alloys.* Materials Science and Technology, 2005. 21(10): p. 1227-1235.

227. Sadeler, R., *Effect of a commercial hard anodizing on the fatigue property of a 2014-T6 aluminium alloy.* Journal of Materials Science, 2006. 41: p. 5803-5809.

228. Zhao, X., et al., *An Analysis of Mechanical Properties of Anodized Aluminum Film at High Stress.* Surface Review and Letters, 2015. 22(1). 1550002.

229. Lee, E., Y. Jeong, and S. Kim, *S-N Fatigue Behavior of Anodized 7050-T7451 Produced in Different Electrolytes.* Metallurgical and Materials Transactions, 2012. 43: p. 2002–2011.

230. Yoganandan, G., et al., *Surface and Electrochemical Characteristics of Novel Chromate-Free Mn-V Oxyanion Sealed Tartaric–Sulfuric Acid Anodized Coating.* Journal of Materials Engineering and Performance, 2018. 27(11): p. 6175-6188.

231. Lee, W. and S.J. Park, *Porous anodic aluminum oxide: Anodization and templated synthesis of functional nanostructures.* Chemical Reviews, 2014. 114(15): p. 7487-7556.

232. Costenaro, H., et al., *Corrosion resistance of 2524 Al alloy anodized in tartaric-sulphuric acid at different voltages and protected with a TEOS-GPTMS hybrid sol-gel coating.* Surface and Coatings Technology, 2017. 324: p. 438-450.

233. Terada, M., et al., *Corrosion resistance of tartaric-sulfuric acid anodized AA2024-T3 sealed with Ce and protected with hybrid sol–gel coating.* Surface and Coatings Technology, 2019. 372: p. 422-426.

234. Whelan, M., J. Cassidy, and B. Duffy, *Sol–gel sealing characteristics for corrosion resistance of anodised aluminium.* Surface and Coatings Technology, 2013. 235: p. 86-96.

235. Whelan, M., et al., *Optimization of Anodic Oxidation of Aluminum for Enhanced Adhesion and Corrosion Properties of Sol-Gel Coatings.* Journal of The Electrochemical Society, 2016. 163: p. C205-C212.

236. *Departments and Agencies of the Department of Defense, Military specification anodic coatings for aluminum and aluminum alloys (MIL-A-8625F)*. 1993.

237. Ma, Y., et al., *Fabrication of Self-Ordered Alumina Films with Large Interpore Distance by Janus Anodization in Citric Acid.* Scientific Reports, 2016. 6. 39165.

238. Bodor, A., et al., *Slow dynamics of aluminium-citrate complexes studied by 1H- and 13C-NMR spectroscopy.* Coordination Chemistry Reviews, 2002. 228(2): p. 163-173.

6. Bibliography

239. Ma, Y., et al., *Pore Nucleation Mechanism of Self-Ordered Alumina with Large Period in Stable Anodization in Citric Acid.* Journal of The Electrochemical Society, 2018. 165: p. E311-E317.

240. Lide, D.R., *CRC Handbook of Chemistry and Physics: A Ready-Reference of Chemical and Physical Data, 85th ed* Journal of the American Chemical Society, 2005. 127(12): p. 4542-4542.

241. Wang, H. and R. Akid, *Encapsulated cerium nitrate inhibitors to provide high-performance anti-corrosion sol–gel coatings on mild steel.* Corrosion Science, 2008. 50(4): p. 1142-1148.

242. Tiringer, U., et al., *Self-healing effect of hybrid sol-gel coatings based on GPTMS, TEOS, SiO2 nanoparticles and Ce(NO3)3 applied on aluminum alloy 7075-T6.* Journal of the Electrochemical Society, 2018. 165(5): p. C213-C225.

243. van Put, M.A., et al., *Potentiodynamic anodizing of aluminum alloys in Cr(VI)-free electrolytes.* Surface and Interface Analysis, 2016. 48(8): p. 946-952.

244. Wittmar, A., et al., *Simple preparation routes for corrosion protection hybrid sol-gel coatings on AA 2024.* Surface and Interface Analysis, 2012. 44(1): p. 70-77.

245. Pirhady, N., S. Sanjabi, and T. Shahrabi, *Evolution of corrosion protection performance of hybrid silica based sol-gel nanocoatings by doping inorganic inhibitor.* Materials and Corrosion, 2011. 62(5): p. 411-415.

246. Trentin, A., et al., *Dual Role of Lithium on the Structure and Self-Healing Ability of PMMA-Silica Coatings on AA7075 Alloy.* ACS Applied Materials and Interfaces, 2019. 11(43): p. 40629-40641.

247. Bartolomé, M.J., et al., *Changes in the specific surface area of porous aluminium oxide films during sealing.* Surface and Coatings Technology, 2006. 200(14): p. 4530-4537.

248. Cambon, J.-B., et al., *Effect of cerium on structure modifications of a hybrid sol–gel coating, its mechanical properties and anti-corrosion behavior.* Materials Research Bulletin, 2012. 47(11): p. 3170-3176.

249. Visser, P., H. Terryn, and J.M.C. Mol, *Active corrosion protection of various aluminium alloys by lithium-leaching coatings.* Surface and Interface Analysis, 2019. 51(12): p. 1276-1287.

250. Visser, P., et al., *Electrochemical Evaluation of Corrosion Inhibiting Layers Formed in a Defect from Lithium-Leaching Organic Coatings.* Journal of The Electrochemical Society, 2017. 164: p. 396-406.

251. Visser, P., et al., *The corrosion protection of AA2024-T3 aluminium alloy by leaching of lithium-containing salts from organic coatings.* Faraday Discussions, 2015. 180(0): p. 511-526.

252. Tiringer, U., et al., *Hybrid sol–gel coatings based on GPTMS/TEOS containing colloidal SiO2 and cerium nitrate for increasing corrosion protection of aluminium alloy 7075-T6.* Journal of Sol-Gel Science and Technology, 2018. 85: p. 546–557.

253. Rosero-Navarro, N.C., et al., *Optimization of hybrid sol–gel coatings by combination of layers with complementary properties for corrosion protection of AA2024.* Progress in Organic Coatings, 2010. 69(2): p. 167-174.

254. Castro, Y., E. Özmen, and A. Durán, *Integrated self-healing coating system for outstanding corrosion protection of AA2024.* Surface and Coatings Technology, 2020. 387. 125521.

255. Bonora, P.L., F. Deflorian, and L. Fedrizzi, *Electrochemical impedance spectroscopy as a tool for investigating underpaint corrosion.* Electrochimica Acta, 1996. 41(7): p. 1073-1082.

256. Thai, T.T., et al., *Influence of the sol-gel mesoporosity on the corrosion protection given by an epoxy primer applied on aluminum alloy 2024 –T3.* Progress in Organic Coatings, 2018. 121: p. 53-63.

257. Zheludkevich, M.L., et al., *Nanostructured sol–gel coatings doped with cerium nitrate as pre-treatments for AA2024-T3: Corrosion protection performance.* Electrochimica Acta, 2005. 51(2): p. 208-217.

258. Thai, T.T., A.T. Trinh, and M.-G. Olivier, *Hybrid sol–gel coatings doped with cerium nanocontainers for active corrosion protection of AA2024.* Progress in Organic Coatings, 2020. 138. 105428.

259. Tiringer, U., et al., *The effects of cerium ions on the curing, polymerisation and condensation of hybrid sol-gel coatings.* Journal of Non-Crystalline Solids, 2019. 510: p. 93-100.

260. Visser, P., et al., *Lithium salts as leachable corrosion inhibitors and potential replacement for hexavalent chromium in organic coatings for the protection of aluminum alloys.* Journal of Coatings Technology and Research, 2016. 13: p. 1-10.

261. Nicu, M., et al., *Use of lithium nitrate as a potentially corrosion inhibitor for radioactive aluminium in cementing systems.* Romanian Journal of Physics, 2015. 60: p. 1193-1202.

262. Guo Jianwei and L. Chenghao, *Inhibition effect of lithium nitrate on carbon steel corrosion in high concentration lithium bromide solution at 173℃.* Corrosion Science and Technology Protection, 2002. 2(4): p. 197-201.

263. Lakshmi, R.V., et al., *EIS and XPS studies on the self-healing properties of Ce-modified silica-alumina hybrid coatings: Evidence for Ce(III) migration.* Surface and Coatings Technology, 2017. 309: p. 363-370.

264. Yu, P., et al., *The Phase Stability of Cerium Species in Aqueous Systems II. The CeIII/IV–H2O–H2O2/O2 Systems. Equilibrium Considerations and Pourbaix Diagram Calculations.* Journal of The Electrochemical Society, 2006. 153(1): p. 74-79.

265. De Damborenea, J., A. Conde, and M.A. Arenas, *Corrosion inhibition with rare earth metal compounds in aqueous solutions*, in *Rare Earth-Based Corrosion Inhibitors*, M. Forsyth, Editor. 2014, Woodhead Publishing Series: Boston. p. 84-116.

266. Santana, I., et al., *Corrosion protection of carbon steel by silica-based hybrid coatings containing cerium salts: Effect of silica nanoparticle content.* Surface and Coatings Technology, 2015. 265: p. 106-116.

267. Kaseem, M., et al., *Recent progress in surface modification of metals coated by plasma electrolytic oxidation: Principle, structure, and performance.* Progress in Materials Science, 2020. 100735.

268. Chen, F., P. Yu, and Y. Zhang, *Healing effects of LDHs nanoplatelets on MAO ceramic layer of aluminum alloy.* Journal of Alloys and Compounds, 2017. 711: p. 342-348.

269. Tsunekawa, S., Y. Aoki, and H. Habazaki, *Two-step plasma electrolytic oxidation of Ti-15V-3Al-3Cr-3Sn for wear-resistant and adhesive coating.* Surface and Coatings Technology, 2011. 205(19): p. 4732-4740.

270. Matykina, E., et al., *AC PEO of aluminium with porous alumina precursor films.* Surface and Coatings Technology, 2010. 205(6): p. 1668-1678.

271. Ikonopisov, S., *Theory of electrical breakdown during formation of barrier anodic films.* Electrochimica Acta, 1977. 22(10): p. 1077-1082.

272. Fattah-alhosseini, A., S.O. Gashti, and M. Molaie, *Effects of Disodium Phosphate Concentration (Na2HPO4·2H2O) on Microstructure and Corrosion Resistance of Plasma Electrolytic Oxidation (PEO) Coatings on 2024 Al Alloy.* Journal of Materials Engineering and Performance, 2018. 27(2): p. 825-834.

273. Du, K., et al., *Effect of PEO Coating Microstructure on Corrosion of Al 2024.* Journal of the Electrochemical Society, 2012. 159: p. C597-C606.

274. Zheng, H.Y., et al., *The effects of Na2WO4 concentration on the properties of microarc oxidation coatings on aluminum alloy.* Materials Letters, 2005. 59: p. 139-142.

275. Sykes, J., et al., *Anodic film formation on high strength aluminium alloy FVS0812.* 1997. 32(18): p. 4909-4916.

276. Fratila-Apachitei, L.E., et al., *A transmission electron microscopy study of hard anodic oxide layers on AlSi(Cu) alloys.* Electrochimica Acta, 2004. 49(19): p. 3169-3177.

277. Xiang, N., et al., *Effects of current density on microstructure and properties of plasma electrolytic oxidation ceramic coatings formed on 6063 aluminum alloy.* Transactions of Nonferrous Metals Society of China, 2016. 26(3): p. 806-813.

278. Tedim, J., et al., *Effect of surface treatment on the performance of LDH conversion films.* ECS Electrochemistry Letters, 2014. 3(1): p. C4-C8.

279. Cao, Y., et al., *Enhanced Corrosion Resistance of Superhydrophobic Layered Double Hydroxide (LDH) Films with Long-Term Stability on Al Substrate.* ACS Applied Materials & Interfaces, 2018. 10(17): p. 15150-15162.

280. Hao, L., et al., *Fabrication and anticorrosion properties of composite films of silica/layered double hydroxide.* Surface and Coatings Technology, 2017. 326: p. 200-206.

281. Zhang, M., et al., *Insights into the Use of Metal–Organic Framework As High-Performance Anticorrosion Coatings.* ACS Applied Materials & Interfaces, 2018. 10(3): p. 2259-2263.

282. Ay, A., B. Zümreoglu-Karan, and L. Mafra, *A Simple Mechanochemical Route to Layered Double Hydroxides: Synthesis of Hydrotalcite-Like Mg-Al-NO3-LDH by Manual Grinding in a Mortar.* Zeitschrift für anorganische Chemie, 2009. 635: p. 1470-1475.

283. A. Sertsova, A., E. N. Subcheva, and E. V. Yurtov, *Synthesis and study of structure formation of layered double hydroxides based on Mg, Zn, Cu, and Al.* Synthesis and Properties of Inorganic Compounds, 2015. 60: p. 23-32.

284. Dou, B., et al., *Growth behaviors of layered double hydroxide on microarc oxidation film and anti-corrosion performances of the composite film.* Journal of the Electrochemical Society, 2016. 163(14): p. C917-C927.

285. Zhang, Y., et al.,, *Investigating the Growth Behavior of LDH Layers on MAO- coated Aluminum Alloy: Influence of Microstructure and Surface Element.* International Journal of Electrochemical Science, 2018. 13: p. 610-620.

286. Li, Y., et al., *Enhanced protective Zn–Al layered double hydroxide film fabricated on anodized 2198 aluminum alloy.* Journal of Alloys and Compounds, 2015. 630: p. 29-36.

287. Kuznetsov, B., et al., *Sealing of tartaric sulfuric (TSA) anodized AA2024 with nanostructured LDH layers.* RSC Advances, 2016. 6(17): p. 13942-13952.

288. Evans, D.G. and R.C.T. Slade, *Structural Aspects of Layered Double Hydroxides*, in *Layered Double Hydroxides*, X. Duan and D.G. Evans, Editors. 2006, Springer Berlin. p. 1-87.

289. Radha, A.V., P. Vishnu Kamath, and C. Shivakumara, *Mechanism of the anion exchange reactions of the layered double hydroxides (LDHs) of Ca and Mg with Al.* Solid State Sciences, 2005. 7(10): p. 1180-1187.

290. Chi, L., et al., *Layered Double Hydroxides Precursor as Chloride Inhibitor: Synthesis, Characterization, Assessment of Chloride Adsorption Performance.* Materials, 2018. 11. 2537.

291. Galvão, T.L.P., et al., *Control of crystallite and particle size in the synthesis of layered double hydroxides: Macromolecular insights and a complementary modeling tool.* Journal of Colloid and Interface Science, 2016. 468: p. 86-94.

292. Cussler, E.L., *Diffusion: Mass Transfer in Fluid Systems*, ed. E.L. Cussler. 2009: Cambridge university press.

293. Serdechnova, M., et al., *PEO Coatings with Active Protection Based on In-Situ Formed LDH-Nanocontainers.* Journal of The Electrochemical Society, 2017. 164: p. C36-C45.

294. Lv, G., et al., *Characteristic of ceramic coatings on aluminum by plasma electrolytic oxidation in silicate and phosphate electrolyte.* Applied Surface Science, 2006. 253(5): p. 2947-2952.

295. Yeh, S.-C., et al., *Influences of urea and sodium nitrite on surface coating of plasma electrolytic oxidation.* Applied Surface Science, 2015. 356: p. 135-141.

296. Kaseem, M., et al., *Effect of sodium benzoate on corrosion behavior of 6061 Al alloy processed by plasma electrolytic oxidation.* Surface and Coatings Technology, 2015. 283: p. 268-273.

297. Wang, K., et al., *Effects of electrolytes variation on formation of oxide layers of 6061 Al alloys by plasma electrolytic oxidation.* Transactions of Nonferrous Metals Society of China, 2009. 19(4): p. 866-870.

298. Shimizu, K., G.E. Thompson, and G.C. Wood, *The electrical breakdown during anodizing of high purity aluminium in borate solutions.* Thin Solid Films, 1982. 92(3): p. 231-241.

299. Rudnev, V.S., et al., *Wear-resistant oxide coatings on aluminum alloy formed in borate and silicate aqueous electrolytes by plasma electrolytic oxidation.* Protection of Metals and Physical Chemistry of Surfaces, 2017. 53(3): p. 466-474.

300. Cheng, Y.-l., et al., *Plasma electrolytic oxidation of an Al-Cu-Li alloy in alkaline aluminate electrolytes: A competition between growth and dissolution for the initial ultra-thin films.* Electrochimica Acta, 2014. 138: p. 417-429.

301. Sato, T., *Studies on the hydrolysis of sodium aluminate solutions. XVII. Effect of the addition of some carbohydrates on the particles precipitated by the decomposition of sodium aluminate solutions with seeding.* Journal of Applied Chemistry, 1959. 9(1): p. 50-58.

302. Sahu, N.K., et al., *Effect of urea on decomposition of sodium aluminate solution.* Journal of the Taiwan Institute of Chemical Engineers, 2014. 45(3): p. 815-822.

303. Voevodin, A.A., et al., *Characterization of wear protective Al-Si-O coatings formed on Al-based alloys by micro-arc discharge treatment.* Surface and Coatings Technology, 1996. 86-87: p. 516-521.

304. Wei-Chao, G., et al., *Investigation of morphology and composition of plasma electrolytic oxidation coatings in systems of Na2SiO3–NaOH and (NaPO3)6–NaOH.* Journal of Materials Processing Technology, 2007. 182(1): p. 28-33.

305. Kamil, M.P., M. Kaseem, and Y.G. Ko, *Soft plasma electrolysis with complex ions for optimizing electrochemical performance.* Scientific Reports, 2017. 7(1). 44458.

306. Al-Dalama, K., B. Aravind, and A. Stanislaus, *Influence of complexing agents on the adsorption of molybdate and nickel ions on alumina.* Applied Catalysis, 2005. 296(1): p. 49-53.

307. Perry, D., *Handbook of Inorganic Compounds*, ed. D. Perry. Vol. 1. 2011: CRC Press. 1250-1456.

308. Stojadinovic, S., et al., *Characterization of the plasma electrolytic oxidation of aluminium in sodium tungstate.* Corrosion Science, 2010. 52(10): p. 3258-3265.

309. Zein El Abedin, S., *Role of chromate, molybdate and tungstate anions on the inhibition of aluminiumin chloride solutions.* Journal of Applied Electrochemistry, 2001. 31: p. 711-718.

310. Kharitonov, D.S., et al., *Surface and corrosion properties of AA6063-T5 aluminum alloy in molybdate-containing sodium chloride solutions.* Corrosion Science, 2020. 171. 108658.

311. Jakab, M.A., F. Presuel, and J. Scully, *Critical Concentrations Associated with Cobalt, Cerium, and Molybdenum Inhibition of AA2024-T3 Corrosion: Delivery from Al-Co-Ce(Mo) Alloys , March 2005.* Corrosion, 2005. 61: p. 123-142.

312. Kharitonov, D., et al., *Corrosion inhibition of AA6063 alloy by vanadates in alkaline media.* Materialwissenschaft und Werkstofftechnik, 2017. 48: p. 646-660.

313. Zeng, X.X., et al., *The effects of surface treatment and stannate as an electrolyte additive on the corrosion and electrochemical performances of pure aluminum in an alkaline methanol–water solution.* Materials Chemistry and Physics, 2010. 121(3): p. 459-464.

314. Chang, X., et al., *Corrosion and Anodic Behaviors of Pure Aluminum in a Novel Alkaline Electrolyte.* Acta Physico-Chimica Sinica, 2008. 24(9): p. 1620-1624.

315. Rogov, A.B., *Plasma electrolytic oxidation of A1050 aluminium alloy in homogeneous silicate-alkaline electrolytes with edta4− complexes of Fe, Co, Ni, Cu, La and Ba under alternating polarization conditions.* Materials Chemistry and Physics, 2015. 167: p. 136-144.

316. Hinton, B.R.W., *Chapter 140 Corrosion prevention and control*, in *Handbook on the Physics and Chemistry of Rare Earths*, B.R.W. Hinton, Editor. 1995, Elsevier. p. 29-92.

317. Toorani, M., M. Aliofkhazraei, and A. Sabour Rouhaghdam, *Microstructural, protective, inhibitory and semiconducting properties of PEO coatings containing CeO2 nanoparticles formed on AZ31 Mg alloy.* Surface and Coatings Technology, 2018. 352: p. 561-580.

318. Matykina, E., et al., *Recent advances in energy efficient PEO processing of aluminium alloys.* Transactions of Nonferrous Metals Society of China, 2017. 27(7): p. 1439-1454.

319. Wen, L., et al., *Corrosion evaluation of microarc oxidation coatings formed on 2024 aluminium alloy.* Corrosion Science, 2010. 52(8): p. 2687-2696.

320. Zhu, Z., et al., *The formation of metallic W and amorphous phase in the plasma electrolytic oxidation coatings on an Al alloy from tungstate-containing electrolyte.* Surface and Coatings Technology, 2019. 361: p. 176-187.

321. Jovović, J., et al., *Spectroscopic characterization of plasma during electrolytic oxidation (PEO) of aluminium.* Surface and Coatings Technology, 2011. 206(1): p. 24-28.

322. Lee, J.H. and S.J. Kim, *Enhancement of wettability by wet surface modification and application of rare-earth element in sealing of ceramic oxide thin film on Al alloy.* Journal of Nanoscience and Nanotechnology, 2016. 16(11): p. 11797-11801.

323. Czelej, K., et al., *Atomic-scale computational design of hydrophobic RE surface-doped Al2O3 and TiO2.* Physical Chemistry Chemical Physics, 2017. 19: p. 21119-21126.

324. Xiang, N., et al., *Formation of corrosion resistant plasma electrolytic oxidation coatings on aluminium alloy with addition of sodium tungstate species.* Corrosion Engineering, Science and Technology, 2015. 51: p. 146-154.

325. Shen, D., et al., *Effect of cerium and lanthanum additives on plasma electrolytic oxidation of AZ31 magnesium alloy.* Journal of Rare Earths, 2013. 31(12): p. 1208-1213.

326. Arunne, T., et al., *Fabrication of multifunctional black PEO coatings on AA7075 for spacecraft applications.* Surface and Coatings Technology, 2016. 307: p. 735-746.

327. Bajat, J., et al., *Corrosion Stability of Oxide Coatings Formed by Plasma Electrolytic Oxidation of Aluminum: Optimization of Process Time.* Corrosion, 2013. 69(7): p. 693–702.

328. Sharifi, H., et al., *A Review on Adhesion Strength of PEO Coatings by Scratch Test Method.* Surface Review and Letters, 2017. 25 (3). 1830004.

329. *Method for producing a hard coating with high corrosion resitance on articles made of anodizable metals or alloys, WO2006007972*. 2006.

330. Shrestha, S., et al., *Some preliminary evaluations of black coating on aluminium AA2219 alloy produced by plasma electrolytic oxidation (PEO) process for space applications.* European Space Agency, (Special Publication) ESA SP, 2003. 540: p. 57-65.

331. Mokhtari, S., et al., *Development of super-hydrophobic surface on Al 6061 by anodizing and the evaluation of its corrosion behavior.* Surface and Coatings Technology, 2017. 324: p. 99-105.

332. He, T., et al., *Super-hydrophobic surface treatment as corrosion protection for aluminum in seawater.* Corrosion Science, 2009. 51(8): p. 1757-1761.

333. Norek, M. and A. Krasiński, *Controlling of water wettability by structural and chemical modification of porous anodic alumina (PAA): Towards super-hydrophobic surfaces.* Surface and Coatings Technology, 2015. 276: p. 464-470.

334. Varshney, P., S.S. Mohapatra, and A. Kumar, *Superhydrophobic coatings for aluminium surfaces synthesized by chemical etching process.* International Journal of Smart and Nano Materials, 2016. 7(4): p. 248-264.

335. Mori, Y., et al., *Characteristics and corrosion resistance of plasma electrolytic oxidation coatings on AZ31B Mg alloy formed in phosphate – Silicate mixture electrolytes.* Corrosion Science, 2014. 88: p. 254-262.

336. Zhu, L., et al., *A mechanism for the growth of a plasma electrolytic oxide coating on Al.* Electrochimica Acta, 2016. 208: p. 296-303.

337. Lima, R., et al., *Plasma Species and Coating Compositions in Aluminum Treated by PEO Using Shot Square Pulse.* Materials Research, 2020. 23: p. 1234-1244.

338. Curran, J.A. and T.W. Clyne, *Thermo-physical properties of plasma electrolytic oxide coatings on aluminium.* Surface and Coatings Technology, 2005. 199(2): p. 168-176.

339. Xue, W., et al., *Analysis of phase distribution for ceramic coatings formed by microarc oxidation on aluminum alloy.* Journal of the American Ceramic Society, 1998. 81(5): p. 1365-1368.

340. Chang, Q., et al., *Hydrophilic modification of Al2O3 microfiltration membrane with nano-sized γ-Al2O3 coating.* Desalination, 2010. 262(1): p. 110-114.

341. Daryaei, E., M. Reza Rahimi Tabar, and A.Z. Moshfegh, *Surface roughness analysis of hydrophilic SiO2/TiO2/glass nano bilayers by the level crossing approach.* Physica A: Statistical Mechanics and its Applications, 2013. 392(9): p. 2175-2181.

342. Anaya, S., et al., *γ-Alumina Modification with Long Chain Carboxylic Acid Surface Nanocrystals for Biocompatible Polysulfone Nanocomposites.* ACS applied materials & interfaces, 2014. 6(16): p. 14460–14468.

343. Megias-Alguacil, D., et al., *Contact angle and adsorption behavior of carboxylic acids on α-Al2O3 surfaces.* Journal of Colloid and Interface Science, 2011. 353(2): p. 512-518.

344. Yin, Y., et al., *Structure stability and corrosion inhibition of super-hydrophobic film on aluminum in seawater.* Applied Surface Science, 2008. 255(5, Part 2): p. 2978-2984.

345. Li, S., et al., *Tribological performance of Mg/Al/Ce layered double hydroxides nanoparticles and intercalated products as lubricant additives.* Applied Surface Science, 2015. 353: p. 643-650.

346. Abdolah Zadeh, M., et al., *Synergetic active corrosion protection of AA2024-T3 by 2D-anionic and 3D-cationic nanocontainers loaded with Ce and mercaptobenzothiazole.* Corrosion Science, 2018. 135: p. 35-45.

347. Tedim, J., et al., *Enhancement of Active Corrosion Protection via Combination of Inhibitor-Loaded Nanocontainers.* ACS applied materials & interfaces, 2010. 2: p. 1528-35.

348. Carneiro, J., et al., *Polyelectrolyte-modified Layered double hydroxide nanocontainers as vehicles for combined inhibitors.* Royal Society of Chemistry Advances, 2015. 5: p. 39916-39929.

349. Wu, J., et al., *In situ formation of decavanadate-intercalated layered double hydroxide films on AA2024 and their anti-corrosive properties when combined with hybrid sol gel films.* Materials, 2017. 10 (4). 426.

350. Zhang, Y., et al., *Enhancement of active anticorrosion via Ce-doped Zn-Al layered double hydroxides embedded in sol-gel coatings on aluminum alloy.* Journal of Wuhan University of Technology-Mater. Scientific edition., 2017. 32(5): p. 1199-1204.

351. Liu, Y., et al., *One-pot synthesis of NiAl–CO3 LDH anti-corrosion coatings from CO2-saturated precursors.* Royal Society of Chemistry Advances, 2015. 5: p. 29552-29557.

352. Zhang, F., et al., *Corrosion Resistance of Superhydrophobic Mg–Al Layered Double Hydroxide Coatings on Aluminum Alloys.* Acta Metallurgica Sinica (English Letters), 2015. 28: p. 1373–1381.

353. Zhang, F., et al., *Corrosion of in-situ grown MgAl-LDH coating on aluminum alloy.* Transactions of Nonferrous Metals Society of China, 2015. 25(10): p. 3498-3504.

354. Syu, J.-H., et al., *Optically transparent Li–Al–CO3 layered double hydroxide thin films on an AZ31 Mg alloy formed by electrochemical deposition and their corrosion resistance in a dilute chloride environment.* Corrosion Science, 2013. 68: p. 238-248.

355. Zhang, Y., et al., *A facile approach to superhydrophobic LiAl-layered double hydroxide film on Al–Li alloy substrate.* Journal of Coatings Technology and Research, 2015. 12(3): p. 595-601.

356. Lin, M.-C., F.-T. Chang, and J.-Y. Uan, *Synthesis of Li–Al-carbonate layered double hydroxide in a metal salt-free system.* Journal of Materials Chemistry, 2010. 20(31): p. 6524-6530.

357. Lin, K., et al., *Enhanced corrosion resistance of LiAl-layered double hydroxide (LDH) coating modified with a Schiff base salt on aluminum alloy by one step in-situ synthesis at low temperature.* Applied Surface Science, 2019. 463: p. 1085-1096.

358. Wang, D.-Y., et al., *Synthesis of Organo Cobalt Aluminum Layered Double Hydroxide via a Novel Single-Step Self-Assembling Method and Its Use as Flame Retardant Nanofiller in PP.* Langmuir: The ACS Journal of Surfaces and Colloids, 2010. 26: p. 14162-14169.

359. Huang, S., et al., *Immobilization of Co-Al Layered Double Hydroxides on Graphene Oxide Nanosheets: Growth Mechanism and Supercapacitor Studies.* ACS applied materials & interfaces, 2012. 4: p. 2242-2249.

360. Wen, X., et al., *The effects of element Cu on the electrochemical performances of Zinc-Aluminum-hydrotalcites in Zinc/Nickel secondary battery.* Electrochimica Acta, 2015. 180: p. 451-459.

361. Guzmán-Vargas, A., et al., *Adsorption and subsequent partial photodegradation of methyl violet 2B on Cu/Al layered double hydroxides.* Applied Surface Science, 2016. 363: p. 372-380.

362. Chitrakar, R., et al., *Fe–Al layered double hydroxides in bromate reduction: Synthesis and reactivity.* Journal of Colloid and Interface Science, 2011. 354(2): p. 798-803.

363. Zhong, Y., et al., *Fe(II)–Al(III) layered double hydroxides prepared by ultrasound-assisted co-precipitation method for the reduction of bromate.* Journal of Hazardous Materials, 2013. 250-251: p. 345-353.

364. Wang, T., et al., *The electrochemical performances of Zn Sn Al-hydrotalcites in ZŽ Ni secondary cells.* 2014. 257: p. 174-180.

365. Millange, F., et al., *Efficient Separation of Terephthalate and Phthalate Anions by Selective Ion-Exchange Intercalation in the Layered Double Hydroxide Ca2Al(OH)6·NO3·2H2O.* Chemistry of Materials, 2000. 12: p. 1990-1994.

366. Meyn, M., K. Beneke, and G. Lagaly, *Anion-exchange reactions of layered double hydroxides.* Inorganic Chemistry, 1990. 29(26): p. 5201-5207.

367. Iqbal, M., et al., *In situ Growth of CaAl-NO3--Layered Double Hydroxide Directly on Aluminum Alloy for Corrosion Resistance.* Dalton Transactions, 2019. 49: p. 3956-3964.

368. Mattoccia, A., et al., *Morphological and structural investigation of (Zn,Al) layered double hydroxides (LDH) nanoplatelets synthesized on aluminum-coated substrates.* Metallurgia Italiana, 2015. 107(9): p. 15-22.

369. Iqbal, M.A. and M. Fedel, *Effect of operating parameters on the structural growth of ZnAl layered double hydroxide on AA6082 and corresponding corrosion resistance properties.* Journal of Coatings Technology and Research, 2019. 16(5): p. 1423-1433.

370. Iqbal, M.A. and M. Fedel, *Effect of synthesis conditions on the controlled growth of MgAl-LDH corrosion resistance film: Structure and corrosion resistance properties.* Coatings, 2019. 9 (1). 30.

371. Yokoi, T., et al., *Synthesis of layered double hydroxide coatings with an oriented structure and controllable thickness on aluminium substrates.* Crystallography Engineering Communications, 2016. 18(7): p. 1207-1214.

372. Dutta, P.K. and M. Puri, *Anion exchange in lithium aluminate hydroxides.* The Journal of Physical Chemistry, 1989. 93(1): p. 376-381.

373. Yang, B., et al., *A superhydrophobic and corrosion resistant layered double hydroxides coating on AA2099-T83 Al-Cu-Li alloy.* Surface and Coatings Technology, 2021. 405. 126629.

374. Wang, Y., et al., *The electrochemical determination of l-cysteine at a Ce-doped Mg–Al layered double hydroxide modified glassy carbon electrode.* Electrochimica Acta, 2012. 70: p. 193-198.

375. Iqbal, M. and M. Fedel, *Protective Cerium-Based Layered Double Hydroxides Thin Films Developed on Anodized AA6082.* Advances in Materials Science and Engineering, 2020. 2020(1): p. 1-12.

376. Vieille, L., et al., *Hydrocalumite and Its Polymer Derivatives. Part 1. Reversible Thermal Behavior of Friedel's Salt: A Direct Observation by Means of High-Temperature in situ Powder X-Ray Diffraction.* Chemistry of materials, 2003. 35: p. 4361–4368.

377. Takeno, N., *Atlas of Eh-pH diagrams - Intercomparison of thermodynamic databases*. 2005.

378. Zhang, Y., et al., *LDHs/graphene film on aluminum alloys for active protection.* Applied Surface Science, 2018. 433: p. 927-933.

379. Choudary, B., et al., *Tungstate-Exchanged Mg-Al-LDH catalyst: An Eco-Compatible Route for the Oxidation of Sulfides in Aqueous Medium.* Journal of the Chemical Society, Perkin Transactions, 2002. 1: p. 2069-2074.

380. Gardner, E. and T.J. Pinnavaia, *On the nature of selective olefin oxidation catalysts derived from molybdate- and tungstate-intercalated layered double hydroxides.* Applied Catalysis A: General, 1998. 167(1): p. 65-74.

381. Maciuca, A.-L., et al., *Mild oxidation of tetrahydrothiophene to sulfolane over V-, Mo- and W-containing layered double hydroxides.* Applied Catalysis A: General, 2008. 338(1): p. 1-8.

382. Wierzbicka, E., et al., *Calcium Doped Flash-PEO Coatings for Corrosion Protection of Mg Alloy.* Metals, 2020. 10 (7). 916.

383. Szabados, M., et al., *Ultrasonically-enhanced mechanochemical synthesis of CaAl-layered double hydroxides intercalated by a variety of inorganic anions.* Ultrasonics Sonochemistry, 2016. 31: p. 409-416.

384. Milagres, J.L., et al., *Preparation and evaluation of the Ca-Al layered double hydroxide for removal of copper(II), nickel(II), zinc(II), chromium(VI) and phosphate from aqueous solutions.* Journal of Environmental Chemical Engineering, 2017. 5(6): p. 5469-5480.

385. Varga, G., et al., *Mn(II)-amino acid complexes intercalated in CaAl-layered double hydroxide - Well-characterized, highly efficient, recyclable oxidation catalysts.* Journal of Catalysis, 2016. 335: p. 125-134.

386. Yang, C., et al., *Synthesis and characterization of Mn intercalated Mg-Al hydrotalcite.* Journal of Colloid and Interface Science, 2016. 479: p. 115-120.

387. Dietmann, K.M., et al., *Layered Double Hydroxides with Intercalated Permanganate and Peroxydisulphate Anions for Oxidative Removal of Chlorinated Organic Solvents Contaminated Water.* Minerals, 2020. 10 (5). 462.

388. Hem, J.D., *Chemical equilibria and rates of manganese oxidation*, in *Geological survey water-supply*. 1963. Visited: 21/12/2020. Available from: https://pubs.usgs.gov/wsp/1667a/report.pdf.

389. Madden, S.B. and J.R. Scully, *Inhibition of AA2024-T351 Corrosion Using Permanganate.* Journal of The Electrochemical Society, 2014. 161(3): p. C162-C175.

390. Kulinich, S.A., M. Farzaneh, and X.W. Du, *Growth of corrosion-resistant manganese oxide coatings on an aluminum alloy.* Inorganic Materials, 2007. 43(9): p. 956-963.

391. Subasri, R., et al., *Environmentally friendly Zn–Al layered double hydroxide (LDH)-based sol–gel corrosion protection coatings on AA 2024-T3.* Journal of Coatings Technology and Research, 2019. 16(5): p. 1447-1463.

392. Pardo, A., et al., *The effect of cerium and lanthanum surface treatments on early stages of oxidation of A361 aluminium alloy at high temperature.* Applied Surface Science, 2007. 254(2): p. 586-595.

393. Revilla, R., H. Terryn, and I. Graeve, *Role of Si in the Anodizing Behavior of Al-Si Alloys: Additive Manufactured and Cast Al-Si10-Mg.* Journal of The Electrochemical Society, 2018. 165: p. C532-C541.

394. Thijs, L., et al., *Fine-structured aluminium products with controllable texture by selective laser melting of pre-alloyed AlSi10Mg powder.* Acta Materialia, 2013. 61(5): p. 1809-1819.

395. Mohedano, M., et al., *PEO of rheocast A356 Al alloy: energy efficiency and corrosion properties.* Surface and Interface Analysis, 2016. 48(8): p. 953-959.

396. Zhu, B., et al., *A study of formation and growth of the anodised surface layer on cast Al-Si alloys based on different analytical techniques.* Materials & Design, 2016. 101: p. 254-262.

397. Gulec, A.E., Y. Gencer, and M. Tarakci, *The characterization of oxide based ceramic coating synthesized on Al–Si binary alloys by microarc oxidation.* Surface and Coatings Technology, 2015. 269: p. 100-107.

398. A Wahab, J. and M. Derman, *Characterization of Porous Anodic Aluminium Oxide Film on Aluminium Templates Formed in Anodizing Process.* Advanced Materials Research, 2011. 173: p. 55-60.

399. Övündür, M., F. Muhaffel, and H. Cimenoglu, *Characterization and Tribological Properties of Hard Anodized and Micro Arc Oxidized 5754 Quality Aluminum Alloy.* Tribology in Industry, 2015. 34: p. 55-59.

400. Sulka, G., *Highly Ordered Anodic Porous Alumina Formation by Self-Organized Anodizing*, in *Nanostructured Materials in Electrochemistry*, A. Eftekhari, Editor. 2008, Wiley-VCH Verlag. p. 1-116.

401. Kan, W.H., et al., *Factors that affect the properties of additively-manufactured AlSi10Mg: Porosity versus microstructure.* Additive Manufacturing, 2019. 29. 100805.

402. Lysenko, V., V. Mali, and A. Anisimov, *Microhardness of Ceramics Obtained by Different Methods from Nanopowders of Different Oxides.* Athens journal of sciences, 2014: p. 269-280.

403. Li, X., et al., *Corrosion protection properties of anodic oxide coatings on an Al–Si alloy.* Surface and Coatings Technology, 2005. 200(5): p. 1994-2000.

404. Slonova, A., et al., *Formation of microplasma coatings on high-silicon aluminum alloy and their characteristics.* Protection of Metals and Physical Chemistry of Surfaces, 2012. 48: p. 86-96.

405. Rogov, A.B., et al., *AC plasma electrolytic oxidation of additively manufactured and cast AlSi12 alloys.* Surface and Coatings Technology, 2020. 399. 126116.

406. Arrabal, R., et al., *Characterization and wear behaviour of PEO coatings on 6082-T6 aluminium alloy with incorporated α-Al2O3 particles.* Surface and Coatings Technology, 2015. 269: p. 64-73.